Development and Characterization of High Performance Electrically Conductive Polymer Nanocomposite for Electromagnetic Interference (EMI) Shielding Applications

by

Saeed Habibpour

A thesis

presented to the University of Waterloo

in fulfillment of the

thesis requirement for the degree of

Doctor of Philosophy

in

Chemical Engineering (Nanotechnology)

Waterloo, Ontario, Canada, 2023

Examining Committee Membership

The following served on the Examining Committee for this thesis. The decision of the Examining Committee is by majority vote.

External Examiner:	Name: Dr. Uttandaraman Sundararaj
	Title: Professor
Supervisor(s):	Name: Dr. Aiping Yu
	Title: Professor
	Name: Dr. Chul B. Park
	Title: Distinguished Professor
Internal Member:	Name: Dr. Costas Tzoganakis
	Title: Professor
Internal Member:	Name: Dr. Tizazu Mekonnen
	Title: Associate Professor
Internal-external Member:	Name: Dr. Giovanni (John) Montesano
	Title: Associate Professor

Author's Declaration

This thesis consists of material all of which I authored or co-authored: see Statement of Contributions included in the thesis. This is a true copy of the thesis, including any required final revisions, as accepted by my examiners.

I understand that my thesis may be made electronically available to the public.

Statement of Contributions

This thesis is based on a combination of published work. Chapters are adapted from the following list of published work. I would like to acknowledge all of my co-authors for their valuable contribution. Also, I acknowledge my supervisors, Prof. Aiping Yu and Prof. Chul B. Park, who provided knowledge, ideas and directions that were pivotal in my entire research and they both were involved in manuscripts' preparation. The following outlines the contributions of each co-author:

Articles Published or Submitted in Refereed Journals

[1] Yun-Seok Jun †, **Saeed Habibpour** †, Mahdi Hamidinejad, Moon Gyu Park, Wook Ahn, Aiping Yu, Chul B. Park, "Enhanced Electrical and Mechanical Properties of Graphene Nanoribbon/ Thermoplastic Polyurethane Composites", **Carbon** (2021), 174, 305-316 (†Equal Contribution)

- Yun-Seok Jun performed the EMI shielding and dielectric performance measurements. Mahdi Hamidinejad assisted in electrical conductivity measurements. Moon Gyu Park and Wook Ahn assisted in analysis of XPS data. Yun-Seok Jun, Chul B. Park and Aiping Yu were involved in manuscript preparation. Discussions regarding the research concepts and presentation of data were continuously conducted with all contributing authors.

[2] **Saeed Habibpour**, Kiyoumars Zarshenas, Maiwen Zhang, Mahdi Hamidinejad, Li Ma, Chul B. Park, Aiping Yu, "Greatly Enhanced Electromagnetic Interference Shielding Effectiveness and Mechanical Properties of Polyaniline-Grafted $Ti_3C_2T_x$ MXene–PVDF Composites", **ACS Applied Materials & Interfaces** (2022), 14, 21521-21534

- Kiyoumars Zarshenas and Maiwen Zhang assisted in synthesis of $Ti_3C_2T_x$ MXene nanomaterial. Mahdi Hamidinejad and Li Ma assisted in EMI shielding measurements and data analysis. Aiping Yu and Chul B. Park were involved in manuscript preparation. Discussions regarding the research concepts and presentation of data were continuously conducted with all contributing authors.

[3] **Saeed Habibpour**, Yasaman Rahimi Darestani, Meysam Salari, Kiyoumars Zarshenas, Chul B. Park, Aiping Yu, "Excellent EMI Shielding Performance with Ultra High EM Wave Absorption by MXene Coated rGOnR/MXene Aerogel Based PDMS Nanocomposite", Ready to submit

- Yasaman Rahimi Darestani assisted in sample preparation and data analysis, Meysam Salari assisted in performing EMI shielding measurements and data analysis, Kiyoumars Zarshenas helped in synthesis of $Ti_3C_2T_x$ MXene nanomaterial and data analysis. Aiping Yu and Chul B. Park were involved in manuscript preparation. Discussions regarding the research concepts and presentation of data were continuously conducted with all contributing authors.

Abstract

The fast-growing pace and massive utilization of compact portable electronic and wireless telecommunication systems provided an easier life for humans. However, this positive progress has come at the expense of significant electromagnetic interference (EMI) pollution, which requires the development of highly efficient shielding materials to impede the malfunction of electronic devices and reduce its deleterious impact on human health. Although metals have been used traditionally as an excellent EMI shielding material, high density, high cost, susceptibility to corrosion, and reflection shielding mechanism limited their applications. Recently, multifunctional conductive polymer nanocomposites (CPnC) have demonstrated great promise as next-generation materials for energy management and EMI shielding components in electronic industries. Such highly desirable and multifunctional properties in CPnCs are achievable by a combination of lightweight, easy to process and chemically stable polymer matrices and a large array of nanosized conductive fillers. In this Ph.D. research, we aimed to develop multifunctional CPnCs for EMI shielding applications. Our goal was enhancing the EMI shielding effectiveness (SE) of the CPnCs, concentrating on amplifying the electromagnetic (EM) wave absorption mechanism as opposed to reflection which could potentially lead to secondary EMI pollutions.

First, narrow elongated strips of graphene with high aspect ratio and abundant edges, namely reduced graphene nanoribbons (GNR), were synthesized from multiwalled carbon nanotubes (MWCNT) through a chemically oxidative unzipping, and subsequent thermal reduction method. The purpose of this study was to gain a comprehensive understanding of how the structural modifications of MWCNTs influence the end characteristics of polymer nanocomposites, especially electrical properties and EMI shielding. GNR and parent MWCNT were added to thermoplastic polyurethane (TPU) and the electrical conductivity, the dielectric property, the EMI SE and the mechanical properties of the nanocomposites were thoroughly investigated and compared. It was found that the electrical conductivity, the EMI SE and the mechanical properties of GNR/TPU nanocomposites were far superior to those of MWCNT/TPU nanocomposites. This greatly heightened performance of GNR added

nanocomposites is mainly attributed to enhanced filler interconnections between GNRs. The individual filler particle flexibility was significantly increased when tubular multi-layered MWCNTs were opened and transformed into long, thin strips. This allows geometrical conversion from line-to-line to sheet-to-sheet contact interfaces, which considerably increases the contact area. The increased flexibility also increased the chances of forming a percolating network between fillers. In addition, the unzipping and exfoliation of MWCNTs increased the number concentration of filler particles, leading to improved electrical and mechanical performance.

To further enhance the EMI SE of the CPnCs, we synthesized $Ti_3C_2T_x$ MXene nanoflakes via the minimally intensive layer delamination (MILD) method. Then, conductive polyaniline (PA) nanofibers were grafted on the surface of the large and low-defect MXene nanoflakes via oxidant free oxidative polymerization at two different MXene to monomer ratios. To investigate the impact of MXene functionalization on electrical properties, EMI SE and mechanical properties of the CPnCs, the synthesized nanomaterials were incorporated in polyvinylidene fluoride (PVDF) via solution blending method. The surface modification of MXene nanoflakes resulted in the outstanding enhancement of EMI SE and absorption coefficient of the PVDF based nanocomposites. The higher EMI SE of the modified nanocomposites at comparable electrical conductivity was attributed to three main reasons: (i) exfoliation of the MXene nanoflakes by the intercalation of PA nanofibers in the inter-gallery spaces, (ii) induction of abundant capacitor-like structures in the interfaces between PVDF chains and nanofiller, especially after increased specific surface area with PA modification, and (iii) the contribution of PA conducting chains in the electron transfer mechanisms and responses to the EM field. Moreover, the mechanical properties of the PVDF nanocomposites showed higher stiffness for PA-grafted MXene nanocomposites due to the sufficient exfoliation of nanoflakes by PA nanofibers' intercalation inside the MXene nanoflakes and the better polymer−filler interactions, which resulted in facilitating load transfer between the nanoflakes and the PVDF chains.

In a follow-up study, we hybridized the reduced graphene oxide nanoribbons (rGOnR) and MXene nanoflakes and used an engineering design to enhance the EMI SE of a thin but highly

electrically conductive MXene sheet. In this research, we took the advantage of excellent hydrophilicity of the GONR and MXene nanofillers to construct a three-dimensional (3D) conductive percolated network employing freeze casting. The constructed GOnR/MXene 3D networks at different GOnR to MXene ratios were then heat treated and infiltrated with a polydimethylsiloxane (PDMS) matrix. This unique approach significantly improves the state of filler dispersion, achieving a high electrical conductivity at lower nanofiller loadings. Electrical properties and EMI SE and shielding mechanism of the nanocomposites were systematically investigated as a function of the specimens' thickness. Furthermore, the influence of the rGOnR/MXene hybridization on enhancing the EMI SE and absorption coefficient of a highly reflective EMI shielding MXene sheet was investigated. It is revealed that the rGOnR/MXene hybridization not only enhances synergistically the EMI SE of the MXene sheet, also plays as an EM waves absorption layer which impedes the environment from the secondary pollutions originating from the reflective dominant shielding mechanism of the highly conductive MXene sheet. It is worth noting that the highly conductive MXene sheet in this study was considered a model material which could be substituted with any conductive coating that possesses efficient EMI SE yet reflection dominant shielding.

Acknowledgements

First and foremost, I want to thank my supervisors Professor Chul B. Park and Professor Aiping Yu. It has been a great honor to be mentored by them. I appreciate all their contributions of time, ideas, and funding to make my Ph.D. experience productive and stimulating. The joy and enthusiasm they have for their research were contagious and motivational for me. I am also thankful for the excellent opportunity they provided allowing me to grow as a research scientist.

I have been also very fortunate to have Professor Uttandaraman Sundararaj (University of Calgary), Professor Costas Tzoganakis (University of Waterloo), Professor Tizazu Mekonnen (University of Waterloo) and Professor Giovanni (John) Montesano (University of Waterloo) for serving as my Ph.D. committee members. They have provided me with inspiration, advice, and support to address the challenges of my dissertation.

I Would like to give special thanks to my colleagues and my co-authors Dr. Yun-Seok Jun, Dr. Jun Geun Um, Dr. Mahdi Hamidinejad, Dr. Kiyoumars Zarshenas, Dr. Maiwen Zhang, Yasaman Rahimi Darestani and Meysam Salari who spent hours helping me with experiments. I gratefully acknowledge my friends Yasaman Rahimi Darestani, Dr. Kiyoumars Zarshenas and Dr. Rasool Nasseri Pourtakalo for their valuable help, consultancy and discussions during tough times in my Ph.D. pursuit.

Lastly, I would like to deeply thank my family for all their love and encouragement. Especially for my deceased father and my dear mother who raised me with a love of science and supported me in all my pursuits. I am ever so grateful to my dearest sister and brother for their unwavering selflessness in providing me with the opportunity to make significant strides toward success. Thank you.

Saeed Habibpour
University of Waterloo
May 2023

Dedication

To my mother,

Alavieh

who taught me to love by expressing their unconditional love and support

To my brother,

Amir

who has been my pillar of strength, embodying the support and encouragement

that our late father would have provided

To my sister,

Roghayyeh

whose unwavering belief in me has given me the strength to persevere

and

to the memories of my father,

Hassan

Table of Contents

Examining Committee Membership ii

Author's Declaration iii

Statement of Contributions iv

Abstract vi

Acknowledgements ix

Dedication x

List of Figures xv

List of Tables xix

List of Abbreviations xx

List of Symbols xxiii

Chapter 1 Introduction 1

1.1 Background 1

1.2 Study objectives and approach 3

1.3 Thesis outline 4

Chapter 2 Literature Review 6

2.1 Summary 6

2.2 Conductive polymer nanocomposites (CPnC) 6

2.2.1 Polymer matrix 7

2.2.2 Conductive nanomaterials 10

2.2.3 Preparation Methods of CPnCs 13

2.2.4 Functional properties of CPnCs 14

2.3 Conclusions and future perspectives 29

Chapter 3 Enhanced Electrical and Mechanical Properties of Graphene Nanoribbon/ Thermoplastic Polyurethane Nanocomposites 30
3.1 Introduction 31
3.2 Experimental Section 33
3.2.1 Materials and sample preparation 33
3.2.2 Characterization 34
3.3 Results and Discussion 35
3.3.1 Material characterizations 35
3.3.2 Microstructure and morphology of the nanocomposites 39
3.3.3 Electrical conductivity and dielectric properties 40
3.3.4 EMI Shielding Effectiveness 43
3.3.5 Mechanical properties 49
3.4 Conclusions 52
3.5 Supporting information 53
Chapter 4 Greatly Enhanced Electromagnetic Interference Shielding Effectiveness and Mechanical Properties of Polyaniline-Grafted $Ti_3C_2T_x$ MXene–PVDF Composites 56
4.1 Introduction 57
4.2 Experimental Section 59
4.2.1 Materials and Chemicals 59
4.2.2 Synthesis of Exfoliated $Ti_3C_2T_x$ MXene 59
4.2.3 Synthesis of Oxidant Free Polyaniline Functionalized MXene (MX_nAN_m) 60
4.2.4 Preparation of PVDF/MXene and PVDF/MX_nAN_m Nanocomposites 61
4.2.5 Characterization 62
4.3 Results and Discussion 64

4.3.1 Material characterization 64
4.3.2 Morphology of the nanocomposites 69
4.3.3 Electrical Conductivity Measurements on the Nanocomposites 70
4.3.4 Electromagnetic Interference Shielding Effectiveness of the Nanocomposites 72
4.3.5 Microstructural Evolution and Thermal Properties of the Nanocomposites 76
4.3.6 Mechanical Properties of the Nanocomposites 78
4.4 Conclusions 81
4.5 Supporting information 82
Chapter 5 Excellent EMI Shielding Performance with Ultra High EM Wave Absorption by MXene Coated rGOnR/MXene Aerogel Based PDMS Nanocomposite 85
5.1 Introduction 85
5.2 Experimental Section 88
5.2.1 Materials 88
5.2.2 Synthesis of graphene oxide nanoribbon (GOnR) 88
5.2.3 Preparation of $Ti_3C_2T_x$ MXene (MX) nanoflakes 88
5.3 Preparation of unidirectionally aligned aerogel based PDMS nanocomposites 89
5.3.1 Characterization 90
5.4 Results and Discussion 92
5.4.1 Material characterization 92
5.4.2 Microstructure of unidirectionally aligned PDMS nanocomposites 96
5.4.3 Electrical conductivity of nanocomposites 98
5.4.4 EMI shielding effectiveness of nanocomposites 102
5.5 Conclusions 108
5.6 Supporting information 109

Chapter 6 Conclusions and Recommendations 113
6.1 Conclusions 113
6.2 Recommendations 116
6.2.1 Material research 116
6.2.2 Processing research 116
References 117

List of Figures

Figure 2.1 General isocyanate/alcohol reaction mechanism [33] 7
Figure 2.2 (a) Global market usage of plastics, (b) demand for TPU worldwide from 2012 to 2022 8
Figure 2.3 (a) Chemical structure of PVDF, (b)chain conformations of PVDF crystals, red, cyan, and blue spheres represent F, C, and H atoms 9
Figure 2.4 Unit chemical structure of a PDMS 9
Figure 2.5 PDMS synthesis reaction mechanism 10
Figure 2.6 Synthesized MXenes so far [63] 13
Figure 2.7 schematic diagram of electrical conductivity measurement setup of (a) in-plane and (b) through-plane conductivity [71] 15
Figure 2.8 Instruments and the home made fixture to measure DC in-plane electrical conductivity... 16
Figure 2.9 (a) Fixture for conductivity measurement with Biologic potentiostat, (b) through-plane, and (c) in-plane conductivity measurement electrodes 16
Figure 2.10 Typical percolation threshold for electrically conductive polymer nanocomposite 18
Figure 2.11 Polarization of dielectric material in an applied electric field 20
Figure 2.12. Polarization schemes in frequency domains [91] 21
Figure 2.13 (a) Electromagnetic wave spectrum, (b) a plane electromagnetic wave, and (c) properties of electromagnetic waves in radio and microwave region [100,102] 23
Figure 2.14 Wave impedance as a function of distance from the source normalized to $\lambda/2\pi$ [105] 24
Figure 2.15 Schematic illustration of EMI shielding mechanism 26
Figure 3.1 Procedure of oxidative unzipping of MWCNT and subsequent thermal reduction process to produce GNR, (Reprinted from S. Habibpour et. al, Chemical Engineering Journal 405, (2021), 126858) [165] 34
Figure 3.2 (a) Schematic illustration of chemical unzipping of MWCNT to produce GNR. TEM images of (b) MWCNT and (c) GNR. 36
Figure 3.3 (a) XRD and (b) Raman spectra of MWCNT, GONR and GNR. 37
Figure 3.4 C 1s high resolution x-ray photoelectron spectroscopy of GONR and GNR 39
Figure 3.5 Cross sectional SEM images of 8.2 vol% (a) MWCNT/TPU and (b) GNR/TPU nanocomposites. Fillers are indicated by the arrows. 40
Figure 3.6 Through plane AC conductivity of (a) MWCNT/TPU, (b) GNR/TPU nanocomposites, and (c) DC conductivity of MWCNT/TPU and GNR/TPU nanocomposites. 41

Figure 3.7 Real permittivity (ε') of (a) MWCNT/TPU and (b) GNR/TPU nanocomposites. (c) Real permittivity (ε') of MWCNT/TPU and GNR/TPU as a function of filler content. Dielectric loss (tan δ) of (d) MWCNT/TPU and (e) GNR/TPU nanocomposites. (f) Dielectric loss (tan δ) of MWCNT/TPU and GNR/TPU nanocomposites as a function of filler content. 43
Figure 3.8 (a) Average SE_T of MWCNT/TPU and GNR/TPU as a function of filler content, EMI SE of (b) MWCNT/TPU and (c) GNR/TPU in P-band frequency range, SE_A and SE_R of (d) MWCNT/TPU and (e) GNR/TPU, and (f) absorption coefficient for nanocomposites versus filler content 45
Figure 3.9 Schematic illustration of EMI SE mechanisms for (a) MWCNT/TPU and (b) GNR/TPU nanocomposites. 47
Figure 3.10 Stress-Strain curve of (a) MWCNT/TPU and (b) GNR/TPU nanocomposites with various amounts of fillers. 49
Figure 3.11 Comparison between the values experimental measured and the values theoretical predicted using Halpin-Tsai model. 52
Figure 3.12 XRD graphs of (a) neat TPU, (b) MWCNT/TPU and (c) GNR/TPU nanocomposites. The peak at 26.5° in MWCNT/TPU spectrum is likely due to the graphitic structure of MWCNT that is not well-dispersed in TPU matrix 53
Figure 3.13 The nitrogen adsorption and desorption isotherms of MWCNT, GNR and the calculated specific surface area 54
Figure 3.14 Illustration of change in interfacial layer thickness by increase in filler content or fillers' number density in a polymer matrix. 54
Figure 3.15 Intrinsic electrical conductivity of compressed MWCNT and GNR powders measured with 4-point probe method. 55
Figure 4.1 Illustration of the synthesis of exfoliated MXene and polyaniline grafted MXene nanoflakes 61
Figure 4.2 Schematic illustration of 4-point probe DC conductivity measurement set up. The photographic picture shows the home-made spring type 4-point probe fixture 63
Figure 4.3 (a) SEM images of MAX phase, (b) MXene nanoflakes, (c) drop cast MXene nanoflakes on aluminum foil substrate, (d) MX_2AN_1 nanoflakes, (e) MX_1AN_1 nanoflakes, (f) EDS mapping of the MX_2AN_1 nanoflakes, and (g-i) AFM surface topography of the delaminated MXene nanoflakes 65

Figure 4.4 Proposed mechanism of the oxidant free polymerization of aniline monomer from the surface of MXene nanoflakes (a), XRD (b), FTIR (c) and Raman spectrum (d) of the nanoflakes..... 67
Figure 4.5 Cross sectional SEM images of the (a) cryo-fractured PVDF and 4.4 vol% PVDF nanocomposites of (b) MX, (c) MX_2AN_1 and (d) MX_1AN_1..... 70
Figure 4.6 (a) DC electrical conductivity of PVDF-MXene and (b) PVDF-MX_nAN_m nanocomposites as a function of volume concentration of nanoflakes. The inset in (a) shows a log-log plot of the electrical conductivity versus (φ-φ_c) 72
Figure 4.7 (a) Average total EMI SE of the nanocomposites versus filler content, (b) EMI SE of the nanocomposites in the P-band frequency range, (c) proposed EMI shielding mechanism of PVDF-MX_nAN_m nanocomposites, (d) nitrogen adsorption and desorption isotherms of MX, MX_2AN_1 and MX_1AN_1 nanoflakes and the calculated specific surface area, (e) the portions of reflection and absorption in the total EMI SE for PVDF-MX, and (f) PVDF-modified MXene nanocomposites 73
Figure 4.8 XRD graph of the pure PVDF and PVDF nanocomposites filled with 4.4 vol% of MXene, MX_2AN_1 and MX_1AN_1..... 78
Figure 4.9 (a) Stress-strain curves of the pure PVDF (inset), PVDF-MX2AN1 and PVDF-MX1AN1 nanocomposites at 4.4 vol% and 6.9 vol%, (b) calculated Young's modulus and elongation at break of the PVDF-MX nanocomposites, and (c1) calculated tensile strength and (c2) Young's modulus of the nanocomposites at 4.4 vol% and 6.9 vol%..... 80
Figure 4.10 (a) High magnification SEM images of the MXene nanoflakes, (b) MX_2AN_1 nanoflakes, (c) MX_1AN_1 nanoflakes, (d) SEM and EDS analysis of the MAX phase, (e) SEM and EDS analysis of the MXene nanoflakes, and (f) EDS mapping of the MXene nanoflakes 82
Figure 4.11 Particle size distribution (a) and average zeta potential of MXene nanoflakes 83
Figure 4.12 (a) Reflection and absorption coefficients of the PVDF-MX and (b) PVDF-MX_nAN_m nanocomposites. 83
Figure 4.13 The crystallization (a) and melting (b) thermograms of PVDF and nanocomposites. XRD graphs of the PVDF-MX nanocomposites at different MX loadings (c), curve fitting and calculation of the relative percentage of β polymorphism in PVDF nanocomposites (e-f)..... 84
Figure 4.14 Stress-strain curve of the PVDF-MX nanocomposites at different MX loadings..... 84
Figure 5.1 Schematic illustration of rGOnR/MX unidirectional foam preparation..... 90

Figure 5.2 SEM images of (a) Ti_3AlC_2 MAX phase, (b) and (c) $Ti_3C_2T_x$ MXene, (d) MWCNT, (e) and (f) GOnR. TEM images of (g) MWCNT, (h) GOnR and (i) AFM topography of $Ti_3C_2T_x$ MXene. Inset in (i) shows the height profile of bilayer $Ti_3C_2T_x$ MXene nanoflakes. 93
Figure 5.3 (a) XRD, (b) FTIR, (c) Raman and (d-h) XPS spectra of $Ti_3C_2T_x$ MXene, GOnR, rGOnR and their Ti_3AlC_2 MAX phase and MWCNT precursors. 95
Figure 5.4 SEM images from the top and side view of the PDMS infiltrated rGOnR/MX aerogels ... 98
Figure 5.5 (a) Broad band electrical conductivity, (b) linear sweep voltammetry, (c) DC electrical conductivity, (d) real permittivity, (e) dielectric loss, and (f) comparison of dielectric properties at the frequency of 10^3 Hz for rGOnR/MX aerogel based PDMS nanocomposites..... 100
Figure 5.6 (a) EMI SE of a 10 μm thin MXene sheet in the P-band frequency range, (b) A-, T-, and R-values of MXene sheet, (c) average EMI SE of the rGOnR/MX aerogel based PDMS nanocomposites as a function of the specimen thickness, (d-g) A-, T-, and R-values of rGOnR/MX aerogel based PDMS nanocomposites, (h) average R-values of rGOnR/MX aerogel based PDMS nanocomposites as a function of thickness and (i) A/R ratio of rGOnR/MX aerogel based PDMS based nanocomposites 104
Figure 5.7 (a) average EMI SE of the rGOnR/MX aerogel based PDMS nanocomposites coated with 10 μm MXene sheet as a function of the specimen thickness, (b-e) A-, T-, and R-values of coated rGOnR/MX aerogel based PDMS nanocomposites, (f) average R-values of coated rGOnR/MX-PDMS nanocomposites as a function of thickness and (g) A/R ratio of coated rGOnR/MX-PDMS nanocomposites, and (h) schematic of impedance sections in series 108
Figure 5.8 (a-b) High magnification FE-SEM images of Ti_3AlC_2 MAX phase, (c) isolated long and exfoliated GOnR, and (d) EDS analysis of the synthesized nano particles..... 109
Figure 5.9 XPS survey of (a) MXene, (b) GOnR, and (c) rGOnR..... 110
Figure 5.10 In-plane electrical conductivity of a 10 μm thick $Ti_3C_2T_x$ MXene sheet as a function of temperature..... 110
Figure 5.11 T-value of rGOnR/MX aerogel based PDMS nanocomposites 111
Figure 5.12 Average total EMI SE of the uncoated and coated nanocomposites versus sample thickness for (a) rGOnR30-PDMS, (b) rGOnR25/MX5-PDMS, (c) rGOnR20/MX10-PDMS, (d) rGOnR15/MX15-PDMS 112

List of Tables

Table 2.1 Factors affecting the shielding effectiveness of CPnC based EMI shielding material 27
Table 3.1 The parameters extracted from XRD and Raman spectra 38
Table 3.2 Comparison of EMI SE with other polymer nanocomposites in literature. 48
Table 3.3 Young's modulus and tensile strength of GNR/TPU and MWCNT/TPU nanocomposites. 50
Table 3.4 Physical properties of the utilized nanomaterials and polymer matrices 53
Table 4.1 Extracted parameters from the XRD graphs 68
Table 4.2 Calculated properties from DSC and XRD graphs of the PVDF and 4.4 vol% filled nanocomposites. 78
Table 4.3 Extracted mechanical properties of the nanocomposites from stress-strain curves..... 81
Table 5.1 Extracted DC conductivity at the frequency of 1 Hz from the broadband conductivity measurement and calculated DC conductivity using LSV technique..... 111

List of Abbreviations

A	Absorption
Ar	Argon gas
SE_A	Absorption Electromagnetic Interference Shielding Effectiveness
AC	Alternating Current
APS	Ammonium Persulfate
AFM	Atomic Force Microscope
BET	Brunauer Emmett Teller
CNT	Carbon Nanotube
CVD	Chemical Vapor Deposition
CPnC	Conductive Polymer Nanocomposite
T_c	Crystallization Temperature
DSC	Differential Scanning Calorimetry
DMM	Digital Multimeters
DMF	Dimethylformamide
DC	Direct Current
DBS	Direct-Broadcast Satellite
EIS	Electrochemical Impedance Spectroscopy
EM	Electromagnetic
EMI	Electromagnetic Interference
EDS	Energy Dispersive X-ray Spectroscopy
FTIR	Fourier Transform Infrared Spectroscopy

FWHM	Full Width at Half Maximum
GNR	Graphene Nanoribbon
GO	Graphene Oxide
GONR	Graphene Oxide Nanoribbon
HCP	Hexagonal Close-Packed
HDI	Hexamethylene Diisocyanate
LiF	Lithium Fluoride
LSV	Linear Sweep Voltammetry
LAN	Local Area Network
MWS	Maxwell-Wagner-Sillars
MDI	Methylene Diphenyl Diisocyanate
MILD	Minimally Intensive Layer Delamination
MWCNT	Multiwalled Carbon Nanotubes
MX	MXene
PA	Polyaniline
PDMS	Polydimethylsiloxane
PVDF	Polyvinylidene Fluoride
rGNR	Reduced Graphene Nanoribbon
R	Reflection
SE_R	Reflection Electromagnetic Interference Shielding Effectiveness
SEM	Scanning Electron Microscope
SE	Shielding Effectiveness
SS	Strain-Stress

TGA	Thermogravimetric Analysis
TPU	Thermoplastic Polyurethane
3D	Three-dimensional
TDI	Toluene Diisocyanate
SE_T	Total Electromagnetic Interference Shielding Effectiveness
T	Transmission
TEM	Transmission Electron Microscope
2D	Two-dimensional
UTM	Universal Testing Machine
XRD	X-ray Diffraction

List of Symbols

Å	Angstrom
ω	Angular Frequency
ρ_f	Density of Filler
ρ_m	Density of Matrix
tan δ	Dielectric Loss
ε'	Dielectric Permittivity
σ	Electrical Conductivity
σ_f	Filler Conductivity
μ_0	Free Space Magnetic Permeability
β	Full Width at Half Maximum
ε''	Imaginary Part of the Dielectric Permittivity
L_a	Inter-Defect Distance
L_c	Inter-Layer Distance
Ω	Ohms
φ_c	Percolation Threshold
τ	Relaxation Time
R	Resistance
ρ	Resistivity
S	Siemens
ν	Velocity

Chapter 1
Introduction

1.1 Background

Next generation advanced multifunctional materials enable the design and development of cutting-edge, high performance and lightweight materials by combining science and engineering knowledge. The importance of these materials lies in their potential to revolutionize various technological and industrial fields such as automotive, energy storage, telecommunication, microelectronics, sensors, and aerospace.

Polymers have a very attractive array of properties such as versatility, lightness and ease of processing which have led them to be building blocks of multifunctional materials in different fields and applications. Historically, they have been considered as insulative materials such as protective layers for metal wires of electrical cable. However, during the last decades, electrically conductive polymer nanocomposites (CPnC) have become one of the most important focal points of research for technological innovations due to their great potential as a highly-desirable class of advanced multifunctional materials. The outstanding features of CPnCs can fulfill specific requirements for various applications such as capacitors and super capacitors [1,2], energy conversion (bipolar plates of fuel cells [3]), EMI shielding [4–7] and electrostatic discharge [8,9]. It is worth mentioning that the global EMI shielding market was valued at USD 6.6 billion in 2022 to USD 8.6 billion by 2027 [10]. Furthermore, CPnCs outperform metals and ceramics in chemical and corrosion resistance, while providing higher ductility and specific toughness [1–3,11–15].

It is of utmost significance to bear in mind the pivotal role that additive nanomaterials play in achieving exceptional characteristics and versatile functionalities in CPnCs. For example, metal nano wires and nano particles comprised of aluminum, steel, iron, copper, and nickel coated glass fibers have been added to the polymer matrices to produce CPnCs [16]. The key parameter in producing CPnCs is the volume fraction of the conductive nanomaterials where the nanomaterials come into contact with one another forming a continuous pathway for electrons to transfer. This particular concentration is called percolation threshold [17]. Different types of carbon allotropes such as carbon black, carbon fiber, graphite, graphene and carbon nanotube have also been employed to enhance the electrical conductivity of the CPnCs. However, the percolation threshold and subsequently electrical conductivity are greatly influenced by the intrinsic properties of the polymers and conductive nanomaterials, their geometrical

properties (i.e. shape, size, aspect ratio), dispersion state of the nanomaterials, degree of nanofiller alignment and quality of polymer-filler interactions [18]. For example, electrical conductivity can be achieved by spherical fillers at loadings around 10-20 wt.%, while using a high aspect ratio CNT can reach the percolation threshold at very small loadings of 0.1 wt.% [18]. Therefore, apart from the economical point of view, keeping the percolation threshold as low as possible is crucial since the high nanomaterials loading not only escalates processability and mechanical properties, also leads to significant damage to the processing equipment [19].

A judicious selection of suitable nanomaterials can aid in meeting the demands of various state-of-the-art applications. Since the first report of Iijima [20] on CNT and the discovery of graphene in 2004 [21], these two nanostructures have become much more popular in enhancing the electrical conductivity of polymer nanocomposites. Graphene and CNT are atomically thin layers with a composition of sp^2 carbon atoms and 2D honeycomb structures. These nanostructures are seen as promising nanomaterials due to their low density, high aspect ratio, huge surface area (~2600 m^2/g)), extraordinary mechanical properties of 130 GPa ultimate strength and 1 TPa Young's modulus, 5000 W/(m.K) thermal conductivity and 6000 S/cm electrical conductivity [22]. Despite significant progress in the development of carbonaceous based nanocomposites, there are still great challenges remaining that need to be addressed. The most critical unresolved issues are excessive aggregation resulting in poor dispersibility, poor control of surface chemistry, and low interfacial interactions with the polymeric matrix [23,24]. Starting from 2011, 2D transitional metal carbides or nitrides, more commonly known as MXenes, have revolutionized the realm of CPnCs [25]. MXene is produced through the delamination process of its MAX phase precursor via selective etching of the A element. This chemical etching procedure results in an abundance of induced surface functional groups that render these nanomaterials highly hydrophilic while exhibiting metallic conductivity that can reach up to 9888 S/cm [26].

As discussed above, the increasing use of electronic devices in various industries, the growing demand for electromagnetic compatibility solutions and the rise in wireless technologies especially after the adoption of 5G technology are some of the key factors driving the growth of using CPnCs as EMI shielding material [27]. However, achieving the necessary level of EMI shielding effectiveness (SE) through an environmentally-friendly absorption mechanism remains a formidable challenge. The key to obtaining high EMI SE lies in enhancing the electrical conductivity of materials, which can be achieved by developing highly conductive nanomaterials and incorporating them into polymer matrices [28]. In order to optimize the electrical conductivity, it is important to carefully engineer the

nanomaterial geometry, aspect ratio, and interaction with the polymer matrix. Although increasing electrical conductivity is crucial for achieving high EMI SE, it can also result in an inferior impedance mismatch between the air and the polymer matrix [29]. This mismatch can cause a significant reflection of the incident electromagnetic waves, which in turn generates severe secondary electromagnetic wave pollution in the surrounding environment. As a result, to obtain absorption dominant EMI shielding material, along with efforts of increasing their electrical conductivity, another challenge that must be addressed is the tuning of the impedance mismatch of the CPnCs. In light of the difficulties associated with increasing electrical conductivity and tuning impedance mismatch, it is of paramount importance to undertake rigorous research on these issues. Only by doing so can we develop advanced CPnCs for EMI shielding that boast exceptional EMI SE and an unprecedented ability to absorb radiated EM power. Such a development would be crucial for achieving optimal performance while simultaneously minimizing any negative environmental impact.

1.2 Study objectives and approach

The goal of this study is to develop electrical CPnCs for EMI shielding applications by integrating polymer matrix with different kinds of conductive nanomaterials. The focus of the thesis is defined (i) to develop CPnCs with enhanced EMI SE, (ii) to improve the portion of absorption shielding mechanism, and (iii) to develop a fundamental understanding of how the CPnCs can achieve high functionalities (i.e. electrical conductivity, electric performances and EMI shielding effectiveness). Achieving higher functionalities and electrical conductivity at lower filler content has been always challenging in the manufacturing of CPnCs [14]. Therefore, the current research points towards the further development of lightweight and functional CPnCs with enhanced functionalities at lower nanomaterial loadings. The studies for these goals were conducted by three parts.

In part 1, long strips of reduced graphene nanoribbons were synthesized from their parent MWCNTs. The synthesized nanomaterials were incorporated with thermoplastic polyurethane (TPU) matrix via solution blending and their electrical and dielectric properties, EMI shielding efficiency and mechanical properties were compared to their corresponding MWCNT nanocomposites.

In part 2, $Ti_3C_2T_x$ MXene (MX) nanoflakes were synthesized from the Ti_3AlC_2 MAX phase. The synthesized nanomaterials were modified by grafting polyaniline nanofibers on the surface of the nanoflakes. Then nanomaterials were incorporated in a polyvinylidene fluoride (PVDF) matrix via solution blending. The electrical conductivity, EMI shielding and mechanical properties of the modified

MXene-PVDF nanocomposite were thoroughly compared to pristine MXene-PVDF nanocomposites. In this part, the impact of surface modification on developing EM wave absorption mechanism (interfacial polarization relaxation) was understood.

In part 3, three dimensional heat treated rGOnR/MX aerogel was first produced with different rGOnR:MX ratios. Poly(dimethylsiloxane) (PDMS) as the elastomeric matrix is then infiltrated into as-produced 3D aerogels. The impact of hybridization and shielding material thickness on enhancing EMI SE and developing highly absorptive EMI shielding material was comprehensively studied.

1.3 Thesis outline

This thesis focuses on the synthesis of electrically conductive carbon based and transitional metal carbide based polymer nanocomposites with functional properties. This includes electrical properties (e.g. electrical conductivity, dielectric properties and EMI shielding performance) as lightweight electrically CPnCs for EMI shielding applications. The thesis consists of six chapters outlined as follows:

- Chapter 1 presents background information on this research, thesis motivations and an outline of the thesis
- Chapter 2 provides a review of recent literatures on conductive polymer nanocomposites, methods of their fabrication, and synthesis methodologies of conductive nanofillers. Fundamentals of electrical conductivity, dielectric properties and EMI shielding of polymer nanocomposites are also reviewed.
- Chapter 3 presents the graphene nanoribbon synthesis method, and the impact of its structural change on electrical conductivity, EMI shielding and mechanical properties of TPU based polymer nanocomposites.
- Chapter 4 describes the synthesis of $Ti_3C_2T_x$ MXene nanoflake and its surface modification with polyaniline nanofibers. The impact of surface modification on electrical conductivity and EMI shielding performance of PVDF based nanocomposites are discussed.
- Chapter 5 presents the fabrication of polymer nanocomposite using the freeze casting method which is the infiltration of a 3D nanofiller matrix. The impact of rGOnR and MXene

hybridization on enhancing impedance matching between air and CPnC for obtaining ultra high absorption EMI shielding properties were elaborated.

- Chapter 7 summarizes the main results drawn from chapters 3 to 5 and proposes some extended future works to follow this thesis work.

Chapter 2
Literature Review

2.1 Summary

In this chapter, a background of recent literatures on conductive polymer nanocomposites (CPnC) and their ingredients is presented. A variety of methods used to fabricate CPnCs are reviewed, along with methods of conductive nanomaterials synthesis and their dispersion in polymer matrices. The functional properties of the CPnCs such as electrical, dielectric, EMI shielding, and mechanical properties are also reviewed.

2.2 Conductive polymer nanocomposites (CPnC)

Polymer nanocomposites are composed of a polymer matrix that is reinforced with particles or fibers that are typically in the 1-100 nanometer size range and can be made of metallic, ceramic, or organic materials. When nanomaterials are incorporated, their unique properties create a synergistic effect that leads to exceptional properties of the resulting nanocomposite. The size reduction to the nanoscale allows for quantum effects and a substantial increase in surface area per volume, which enhances interactions between the elements and results in behaviors that are significantly different from those of bulk materials [30,31]. By adding specific functional nanomaterials to the polymer matrices, multifunctional polymer nanocomposites, including electrically conductive polymer nanocomposites (CPnC), can be produced. CPnCs are typically made by incorporating conductive nanoparticles, such as carbon nanotubes, graphene, or metallic nanoparticles or nanofibers, into a polymer matrix. The addition of conductive nanoparticles to polymers can greatly enhance their electrical conductivity, which is important for a variety of applications. The electrical conductivity can be tuned by varying the type, concentration, and arrangement of nanoparticles in the polymer matrix. CPnCs have shown promise in various applications, including in flexible electronics, transparent conductive coatings, electrostatic discharge protection, and electromagnetic interference (EMI) shielding. The ability to integrate electrical conductivity with the other desirable properties of polymer nanocomposites makes them an attractive material for a wide range of applications [32]. In this thesis, thermoplastic polyurethane, polyvinylidene fluoride and polydimethylsiloxane were used as polymer matrices. Carbon based nanomaterials and 2D transitional metal carbide were used as conductive nanofillers.

2.2.1 Polymer matrix

2.2.1.1 Thermoplastic polyurethanes

Polyurethanes are a type of engineering polymer that is receiving significant attention from both industry and academia. They have a wide range of applications, including coatings, adhesives, injection-moulded parts, and elastomers, which are commonly used in everyday life, as well as biomedical and advanced engineering applications. Thermoplastic polyurethanes (TPU) are typically produced by reacting a diol and a diisocyanate, although recently some methods that do not require diisocyanates have been proposed for the preparation of thermoplastic polyurethanes, Figure 2.1.

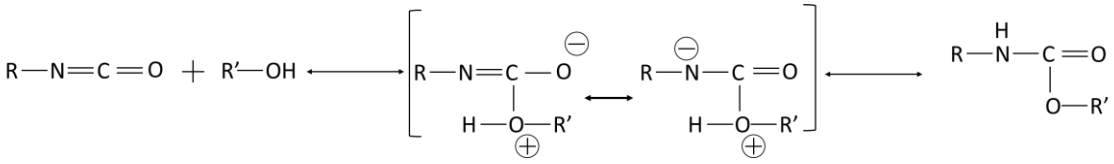

Figure 2.1 General isocyanate/alcohol reaction mechanism [33]

Polyurethanes are formed from three main building blocks: polyols, isocyanates, and chain extenders. The choice of these building blocks can result in a wide range of properties for polyurethane products. Polyols typically have long flexible chains, while isocyanates and chain extenders are short and stiff molecules. Many different types of polyols are available for polyurethane synthesis, including polyester, polyether, polycarbonate, polytetrahydrofuran, acrylate, polyolefin, and silicone-based polyols. However, there are only a few aromatic and aliphatic isocyanates that are commonly used for polyurethane syntheses, such as methylene diphenyl diisocyanate (MDI), toluene diisocyanate (TDI) and hexamethylene diisocyanate (HDI). The reaction between these building blocks creates a segmented structure for polyurethane molecules, with alternating sequences of isocyanate and chain extender forming the hard segment and the flexible polyol chain forming the soft segment. These two segments are linked together by covalent bonds to create block-copolymers. As illustrated in Figure 2.2-a, polyurethanes account for 6% of global plastic usage. The global market demand for TPU from 2012 to 2022 can be seen in Figure 2.2-b [33,34].

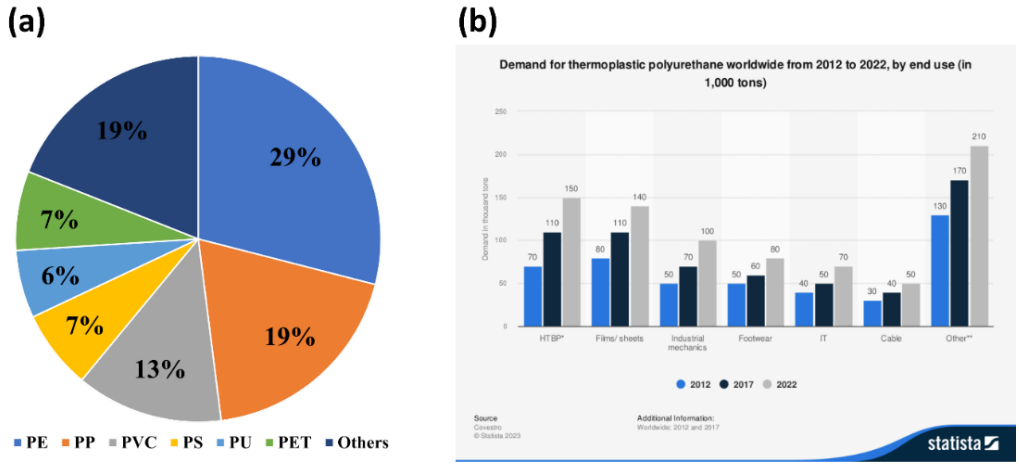

Figure 2.2 (a) Global market usage of plastics, (b) demand for TPU worldwide from 2012 to 2022

TPU nanocomposites are commonly used in a variety of engineering applications. There are three main methods for preparing TPU nanocomposites: melt compounding [35–37], solvent blending [7,38], and in-situ polymerization [39]. Melt compounding is a scalable method, but it has a lower capability for dispersing nanomaterials. Solvent blending is typically used in lab-scale settings and has the capability for high loading and good dispersion of nanomaterials. In-situ polymerization is also an efficient method for nanomaterial dispersion, but it is challenging to achieve high nanomaterial loading due to the significant increase in viscosity [33].

2.2.1.2 Polyvinylidene fluoride

PVDF is a type of thermoplastic that belongs to the fluoropolymer family and is known for its highly non-reactive nature, Figure 2.3-a. It is a semi-crystalline polymer with an average density of 1.78 g/cm^3 and impressive mechanical properties, chemical resistance, and thermal stability. Additionally, PVDF demonstrates excellent electrical insulation properties, UV resistance, and weather ability. This material finds use in a wide range of fields, including electronics, medicine, textiles, acoustics, and solar cell and piezoelectric element manufacturing [40]. PVDF can exist in different crystal polymorphs, including α (TGTG′), β (TTTT), γ (TTTGTTTG′) and δ forms. T and G stand for the trans and gauche chain conformations, respectively, Figure 2.3-b. α-phase is the most commonly found non-polar phase, and the others are electrically active polar phases. The polar β-phase, in particular, is attractive due to its piezoelectric, pyroelectric, and ferroelectric characteristics, and can be induced through stretching PVDF or the addition of certain nucleating agents [41].

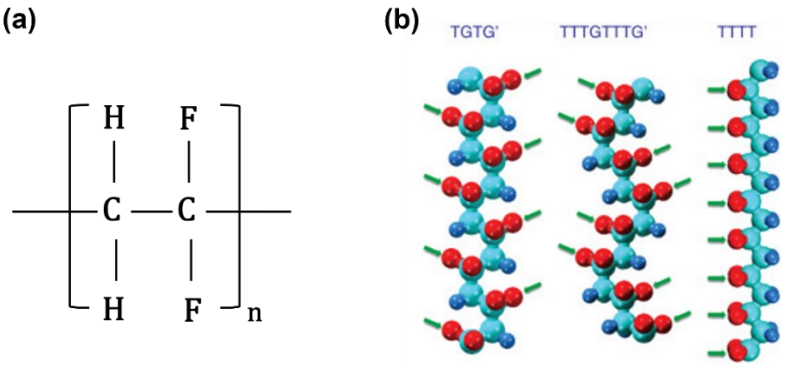

Figure 2.3 (a) Chemical structure of PVDF, (b)chain conformations of PVDF crystals, red, cyan, and blue spheres represent F, C, and H atoms.

2.2.1.3 Poly (dimethylsiloxane)

Poly (dimethylsiloxane) or PDMS, is a type of silicone polymer that is widely used in various industries due to its unique properties [42]. It consists of an inorganic backbone linked with silicon and oxygen. Methyl groups are bonded to silicon atoms that establish a repeating unit in the polymer chain with a monomer molecular weight of 74 g/mol, Figure 2.4.

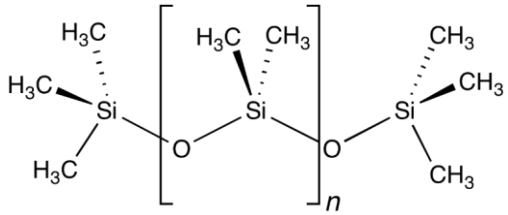

Figure 2.4 Unit chemical structure of a PDMS

As a silicon elastomer, versatile applications for PDMS have been developed, such as medical devices, prostheses and internal body applications due to its biocompatibility, antifoaming agent, heat-resistant lubricants, fire retardants, in cosmetics and as a matrix of CPnC in sensors, energy storage, and EMI shielding. PDMS is also considered inert, non-toxic and non-flammable [43]. Economically, PDMS may not account for a significant portion of global plastic usage but plays an important role in many industries and applications due to its unique properties and versatility.

PDMS was first synthesized in the 1940s by Eugene G. Rochow, who was studying the properties of silicones at the General Electric Company [42]. He synthesized dimethyldichlorosilane, $(CH_3)_2SiCl_2$, as the initial material for PDMS synthesis. Rochow designed an experiment in which HCl:CH_3Cl gas

mixture (1:50 ratio) passes through a silicone (Si)/cupper alloy inside a 370 °C furnace. The gaseous mixture reacts with Si and resulted in $(CH_3)_2SiCl_2$. The obtained product readily reacts with the surrounding water molecules to produce $(CH_3)_2Si(OH)_2$. Condensation of the produced $(CH_3)_2Si(OH)_2$ results in PDMS. Figure 2.5 shows the reaction mechanism:

$$Si + 2CH_3Cl \rightarrow (CH_3)_2SiCl_2$$

$$(CH_3)_2SiCl_2 + 2H_2O \rightarrow (CH_3)_2Si(OH)_2 + 2HCl$$

$$2(CH_3)_2Si(OH)_2 \rightarrow OH\text{—}Si(CH_3)_2\text{—}O\text{—}Si(CH_3)_2\text{—}OH + H_2O$$

Figure 2.5 PDMS synthesis reaction mechanism

PDMS is a two part polymer consisting of a base and curing agent. Both parts are siloxane oligomers with vinyl end groups. the base includes a platinum based catalyst which helps cure the elastomer by an organometallic crosslinking reaction. Crosslinking siloxane oligomers with a minimum of three silicon-hydride bonds are in the curing agent. The combination of the base and the curing agent, with the aid of a catalyst, leads to a process called hydrosilation of double bonds. During this process, the Si-H bonds in the curing agent react with the double bonds in the base, resulting in the formation of a Si-CH_2-CH_2-Si chain. Notably, this reaction does not generate any waste products. The curing agent contains multiple reaction sites, which enable three-dimensional networking to occur. The stiffness of the cured elastomer depends on the ratio of curing agent to base, with higher ratios resulting in more rigid elastomers [44].

2.2.2 Conductive nanomaterials

Conductive nanomaterials are materials with electrical conductivity at the nanoscale level. They are typically made up of metallic, carbon-based nanoparticles, and recently transitional metal carbides or nitrides that are highly conductive and have unique properties such as high surface area and tunable electronic properties. The dimensionality of the conductive nanomaterial ranges from zero to three (graphite). Some common examples of conductive nanomaterials include carbon black or metal nanoparticles (0D), carbon nanotube (CNT) or metallic nanowires (1D), graphene nanoribbon (semi 2D), graphene or MXene (2D), and graphite (3D) and conducting polymers. In this thesis we have used

multiwalled carbon nanotube (MWCNT), graphene nanoribbon and $Ti_3C_2T_x$ MXene as conducting nanomaterials.

2.2.2.1 Graphene nanoribbon

Carbon is a common element in the universe, ranking fourth by mass after hydrogen, helium, and oxygen. It is present in various forms, such as diamond, graphite, graphene, buckminsterfullerene (nano- sized spheres of rolled-up graphene), and nanotubes [45]. Each of the carbon forms has been a star material at one time. For example, graphene which is a single atomic layer of sp^2 hybridized carbon atoms has been given nicknames as "super carbon" [46]. This is due to its intrinsic high electrical (6,000 S/cm) and thermal (5,000 W/(m.K)) conductivity, excellent mechanical strength (130 GPa) and flexibility, large surface area (~2630 m^2/g) and exceptional catalytic properties [47]. Since the development of CPnCs, there has been a great deal of interest in the properties of carbon based nanomaterials owing to their substantial π-electron delocalization. Furthermore, fast developments in miniaturized portable electronics have pushed researchers to nanostructures via the top-down approach. In recent decades, carbon based nanostructures such as 2D graphene or 1D CNTs, are among the most promising candidates for CPnC based electronics.

Graphene nanoribbons (GNRs) as thin, elongated strips of graphene that possess abundant edges along with a high length-to-width ratio have become an important subclass of graphene materials. They represent a particularly versatile variety of graphene in which its electrical properties change from semiconductors to semimetals as their width is increased. GNRs can be produced using several different techniques, and most of the techniques use graphene or CNTs as a starting material. Starting with graphene as the precursor of GNR, various methods such as plasma etching, metal catalyzed graphene sheet cutting, sonochemical cutting of graphene, and lithographic techniques have been reported [48–50]. Synthesis of GNR from MWCNT was also reported through different approaches such as etching by Argon plasma, chemical attack by strong oxidizing agents, lithium and ammonia induced exfoliation, and metal catalyzed MWCNT cutting, and chemical vapor deposition (CVD) technique [51–55]. Among these approaches, simple, efficient (yield ~100%), and scalable longitudinal oxidative unzipping of MWCNTs is the most promising. In this thesis, this technique was used to synthesize graphene nanoribbons and the method is described in Chapter 3. Owing to the high available surface area, high mechanical strength and electrical conductivity of GNRs, and the scalability of the synthesis they have been investigated for the fabrication of nanocomposites and use in batteries, supercapacitors

and fuel cells [56–60]. In this thesis, nomenclatures of GNR in chapter 3 and rGOnR were used for reduced graphene oxide nanoribbon.

2.2.2.2 MXene

After the rise of graphene in 2004 [21,61], the number of research on 2D nanomaterials has increased and led to the discovery of MXene in 2011 [25]. MXene is synthesized from the MAX phase which stands for the chemical formula of M, A and X compounds. MAX phase belongs to the group of ternary carbides and nitrides of transition metals with stacked-layer structure. These layered structures have the formula of $M_{n+1}AX_n$ where M is an early transition metal, A is from group 13-16 elements (such as aluminum, silicon, or carbon), and X can be either carbon, nitrogen or both. The value of n determines the number of M-A layers and X layers in the crystal structure and can be 1 to 3 [62]. The chemical structure of MAX phases is based on a hexagonal close-packed (HCP) arrangement of atoms. They have a layered structure with alternating planes of M and A elements, and a single plane of X elements in between. The M and A elements occupy octahedral sites in the HCP lattice, while the X elements occupy tetrahedral sites [63]. In a wet chemical reaction, the A layer is selectively removed by hydrofluoric acid at room temperature and $M_{n+1}X_n$ layers were then delaminated by sonication. Chemical etching of the MAX phase introduces surface functional groups such as oxygen, hydroxyl and fluoride at the surface of MXene nanoflakes and denoted in the MXene structure name as T_x. For example, chemical etching of the Ti_3AlC_2 MAX phase produces $Ti_3C_2T_x$ MXene nanoflakes. The surface functional groups of MXene devoted super hydrophilicity to MXene which is very important in its various applications [64]. $Ti_3C_2T_x$ was the first synthesized MXene, and 19 different MXene compositions have subsequently been synthesized (marked with blue in Figure 2.6), with dozens more predicted to exist and studied in silico (marked with grey in Figure 2.6) [63].

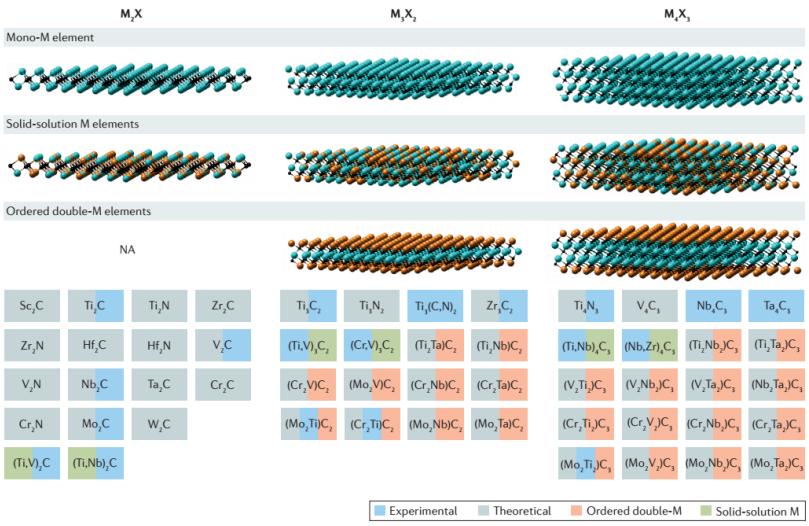

Figure 2.6 Synthesized MXenes so far [63]

MXene has outstanding electrical conductivity due to its metallic nature which makes it attractive for a range of potential applications such as energy storage devices, EMI shielding, transparent conductive coatings, and sensors. Furthermore, other unique properties of MXene such as liquid phase processability, excellent mechanical properties and tunable surface functionalities attracted a great deal of attention from academia [62].

2.2.3 Preparation Methods of CPnCs

A range of methods has been documented for creating CPnCs, including solution mixing, melt blending, and in situ polymerization. Each technique has its strengths and limitations, and the method chosen will depend on the specific properties and requirements of the final product. Solution mixing is often the easiest approach, where a suitable solvent is used to dissolve the polymer and nanoparticles, which are then mixed together and the solvent is evaporated. This method can be particularly useful for producing small quantities of CPnCs with a high level of control over the nanoparticle dispersion. However, solution mixing may not be suitable for producing larger quantities of CPnCs, and alternative techniques such as melt blending or in situ polymerization may be more appropriate. Melt blending involves melting the polymer and nanoparticles together and mixing them while they are still in a molten state. Even though melt mixing is less efficient than solution mixing in breaking the nanoparticle aggregates, melt processing is a widely applied process in industrial practices due to the lack of solvent evaporation [65,66]. In situ polymerization involves the polymerization of monomers in the presence

of nanoparticles, resulting in the formation of CPnCs. This method can be particularly useful for producing CPnCs with a high level of control over the nanoparticle dispersion and for creating CPnCs with tailored properties. However, in situ polymerization can be challenging if the nanoparticles interfere with the polymerization process or if the monomers and nanoparticles have different reactivity. Overall, the choice of method will depend on various factors, including the desired properties of the final product, the quantity of CPnCs required, and the equipment and expertise available.

An alternative approach for preparing CPnCs involves the fabrication of a 3D interconnected aerogel structure of nanomaterials, followed by the infiltration of a polymer matrix into the aerogel. To create the aerogel, hydrogels are dried in a way that maintains their original structure, as conventional drying methods can collapse the pore structure due to capillary action and surface tension. Freeze-drying is commonly used to minimize stress on the porous structure during the drying process. Once the hydrogel is transformed into an aerogel, the polymer is then infiltrated into it in its liquid state. Due to the low viscosity of the polymer, it diffuses into the aerogel without disrupting the original structure and network. This method provides an efficient and straightforward way to produce a 3D architecture of porous nanomaterials with a polymer matrix. However, the process can be time-consuming and requires careful control to achieve the desired structure and properties of the final material. The primary driving forces behind the infiltration of polymers are capillary action and gravity, with capillary action playing a more significant role in nano-scale nanocomposites. The effectiveness of capillary infiltration is influenced by various factors, including the interaction between the surface and the polymer, temperature, and the geometry of the pores [67–70].

2.2.4 Functional properties of CPnCs

2.2.4.1 Electrical conductivity

Electrical conductivity (σ) is reciprocal of the resistivity (ρ). Resistivity is the specific electrical resistance of a material which is defined as a measure of how strongly a material opposes the flow of electric current:

$$\boldsymbol{\sigma = \frac{1}{\rho}} \qquad \textbf{2.1}$$

The material resistance (R) is proportional to the intrinsic resistivity and specimen dimension:

$$\boldsymbol{R = \rho \frac{l}{A}} \qquad \textbf{2.2}$$

where l is the length between the two points at which the voltage is measured, and A is the cross-sectional area perpendicular to the direction of the current. The units of R, ρ and σ are ohms (Ω), Ω.cm, and siemens (S)/cm, respectively. The electrical current flowing through a fixed linear resistance is directly proportional to the voltage applied across it, and also inversely proportional to the resistance. This relationship between the voltage, current and resistance forms the basis of Ohm's law and is shown below:

$$\boldsymbol{Current\ (I) = \frac{Voltage\ (V)}{Resistance\ (R)}} \qquad \textbf{2.3}$$

2.2.4.1.1 Direct Current Electrical Conductivity Measurement

Based on the probe arrangement on the sample, there are two approaches for measuring direct current (DC) electrical conductivity: in-plane and through-plane. Figure 2.7 illustrates the position of the probes against the sample in two different approaches to conductivity measurement.

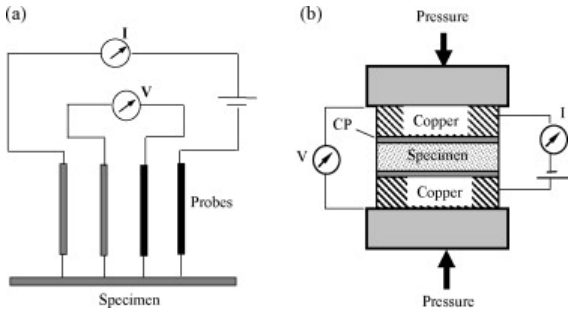

Figure 2.7 schematic diagram of electrical conductivity measurement setup of (a) in-plane and (b) through-plane conductivity [71]

If probes are located on each side of the sample and the electric current path through the specimen, through-plane conductivity will be measured. According to the below equation, through-plane electrical conductivity can be calculated:

$$\boldsymbol{\sigma_T = \frac{1}{\rho} = \frac{1}{\frac{R.A}{t}} = \frac{t}{R.A} \quad S/cm} \qquad \textbf{2.4}$$

Where t, R, and A are sample thickness, Resistance and surface area, respectively. If the probes are on one side of the sample, parallel to the current direction, the in-plane conductivity will be measured. ASTM D257-99 explains the in-plane electrical conductivity via a conventional four-point probe conductivity measurement device as below equation [71]:

$$\sigma_I = \frac{1}{\rho} = \frac{I}{R.t} = \left(\frac{ln2}{\pi.t}\right)\frac{I}{V} \quad S/cm \qquad 2.5$$

Where ρ is the electrical resistivity, t is the sample thickness, I is the applied current, and V is the measured voltage drop.

In this thesis DC electrical conductivity is measured with two different instruments. First, an in-plane four-point probe fixture was designed and fabricated in the laboratory. A DC voltage was applied with a DC power supply and the current and voltage drop was measured with digital multimeters, Figure 2.8.

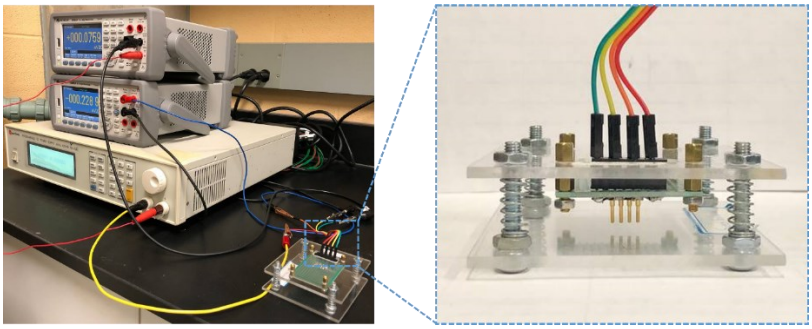

Figure 2.8 Instruments and the home made fixture to measure DC in-plane electrical conductivity

DC conductivity was also measured through a Biologic potentiostat under a linear sweep voltammetry technique. An in-plane interdigitated four-point probe was used for this measurement, Figure 2.9.

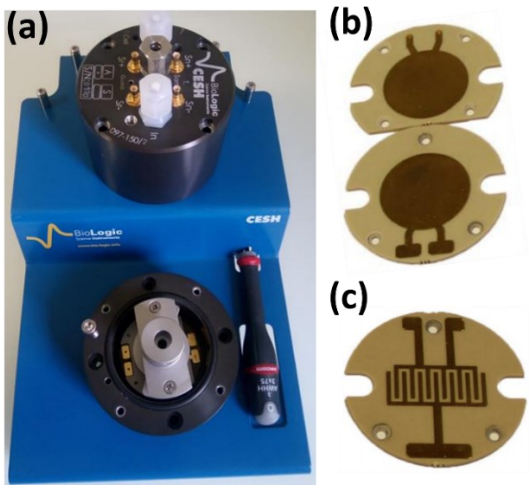

Figure 2.9 (a) Fixture for conductivity measurement with Biologic potentiostat, (b) through-plane, and (c) in-plane conductivity measurement electrodes

2.2.4.1.2 Alternating Current Electrical conductivity

Alternating current (AC) conductivity measurement is an important technique used to study the electrical properties of conductive polymer nanocomposites. AC conductivity measurements involve applying an alternating current or voltage to the nanocomposite material and measuring the resulting current that flows through the material. The electrical conductivity of the material can then be calculated using Ohm's law as discussed above. Usually, AC electrical conductivity at a frequency of 1 Hz is considered DC conductivity. The AC conductivity measurement technique can be used to optimize the design and performance of CPnCs for a range of applications, including electronic devices, sensors, and energy storage systems. Herein, we used biologic potentiostat and through-plane electrodes to measure broadband AC conductivity in the frequency range of 1 to 10^6 Hz, Figure 2.9.

2.2.4.2 Percolation theory

Percolation means the formation of a connected network of conductive fillers inside the insulative polymer matrix allowing electrons to path from one side to the other side of the sample. The formation of a conductive network (percolation) within conductive polymer nanocomposites can be defined and predicted by various geometric-, thermodynamic-, and statistical-based models [72–75]. The percolation threshold defines as the concentration at which the connected path occurs. The percolation threshold is dependent on the geometry, size, and shape of the conductive fillers, as well as the properties of the matrix material. By controlling the concentration and properties of the conductive fillers, it is possible to tailor the electrical conductivity of the CPnCs for specific applications. The most popular prediction model of percolation is the statistical percolation theory which is valid only for the filler concentrations above the percolation threshold. In this model, the estimation of percolation concentration begins with finite regular arrays of points and bonds. Typically, such arrays can be a simple cubic lattice. By computer simulation, one can predict the fraction of existing points or bonds that exist in a cluster. The points are in contact with one another in a cluster. The percolation point is achieved when the cluster spans the boundary of the arrays [76]. To obtain equations that relate conductivity and filler concentration, it is necessary to convert the predicted values into volume fractions. The following equation correlates the electrical conductivity of real mixtures with the volume fraction of the conductive filler:

$$\boldsymbol{\sigma = \sigma_f(\varphi - \varphi_c)^t} \qquad \textbf{2.6}$$

where φ_c is the percolation threshold, φ is the volume fraction of the conductive filler, σ_f is the conductivity of the filler and σ is the nanocomposite conductivity. The critical exponent, t, characterizes the rate of increase in conductivity as the filler content approaches the percolation threshold. It is noteworthy that the electron transferring in CPnCs is not required direct contact with the nanofillers. Electron conduction can happen through different mechanisms such as tunnelling and hopping between fillers which are separated from each other via a thin layer (about 1.8 nm) of polymer matrix [77,78]. Figure 2.10 shows a typical percolation curve of CPnC. Generally, the percolation curves have three distinctive zones: (i) insulative zone below the percolation threshold, (ii) percolation zone and (iii) conductive zone which is above the percolation threshold. When the concentration exceeds the percolation threshold, conductivity will be less sensitive to filler concentration.

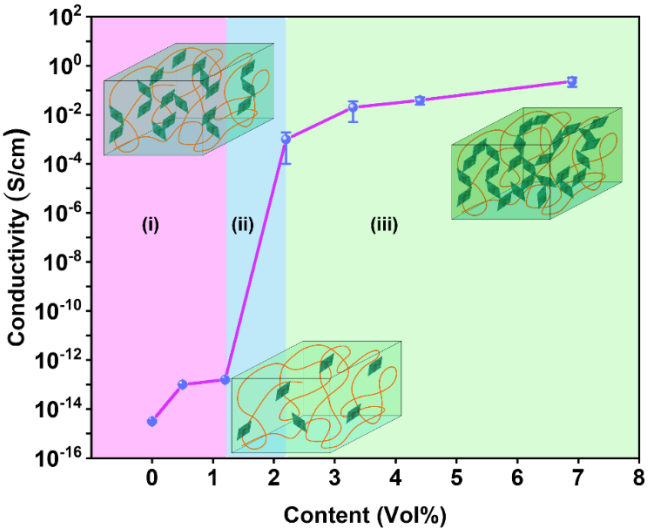

Figure 2.10 Typical percolation threshold for electrically conductive polymer nanocomposite

When the concentration of conductive fillers is low, insulating zone (i), the nanofillers are spaced far apart from each other. As a result, the transportation of electrons is controlled by the polymer matrix. Consequently, the electrical conductivity of CPnC is similar to that of neat polymers in the range of 10^{-13} –10^{-11} S/cm. Since the filler loading is low in this zone, the gap between insulators is extensive, and the possibility of charge transport between conductive fillers is minimal.

Increasing the filler loading causes a decrease in the insulating gaps between the fillers. When the distance between particles reduces to less than 1.8 nm, the electron transport mechanism is governed by electron tunnelling and hopping, (Zone (ii)) [77,78]. Essentially, a narrower insulating gap can

generate a much higher electric field than the macroscopic applied electric field by a factor of N. The N factor is determined by the ratio of the average size of conductive fillers to the average interparticle distance [79]. This higher electric field provides enough energy for free electrons to hop or tunnel over the insulating gaps. In the tunnelling mechanism, the insulating gap must be narrow enough for the tail of the electron wavefunction to pass through a barrier. However, in the hopping mechanism, an electron requires sufficient energy to overcome an energy barrier for changing its lattice site [80].

When percolation reached (Zone (iii)), direct contact between the nanofillers happens and allows free electrons to pass through the nanocomposite. This is why in the percolation zone, the conductivity of CPnC significantly increases by several orders of magnitudes. From now, incorporating more conductive nanofillers in the polymer matrix does not impact the electrical conductivity significantly. The slow increase in the slope of conductivity versus nanofiller loading may be attributed to the high contact resistance between the nanofillers [81]. Achieving a low percolation threshold in CPnCs is important and favorable from different perspectives. When the percolation threshold is high, a larger concentration of fillers is required to achieve the same level of electrical conductivity, which can increase the cost of the material and negatively impact mechanical and processing properties. Furthermore, high filler concentrations can lead to filler agglomeration, which can cause non-uniform electrical conductivity and structural defects in the nanocomposite. By achieving a low percolation threshold, CPnCs can be produced with lower filler concentrations, resulting in improved nanocomposite properties and reduced cost. The percolation threshold of CPnCs is influenced by several parameters, such as the shape, size and aspect ratio of the fillers. The aspect ratio is defined as the ratio of the longest dimension to the shortest dimension. For nanotubes, the aspect ratio is the ratio of the length to the diameter of the nanotubes, while for planar materials such as graphene, graphite flakes or MXene it is taken to be the ratio of the lateral dimension to the thickness of the flakes. Higher aspect ratio fillers or larger particles reduce the percolation threshold due to efficient network formation in which the number of individual particles in contact to make a conductive pathway is reduced [82]. For instance, graphene sheets are more effective than CNT in enhancing the electrical conductivity of nanocomposites [83]. However, their lower aspect ratio increases the electrical percolation threshold compared to the 1D highly entangled MWCNT networks with a very high aspect ratio [84,85]. Gao et al. [86] investigated the effect of GnP flake size on the electrical, thermal and mechanical properties of poly(lactic acid) nanocomposite and concluded that the larger GnP flakes size improves young modulus and reduces the electrical percolation threshold. Processing condition, intrinsic properties of the matrix,

and degree of polymer-filler interactions which impact on quality of the fillers dispersion in polymer matrix are the other parameters that affect the percolation threshold and need to be considered to achieve CPnCs with lower percolation threshold [87].

2.2.4.3 Dielectric properties

Dielectric materials are insulating materials that can store and release electrical energy. High performance dielectric materials have advanced properties that make them potential candidates for the next generation of portable electronic devices. Dielectric materials react to the electric field due to the displacement ability of their charge carriers. High dielectric permittivity (ε') and low dielectric loss (tan δ) of such novel materials lead them to find their application in a broad range of advanced energy harvesting and storage systems [88], piezoelectric generators [89], and inverters and transistors [90]. Although polymers have a lower dielectric constant between ε' = 3 to 10, compared to inorganic material, they are attractive materials as dielectrics due to extremely low dielectric loss and high dielectric breakdown strength [91]. Incorporating conductive or non-conductive fillers in a polymer matrix can improve polymer nanocomposites' dielectric properties. As illustrated in Figure 2.11, the concept of dielectric materials can be defined based on charge polarization in a parallel plate capacitor in an applied electric field. Polarization is defined as total dipole moments in a dielectric per unit volume.

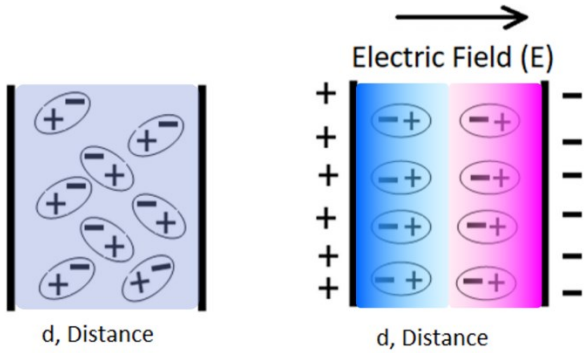

Figure 2.11 Polarization of dielectric material in an applied electric field

When a voltage (V) is applied to a material, the generated electric field (E=V/d) between two plates separated by a distance d polarizes the dielectric material by the separation of positive and negative charges. However, polarization is not the only phenomenon that occurs in a dielectric material. The electric field induced motion in bound charges is also happening at the same time, which is known as

dielectric loss. Taking both polarization and losses into account, dielectric constant can be defined as a complex function as below:

$$\boldsymbol{\varepsilon(\omega) = \varepsilon'(\omega) - i\varepsilon''(\omega)} \qquad \textbf{2.7}$$

where ω is the angular frequency, ε'(ω) is the real part, and ε''(ω) is the imaginary part of the dielectric permittivity. Dialectic loss (tan δ) is defined as the ratio of the imaginary part to the real part. Four main types of polarizations exist in a dielectric material: electronic, ionic, dipolar, and interfacial polarizations, as shown in Figure 2.12. As shown in Figure 2.12, each polarization mechanism occurs at specific frequency ranges which are associated with a peak in dielectric loss (ε''). Electronic polarization is associated with the displacement of electron clouds with respect to the nucleus under the influence of an applied electric field. Ionic polarization is present in ionic materials in which ion charge displacement and positive and negative charge separation occur in a crystal lattice. This type of relaxation mainly exists in ceramics, inorganic crystals and glass [92]. Both electronic and ionic polarization show resonance at frequencies in the optical and IR range, respectively. Thus, these are classified in the resonance regime. It should be noted that more complicated frequency dependencies can be induced by various structures within the material [93,94].

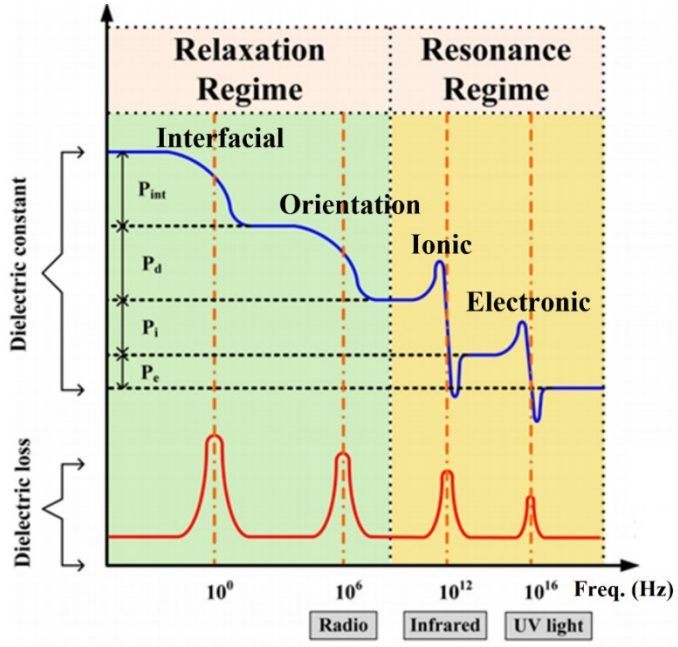

Figure 2.12. Polarization schemes in frequency domains [91]

Dipolar polarization in polymer nanocomposites is due to the orientation of permanent molecular dipole moments [95]. Dipolar relaxation occurs between 0.1 Hz to 10 MHz frequency range depending on the nature of dipoles, temperature and frequency. Therefore, it is important to control the structure and density of dipoles in the synthesis of nanocomposite to obtain various levels of real permittivity and dielectric loss. As shown in Figure 2.12, the main cause of material polarization in the frequency range of 1 kHz to 1 MHz is interfacial polarization which is associated with the polarization in the interface between filler and matrix [96]. Considerable difference in the electrical conductivity of the matrix and filler leads to charge accumulation at their interface (based on Maxwell-Wagner-Sillars (MWS) effect) [97]. This phenomenon can be explained by the concept of relaxation time ($\tau=\varepsilon/\sigma$). Indeed, different conductivity between two components of a dielectric material (matrix and nanofiller) causes charge accumulation at the interface with different relaxation times. The more difference in conductivity of the components, the more interfacial polarization takes place. [98].

2.2.4.4 EMI shielding effectiveness

Electromagnetic interference (EMI) is defined as "the process by which disruptive electromagnetic energy is transmitted from one electronic device to another via radiated or conducted paths or both" [99]. The rapid development of portable electronic devices and telecommunication systems, especially after the emergence of 5G technology, has brought easier life for the human being. However, as a consequence of such developments, EMI has turned into an ever-increasing concern due to its deleterious effect on the proper functioning of electronic devices and human health [100]. For example, the EMI produced in the power system of laptops can deteriorate the function of a TV antenna or its wireless communications with remote control systems.

Electromagnetic energy of any frequency in the spectrum can cause EMI problems, but mainly it occurs due to the radiation in the radio wave and microwave regions as mentioned in Figure 2.13. Therefore, the need for shielding our environment from the radiation that is emitted from high frequency (GHz) products is crucial, Figure 2.13-c. These products include cellphones or communication devices, microwave remote sensors, wireless Local Area Network (LAN) communications satellites, cable and satellite television broadcasting, direct-broadcast satellite (DBS), and radio astronomy. Therefore, industries demand materials with effective EMI shielding properties as well as being lightweight and easy to process. The commercialized EMI shielding materials should have values of at least 20 dB and 30 dB in order to block 99 and 99.9 percent of the incident EM waves [101].

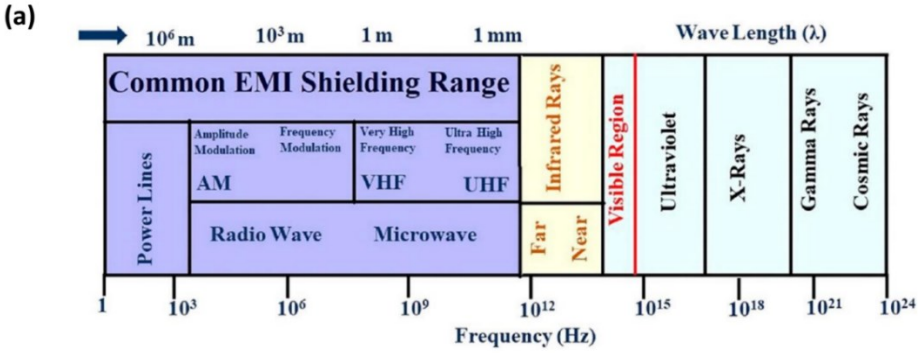

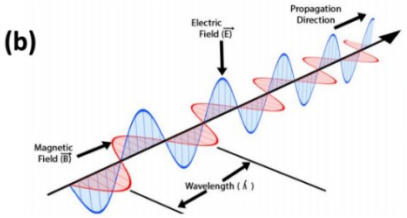

(c)

Property range	Radio waves	Microwaves
Frequency (Hz)	3 kHz to 300 GHz	300 MHz to 300 GHz
Wavelength (m)	100 km to 1 mm	1 m to 1 mm
Energy (eV)	Micro-eV to milli-eV	Milli eV to eV

Figure 2.13 (a) Electromagnetic wave spectrum, (b) a plane electromagnetic wave, and (c) properties of electromagnetic waves in radio and microwave region [100,102]

A plane electromagnetic wave contains electric and magnetic fields which have normal to each other and are in a plane which is perpendicular to the direction of wave propagation, Figure 2.13-b. According to Lorentz's force law, the response of electrons to electromagnetic fields in an EMI shielding material is as below:

$$\vec{F}=\overrightarrow{qE}+\overrightarrow{qv}\times\mu_0\vec{B} \qquad \textbf{2.8}$$

Where $\vec{E}$ and $\vec{B}$ are the strength of electric and magnetic fields, respectively, and q is the charge of transferring particle with a velocity of $\vec{v}$, and μ_0 is the free space magnetic permeability which is equal to $4\pi\times10^{-7}$ h.m^{-1} (Henries/meter) [103].

As illustrated in Figure 2.14, two regions can be distinguished based on the distance between the EMI source and its receptor. The first is the near field, which exists when the distance between the source and the receptor is less than $\frac{\lambda}{2\pi}$. In this region, the characteristics of the field are mainly determined by the properties of the source. The second region is the far field, which exists when the distance between the source and the receptor is more than $\frac{\lambda}{2\pi}$. In this region, the properties of the field are determined by the medium through which the EM wave propagates [104,105]. In this thesis, we have focused on the second region.

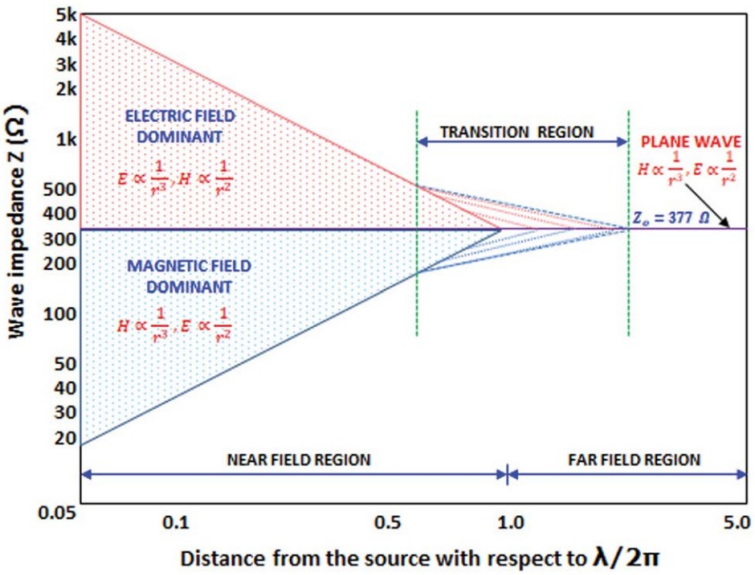

Figure 2.14 Wave impedance as a function of distance from the source normalized to λ/2π [105]

The effectiveness of EMI shielding material is determined by comparing the power of incident EM wave to the power of outgoing radiation wave from the medium or shielding material. The difference between incident and outgoing EM waves depends on the frequency of the wave, the electrical conductivity and the thickness of the shielding material. A propagating EM wave from a source can be reflected, absorbed, and transferred. Reflection, absorption and internal multiple reflections are the shielding mechanisms of EMI shielding material [106], Figure 2.15. The reflection mechanism is the reflection of a proportion of the incident EM waves from the surface of the shielding material which is due to the abundant free surface charge carriers at the surface of the shielding material [7]. However, the absorption mechanism which originates from polarization and ohmic losses is a proportion of the transmitted EM wave within the shield that is dissipated by absorption and turning to heat [107]. As discussed in section 2.2.4.3, polarization loss pertains to the interfacial polarization density which is thereby related to the dielectric properties of the shielding material. Ohmic loss attenuates the energy of EM wave via current flow through the conduction and tunnelling mechanisms. The internal multiple reflection mechanism refers to the phenomenon where electromagnetic waves that have already been reflected within an EMI shielding material undergo further reflections [106]. Amplifying the absorption shielding mechanism of EMI shielding material is crucial because relying solely on a reflective shielding mechanism can cause secondary EMI pollution when the reflected EM waves interact with other devices.

EMI shielding effectiveness (SE) can be quantitatively analyzed by comparing the power of incident (P_i) and transmitted (P_t) EM waves, in decibel (dB) units. EMI SE defines as below equation:

$$\boldsymbol{EMI\ SE = 10\log_{10}(\frac{P_i}{P_t}) = 10\log_{10}(\frac{{E_i}^2}{{E_t}^2})} \quad \textbf{2.9}$$

Where E_i and E_t are the strength of the electric field of the incident and transmitted electromagnetic waves, respectively. For thick material in which the total shielding effectiveness is higher than 15 dB, multiple reflection shielding mechanism is being neglected and the total EMI SE is calculated according to Simon's formula [108]:

$$\boldsymbol{EMI\ SE = 50 + 10\log\left(\frac{\sigma}{f}\right) + 1.7t\sqrt{\sigma f}} \quad \textbf{2.10}$$

Where σ is the electrical conductivity (S/cm), f is the frequency (MHz) and t is the sample thickness (cm). The first two terms of the formula indicate reflection based EMI shielding and the last term represents absorption based EMI shielding.

In this thesis we measured EMI shielding performance of the nanocomposites using wave guide method in the P-band frequency range (12.4-18 GHz) and varying sample thickness. According to ASTM D5568-08, reflection effectiveness (SE_R) and absorption effectiveness (SE_A) can be calculated from the scattering parameters (S-parameters) which are obtained by a vector network analyzer (VNA). Reflection parameters (S_{11} and S_{22}) were used to calculate the reflection (R) coefficient and transmission parameters (S_{12} and S_{21}) were used to calculate the transmission (T) coefficients, via the below equations [106,109,110]. The absorption coefficient is calculated via equation 2.13.

$$\boldsymbol{R = |S_{11}|^2 = |S_{22}|^2} \quad \textbf{2.11}$$

$$\boldsymbol{T = |S_{12}|^2 = |S_{21}|^2} \quad \textbf{2.12}$$

$$\boldsymbol{A = 1 - R - T} \quad \textbf{2.13}$$

The total EMI shielding effectiveness (SE_T) of the nanocomposites is equal to the sum of SE_R and SE_A, which could be described by the following equations:

$$\boldsymbol{SE_T = SE_R + SE_A} \quad \textbf{2.14}$$

$$\boldsymbol{SE_R = -10 \cdot log_{10}(1 - R)} \quad \textbf{2.15}$$

$$\boldsymbol{SE_A = -10 \cdot log_{10}\left(\frac{T}{1-R}\right)} \quad \textbf{2.16}$$

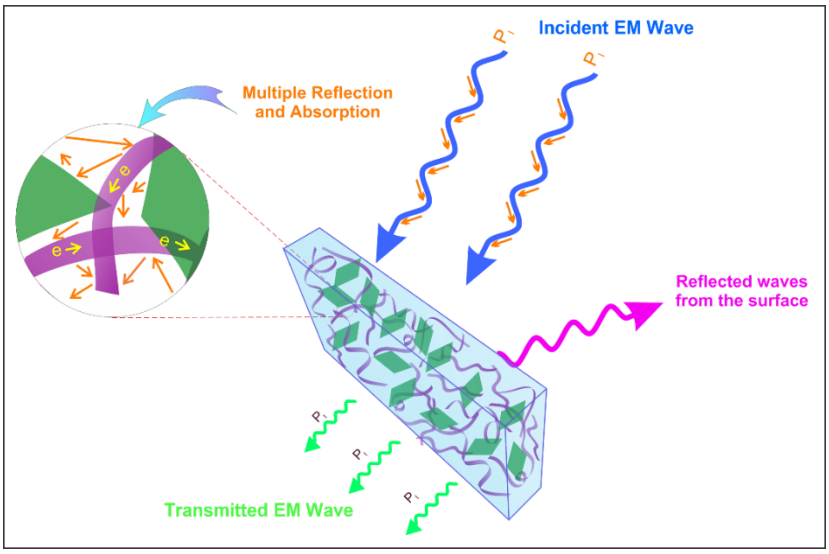

Figure 2.15 Schematic illustration of EMI shielding mechanism

The efficiency of EMI shielding in CPnCs relies on specific factors and characteristics, such as the electrical and magnetic properties of the conductive nanomaterials and insulative polymer matrices, as well as the nanocomposite's fabrication techniques, structure, and filler content. For example, higher conductivity and dielectric constant of the polymer matrix can increase the EMI shielding effectiveness. Furthermore, other properties of the matrix, such as high molecular weight (which results in high viscosity during processing) or low thermodynamic affinity between the polymer matrix and filler material, decrease the quality of nanomaterial dispersion and subsequently decrease CPnC's conductivity by increasing the percolation threshold. As we discussed in section 2.2.4.2, intrinsic properties of the conductive nanomaterials, such as electrical conductivity, size, shape, and aspect ratio, play a crucial role in the quality of the created conductive network and determine the electrical conductivity of the CPnC. With high electrical conductive nanomaterial, extra-large aspect ratio, and planar structure, a very high electrical conductivity of CPnC is achievable, resulting in excellent EMI SE. The processing method of the CPnCs is also highly important in creating an efficient conductive filler network. Solvent blending is much more effective than melt blending to obtain good nanomaterial dispersion, while the environmental concerns of using solvents impede this method from industrialization. Due to the significant viscosity rise at higher nanomaterial loadings, in-situ polymerization is more efficient in lower loadings. Besides the material properties, considering engineering aspects in designing CPnC can further help in enhancing EMI SE. For instance, increase the thickness of the shielding material can enhance EMI SE. Moreover, introducing microcellular

structure in CPnC can improve the EMI SE mostly by absorption mechanism. Incident EM waves trap inside the conductive cell walls and dissipate through multiple internal reflections. A layered structure design with a gradient change of conductivity is another approach to tune the surface impedance mismatch and create highly efficient EMI shielding CPnCs. [111]. In summary, a successful design for highly efficient EMI shielding CPnC requires an essential to optimize the constituents, quantities, types, structure, morphology, and processing methods. In summary, a highly efficient EMI shielding CPnC design requires optimization of the constituents, quantities, types, structure, morphology, and processing methods [100,112]. Table 2.1 presents a summarized list of various factors that are necessary to consider when designing a conductive polymer composite with highly efficient EMI shielding capabilities.

Table 2.1 Factors affecting the shielding effectiveness of CPnC based EMI shielding material

Matrix/Nanomaterial Properties	• Molecular weight • Crystallization • Dielectric properties (Permittivity, Permeability etc.) • Polymer-filler interactions • Status of the filler dispersion
Nanomaterials	• Electrical conductivity • Magnetic properties • Concentration • Type • Size • Shape • Aspect ratio
Nanocomposite fabrication method	• Melt blending • Solvent blending • In situ polymerization
Engineering design of CPnC	• Bulk nanocomposite • Multilayered nanocomposite • Segregated structure • Microcellular structure • Coated layered structure • Layered film/foam structure • Nanocomposite thickness

2.2.4.5 Mechanical properties

Mechanical properties are important in developing high performance CPnCs for various applications including EMI shielding for several reasons:

- **Durability**: CPnCs used for EMI shielding applications are often subjected to mechanical stresses during their service life, such as impact, vibration, and bending. Mechanical properties such as strength, toughness, and ductility are crucial to ensure that the nanocomposite can withstand these stresses without failure or degradation.
- **Processing**: CPnCs are typically produced through a combination of mechanical and chemical processing steps, such as solution mixing, extrusion, and injection moulding. Mechanical properties such as viscosity, melt flow rate, and elasticity can significantly affect the processing behavior of the nanocomposite, and ultimately determine the final product quality.
- **Adhesion**: CPnCs are often used as coatings or films on substrates such as metals or plastics. Good adhesion between the nanocomposite and the substrate is critical to ensure proper EMI shielding performance. Mechanical properties such as adhesion strength and interfacial bonding can impact the adhesion between the nanocomposite and the substrate.
- **Weight**: High-performance EMI shielding applications often require lightweight materials that can be easily moulded or shaped into complex geometries. Mechanical properties such as density, stiffness, and impact resistance can affect the weight and formability of the nanocomposite, and ultimately the ease of manufacturing and transportation.

It is important to note that the mechanical properties of CPnC and its EMI shielding effectiveness are closely connected. The mechanical properties of CPnCs are crucial to ensure that it meets the required performance standards in terms of strength, durability, and flexibility while performing highly efficient EMI shielding functionality. The mechanical properties of CPnCs depend on several factors such as the type of polymer matrix used, the filler materials, polymer-filler interactions and their processing methods.

A universal testing machine (UTM) is a simple instrument that makes mechanical property characterization feasible. In this thesis, we characterized the mechanical properties of the nanocomposite via this instrument. To analyze the tensile properties of the polymeric materials, based on ASTM D638-14 “Standard Test Method for Tensile Properties of Plastics”, sample is clamped between two grips and elongated at a constant rate. The Strain-stress curve (SS curve) is obtained by

the test and the mechanical properties such as a tensile modulus (Young's modulus), tensile strength, and elongation at break are calculated by the curve. The tensile modulus represents the stiffness of a material using the initial slope of the SS curve. Tensile strength is a measurement of the force required to pull material to the point where it breaks. The tensile strength of a material is the maximum amount of tensile stress that it can take before failure. The elongation at break presents the maximum strain when the specimen is ruptured and represents the ductility of the material.

2.3 Conclusions and future perspectives

In summary, the demand for EMI shielding materials is increasing rapidly due to the growing use of electronic devices in various industries such as telecommunications, automotive, aerospace, and healthcare. The current research aims to develop shielding materials that can satisfy the requirement for shielding effectiveness without the drawbacks of traditional metallic shields. CPnC has several advantages over other EMI shielding materials such as metals, including its light weight, high strength, and low cost. Additionally, it is easy to process and can be moulded into complex shapes, making it ideal for use in a wide range of electronic devices. The market for EMI shielding materials based on CPnC is expected to grow significantly in the coming years, driven by the increasing demand for reliable and safe electronic devices. Despite advancements in laboratory-level preparation of shielding materials, there is still a significant disparity between their performance in controlled settings and their practical use in industrial applications. Therefore, further research in developing advanced CPnCs, including the development of new polymer matrices and conductive nanomaterials, are required and expected to improve its mechanical and electrical properties further, leading to the development of durable, flexible lightweight and more efficient EMI shielding materials.

Chapter 3

Enhanced Electrical and Mechanical Properties of Graphene Nanoribbon/ Thermoplastic Polyurethane Nanocomposites

This chapter is reprinted in adapted form from the article below with permission from Elsevier.

Yun-Seok Jun †, **Saeed Habibpour** †, Mahdi Hamidinejad, Moon Gyu Park, Wook Ahn, Aiping Yu, Chul B. Park, "Enhanced Electrical and Mechanical Properties of Graphene Nanoribbon/ Thermoplastic Polyurethane Nanocomposites", Carbon (2021), 174, 305-316 (†Equal Contribution)

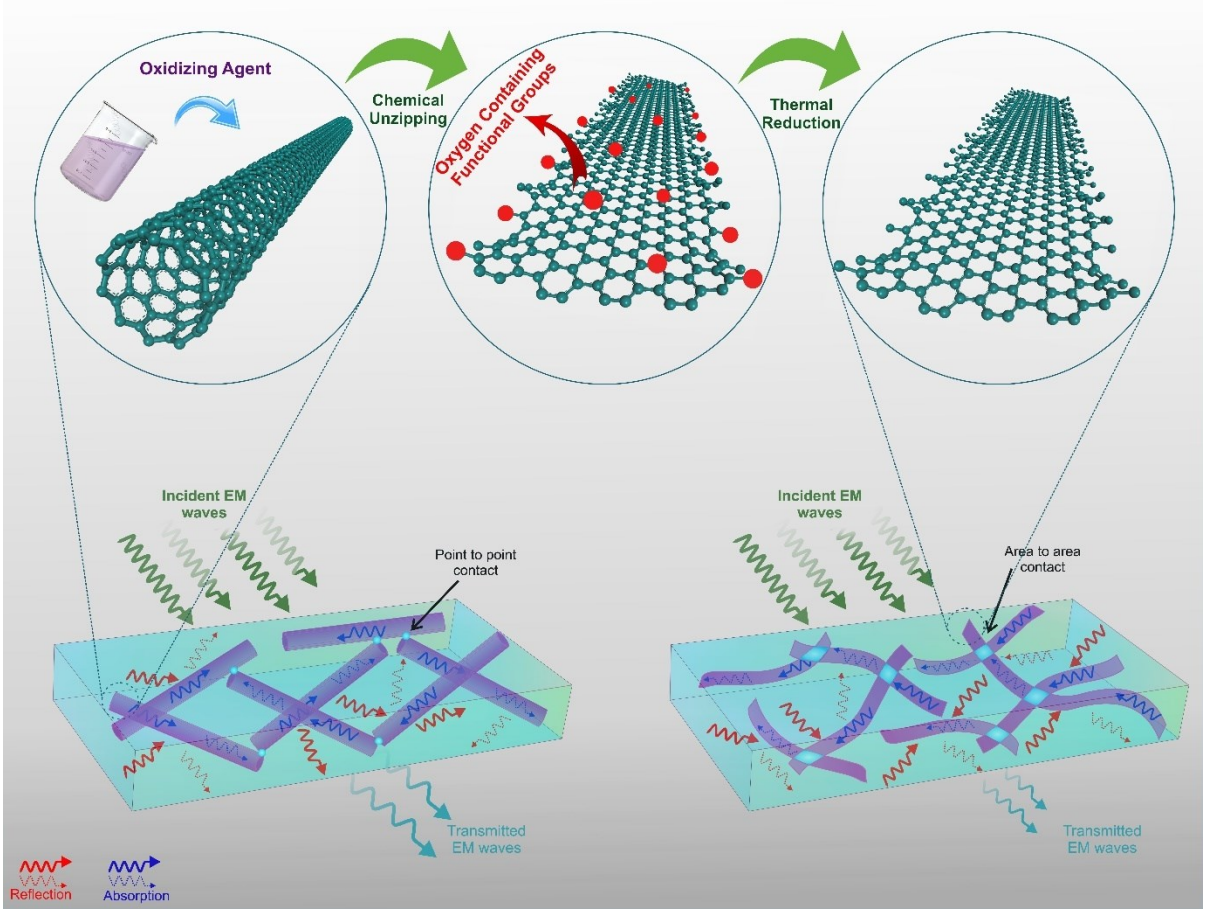

3.1 Introduction

In recent decades, electrically conductive polymer nanocomposites (CPnCs) have attracted a great deal of attention from both academia and industry as highly desirable and advanced materials due to their functionality, lightweight [6], ease of fabrication [87,113] and low cost [114]. CPnCs have great potential for an array of applications including sensors[115–119], energy storage devices [120–122], electromagnetic interference (EMI) shielding [123–128], electrostatic dissipation [129,130] and energy conversion [131]. The electrical properties of the polymer nanocomposites can be tuned by adjusting the intrinsic polymer properties and the morphology of conducting filler. The rapid growth of the electronics industry in modern society requires advanced materials that mask the released electromagnetic fields to ensure, not only undisturbed and precise operation of the equipment, but also guard human beings from deleterious effects of the electromagnetic waves [123,132]. CPnCs are one of the best candidates for halting electromagnetic pollution.

Among many carbonaceous nanofillers, multi-walled carbon nanotubes (MWCNTs) and graphene are the two best candidates for developing multifunctional polymer nanocomposites [125,126,133–137]. When incorporated into polymer matrices, their different geometrical and structural features lead to a massive variety of network formations and final properties of the nanocomposites [84,138–142]. While MWCNTs have a one dimensional tubular structure with a high length-to-diameter aspect ratio and electrical conductivity of 10^6-10^7 S/m [143,144], graphene is the world's first two dimensional material with extraordinary properties [145–147]. Although graphene provides better bridging properties that enhance the polymer-filler or filler-filler interactions in polymer nanocomposites due to its exceptional surface area [148,149], the lower length-to-width aspect ratio and easy stacking of graphene sheets often result in a high electrical percolation threshold as compared to the highly entangled MWCNT networks [150].

To take advantage of both MWCNTs and graphene, researchers have used hybrids of the two fillers when fabricating nanocomposites, and this often leads to enhanced electrical and EMI shielding properties of CPCs. For instance, Zhao et al. [123] compared the effect of a hybrid of MWCNTs and graphene on the EMI shielding efficiency of polyvinylidene fluoride (PVDF) nanocomposites. They showed that a higher EMI shielding value can be achieved by hybridizing 5 wt% MWCNTs with 10 wt % graphene (27.58 dB), as compared to using 15 wt% graphene alone (22.58 dB). Zhang et al.[151] also observed very high dielectric properties of cyanate ester resin/expanded graphite (EG)/MWCNT

nanocomposite due to the synergistic effect of EG and MWCNTs. In their system, EG was found to improve MWCNT dispersion and provide an effective filler network by serving as a bridging agent between adjacent MWCNTs.

A similar yet more advanced approach can be the integration of the morphological characteristics of graphene and MWCNTs into a single structure. Graphene nano-ribbon (GNR) is a long strip of graphene sheet with a very high length-to-width ratio (100–500) [152–154]. Owing to its distinctive benefits, researchers have made significant efforts to produce GNR by several different methods, including Argon plasma carving [155], a sonochemical method [156], chemical vapor deposition[157], electron-beam lithography [158] and lengthwise unzipping of MWCNTs by chemicals [153,159,160]. Being scalable with a potential for high production yield, the chemical unzipping of MWCNTs is the most promising method for polymer nanocomposite study.

The effect of GNR when incorporated into a polymer is rather controversial. For example, Sinitskii et al. [161] fabricated four terminal devices based on GNR and observed that the reduced monolayer of GNR has average electrical conductivity of 1–3 order of magnitude higher than reduced GO flakes. Yang et al. illustrated that the use of GNR enhanced both electrical and mechanical performance of polyvinyl alcohol/GNR nanocomposites. As compared to MWCNTs, 32.5% increase in electrical conductivity and 490% in Young's modulus were reported [162]. On the other hand, Arjmand et al. [163] compared the conductivity of PVDF/GNR and PVDF/MWCNT nanocomposites and showed that MWCNTs were able to form a better conductive network, enhancing the electrical conductivity. Furthermore, Sadeghi et al. [164] suggested that inferior performance of GNR nanocomposite could be due to lower interlacing ability of the GNR strips and excessive adhesion of polymer chains on the GNR interface that increases the surface resistivity. There could be many different reasons for such conflicting results. Depending on the GNR fabrication methods, the physical and chemical properties of GNR may vary dramatically. Moreover, the nanocomposite processing method is another crucial issue that directly impact the properties of the nanocomposites. The chemistry and physical properties of polymer matrix also influence the affinity between the matrix and filler and the degree of dispersion.

In this work, GNR and parent MWCNTs were added to thermoplastic polyurethane (TPU) and the electrical conductivity, the dielectric property, the EMI shielding effectiveness (SE) and the mechanical properties of the nanocomposites were thoroughly investigated and compared. It was found that the electrical conductivity, the EMI SE and the mechanical properties of GNR/TPU nanocomposites were

far superior to those of MWCNT/TPU nanocomposites. This greatly heightened performance of GNR added nanocomposites is mainly attributed to enhanced filler interconnections between GNRs. The individual filler particle flexibility was significantly increased when tubular multi-layered CNTs were opened and transformed into long, thin strips. This allows geometrical conversion from line-to-line to sheet-to-sheet contact interfaces, which considerably increases the contact area. The increased flexibility also increased the chances of forming a percolating network between fillers. In addition, the unzipping and exfoliation of MWCNTs resulted in the increase of the number concentration of filler particles, leading to improved electrical and mechanical performance.

3.2 Experimental Section

3.2.1 Materials and sample preparation

MWCNTs with a diameter of 20–30 nm and a length of 10–30 μm were purchased from Cheap-Tubes Inc. Hydrogen peroxide (30%), phosphoric acid, sulfuric acid and dimethylformamide (DMF) were acquired from Sigma Aldrich. Potassium permanganate was purchased from EMD Chemicals. Aromatic polyether-based thermoplastic polyurethane (TPU), Estane® 58123-Lubrizol, was used as the polymer matrix.

As illustrated in Figure 3.1, by utilizing the improved Hummer's method proposed by James Tour and co-workers, MWCNTs were longitudinally unzipped to produce graphene oxide nano-ribbon (GONR) solution [153,165]. GONR solution was freeze-dried to obtain GONR powder. GONR powder was subsequently thermally reduced at 900 °C to produce GNR powder. Both GNR and MWCNT powders were used as conductive fillers for a comparative study. MWCNT/TPU and GNR/TPU nanocomposites were prepared by solution processing and compression molding as follows. 10 g of TPU was dissolved in 100 mL of DMF and stirred at 90 °C for 3 hours. A certain amount of filler was added to the DMF solution and sonicated for 5 hours in a bath sonicator. The bath temperature was fixed at 20 °C to enhance the efficiency of the sonication process, promoting the degree of filler dispersion [166]. This mixture was then placed in an evaporating dish and dried in a convection oven at 70 °C for 3 days. The dried powders were compression molded into circular samples with a diameter of 20 mm at a temperature and pressure of 200 °C and 5 MPa, respectively. The prepared samples had filler contents of 1.0, 3.1, 5.3 and 8.2 vol%. The prepared samples have contents of 2, 6, 10 and 15 wt.%. The corresponding volume percentage loading of the nanocomposites were calculated according to the equation provided in section 3.5 and were as 1.0, 3.1, 5.3 and 8.2 vol%, respectively.

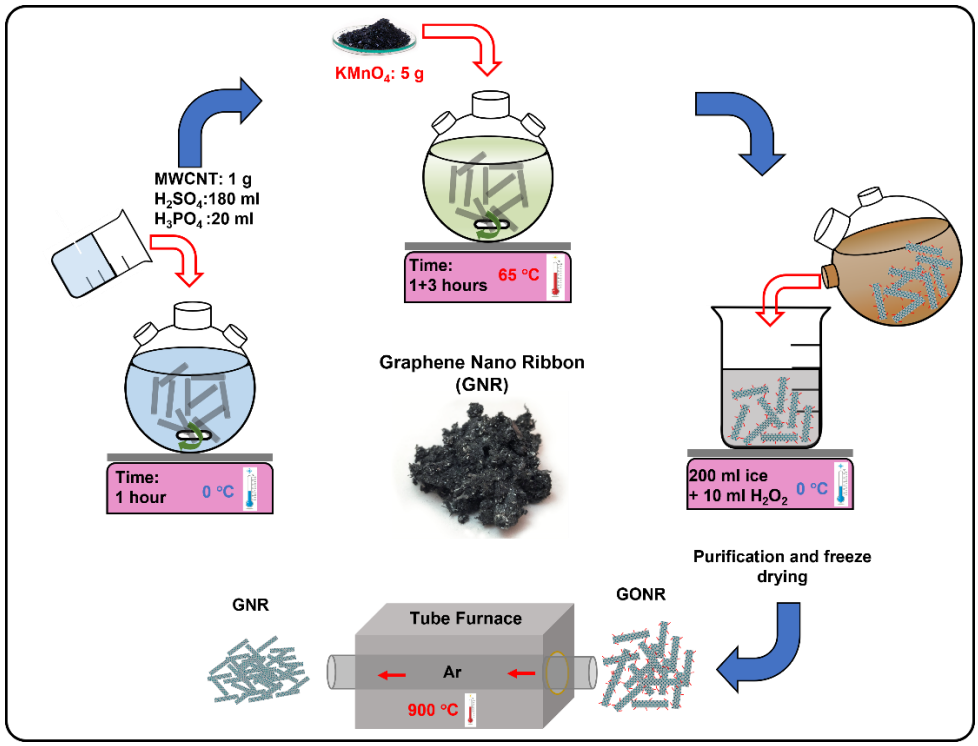

Figure 3.1 Procedure of oxidative unzipping of MWCNT and subsequent thermal reduction process to produce GNR, (Reprinted from S. Habibpour et. al, Chemical Engineering Journal 405, (2021), 126858) [165]

3.2.2 Characterization

The individual MWCNT and the unzipped GNR were imaged by transmission electron microscopy (TEM) (JEOL 2010F) for verification of longitudinal unzipping reaction. The morphology of the nanocomposite samples was characterized by scanning electron microscope (SEM) (Quanta EFG250). The nanocomposite samples were cryo-fractured and subsequently sputter-coated with gold for SEM imaging. X-ray diffraction (XRD) (Rigaku Miniflex 600) was used to investigate the alteration of crystal structure of MWCNT induced by oxidation and reduction processes. The defects and disorders of MWCNT and GNR were explored by means of Raman spectroscopy (Bruker Senterra, 532 nm).

The electrical conductivity, the dielectric constant (permittivity) and the dielectric loss of the samples with a 20 mm diameter and a thickness of 1.3 mm were measured using an Alpha-A high performance dielectric impedance analyzer (Novocontrol Technologies GmbH & Co. KG). The broadband

alternating current (AC) electrical properties of MWCNT/TPU and GNR/TPU nanocomposite samples were measured for frequencies from 1×10^{-1} to 1×10^{5} Hz. The electrical conductivity at a frequency of 0.1 Hz was reported as the direct current (DC) electrical conductivity. The parallel analyses of the dielectric properties were performed at a frequency of 1×10^{3} Hz.

The EMI SE of the MWCNT/TPU and GNR/TPU nanocomposite samples with dimensions of $16\times8.0\times1.3$ mm^3 was analyzed over a frequency range of 12.4–18 GHz (P-band) using an Agilent N5234A vector network analyzer. The reflection (R), transmission (T) and absorption (A) coefficients were calculated from the S-parameters (S_{11} and S_{21}) based on the following equations.

$$\boldsymbol{R = |S_{11}|^2} \quad \textbf{3.1}$$

$$\boldsymbol{T = |S_{21}|^2} \quad \textbf{3.2}$$

$$\boldsymbol{A = 1 - R - T} \quad \textbf{3.3}$$

The total EMI shielding effectiveness (SE_T), the EMI shielding by absorption (SE_A), the EMI shielding by the reflection (SE_R) were determined by the following equations:

$$\boldsymbol{SE_T = SE_R + SE_A} \quad \textbf{3.4}$$

$$\boldsymbol{SE_R = -10 \cdot log_{10}(1 - R)} \quad \textbf{3.5}$$

$$\boldsymbol{SE_A = -10 \cdot log_{10}\left(\frac{T}{1-R}\right)} \quad \textbf{3.6}$$

Tensile testing was performed on an ADMET universal testing machine (eXpert 7603, USA) with a crosshead speed of 5 mm/min. Nanocomposites were cut into a rectangular shape of $11\times5\times0.5$ mm^3. The tensile modulus was determined by the linear slope of the initial stress-strain curve in the strain range of 2-10%.

3.3 Results and Discussion

3.3.1 Material characterizations

Figure 3.2-a is a schematic illustration of a lengthwise MWCNT unzipping to produce GNR. Figure 3.2-b and c are the TEM images of MWCNT and GNR, respectively, which clearly demonstrate that thin and elongated strips of GNR is successfully prepared from MWCNT. The unzipped GNR exhibits a very high length-to-width aspect ratio (100-500) with a length

of 10-30 µm and a width of 60-90 nm, approximately.

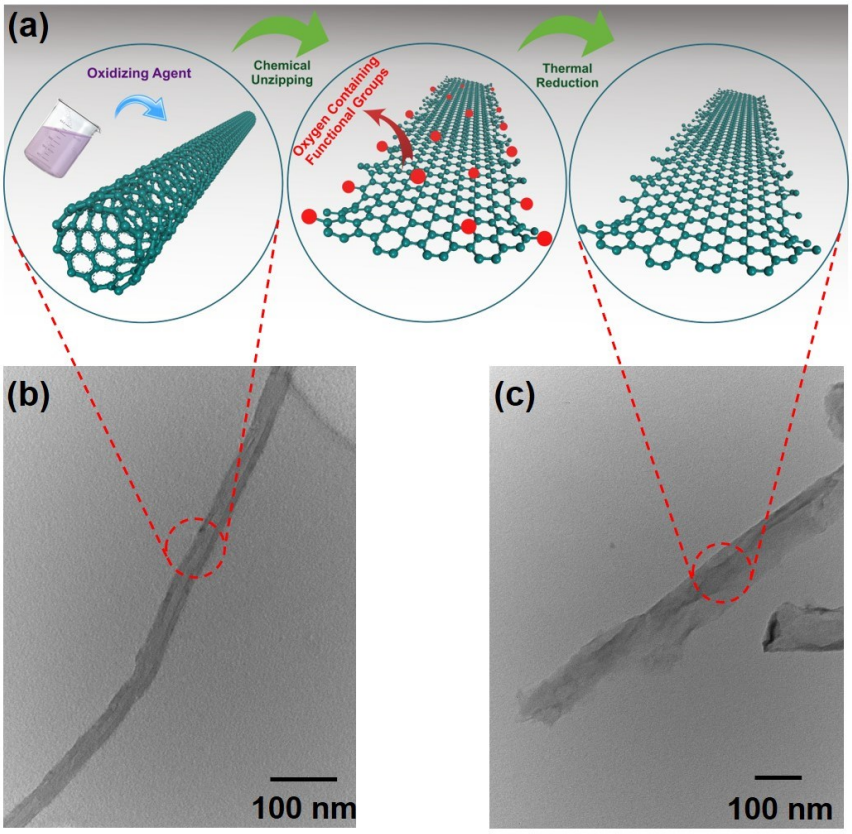

Figure 3.2 (a) Schematic illustration of chemical unzipping of MWCNT to produce GNR. TEM images of (b) MWCNT and (c) GNR.

The structural alteration of MWCNT due to the oxidation and reduction reactions is explored by means of XRD, Figure 3.3-a. Brag's equation can be used to determine the interlayer distances (d) between graphitic layers, and Scherrer-Debye equation provides size of the graphitic crystalline structures (τ). The average number of graphitic layers in nanoparticles was determined by dividing the crystal size over the interlayer distance [165].

$$\mathbf{d} = \frac{\lambda}{2sin(\theta)} \qquad \mathbf{3.7}$$

$$\boldsymbol{\tau} = \frac{0.89\lambda}{\beta\, cos(\theta)} \qquad \mathbf{3.8}$$

$$\mathbf{Number\ of\ layers} = \frac{\tau}{d} \qquad \mathbf{3.9}$$

where λ is the wavelength of X-rays and β is the Full Width at Half Maximum peak. The MWCNTs showed a 2θ peak at 26.06, indicating an interlayer distance of 3.43 Å. The 2θ peak for GONR appeared at 9.90° with a calculated interlayer distance of 8.92 Å. The interlayer distance increased from 3.43 Å to 8.92 Å since the functional groups intercalated between the multi-layers of MWCNT during the oxidation reaction. The 2θ peak for GNR was located at 26.08°, implying that the intercalated functional groups were removed by the thermal reduction. The calculated interlayer distance was 3.41 Å. It is notable that the 2θ peak for GNR broadened and its intensity was also significantly reduced, which implies that MWCNTs have been highly exfoliated and GNR existed in a few-layer structure. The calculated parameters are summarized in Table 3.1.

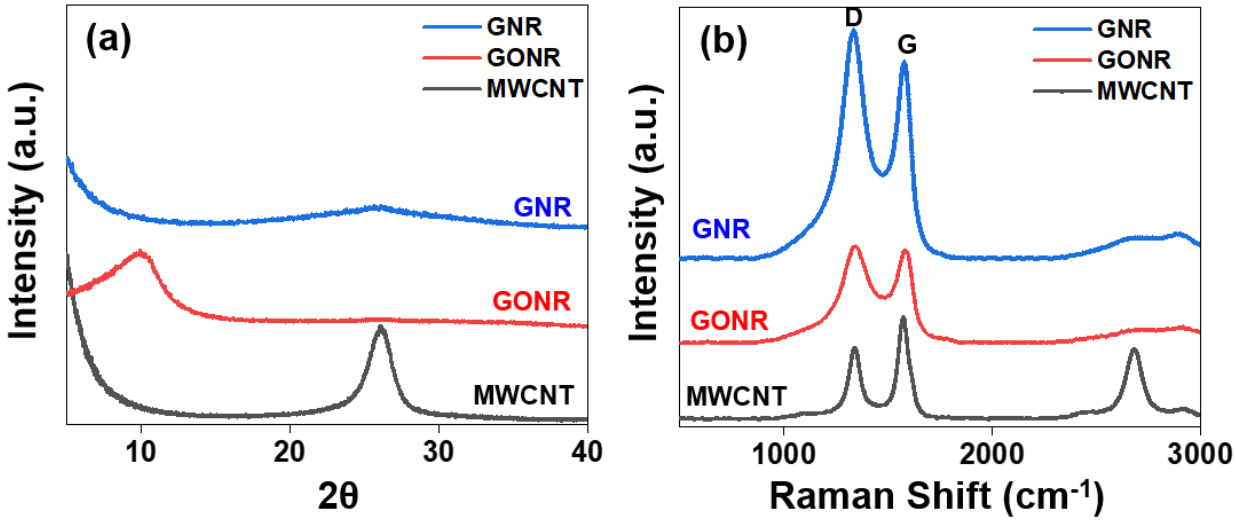

Figure 3.3 (a) XRD and (b) Raman spectra of MWCNT, GONR and GNR.

MWCNT also experiences significant defects and disorders on their sp^2 structures during oxidation and reduction processes. Raman spectroscopy has been effectively used to quantify these defects and disorders when carbonaceous materials oxidize and reduce [159,161]. Figure 3.3-b describes the Raman spectra of MWCNT, GONR and GNR, respectively. The D-band on the Raman spectra is the measure of the lateral density of scattering defects in graphene [167]. The intensity ratio of I_D/I_G which is expressed by the sp^3/sp^2 carbon ratio, is commonly used to estimate the quality of carbon materials. When MWCNT is oxidized and transformed to GONR, I_D/I_G increased from 0.70 to 1.04. This indicates the creation of edge structures of GNR by the unzipping process. The edge structures act as defects and escalate the D peak intensity. When GONR is thermally reduced to produce GNR, I_D/I_G is further

heightened to 1.17. This has been previously studied and understood that the increase of I_D/I_G is explained as a decrease in the average size but an increase in the number of sp^2 domains upon reduction. Thermal reduction enhances the number of sp^2 domains, but their overall sp^2 domain size on the plane strongly decreases [168]. The calculated parameters including the inter-defect distance (L_a) is illustrated in Table 3.1. The inter-defect distance (L_a) is calculated by combining the relative intensity ratio (I_D/I_G) into the Tuinstra & Koenig equation:

$$L_a = \left(2.4 \times 10^{-10}\right)\lambda^4 \left(\frac{I_D}{I_G}\right)^{-1} \quad \textbf{3.10}$$

where λ is the excitation laser wavelength (532 nm) [169].

Table 3.1 The parameters extracted from XRD and Raman spectra

Materials	XRD					Raman		XPS (Area %)	
	2θ°	Interlayer Distance (Å)	FWHM (radian)	τ (Å)	Number of layers	I_D/I_G	L_a (nm)	C=C C-C	C-O C=O O-C=O
MWCNT	26.06	3.43	0.0348	40.88	11.97	0.70	27.61	-	-
GONR	9.90	8.92	0.0974	14.28	1.60	1.04	18.40	29.9	70.1
GNR	26.08	3.41	0.2558	5.56	1.63	1.17	16.47	77.3	22.7

The surface element composition of GONR and GNR samples was analyzed by XPS. The high resolution C 1s spectra of GONR and GNR are described in Figure 3.4. The obtained XPS spectra were deconvoluted to reveal sp^2 and sp^3 hybridized carbon atoms (C=C and C-C at 284.6-285.5 eV) and the oxygen containing functional groups (C-O at 286.1 eV, C=O at 287.7-287.9 eV, and O-C=O at 288.7-288.9 eV). The removal of functional groups by the thermal reduction can be confirmed by calculating the area ratio of C=C and C-C as summarized in Table 3.1. The area ratio of C=C and C-C for GONR was 29.9% while after reduction it increased to 77.3%. This indicates that the oxygen-containing functional groups were successfully removed by the thermal treatment.

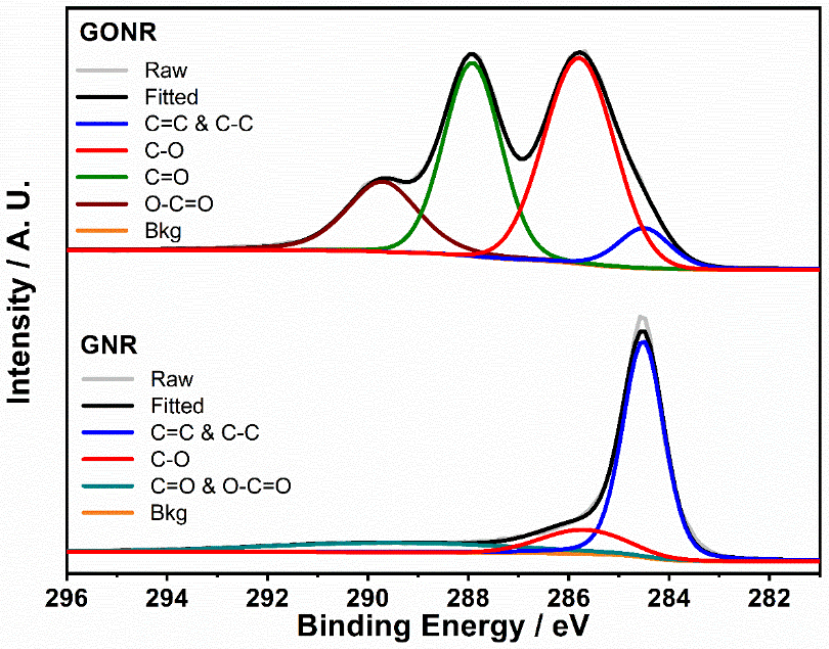

Figure 3.4 C 1s high resolution x-ray photoelectron spectroscopy of GONR and GNR

3.3.2 Microstructure and morphology of the nanocomposites

The microstructures of the cross sectional area of the MWCNT/TPU and GNR/TPU nanocomposites with 8.2 vol% of MWCNT and GNR are illustrated in Figure 3.5. The dispersed MWCNT and GNR are signified by the white arrows in the images. In Figure 3.5-a, the end of MWCNT that pulled out of TPU phase as well as the bent MWCNTs are indicated by the arrows. As indicated by the arrows in Figure 3.5-b the GNR that exist in planar shapes. Both the SEM images confirms the high degree of filler dispersion inside the polymer matrix. It is notable that in the MWCNT/TPU images the MWCNT is often pulled out of TPU matrix while GNR is completely embedded in the nanocomposite. This may indicate that stronger interfacial bonding was established between GNR and TPU that surpasses the bonding between MWCNT and TPU. It has been reported that no observation of GNR pullout implicates the superior bonding between filler and matrix [170].

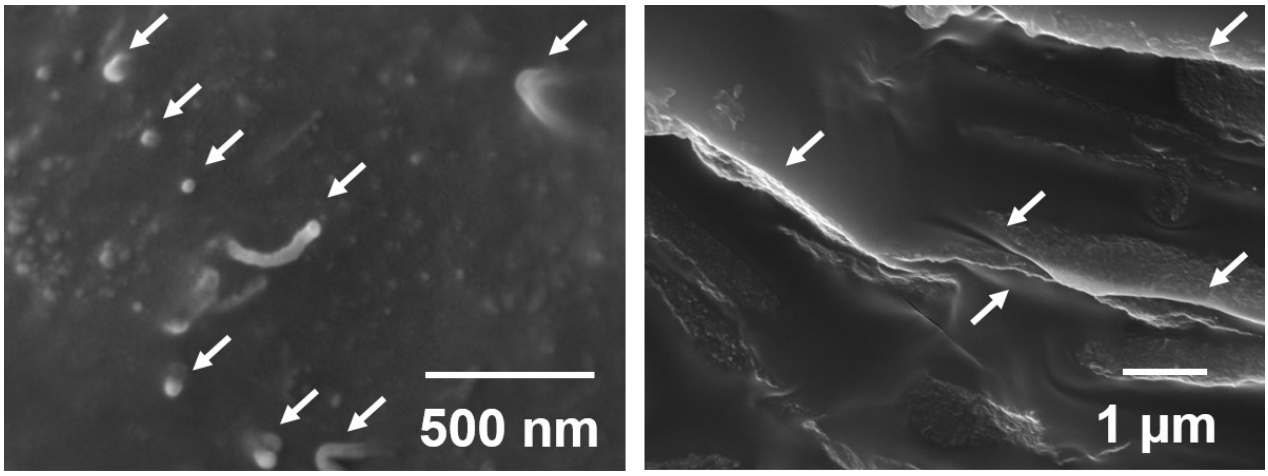

Figure 3.5 Cross sectional SEM images of 8.2 vol% (a) MWCNT/TPU and (b) GNR/TPU nanocomposites. Fillers are indicated by the arrows.

To further investigate the high degree of filler dispersion, XRD analysis on GNR/TPU and MWCNT/TPU nanocomposites were conducted and compared to the neat TPU as illustrated in Figure 3.12 of supporting information section. The MWCNT/TPU nanocomposite showed a broad peak around 20° and a small peak at 26.02°. The former peak is attributed to the presence of short-range ordered structure in both hard and soft domains and disordered structure of amorphous phase of TPU. It is clearly observed that the intensity of the MWCNT's characteristic peak at 26.02° was reduced and broadened. Moreover, the characteristic peak of GNR in the GNR/TPU nanocomposite disappeared. This reduction in intensity and disappearance of MWCNT and GNR peaks in the nanocomposites indicate that the fillers were sufficiently intercalated and dispersed in the polymer matrix [171].

3.3.3 Electrical conductivity and dielectric properties

Alternative current (AC) electrical conductivity of MWCNT/TPU nanocomposite is described in Figure 3.6-a and GNR/TPU nanocomposites in Figure 3.6-b. 1.0, 3.1 and 5.3 vol% of MWCNT/TPU showed a frequency-dependent trend over the entire frequency range. This frequency-dependent behavior of AC conductivity is typically observed in insulating polymer nanocomposites. The frequency-independent behavior appeared at frequency ranges below 1 x 10^3 Hz when the MWCNT content reached 8.2 vol%, indicating that a percolation network of MWCNT has been established. On the contrary, AC conductivity dramatically increased when GNR is used as conductive fillers. 1.0 vol% of GNR/TPU exhibited electrically insulating, but GNR/TPU nanocomposites turned into conductive with

the addition of 3.1 vol% of GNR. Both 3.1 and 5.3 vol% GNR/TPU nanocomposites exhibited a frequency-independent trend at frequency up to approximately 1 x 10^4 Hz. 8.2 vol% GNR/TPU nanocomposites showed completely frequency-independent behavior over the entire frequency range.

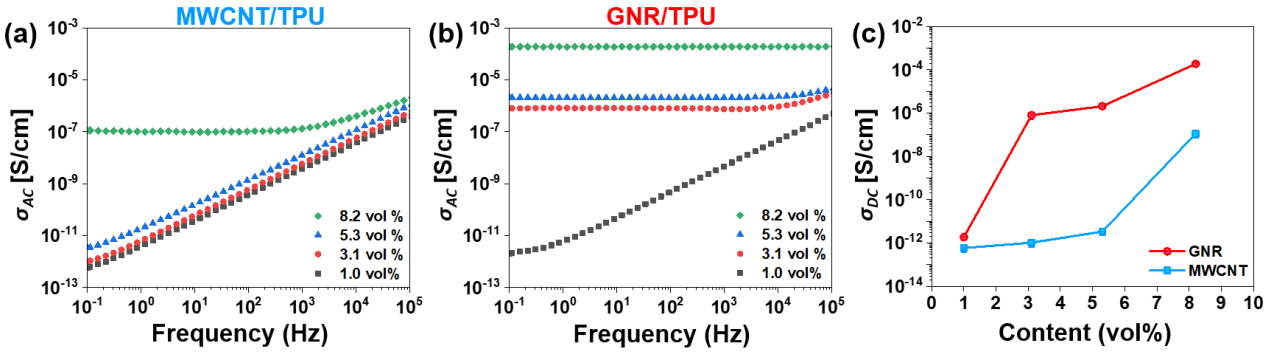

Figure 3.6 Through plane AC conductivity of (a) MWCNT/TPU, (b) GNR/TPU nanocomposites, and (c) DC conductivity of MWCNT/TPU and GNR/TPU nanocomposites.

Figure 3.6-c clearly demonstrates the dramatic enhancement of electrical conductivity of GNR/TPU nanocomposites as compared to MWCNT/TPU nanocomposites. AC conductivity at 0.1 Hz was used as DC conductivity. At 1.0 vol% content, electrical conductivities of both MWCNT/TPU and GNR/TPU nanocomposites are very low. As the filler content increases, both MWCNT/TPU and GNR/TPU nanocomposites showed a clear insulation-conduction transition in electrical conductivity. This abrupt increase in conductivity of GNR/TPU nanocomposites takes place at a considerably lower content than that of MWCNT/TPU nanocomposites. The percolation threshold for GNR/TPU nanocomposites appeared at loadings lower than 3.1 vol%, which far outperforms the MWCNT/TPU nanocomposites where the percolation threshold appeared at loadings lower than 8.2 vol%. At 8.2 vol%, the electrical conductivity of MWCNT/TPU nanocomposite was 1.1 × 10^{-7} S/cm while GNR/TPU nanocomposite presented a conductivity of 1.9 × 10^{-4} S/cm. It is worth mentioning that the percolation for MWCNT in our system appeared at relatively high loadings than the literatures [115], which is likely due to the lower intrinsic conductivity of the parent MWNCT, Figure 3.15.

In general, the dielectric permittivity is depicted in a complex function as follows:

$$\boldsymbol{\varepsilon(\omega) = \varepsilon'(\omega) - i\varepsilon''(\omega)} \qquad \textbf{3.11}$$

where ω is the angular frequency, $\varepsilon'(\omega)$ is the real part, and $\varepsilon''(\omega)$ is the imaginary part of the dielectric permittivity. The real part of the equation (3.11) pertains to the charge displacement in the material.

Although this is influenced by several different types of polarization, it is usually the interfacial polarization that occurs in the case of polymer nanocomposites in a frequency less than 1 MHz. According to the Maxwell-Wagner-Sillars effect, charges are collected at the interfaces between the conductive fillers and polymer matrix due to their considerable difference in relaxation time when a current flow across the interfaces of two different materials. On the other hand, the imaginary part is used to calculate the dielectric loss or energy dissipation (tan δ), defined by a ratio of ε'' to ε'. The dielectric loss in polymer nanocomposites is usually due to polarization loss, Ohmic loss and the molecular dipole movement.

Figure 3.7-a and b illustrate the real permittivity of MWCNT/TPU and GNR/TPU nanocomposites over a frequency of 10 to 10^5 Hz, respectively. An increased filler content enhanced the real permittivity of both MWCNT/TPU and GNR/TPU nanocomposites. When the filler content increased, both the interfacial area between the filler and polymer matrix and the density of the interfacial polarization were amplified, which enhanced the real permittivity. When comparing the real permittivity at 10^3 Hz between MWCNT/TPU and GNR/TPU nanocomposites (Figure 3.7-c), it is clearly notable that the use of GNR dramatically increased the real permittivity than that of MWCNT. At 8.2 vol%, the real permittivity increased from 108 to 298 when GNR was used instead of parent MWCNT. This is attributed to the increased number density and enlarged surface area induced by the exfoliation of MWCNT. During the chemical unzipping and thermal reduction process, the number of layers of MWCNT is significantly reduced as seen from XRD. As the MWCNT is exfoliated, not only does the number density of fillers increase, but also the surface area of fillers. The increased number density and the creation of two-dimensional GNR from one dimensional tube could decrease the interspatial distance between nearby fillers, further boosting the real dielectric permittivity. This synergistic effect of exfoliation could significantly increase the real permittivity of GNR/TPU nanocomposites.

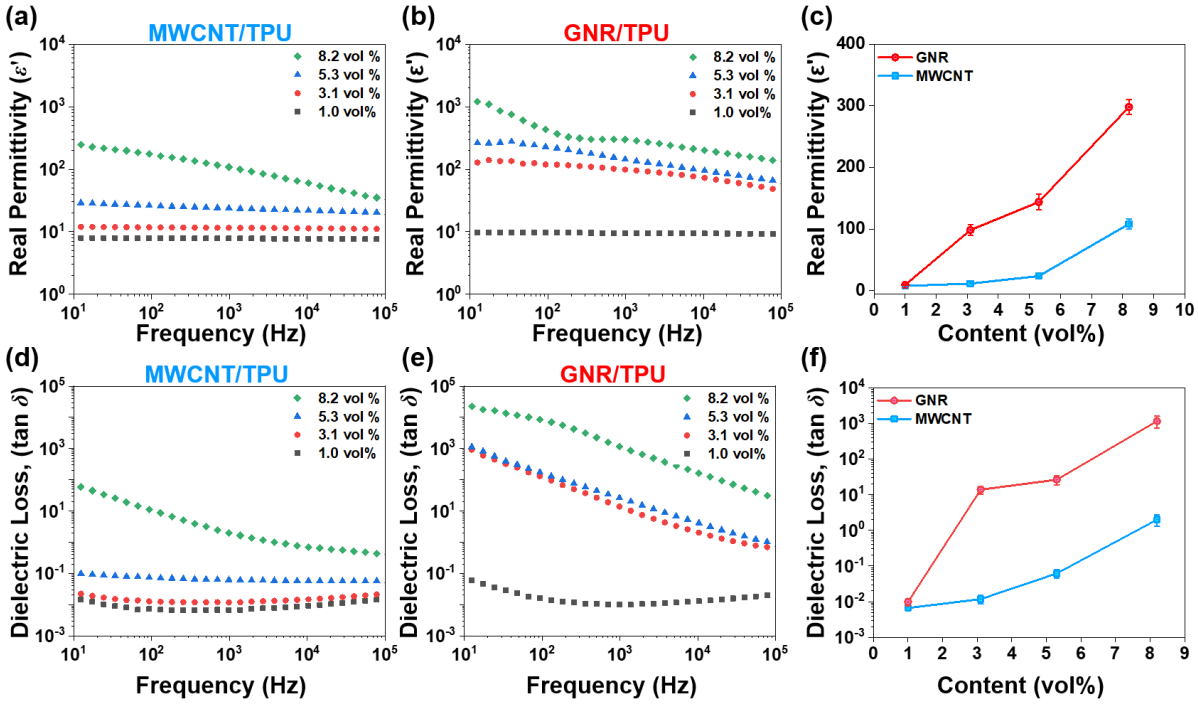

Figure 3.7 Real permittivity (ε') of (a) MWCNT/TPU and (b) GNR/TPU nanocomposites. (c) Real permittivity (ε') of MWCNT/TPU and GNR/TPU as a function of filler content. Dielectric loss (tan δ) of (d) MWCNT/TPU and (e) GNR/TPU nanocomposites. (f) Dielectric loss (tan δ) of MWCNT/TPU and GNR/TPU nanocomposites as a function of filler content.

Figure 3.7-d and e describe the dielectric loss of MWCNT/TPU and GNR/TPU nanocomposites, respectively. The variation of tan δ as a function of filler content is summarized in Figure 3.7-f for both MWCNT/TPU and GNR/TPU nanocomposites. Tan δ at 10^3 Hz for both MWCNT and GNR with a content of 1.0 vol% were very small (<0.01). With the addition of 3.1 vol% of GNR, the dielectric loss significantly increased as compared to the same amount of MWCNT. With the percolation threshold of GNR estimated to be around 3.1 vol%, this dramatic increase of tan δ is largely attributed to the Ohmic loss. At 3.1 vol%, GNR formed a percolation network, dramatically increasing electrical conductivity, which in turn leaded to considerable current leakage.

3.3.4 EMI Shielding Effectiveness

Figure 3.8-a illustrates the average SE_T values for each MWCNT/TPU and GNR/TPU nanocomposite as a function of filler contents. Figure 3.8-b and c demonstrate the entire EMI SE across P-band

frequency range for MWCNT/TPU and GNR/TPU, respectively. Notably, the EMI SE of GNR/TPU nanocomposite increased much more considerably than that of MWCNT/TPU nanocomposite. For instance, EMI SE for 8.3 vol% of MWCNT/TPU was 9.3 dB while the corresponding GNR/TPU nanocomposite exhibited EMI SE of 24.9 dB. This dramatic enhancement of EMI SE is largely attributed to the strengthened filler-filler interaction. Upon unzipping, the tubular MWCNT transformed into two dimensional ribbons, which significantly changes the filler-filler contact dimensionality. When MWCNTs come together to make a connection, it is mostly either point-to-point or line-to-line contact due to their one dimensional tubular structure. On the other hand, when MWCNT is transformed into flexible and long strips of GNR, it is highly likely that GNR forms sheet-to-sheet contact interface. This geometrical conversion from zero or one-dimensional to two-dimensional interconnection dramatically boosts the contact area, enhancing the electrical performance of the nanocomposites. It is also highly probable that the improved flexibility of individual GNRs significantly increases the chance of constructing a percolating network. In addition, it was revealed by Brunauer-Emmett-Teller (BET) analysis that GNRs possessed significantly greater surface area of 382.6 m^2/g while MWCNT's surface area was 158.2 m^2/g (Figure 3.13 of supporting information section). By unzipping, the surface area increased by 141%. This increased surface area of GNR is likely to offer better chances of building filler connection with enlarged filler-filler contact areas.

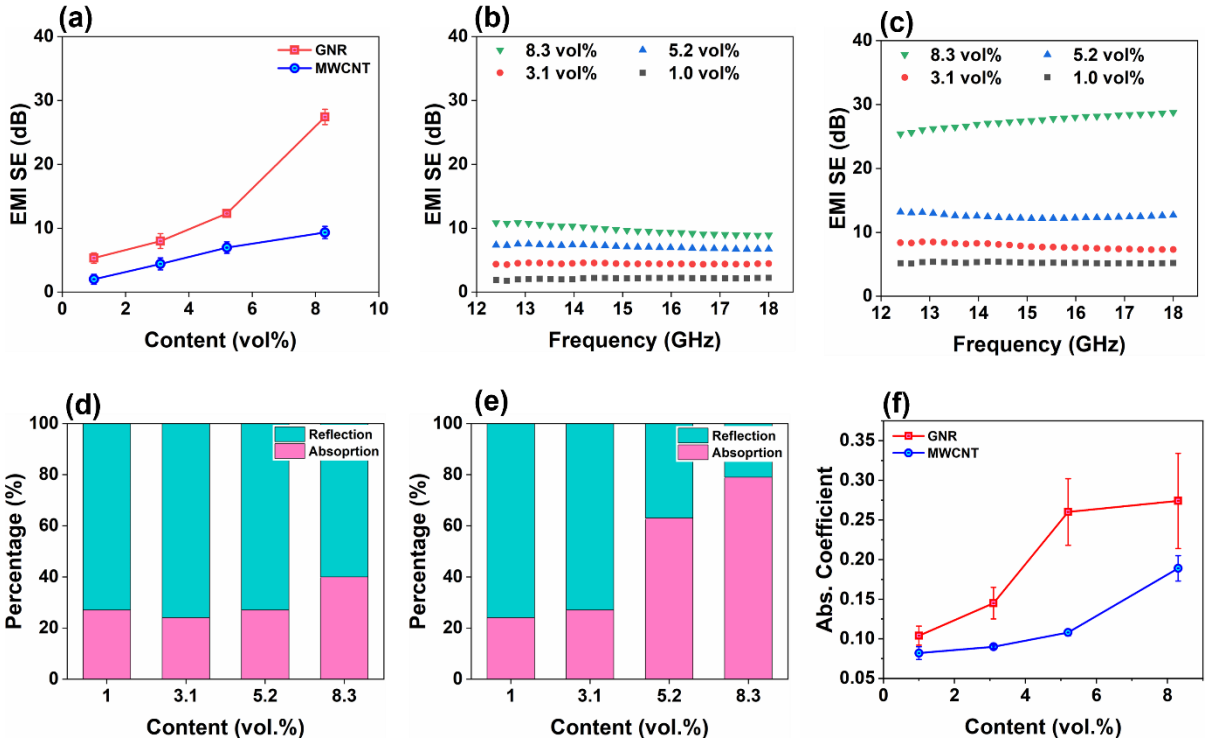

Figure 3.8 (a) Average SE_T of MWCNT/TPU and GNR/TPU as a function of filler content, EMI SE of (b) MWCNT/TPU and (c) GNR/TPU in P-band frequency range, SE_A and SE_R of (d) MWCNT/TPU and (e) GNR/TPU, and (f) absorption coefficient for nanocomposites versus filler content

Figure 3.8-d and e describe the contribution of reflection and absorption to the total EMI SE for MWCNT/TPU and GNR/TPU nanocomposites, respectively. Both nanocomposites show that the contribution of absorption to the total EMI SE of the nanocomposites enlarged by increasing the filler content [123]. It is also evident from the Figure 3.8-f that the absorption coefficient of the of the nanocomposites increased by increasing the filler content. The absorption coefficient of GNR/TPU nanocomposites outperform the MWCNT/TPU nanocomposite. While the absorption coefficient gradually increased for MWCNT/TPU nanocomposites, the GNR/TPU exhibited a dramatic increase in absorption with the increase of GNR content. This augmented absorption with less reflection is favorable for creating eco-friendly environments with reduced secondary radiations [172].

While the reflection is largely due to the surface charge or mobile charge carriers that cause impedance mismatch between the air and the shielding material [123], the absorption originates from the

conduction loss (i.e., the ohmic loss) and the polarization relaxation and multiple scattering [173]. The conduction loss is associated with attenuation of energy through the current flow carried out by the migration, hopping, and tunneling mechanisms. The polarization relaxation takes place when the dipoles are unable to reorient in the alternating EM field. Energy is consumed when overcoming the momentum that suppress the reorientation of dipoles. The polarization is greatly associated with the materials' characteristics, such as functional groups, defects, and interfaces [174].

In GNR/TPU nanocomposite, as described previously the unzipping process induced the geometrical conversion for the contact interfaces, which significantly strengthen the percolation network of fillers (Figure 3.9). This will considerably amplify the conduction loss in the GNR/TPU nanocomposites. This amplified conduction loss is also indicated by the greater dielectric loss of GNR/TPU nanocomposites in Figure 3.7-f. Moreover, the exfoliation of MWCNT by unzipping drastically enhanced the interfacial areas between the fillers and matrices. It is very likely that the enlarged interfacial areas will effectively accumulate dipoles, and the high number of dipoles resulted in augmented interfacial polarization relaxation. Further, GNR's two dimensional structure with high aspect ratio form three dimensional interconnected conductive network that promotes the absorption mechanism by multiple scattering [175]. The enlarged interfacial area of GNR can also increase the chances of multi-scattering of EM waves in the nanocomposites. In addition, the unzipping process inevitably leaves defects on GNR due to the oxidation. This defects on the GNR surface can also induce polarization relaxation [176]. Therefore, augmented conduction loss and interfacial geometry and areas, together with the defects on GNR, resulted in the strengthened contribution of the absorption to the total shielding mechanism for GNR/TPU nanocomposites.

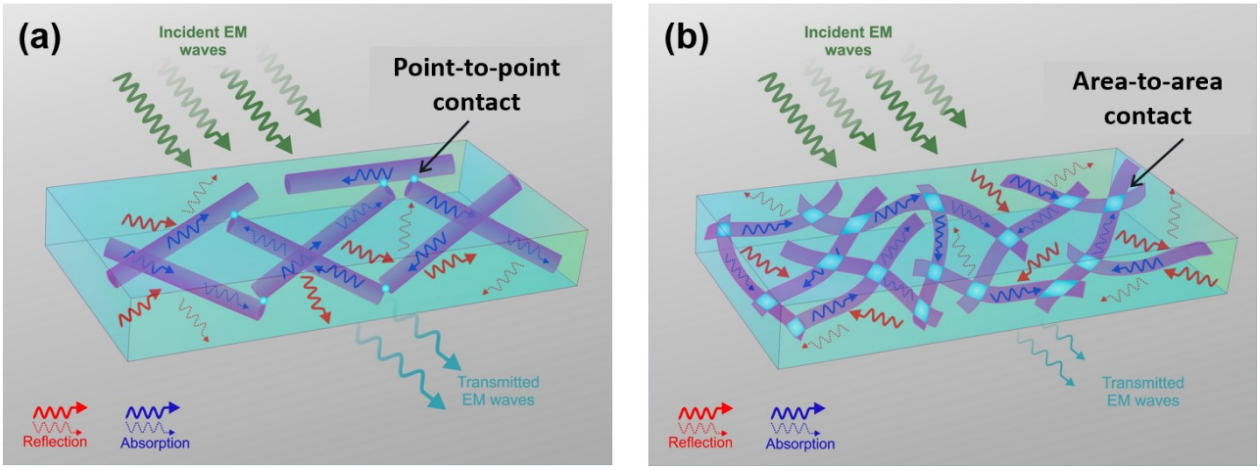

Figure 3.9 Schematic illustration of EMI SE mechanisms for (a) MWCNT/TPU and (b) GNR/TPU nanocomposites.

Table 3.2 compares the EMI SE with other polymer nanocomposites in literature. Overall, the EMI SE of the GNR/TPU nanocomposite prepared in this study was comparable to that of the other nanocomposites reported in literature, yet in thinner thickness. Usually, the EMI SE is proportional to the thickness of the sample. Therefore, the similar level of EMI SE with a lower thickness shows that GNR is a very effective filler for improving electrical properties of polymer nanocomposites.

Table 3.2 Comparison of EMI SE with other polymer nanocomposites in literature.

Polymer Nanocomposite	Filler Content	EMI SE (dB)	Thickness (mm)	Fabrication Method	Ref.
GnP/HDPE	19 vol%	21.8	3	Melt blending	[124]
Graphene/PMMA	4.23 vol%	30	3.4	Solvent blending	[177]
GnP/WPU	5 vol%	32	2	Solvent blending	[178]
SWCNT/PMMA	20 wt.%	30	4.5	Solvent blending	[179]
CNT/Graphene /PVDF	15 wt.% (5 wt.% CNT+10 wt.% Graphene)	27.58	0.1	Solvent blending	[123]
Graphene/epoxy	8.8 vol%	21	-	Solvent blending	[180]
MWCNT/PP	5 wt.%	25	1.85	Melt blending	[181]
Graphene/TPU	20 wt.%	21	2.4	Solvent blending	[182]
PAM/CNF/MWCNT Foam	1 wt.%	28.5	2	In-situ polymerization	[183]
rGO-MWCNT/TPU	10 wt.%	32	3	Solvent blending	[184]
GnP-MWCNT/PU	10 wt.%	47	3	Solvent blending	[185]
SWCNT/PU	20 wt.%	17	2	Solvent blending	[186]
GNR/PVA	2.5 wt.%	45	0.6	Solvent blending	[187]
GNR/PANI/Epoxy	5 wt.%	44	3.4	In-situ polymerization/ solvent blending	[188]
GNR/PVDF	2 wt.%	6	1.1	Melt blending	[189]
MWCNT/PLLA Foam	10 wt.%	23	2.5	Physical mixing and compression molding	[190]
GNR/TPU	**8.2 vol%**	**24.9**	**1.3**	**Solvent blending**	**This study**

3.3.5 Mechanical properties

Figure 3.10 illustrate the stress-strain curves for (a) MWCNT/TPU and (b) GNR/TPU nanocomposites.

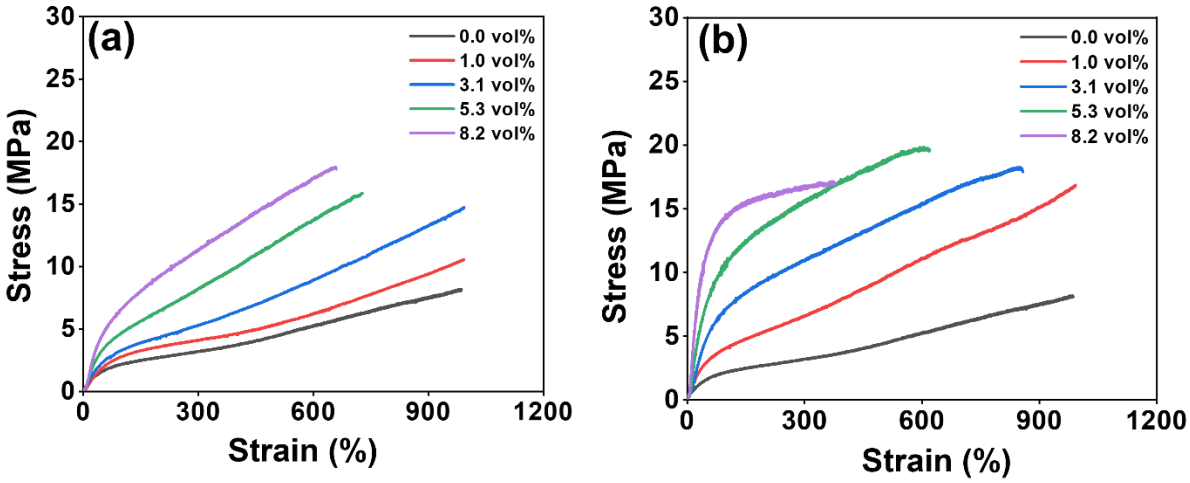

Figure 3.10 Stress-Strain curve of (a) MWCNT/TPU and (b) GNR/TPU nanocomposites with various amounts of fillers.

While the increase in filler contents increased Young's modulus for both nanocomposites, the GNR/TPU nanocomposites experienced much more significant augmentation as illustrated in Figure 3.10. This is because of the stronger polymer-filler interaction that can be attributed to three main reasons: (i) the higher surface area of the GNR induced by unzipping and exfoliation of the nanotubes [170]; (ii) the formation of a higher number of edge structures in GNR during unzipping, which can increase the polymer-filler interaction sites; (iii) the superior ability of the polymer chains to lie down on the planar surface of GNR instead of wrapping around the smooth surface of MWCNTs. When a MWCNT is unzipped and subsequently exfoliated, all of the transformed GNR strips become available to interact with the polymer chains and play a load-bearing role. In contrast, the multi-layered CNTs are enclosed in the MWCNT before unzipping, and these enclosed CNTs are not able to directly bond with the polymer matrix and cause inter-tube slippage, resulting in less reinforcing effect in the nanocomposites [191].

Along with Young's modulus, the tensile strength of the nanocomposites also increased for both GNR and MWCNT nanocomposites, but much more for GNR/TPU nanocomposites, as shown in Table 3.3. It is noted that the tensile strength of the GNR/TPU nanocomposites decreased at 8.2 vol% loading.

This could be due to the fact that the number of polymer chains that exist between filler particles is not large enough to efficiently interact with the filler (Figure 3.14). When the filler content is low, the inter-filler distance is sufficiently far and the polymer chain concentration between filler particles is large enough to create strong polymer-filler interactions, showing efficient load transferring behavior. When the filler content is very high, the inter-filler distance decreases, reducing the number of polymer chains between nanoparticles. The filler particles are now near enough together to create stronger filler-filler interactions that exceed the polymer-filler interactions. This will weaken the load transfer between matrix and filler, decreasing the strength of the nanocomposite [192].

Table 3.3 Young's modulus and tensile strength of GNR/TPU and MWCNT/TPU nanocomposites

Filler Contents (Vol.%)	Young's Modulus (MPa)		Tensile Strength (MPa)	
	GNR/TPU	**MWCNT/TPU**	**GNR/TPU**	**MWCNT/TPU**
0	3.6 ± 0.3		11.0 ± 1.4	
1.0	9.6 ± 0.2	5.3 ± 0.3	16.8 ± 1.9	10.4 ± 0.7
3.1	13.6 ± 0.2	6.4 ± 0.1	18.0 ± 2.0	14.6 ± 1.9
5.3	28.5 ± 1.2	8.6 ± 0.1	19.6 ± 2.2	15.8 ± 1.5
8.2	37.2 ± 1.6	12.7 ± 0.3	17.0 ± 0.5	17.8 ± 1.0

By applying a semi-empirical mechanical property prediction model (Equations 3.12 - 3.16), the effect of MWCNT unzipping on the reinforcement of the nanocomposites can be further scrutinized. This relation originally developed by Pagano for randomly oriented/distributed discontinuous fiber-reinforced polymer nanocomposites.

$$\mathbf{E_c = E_m}\left[\frac{3}{8}\times\frac{1+\eta_L\xi\varphi}{1-\eta_L\varphi}+\frac{5}{8}\times\frac{1+2\eta_T\varphi}{1-\eta_T\varphi}\right] \quad \textbf{3.12}$$

$$\boldsymbol{\eta_L} = \frac{\left(\frac{E_f}{E_m}\right)-1}{\left(\frac{E_f}{E_m}\right)+\xi} \quad \textbf{3.13}$$

$$\boldsymbol{\eta_T} = \frac{\left(\frac{E_f}{E_m}\right)-1}{\left(\frac{E_f}{E_m}\right)+2} \quad \textbf{3.14}$$

$$\xi_{GNR} = \frac{w + l}{t} \quad \textbf{3.15}$$

$$\xi_{MWCNT} = \frac{2l}{d} \quad \textbf{3.16}$$

$$E_f = E_{MWCNT} = E_{GNR} = 1\ TPa \quad \textbf{3.17}$$

where E_c, E_f, and E_m represent the Young's modulus of the nanocomposite, fillers, and polymer matrix, respectively. f, w, l, t and d represent the volume fraction, width, length, thickness of the fillers, respectively. The Halpin-Tsai model assumes that both filler and polymer matrix have perfect interfacial bonding, are equally strained and the filler particles are randomly distributed in the matrix [193]. The same degree of filler dispersion can be assumed for both GNR/TPU and MWCNT/TPU nanocomposites when both nanocomposites were prepared by the identical process and with the same conditions. While the aspect ratio of these two fillers are very similar, the greatest differences are the geometrically changed morphology of GNR and the significantly increased number density due to exfoliation. We assumed GNR has a rectangular shape. Based on the theoretical calculations and information obtained by TEM images, the average width of the GNR was estimated to be 80 nm. The XRD results showed that the final average number of layers for GNR was 1.63. Therefore, based on the average thickness of the GNR reported in literature [194] (around 3.5-5 nm), we assumed the thickness of the GNR to be 8 nm. The average diameter of the MWCNT was 25 nm. The average length of the MWCNT and GNR were assumed to be 3 μm.

The experimentally determined Young's moduli were compared with the modulus predicted by the Halpin-Tsai model in Figure 3.11. It is clearly demonstrated that the experimentally measured modulus of GNR/TPU nanocomposite deviated much less from the predicted value as compared to the MWCNT/TPU nanocomposite. This can be largely attributed to the enhanced interfacial bonding between TPU and GNR. As the multi-tubular MWCNT is unzipped and transformed into flexible few-layered two dimensional sheets, the adhesion between polymer matrix and filler greatly increased. Also, the exfoliation made all the inner tubes available for reinforcing, which dramatically increases the total surface area of filler in the nanocomposite. The geometrical conversion and significantly increased surface area of GNR by exfoliation resulted in exceptionally strong adhesion between polymer matrix and filler. Furthermore, the investigation of the fracture surface of the nanocomposites also confirmed the strong interfacial adhesion of GNR, while weaker adhesion between MWCNT and polymer resulted in MWCNT pullout [195], as shown in the SEM images of Figure 3.5.

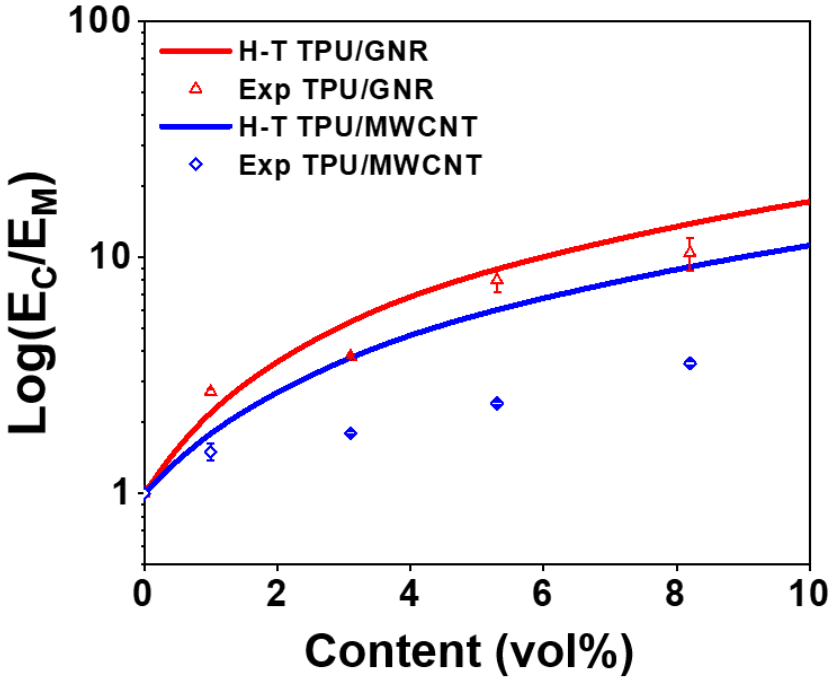

Figure 3.11 Comparison between the values experimental measured and the values theoretical predicted using Halpin-Tsai model.

3.4 Conclusions

Long and thin strips of two-dimensional GNR were produced by chemically treating one-dimensional tubular MWCNTs. Such dimensional transformation was confirmed by TEM, XRD and Raman spectra. GNR exhibited a much reduced percolation threshold of 3.1 vol% while 8.2 vol% was required for MWCNTs to construct a conductive network. GNR also presented a superior electrical conductivity, real permittivity and dielectric loss (tan δ) values. Consequently, the EMI SE of GNR/TPU (24.9 dB) was significantly greater than that of MWCNT/TPU nanocomposite (9.3 dB) with enhanced contribution from absorption. The improved electrical properties are mainly due to the geometrical conversion of contact interfaces and enhanced filler-filler area, producing a robust percolating network. The greater surface area induced by unzipping and exfoliation of MWCNT along with edge structures also significantly boosted filler-matrix bonding, leading to superior reinforcing effect of GNR. Therefore, although the conflicting results for GNR have been reported, the change in contact interface and the increase in filler number density due to unzipping are the foremost features that surpass other miscellaneous issues, leading to excellent performances of GNR nanocomposite.

3.5 Supporting information

The volumetric fraction of the fillers (φ) in the nanocomposites can be converted from weight fraction by the following equation as follows:

$$\varphi = \frac{\varphi_w}{\varphi_w + (1-\varphi_w)\rho_f/\rho_m} \quad \textbf{3.18}$$

where φ_w is the weight fraction, ρ_f and ρ_m are the densities of the fillers and polymer matrix, respectively.

The bulk density of the nanomaterials was shown in Table 3.4.

Table 3.4 Physical properties of the utilized nanomaterials and polymer matrices

Nanomaterial	Bulk Density (g/cm^3)	Density (g/cm^3)
MWCNT	2.2	-
GNR	2.2	-
TPU	-	1.06

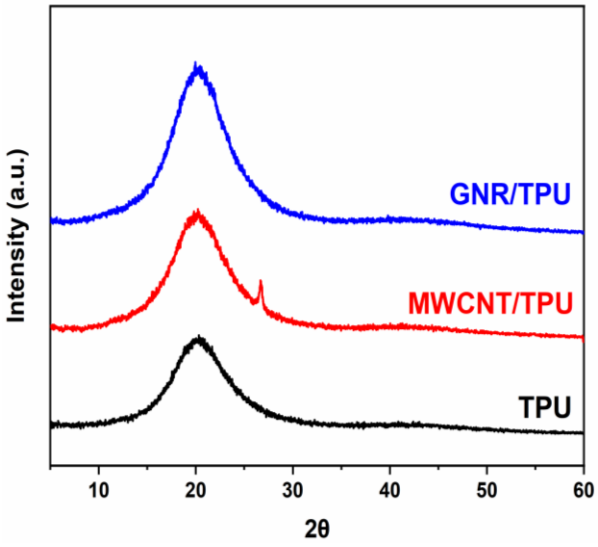

Figure 3.12 XRD graphs of (a) neat TPU, (b) MWCNT/TPU and (c) GNR/TPU nanocomposites. The peak at 26.5° in MWCNT/TPU spectrum is likely due to the graphitic structure of MWCNT that is not well-dispersed in TPU matrix.

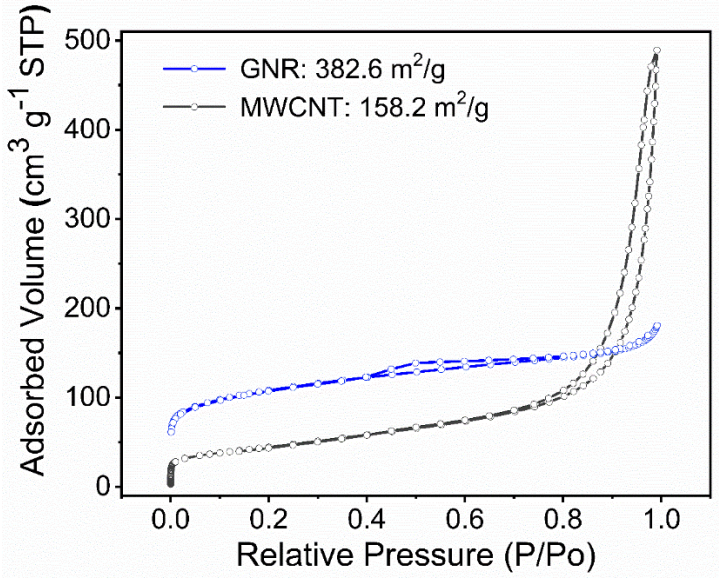

Figure 3.13 The nitrogen adsorption and desorption isotherms of MWCNT, GNR and the calculated specific surface area

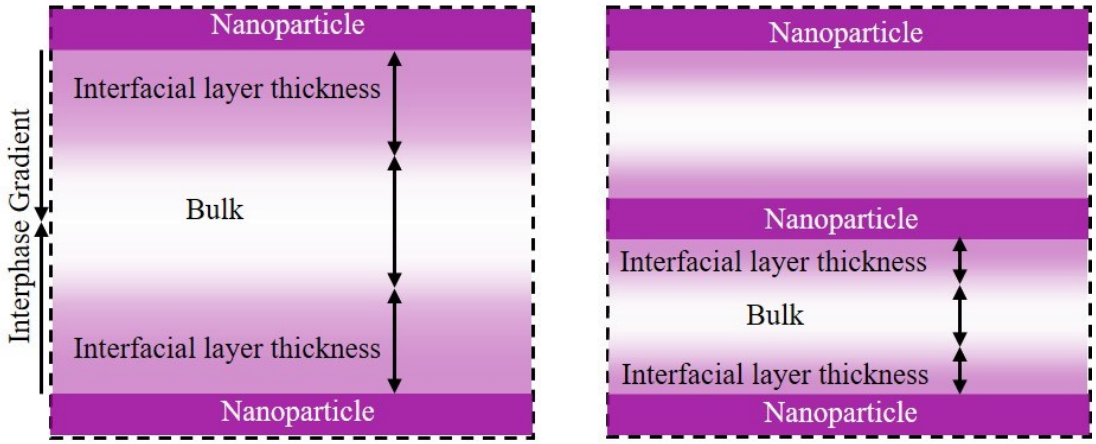

Figure 3.14 Illustration of change in interfacial layer thickness by increase in filler content or fillers' number density in a polymer matrix.

When the filler content is low, the inter-filler distance is sufficiently far and the polymer chain concentration between fillers is large enough to create strong polymer-filler interactions, showing

efficient load transferring behavior (a). When the filler contents are exceedingly high, the inter-filler distance decreases, reducing the amount of polymer chains between nanoparticles (b). The fillers are now adjacent enough to create stronger filler-filler interactions that exceeds the polymer-filler interactions. This will weaken the load transfer between matrix and particles, decreasing the strength of nanocomposite.

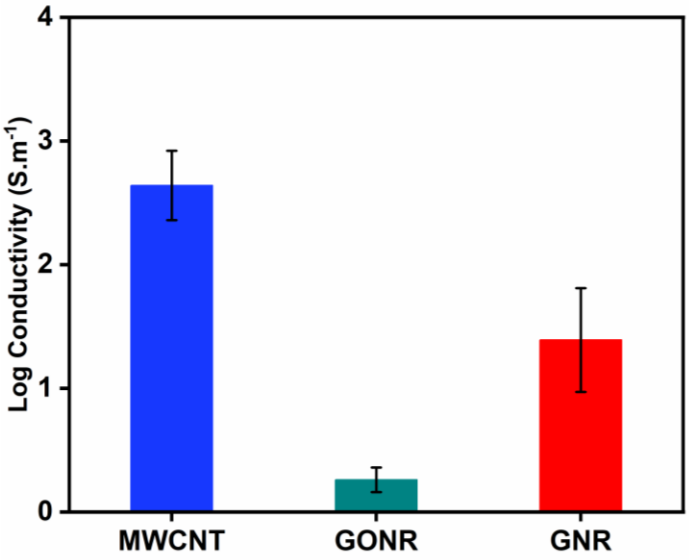

Figure 3.15 Intrinsic electrical conductivity of compressed MWCNT and GNR powders measured with 4-point probe method.

The electrical conductivity of MWCNT, GONR, and GNR are 436.5, 1.8, and 24.5 S/m, respectively. GONR showed the lowest conductivity due to sp3 hybridization. After reduction, the electrical conductivity of GNR dramatically increased and the electrical conductivity of the GNR powders is in a good agreement with previously reported data [196], However, the electrical conductivity of MWCNT is greater than that of GNR. This is because the restoration of sp^2 hybridization is not perfect, and there are always defects that remained on GONR. Furthermore, the residual functional groups may disrupt the π-π electron network [52].

Chapter 4

Greatly Enhanced Electromagnetic Interference Shielding Effectiveness and Mechanical Properties of Polyaniline-Grafted $Ti_3C_2T_x$ MXene–PVDF Composites

This chapter is reprinted in adapted form from the article below with permission from ACS.

Saeed Habibpour, Kiyoumars Zarshenas, Maiwen Zhang, Mahdi Hamidinejad, Li Ma, Chul B. Park, Aiping Yu, "Greatly Enhanced Electromagnetic Interference Shielding Effectiveness and Mechanical Properties of Polyaniline-Grafted $Ti_3C_2T_x$ MXene–PVDF Composites", ACS Appl. Mat. & Int. (2022), 14, 21521−21534

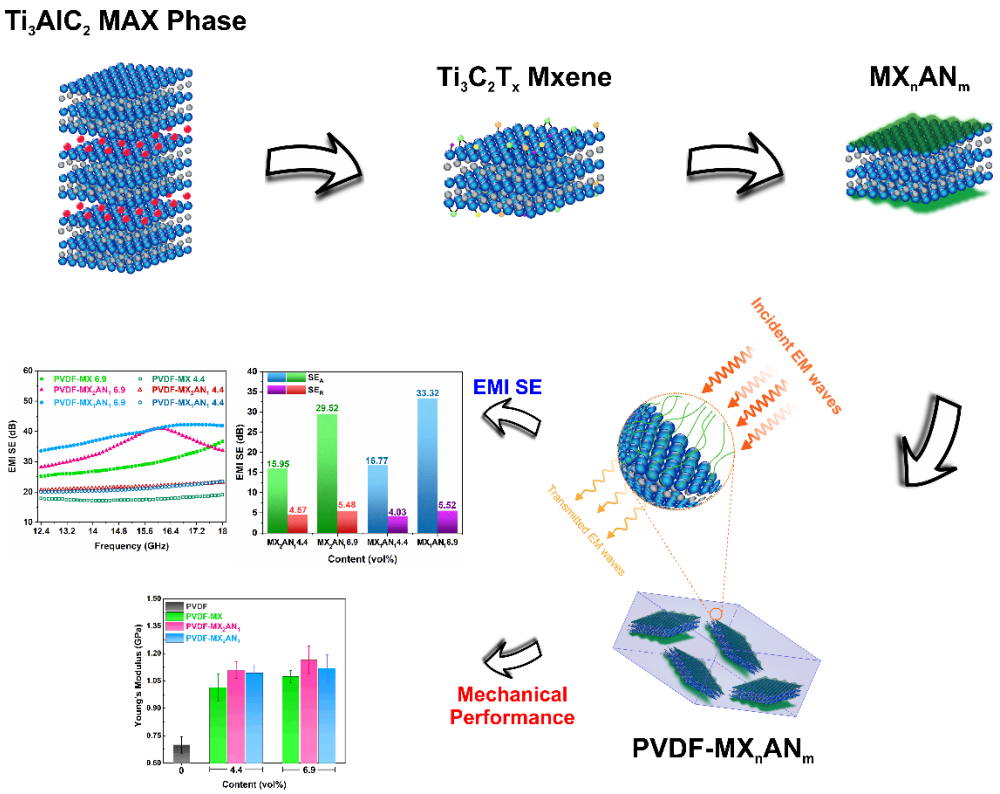

4.1 Introduction

The fast growing pace of advances in mobile electronic and telecommunication systems and their large-scale utilization in various industries have provided easier life for humans [197,198]. However, these advantages also have negative consequences, such as electromagnetic interference (EMI) pollution [199–201]. Electrical and magnetic fields generated in a wide range of frequencies by the electronic and communication devices may cause device malfunction, failure of other nearby devices, information leakage and even threaten human health [7,202]. This concern is made even more worthy of study by the emergence and commercialization of 5G technology, which is about two orders of magnitude faster in data transfer than the latest 4G cellular networks [199,203]. Furthermore, there is no doubt that the more complex 5G technology will massively increase the production and utilization of wireless electronic systems and result in much more EMI pollution. Therefore, the development of highly efficient advanced materials with specific properties such as low thickness, light weight and easy processibility is of paramount importance for EMI shielding in a wide range of applications, including medical [204], nonmilitary [205], and military [205].

The primary function of EMI shielding material is the reflection of the incident electromagnetic waves (EMW) or dissipation of their energy by absorption mechanisms, and thus minimizing the degree of wave transmittance. High electrical conductivity and high electron cloud density are prerequisites for the effective screening of EM radiation [206]. Reflection, which originates from the impedance mismatch between air and the absorber, is less favorable as the dominant mechanism due to the secondary interference from reflected waves [207]. In contrast, the environmentally favorable absorption shielding occurs when dissipation of incident EMWs through conduction and polarization losses is dominant. The former originates from the electrical conductivity, and the latter arises from dipole polarization in the heterogeneous interfaces such as surface functional groups, dangling bonds and microstructural defects [197,206,208]. Traditional metal-based EMI shielding materials exhibit outstanding shielding efficiency due to their copious mobile charge carriers. However, applications of the metals have been limited by their negative properties such as low chemical corrosion resistance, high density, low flexibility and dominant reflection shielding mechanism [200].

Adjustable electrical conductivity in conductive polymer nanocomposites , along with their favorable low density, low corrosion susceptibility, easier machinability and tunable design, offers a promising design route to develop advanced functional materials for various applications [209] and specially

absorption dominant EMI shielding applications. To date, various conductive 0 to 3 dimensional nanomaterials have been applied to mask electromagnetic waves [199,202,210–215]. In 2011 [25], transitional metal carbides, nitrides or carbonitrides, MXene, were discovered by Yury Gogotsi and introduced as a novel 2D nanomaterial with the highest electrical conductivity of all ever synthesized 2D nanomaterials. The MXene layered structure can be derived from its ternary $M_{n+1}AX_n$ (n = 1 to 3) phase precursor where M is a transitional metal, A is from group A elements and X is carbon or nitrogen. Selective etching of the A layers results in MXene ($M_{n+1}X_nT_x$) flakes, in which n layers of carbon or nitrogen are interleaved between n+1 layers of transitional metals with various surface functional groups (T_x) such as oxygen, fluorine, hydroxyl or chlorine, which arise from different etchant solutions [4,25,216]. Owing to superior electrical conductivity with tunable surface chemistry and mechanical properties, MXene is an excellent candidate for developing conductive polymer nanocomposites for EMI shielding applications [211,217–222]. Shahzad et al. [223] demonstrated superior EMI shielding effectiveness (SE) of 57 dB for 8 μm thick and 90 wt.% loaded MXene-sodium alginate polymer nanocomposite with absorption dominant shielding rather than the reflection of pristine MXene film. Nonetheless, high filler loading may adversely impact the processability and mechanical properties of the nanocomposites. Sun et al. [224] fabricated a segregated conductive MXene structure on polystyrene via an electrostatic assembly approach to obtain a low percolation threshold of 0.26 vol% and EMI SE of 54 dB at 1.9 vol%.

Thanks to abundant active surface functional groups, MXene-hybrid materials can be obtained by substituting MXene terminal surface groups with other conductive or insulative functional materials. Lee et al. [225] grafted insulative polydopamine onto the MXene surface and enhanced EMI SE, mechanical properties and environmental stability of the MXene flakes. Enhanced SE was attributed to the additional dipole polarization loss from the polydopamine. Furthermore, surface modification of MXene flakes with low conductivity materials can also enhance the impedance matching and, subsequently, the EMW absorption by enhancing dipole and interfacial polarization losses [226,227]. For example, EMI SE of MXene-poly(3,4-ethylene dioxythiophene): poly(styrene sulfonate) (PEDOT: PSS) polymer nanocomposites was investigated [228,229]. Improved EMI SE of the nanocomposites was attributed to the multiple interface reflection and polarization between the MXene and PEDOT: PSS interfaces. Zhang et al. [222] prepared a brick-mud structure of MXene-polyaniline nanocomposite and improved its EMI SE. Enhanced EMI SE was attributed to the conduction loss via superior electrical conductivity, multiple reflection loss between layered structures and polarization loss

between MXene and polyaniline. Despite superior EMI SE, poor mechanical properties of the binary MXene/polyaniline-based nanocomposites and also processing challenges of grafted conjugated polymers on MXene limit their applications [227]. To avoid this, incorporating the modified MXene flakes in engineering thermoplastics such as PVDF is a promising approach to simultaneously take advantage of enhanced design flexibility, higher mechanical properties and superb EMI SE [198,230]. PVDF-based polymers have attracted continued attention in EMI shielding applications due to their intrinsic dipole and interfacial polarization effects, which can further enhance dissipation of EM radiation [199].

In this study, low defect polyaniline grafted MXene nanoflakes were synthesized through a minimally intensive layered delamination (MILD) approach [64] followed by oxidant free in-situ polyaniline surface polymerization. Modified MXene nanoflakes were added to PVDF, and the electrical conductivity, EMI SE and mechanical properties of the nanocomposites were thoroughly investigated. It was found that the surface polymerization of conducting polyaniline did not enhance the electrical conductivity of the PVDF nanocomposites. However, the EMI SE and mechanical properties of the modified PVDF-MXene nanocomposites outperformed pristine PVDF-MXene nanocomposites. This incredibly high performance of the added nanocomposites was mainly attributed to the enhanced interfacial and dipole polarization by grafted polyaniline chains. The enhanced mechanical properties of the polyaniline grafted PVDF-MXene nanocomposites were also ascribed to better polymer-filler interactions, and a subsequent higher degree of filler dispersion in the PVDF matrix.

4.2 Experimental Section

4.2.1 Materials and Chemicals

Ti_3AlC_2 MAX powder (size ≥ 400 mesh), lithium fluoride powder (LiF; ≥ 99%), hydrochloric acid (HCl; 37%), N, N-dimethylformamide (DMF) and aniline monomer (≥ 99.5%) were purchased from Sigma Aldrich and used without further purification. Commercial Kynar 710 grade of PVDF with a specific gravity of 1.78 g/cm^3 was kindly supplied by Arkema, France, and was dried for 24 hours at 60°C prior to use.

4.2.2 Synthesis of Exfoliated $Ti_3C_2T_x$ MXene

Large, low defect MXene nanoflakes were synthesized via selective etching of the aluminum layer from the Ti_3AlC_2 MAX phase with a few optimizations on well-established minimally intensive layer

delamination (MILD) method [231]. In a typical experiment, 3.2 g of LiF was dissolved in 40 ml of 9 molar (M) HCl in a Teflon vessel and stirred for 30 minutes at room temperature. Then, 2 g of Ti_3AlC_2 MAX was gradually added to the solution over a period of 15 minutes to avoid excessive hydrogen bubbling due to the exothermic reaction of the etching process. The mixture was stirred for 24 hours at 37 ± 1°C in a water bath. Next, the acidic product was transferred to 50 ml Falcon tubes, washed copiously with ultra-pure water, followed by centrifugation at 8000 RPM for 10 minutes. The washing process continued until the pH level reached 5–6, and a clay-like sediment with dark green supernatant started to form. The clay-like sediment proved that the expansion of the etched layers occurred by the intercalation of water molecules between the inter-gallery spaces of the flakes. The appearance of the dark green supernatant indicates that delamination of the MXene flakes had commenced. To facilitate the delamination process, the mixture was sonicated for 1 hour in a bath sonicator under argon flow. Argon flow started 10 minutes prior to the sonication and continued during sonication to extract potentially dissolved oxygen molecules to minimize oxidation of MXene flakes. Lastly, the $Ti_3C_2T_x$ suspension was centrifuged at 3500 RPM for 45 minutes, and exfoliated flakes of MXene were collected and dried in a lyophilizer.

4.2.3 Synthesis of Oxidant Free Polyaniline Functionalized MXene (MX_nAN_m)

Polyaniline (PA) grafted MXene flakes were synthesized at two different MXene to aniline ratios of 2:1 and 1:1. To prepare polyaniline grafted MXene flakes with MXene to aniline ratio of 2:1 (MX_2AN_1), 300 mg of MXene flakes were dispersed in 150 ml DI water at 4°C, stirred for 2 hours and bath sonicated for 30 minutes under argon flow. 147 µl of aniline monomer was dissolved in 20 ml 1M HCl and stirred for 30 minutes. The aniline/HCl solution was added dropwise to the MXene in water solution. On addition of the aniline/HCl solution, aniline monomers started to adsorb on the hydroxyl and oxygen functional groups on the surface of MXene flakes due to electrostatic attraction between negatively charged surface functional groups of MXene (Zeta potential = -33.1 mv) and positively charged aniline cation radicals [232]. The polymerization reaction was allowed to continue for 6 hours at 4°C. All procedures were performed under a flow of argon gas. Polyaniline functionalized MXene flakes were then washed three times with DI water followed by centrifugation to remove any residue of unreacted monomers. Afterwards, the sediment was dispersed in DI water and dried via lyophilization. MX_1AN_1 was also synthesized by the same procedure with a designated MXene to aniline ratio of 1:1. Nanoflakes were kept in a desiccator with a dry nitrogen atmosphere before use.

Figure 4.1 illustrates the strategy for the synthesis of MXene and polyaniline grafted MXene nanoflakes.

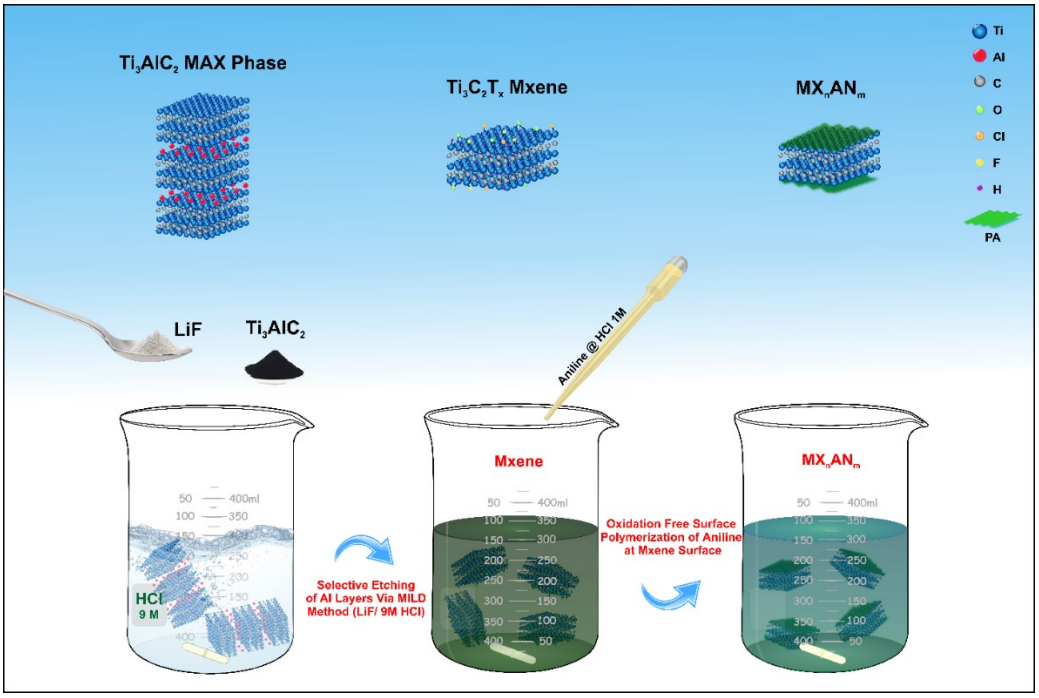

Figure 4.1 Illustration of the synthesis of exfoliated MXene and polyaniline grafted MXene nanoflakes

4.2.4 Preparation of PVDF/MXene and PVDF/MX_nAN_m Nanocomposites

PVDF nanocomposites were prepared by solution blending and subsequent compression molding as follows. A desired amount of PVDF was dissolved in DMF solution by magnetic stirring at 90°C for 4 hours. The concentration of PVDF in the DMF solution was designed to be about 10 wt.%. A certain amount of nanoflakes was added to DMF solution with a concentration of 2 mg/ml and stirred for 2 hours, bath sonicated for 30 minutes, followed by 1 hour mechanical stirring, all under argon flow. The two DMF solutions were mixed and stirred for 2 hours, and the solution was cast in an evaporating dish and dried in a convection oven at a temperature of 60°C for three days. The dried films were shredded into small pieces and compression molded into 8×16×1.7 mm^3 rectangular samples at a temperature of 190°C and pressure of 5 MPa. PVDF-MXene (MX) nanocomposites were prepared with various MXene contents of 5, 7.5, 10 and 15 wt.%. The corresponding volume percentage loading of the nanocomposites were calculated according to the equation provided in Chapter 3, section 3.5 and were

as 2.2, 3.3, 4.4 and 6.9 vol%. The bulk density of the MXene based nanoflakes assumed to be 4.26 g/cm^3 [233]. The density of the PVDF matrix obtained from the datasheet as 1.78 g/cm^3. PVDF-MX_nAN_m nanocomposites were prepared with MX_nAN_m contents of 4.4 and 6.9 vol%.

4.2.5 Characterization

Morphology and microstructure of the exfoliated MXene flakes, polyaniline grafted MXene flakes and cross-sectional area of the PVDF nanocomposites were examined by a field emission scanning electron microscope (Zeiss UltraPlus FE-SEM). Coupled with SEM, the chemical elemental distribution of nanoflakes was characterized via energy dispersive X-ray spectroscopy (EDS) mapping. For SEM analysis of the PVDF nanocomposites, samples were cryo-fractured in liquid nitrogen, and subsequently sputter-coated with a thin layer of gold. Atomic force microscopy (AFM) (Bruker Innova AFM, USA) was utilized in tapping mode to further characterize the isolated single MXene nanoflakes. Crystallography and molecular fingerprints of the samples were characterized by X-ray diffraction (XRD) (Rigaku Miniflex 600) with a Cu-K_α radiation (λ = 1.54184 Å) source, Raman spectroscopy (Bruker Senterra, 532 nm laser source) and Fourier transform infrared spectroscopy (FTIR) (Nicolet 6300, Thermo-Fisher) with a scanning resolution of 4 cm^{-1}. Crystallinity and thermal properties of the nanocomposites were also characterized by differential scanning calorimetry (DSC Q2000 TA Instruments, USA) at a heating/cooling rate of 5°C per minute and with a nitrogen atmosphere. Samples were heated to 200°C and isothermally annealed for 10 minutes to remove thermal history. Then, samples were cooled to 30°C to obtain crystallization behaviour, and again heated to 200°C to characterize the melting behaviour. DC electrical conductivity of the PVDF nanocomposites was measured by the 4-point probe method. As schematically illustrated in Figure 4.2, a spring-type 4-point probe fixture was fabricated and connected to two digital multimeters (DMM Keysight 34465A) and a DC power supply. Various voltages were applied through the DC power supply, and voltage drop and current were measured. Electrical conductivity was calculated through the following equation [37]:

$$\boldsymbol{\sigma = \frac{1}{\rho} = \frac{1}{Rt} = \left(\frac{ln2}{\pi t}\right)\frac{I}{V}} \qquad \textbf{4.1}$$

where ρ is the electrical resistivity, t is the sample thickness, R is the electrical resistance of the sample, I and V are the measured current and voltage drop, respectively.

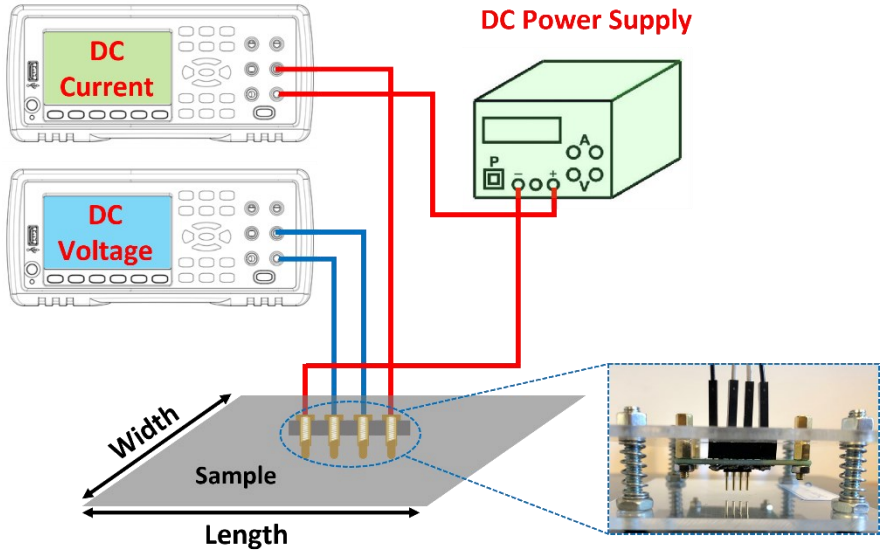

Figure 4.2 Schematic illustration of 4-point probe DC conductivity measurement set up. The photographic picture shows the home-made spring type 4-point probe fixture

The EMI SE of the PVDF/MX and PVDF/MX_nAN_m nanocomposites was analyzed in the P-band frequency range (12.4–18 GHz) via an Agilent N5234A vector network analyzer. S parameters (S_{11} and S_{21}) were obtained from the instrument and the following equations were used to calculate the reflection (R), transmission (T) and absorption (A) coefficients of the shielding efficiency [202]:

$$\boldsymbol{R = |S_{11}|^2} \quad \textbf{4.2}$$

$$\boldsymbol{T = |S_{21}|^2} \quad \textbf{4.3}$$

$$\boldsymbol{A = 1 - R - T} \quad \textbf{4.4}$$

The total EMI shielding effectiveness (SE_T) of the nanocomposites is equal to the sum of reflection effectiveness (SE_R) and absorption effectiveness (SE_A), which could be described by the following equations:

$$\boldsymbol{SE_T = SE_R + SE_A} \quad \textbf{4.5}$$

$$\boldsymbol{SE_R = -10 \cdot log_{10}(1 - R)} \quad \textbf{4.6}$$

$$\boldsymbol{SE_A = -10 \cdot log_{10}\left(\frac{T}{1-R}\right)} \quad \textbf{4.7}$$

The mechanical properties of the nanocomposites were investigated via an ADMET universal testing machine (UTM eXpert 7603, USA) in the tensile mode at a crosshead speed of 5 mm/min with 6 replicates for each specimen. Samples were cut into a rectangular shape with dimensions of 50×5×0.5 mm^3, and the distance between the grips was 20 mm. The linear portion of the stress-strain curve in the strain range of 1–2% was considered to calculate the Young's modulus.

4.3 Results and Discussion

4.3.1 Material characterization

Figure 4.3-a shows the SEM images of the Ti_3AlC_2 MAX powder in which Al layers were interleaved between very closely packed titanium crystals and formed laminated structures [25]. The EDS profile in Figure 4.10-d also shows the elemental analysis of Ti_3AlC_2 MAX powder, in which 17.07 atomic percent of elements belong to Al atoms. Al atoms in Ti_3AlC_2 are more reactive because the bond strength of Ti and C layers is relatively higher than the bond between Ti and Al [25,216]. Therefore, as illustrated in Figure 4.1, highly reactive Al layers in Ti_3AlC_2 were selectively etched in an aqueous in situ HF solution. After Al layer removal, the interlayer interactions between Ti_3C_2 layers were weakened, leading to the nanoflakes delaminating due to the lack of solid metallic bonding [25]. In comparison to the stacked layers of the MAX phase powder in Figure 4.3-a, delaminated transparent nanoflakes of MXene in Figure 4.3-b confirmed the successful elimination of the Al layers. The lack of Al atoms and appearance of F and O atoms in the elemental analysis of MXene flakes in Figure 4.10-e also verified a successful etching reaction. Figure 4.3-c is an SEM image of individual flakes of MXene that was prepared by drying a drop of very dilute colloidal solution of MXene on aluminum foil under a nitrogen atmosphere. As is clear from Figure 4.3-c and Figure 4.10, large MXene flakes were obtained by using the MILD synthesis method. It is noteworthy that large and less defective nanoflakes are required to fabricate highly electrically conductive polymer nanocomposite at a very low percolation threshold [64,206,234]. Figure 4.3-d, and e present SEM images of the polyaniline grafted MX_2AN_1 and MX_1AN_1 nanoflakes, respectively. Higher magnification of the functionalized MX_nAN_m flakes is also shown in Figure 4.10-b and c. Figure 4.3-f and Figure 4.10-f show the EDS mapping spectra of the MX_2AN_1 and MXene nanoflakes, respectively. Substitution of fluorine or oxygen-containing functional groups in MXene with aniline groups reduced the atomic percentage of F and O atoms and caused the appearance of 8.26% nitrogen (N) atoms, which were well distributed on the nanoflake surfaces. It is also worth mentioning that the substitution of the oxygen containing

functional groups in MXene with aniline groups would probably prevent oxidation of MXene and improve environmental stability of the nanoflakes [235]. The surface topography of the delaminated MXene nanoflakes was further studied by AFM and is shown in Figure 4.3-g-i. The inset of Figure 4.3-i shows the height profile of a single $Ti_3C_2T_x$ flake with a measured layer thickness of 1.6 ± 0.2 nm, which is in a good agreement with reported thickness values for monolayer MXene nanoflake [236].

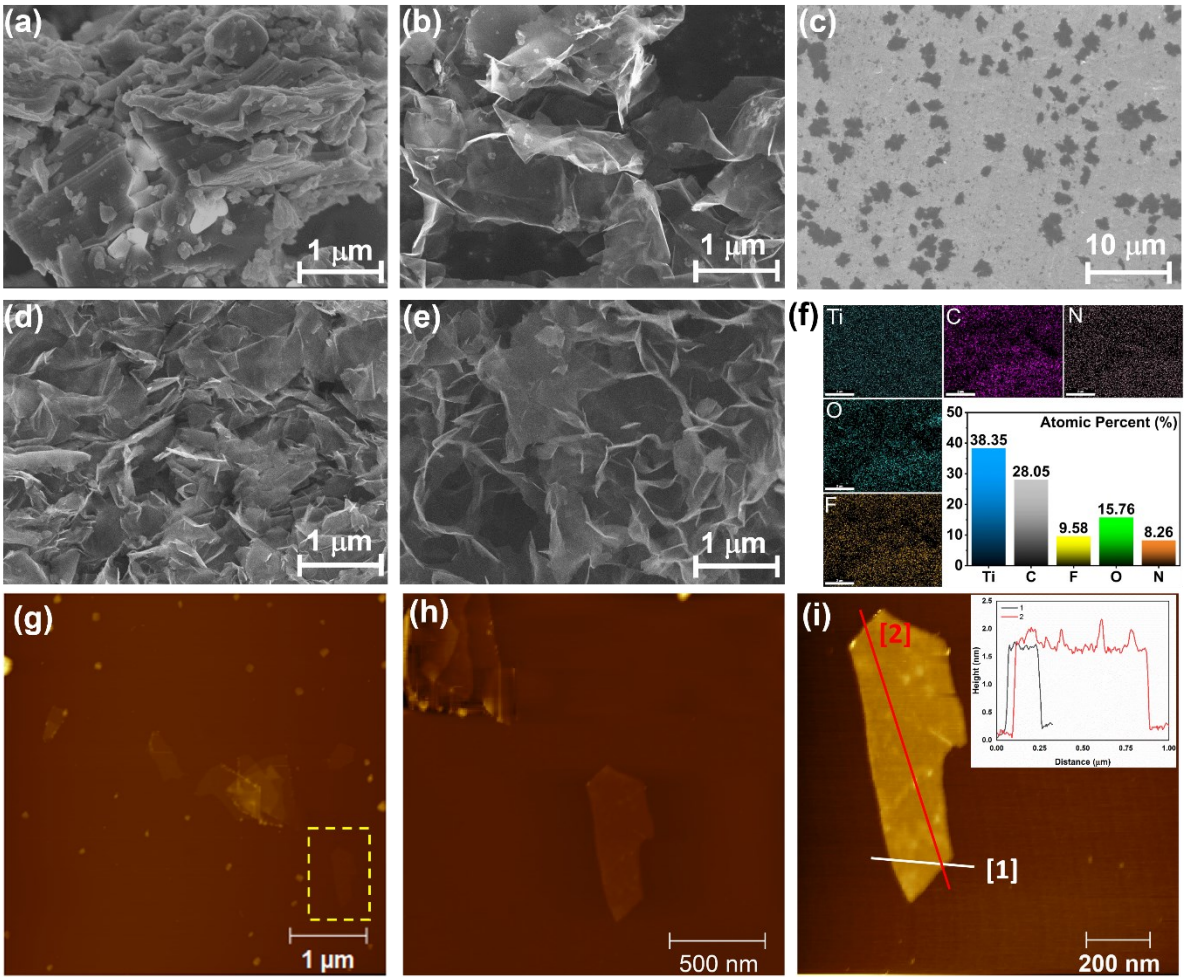

Figure 4.3 (a) SEM images of MAX phase, (b) MXene nanoflakes, (c) drop cast MXene nanoflakes on aluminum foil substrate, (d) MX_2AN_1 nanoflakes, (e) MX_1AN_1 nanoflakes, (f) EDS mapping of the MX_2AN_1 nanoflakes, and (g-i) AFM surface topography of the delaminated MXene nanoflakes

Oxidative polymerization is a classical chemical synthesis method for aniline polymerization. In a strong mineral acid dopant environment, such as hydrochloric acid, an oxidant such as ammonium

persulfate (APS) oxidizes aniline monomer and initiates the polymerization reaction. However, a few studies showed that the presence of oxidizing surface functional groups in nanomaterials could also trigger oxidative polymerization reactions of conjugated polymers [237–239]. For example, Mohamadzadeh et al. [237] used graphene oxide (GO) as an oxidant to polymerize aniline monomer from the surface of GO sheets. In situ GO-assisted polymerization of aniline resulted in polyaniline nanofibers with higher electrical conductivity than the general APS-assisted aniline polymerization. Higher electrical conductivity of GO-assisted polyaniline was attributed to the highly crystalline structure of the polyaniline and induced nanofiber alignment due to the confined polymerization spaces [240]. It is highly likely that the confined geometry and the existing hydrogen bonding between N-H groups of aniline and fluorine or oxygen terminated surface groups of MXene flakes facilitate the self-alignment of the polyaniline chains [232,239]. Furthermore, classical oxidant-assisted polyaniline polymerization generally results in two forms of surface grafted aligned polyaniline nanofibers and aggregates of non-grafted PA nanoparticles between the MXene flakes. However, the non-oxidant polyaniline polymerization will probably lead to only the surface grafted polyaniline nanofibers due to the lack of free oxidizing agent [232].

Figure 4.4-a shows the oxidizing agent role of MXene nanoflakes in oxidative polymerization of aniline monomer. The acid-base reaction between basic aniline monomers and hydrochloric acid resulted in the delocalization of lone pair of electrons in aniline into the benzene ring and made it available for protonation. Accordingly, aniline monomers were acidized to cation radicals and formed positively charged hydrochloride. Zeta potential analysis of the MXene solution was also conducted and illustrated in Figure 4.11-b which confirmed the negative surface charge of the MXene nanoflakes. Therefore, adding the acidic aniline solution to the MXene solution resulted in electrostatic attraction between the cation radicals of acidized aniline monomers and the negatively charged oxygen and hydroxyl functional groups in MXene nanoflakes. In addition, hydrogen bonding between N-H groups of aniline monomer and pendant fluorine or oxygen functional groups was established. Then, polymerization was initiated with the oxidation of anchored aniline monomers by the oxygen and hydroxyl functional groups. First, aniline dimers were formed by electrophilic substitution of the hydrogen atoms in benzene rings. The dimers produced are much more reactive than the aniline monomers due to their lower oxidation potential compared to the aniline monomers. Therefore, the dimers could immediately oxidize and react with the rest of the aniline cation radicals, and propagate the polymerization by producing trimers, oligomers and then polyaniline nanofibers [241].

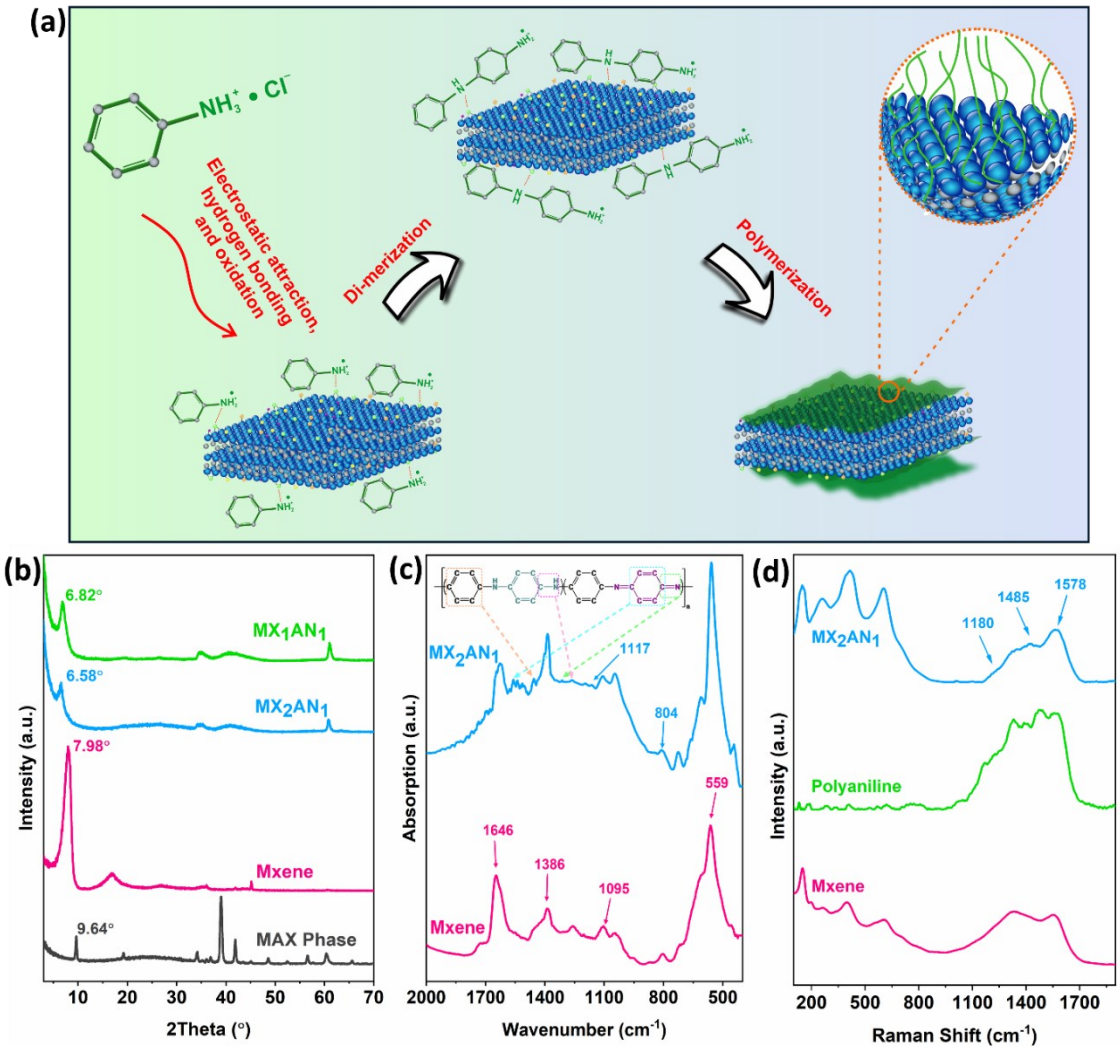

Figure 4.4 Proposed mechanism of the oxidant free polymerization of aniline monomer from the surface of MXene nanoflakes (a), XRD (b), FTIR (c) and Raman spectrum (d) of the nanoflakes.

To verify the successful polymerization of polyaniline on the surface of MXene flakes, XRD, FTIR and Raman spectra were recorded from the samples and are illustrated in Figure 4.4-b-d. Alteration of crystal structure and interlayer d-spaces of the MXene layers after selective etching of aluminum layers and polymerization of aniline are shown in Figure 4.4-b. After solution etching of MAX phase, the characteristic peak at $2\theta = 39°$ disappeared, and the (002) peak at $2\theta = 9.64°$ broadened and shifted to $2\theta = 7.98°$, indicating successful increase in inter-layer d-spaces and delamination of MXene nanoflakes. Interlayer d-spaces and size of the crystalline structures of the delaminated nanoflakes were

calculated by Bragg's and Sherer's equations, respectively, and tabulated in Table 4.1 [202]. Interlayer d-spaces of the (002) basal plane increased from 9.16 Å in the MAX phase to 11.06 Å in MXene flakes. This is because of the appearance of oxygen, fluorine and hydroxyl ligands after solution etching, which satisfies two exposed layers of Ti atoms. Also, the growth of polyaniline nanofibers on the MX_2AN_1 and MX_1AN_1 surfaces further moved the (002) peak to $2\theta = 6.58°$ and $2\theta = 6.82°$, respectively. These peaks at lower diffraction angles corresponded to the increased interlayer d-spaces of 13.43 Å and 13.07 Å. To determine the degree of nanoflake delamination, the average number of stacked nanoflakes was calculated by dividing crystal size by interlayer d-spaces. Solution etching of the MAX phase reduced the average number of layers from 28.3 in the MAX phase to 3.7 for MXene. Aniline intercalation between MXene flakes and their polymerization further reduced the average number of layers to 2.4 and 2.9 for MX_2AN_1 and MX_1AN_1, respectively.

Table 4.1 Extracted parameters from the XRD graphs

Materials	XRD				
	2θ (degree)	Interlayer Distance (Å)	FWHM (radian)	τ (Å)	L_x
MAX phase	9.64	9.16	0.005	259.5	28.3
MXene	7.98	11.06	0.034	41.1	3.7
MX_2AN_1	6.58	13.43	0.057	33.1	2.4
MX_1AN_1	6.82	13.07	0.036	38.6	2.9

The FTIR analysis of the chemical structure of the synthesized nanoflakes is illustrated in Figure 4.4-c. MXene flakes showed characteristic peaks of Ti-O at 559 cm-1, C-F at 1095 cm-1, O-H at 1386 cm^{-1} and C=O at 1646 cm^{-1} [232]. Polymerization of aniline monomers at the surface of MXene introduced C=C stretching vibration of the quinoid and benzenoid ring bands of polyaniline at 1541 cm^{-1} and 1457 cm^{-1}, respectively. C=N stretching vibration of the quinoid ring appeared at 1311 cm^{-1}, and the peak at 1259 cm^{-1} is ascribed to the C-N stretching vibration of the benzenoid ring. The bands centered at 1147 cm^{-1} and 804 cm^{-1} were attributed to the aromatic C-H in-plane and out of plane bending vibrations, respectively [228,241,242].

In conjunction with the FTIR analysis, Raman spectroscopy was conducted to further investigate the chemical bonding structure and verify polyaniline polymerization on the MXene surface. As illustrated in Figure 4.4-d, polymerization of polyaniline from the surface of MXene flakes added the main characteristic peaks of polyaniline at 1180 cm^{-1} for C-H in-plane bending, at 1485 cm^{-1} for C=N stretching of quinoid rings and at 1578 cm^{-1} for C-C stretching of benzenoid rings [243,244]. These results confirmed the successful surface modification of MXene flakes with the polyaniline chains without the utilization of external oxidation agents [239,241].

4.3.2 Morphology of the nanocomposites

Figure 4.5 illustrates the microstructure of the cryo-fractured cross-sectional area of the pure PVDF and corresponding PVDF nanocomposites incorporating 6.9 vol% MX, MX_2AN_1 and MX_1AN_1. The lack of nanoflake aggregation in SEM images of the nanocomposites confirmed the high degree of nanoflake dispersion in the polymer matrix. The high dispersion quality of the nanoflakes can be attributed to the appropriate interactions between polymer chains and nanoflakes, which resulted in their diffusion into inter-gallery spaces of the nanoflakes. Intercalation of polymer chain between nanoflakes, along with mixing, induced shearing forces to peel apart stacked layers of nanoflakes and enhance dispersion [233]. Structural units of polar PVDF chain are comprised of two H atoms and two F atoms. Therefore, good PVDF-MX interactions are expected to originate from the hydrogen bonds between negatively charged F or O atoms on the MXene surface and H atoms in the PVDF backbone. Likewise, the high dispersion quality of polyaniline grafted nanoflakes in PVDF matrix also originated from the interactions between the positively charged polyaniline chains and negatively charged PVDF backbone [232,241,242]. Interestingly enough, the surface roughness of the cross-sectional areas of pure PVDF and PVDF-MX nanocomposite were comparable. However, the surface roughness of the PVDF-MX_2AN_1 and PVDF-MX_1AN_1 significantly decreased in comparison to the pure PVDF. Shtein et al. [245] quantitatively investigated the correlation between surface roughness and fracture toughness of polymer-nanotube nanocomposites and showed that the material with lower fracture toughness has a smooth fracture surface. Therefore, PVDF-MX_2AN_1 and PVDF-MX_1AN_1 nanocomposites could be expected to show low fracture toughness yet higher Young's modulus.

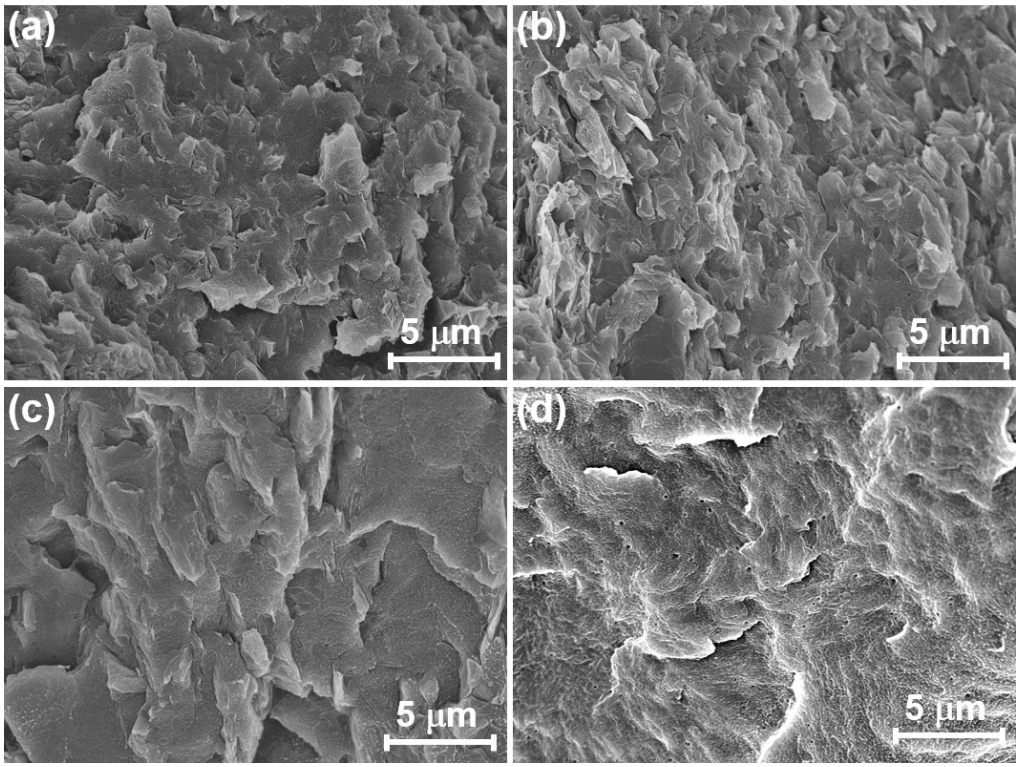

Figure 4.5 Cross sectional SEM images of the (a) cryo-fractured PVDF and 4.4 vol% PVDF nanocomposites of (b) MX, (c) MX_2AN_1 and (d) MX_1AN_1

4.3.3 Electrical Conductivity Measurements on the Nanocomposites

The in-plane DC electrical conductivity of the PVDF-MX nanocomposites is shown in Figure 4.6-a as a function of nanoflake loading. The electrical conductivity of PVDF-MX nanocomposites was enhanced by increasing MXene volume fraction. For example, the electrical conductivity increased from 1.1×10^{-4} S/cm at 2.2 vol% to 2.3×10^{-1} S/cm at 6.9 vol% MXene loading. The electrical conductivity of conductive polymer nanocomposites can be related to the conductive filler content through a power law equation as follows:

$$s = \sigma_f (\varphi - \varphi_c)^t \quad for \quad \varphi > \varphi_c \qquad 4.8$$

where σ is the electrical conductivity of the nanocomposite, σ_f is a constant ascribed to the intrinsic conductivity of the filler, φ is the volume fraction of the conductive filler, φ_c is the percolation threshold and t is a critical exponent describing the dimensionality of the connected network in the nanocomposite

system [37]. In the nanocomposites of this study, as schematically illustrated in Figure 4.6-a, concentration for the percolation threshold is where MXene or MX_nAN_m flakes come into contact or close enough to each other and make a continuous path to transfer the electrons across the nanocomposite. The percolation threshold was estimated by fitting the measured values from the experiment to the power law mentioned above. The inset of Figure 4.6-a shows the log-log plot of electrical conductivity versus $(\varphi-\varphi_c)$. The parameters of the power law were extracted from the best fit to the power law equation. For PVDF-MX nanocomposites, the percolation threshold was determined to be 1.8 vol% with a critical exponent (t) of 2.05. The percolation threshold obtained is much lower than the reported percolation thresholds for PVDF based MXene nanocomposites [211,233]. This could be because of the higher quality of synthesized MXene flakes with low defects that maintain their high electrical conductivity. Also, as described in a previous study [202], higher exfoliation of conductive filler could increase the surface area and the number density of the conductive particles, and hence make a percolated conductive network at lower loadings. Critical exponent values provide an overview of the dimensionality of the conductive filler network created in a polymer matrix. Values between 1.6 to 2 usually indicate that the filler formed a 3D network structure [211,246]. Therefore, the exponent value of 2.05 in PVDF-MX nanocomposites suggested that the MXene nanoflakes were well dispersed in all three dimensions in the PVDF matrix.

To investigate the effect of polyaniline grafting on electrical conductivity of the MXene flakes, electrical conductivity of the PVDF-MX_nAN_m nanocomposites was also measured and is illustrated in Figure 4.6-b. PVDF-MX_2AN_1 nanocomposite showed electrical conductivity of 5.1×10^{-2} S/cm and 0.195 S/cm at filler loadings of 4.4 vol% and 6.9 vol%. The electrical conductivity of PVDF-MX_1AN_1 nanocomposites also showed values of 3.82×10^{-2} S/cm and 0.170 S/cm at MX_1AN_1 loadings of 4.4 vol% and 6.9 vol%, respectively. Due to the comparable conductivity values for MX_2AN_1 and MX_1AN_1 incorporated PVDF nanocomposites to PVDF-MX nanocomposites, nearly the same electrical percolation threshold was assumed for the PVDF-MX_nAN_m nanocomposites.

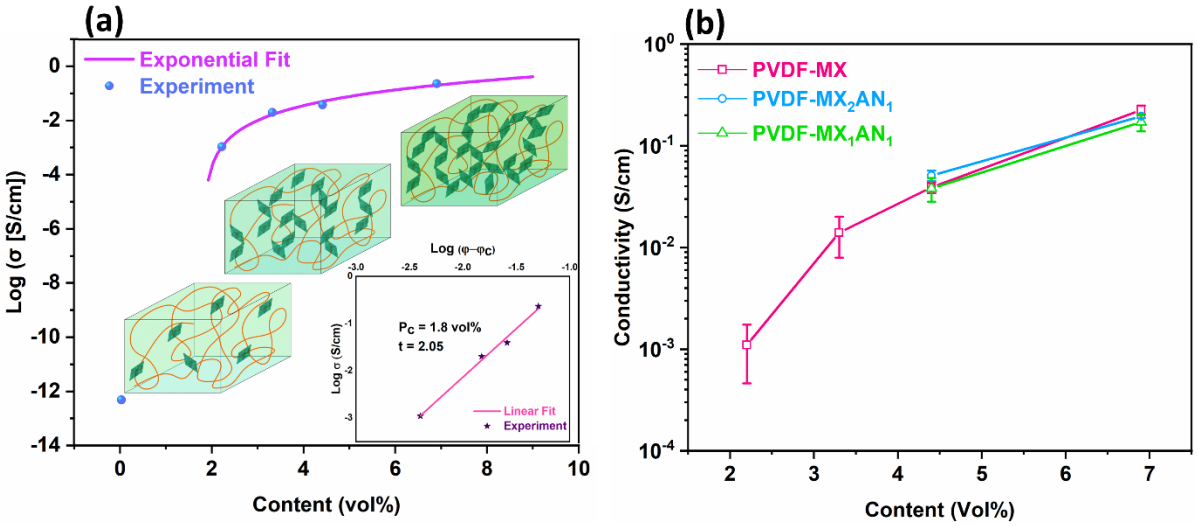

Figure 4.6 (a) DC electrical conductivity of PVDF-MXene and (b) PVDF-MX_nAN_m nanocomposites as a function of volume concentration of nanoflakes. The inset in (a) shows a log-log plot of the electrical conductivity versus (φ-φ_c)

4.3.4 Electromagnetic Interference Shielding Effectiveness of the Nanocomposites

The excellent EMI shielding performance of the MXene nanoflakes is ascribed to the superior intrinsic properties of MXene, such as high metallic electrical conductivity, layered structure and abundant surface functionalities [206,216]. The synergistic effect of the high metallic electron conductivity and layered morphology cause shielding performance of MXene to outperform metal foils such as Cu and Ag with much higher conductivity [203]. Furthermore, the surface functional groups of MXene can act as strong dipole sites or be modified by other functional components, such as either low conductivity material or magnetic material, to further enhance microwave and electromagnetic wave dissipation [201]. Figure 4.7-a illustrates the average of the total shielding effectiveness (SE_T) of the MXene and MX_nAN_m incorporated PVDF nanocomposites as a function of filler content. SE_T of the PVDF-MX nanocomposites increased from 9.77 dB at 2.2 vol% to 29.26 dB at 6.9 vol%, which is higher than the minimum SE_T of 20 dB of commercial EMI shielding material to block 99% of the incident electromagnetic waves [7]. Such an excellent EMI SE of the PVDF-MX nanocomposites was attributed to the synergistic effect of higher electrical conductivity of the nanoflakes and their layered structure. Furthermore, as illustrated in Figure 4.3, exfoliated and low defect flakes of MXene with various surface functional groups play a decisive role in the outstanding EMI SE of the nanocomposites.

Modification of MXene nanoflakes with polyaniline nanofibers further enhanced the total EMI SE of the nanocomposites. As illustrated in Figure 4.7-a, PVDF-MX nanocomposite showed an SE_T of 17.29 dB at 4.4 vol%, while SE_T of PVDF-MX_2AN_1 and PVDF-MX_1AN_1 nanocomposites increased to 20.52 dB and 20.8 dB, respectively, at the same loading. Further increase of nanoflake loading to 6.9 vol% increased the SE_T of the PVDF-MX_2AN_1 and PVDF-MX_1AN_1 nanocomposites to 35 dB and 38.84 dB, respectively. Figure 4.7-b illustrates the EMI SE across the entire P-band (12.4-18 GHz) frequency range for PVDF-MX, PVDF-MX_2AN_1 and PVDF-MX_1AN_1 nanocomposites with filler loadings of 4.4 and 6.9 vol%. PVDF-MX_2AN_1 and PVDF-MX_1AN_1 nanocomposites showed the highest SE_T in the entire frequency range with a maximum SE_T of 40.43 dB and 42.24 dB at frequencies of 16 GHz and 16.9 GHz, respectively. However, the maximum SE_T of 36.75 dB was obtained for PVDF-MX nanocomposite at a frequency of 18 GHz.

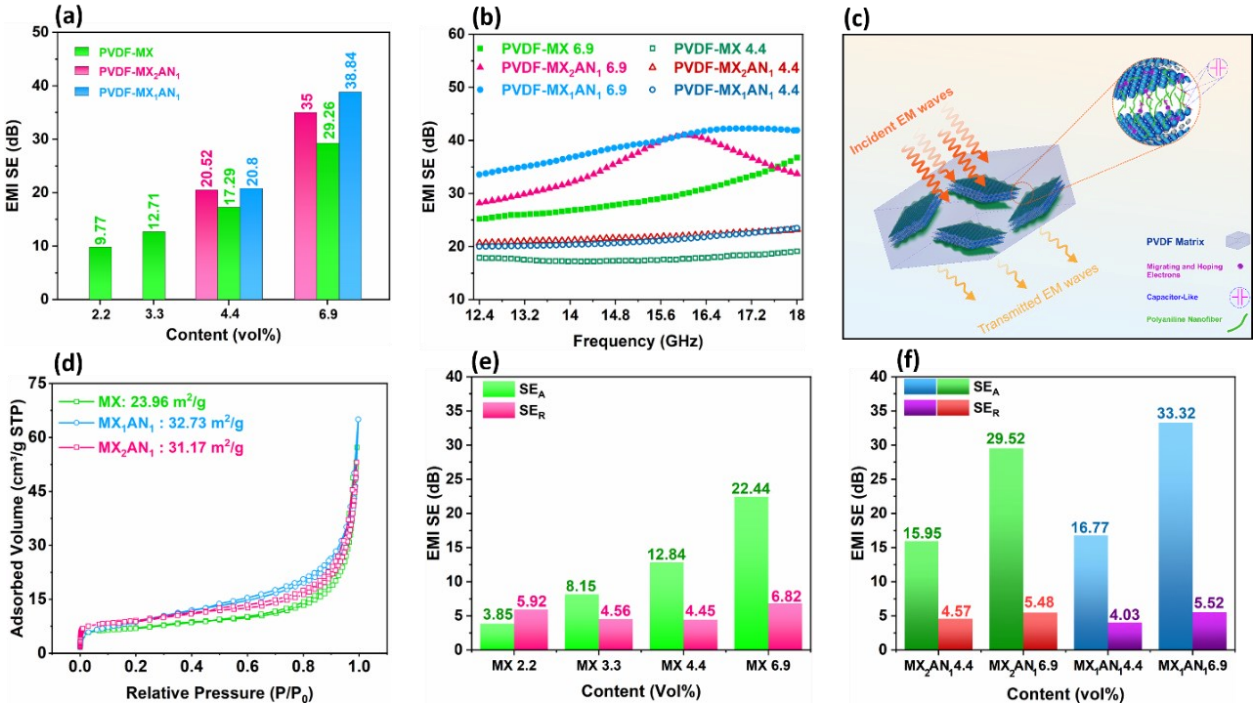

Figure 4.7 (a) Average total EMI SE of the nanocomposites versus filler content, (b) EMI SE of the nanocomposites in the P-band frequency range, (c) proposed EMI shielding mechanism of PVDF-MX_nAN_m nanocomposites, (d) nitrogen adsorption and desorption isotherms of MX, MX_2AN_1 and MX_1AN_1 nanoflakes and the calculated specific surface area, (e) the portions of

reflection and absorption in the total EMI SE for PVDF-MX, and (f) PVDF-modified MXene nanocomposites

Conduction loss, dielectric loss and multiple internal reflection loss are considered the main potential sources of either reflection or absorption of the incident electromagnetic waves in EMI shielding material [200,247]. The conduction loss is attributed to the energy dissipation through the current flow produced by electron transfer mechanisms such as migration, hopping and tunnelling [7,202,210]. Unlike excellent intra-flake conductivity, MXene has poor inter-flake conductivity [248]. Therefore, constructing a 3D conductive network by highly conductive and exfoliated 2D structures of MXene flakes plays a crucial role in facilitating the intra-flake electron migration and electron hopping in pores, defects and inter-flake [201]. Such electron transfer provides an improved and efficient conduction loss in PVDF nanocomposites.

It is worth mentioning that the conduction loss can be further improved by engineering the factors affecting the conductive network of the nanocomposite. For instance, MXene flake size and the concentration of defects, which can be tuned by the chemical synthesis procedure and post oxidation of the flakes, affect the final electroconductive properties of the material [249,250]. Modifying the surface functional groups with conductive components can also reduce inter-flake resistivity, facilitate the electron transfer in a 3D conductive network and improve conduction loss in the EM field.

Dielectric loss is mainly related to ionic, electronic, space charge, dipole and interfacial polarization. However, the main dielectric losses in the GHz frequency range are merely dipole and interfacial polarization [197]. Dipoles in MXene flakes are induced at surface functional groups, defects, interfaces and dangling bonds [233]. In an electromagnetic field, when the dipoles cannot reorientate, energy is consumed by overcoming the momentum that suppresses the reorientation of the dipoles, and relaxation loss occurs [202]. It is worth mentioning that the defects can negatively affect the structural integrity of the MXene flakes and, subsequently, reduce the electrical conductivity and conduction loss. Nevertheless, defects also enhance dielectric loss due to increased surface area, dipole polarization and multiple reflections from multiple interfaces, thus amplifying the response to the incident electromagnetic waves. Therefore, if the enhancement of the dielectric loss is more than the negative effect from losing conduction loss, the resultant SE_T will be increased. Therefore, the higher EMI SE of the PVDF-MX_nAN_m nanocomposites could be explained by the fact that grafting conductive polyaniline chains at the surface of MXene flakes facilitated the construction of an efficient 3D

conductive network and improved the conduction loss and dielectric loss of the nanocomposites in the EM field.

The decisive role of polyaniline chains is illustrated in Figure 4.7-c and explained as follows: i) As illustrated in Figure 4.4-a and Table 4.1, intercalation and polymerization of aniline monomer between MXene flakes increased the inter-gallery spaces and, subsequently, the number density of the nanoflakes by exfoliation of the multilayered flakes to few or even monolayered flakes. Furthermore, electrically conductive polyaniline could reduce the contact resistance between the nanoflakes. These two factors facilitated the construction of a 3D conductive network in the PVDF matrix and enhanced the EMI SE. ii) Different conductivity of the fillers and PVDF matrix induces a capacitor-like structure in interfaces between PVDF chains and fillers, leading to charge accumulation, and thus interfacial polarization. As illustrated in Figure 4.7-d, specific BET surface area of nanoflakes' significantly increased from 23.96 m^2/g in pristine MXene to 31.17 m^2/g and 32.73 m^2/g for MX_2AN_1 and MX_1AN_1 nanoflakes, respectively. Therefore, enhanced surface area leads to higher interfacial polarization and better EMW attenuation [251]. iii) The intrinsic conductivity of the polyaniline chains would be involved in the electron transfer mechanisms and respond to the EM field.

Reflection (R) and absorption coefficients (A=1-R-T) of the nanocomposites were calculated and illustrated in Figure 4.12. It is unambiguous that the majority of the incident electromagnetic waves were reflected from the surface of the electrically conductive nanocomposites, and only a minor portion of the incident waves was concentrated inside the nanocomposite by absorption. This is also in good agreement with the electrical conductivity measurements illustrated in Figure 4.6-b. As the electrical conductivity of the nanocomposites increased by increasing the conductive nanoflakes content, the amount of the reflected EMWs from the nanocomposites' surface increased. Such a reflection mechanism originates from surface charges or charge carriers due to the enhanced electrical conductivity, which causes impedance mismatch between nanocomposites and air [252]. Interestingly, as illustrated in Figure 4.12, the absorption coefficient of the modified MXene based PVDF nanocomposites increased compared to the PVDF-MX nanocomposites. To further investigate the reasons for the increased absorption attenuation for the portions of EMWs concentrated in the nanocomposites, the contributions of reflection and absorption to the total EMI SE for PVDF-MX, PVDF-MX_2AN_1 and PVDF-MX_1AN_1 were calculated and are shown in Figure 4.7-e and f. The contribution of absorption to the total EMI shielding increased for all nanocomposites with increasing filler content [202]. However, at constant filler loadings of 4.4 vol% and 6.9 vol%, the contribution of

absorption in SE_T for the PVDF-MX_2AN_1 was 15.95 dB and 29.52 dB, and for PVDF-MX_1AN_1 nanocomposites was 16.77 dB and 33.32 dB, respectively, which are higher than 12.84 dB and 22.44 dB for the PVDF-MX nanocomposites. Therefore, the majority of the concentrated EMWs in nanocomposites were being absorbed. As EMWs absorption arises from polarization and ohmic losses, thus the absorption dominant shielding of the concentrated EMWs in polyaniline grafted MXene flakes agreed with the higher potential interfacial and dipole polarization in MX_nAN_m nanoflakes. This augmented absorption contribution with less reflection is much more favorable for creating environmentally safe shielding materials with the least secondary radiation.

4.3.5 Microstructural Evolution and Thermal Properties of the Nanocomposites

In addition to the intrinsic properties of the conductive filler itself, its interaction with the polymer matrix could also cause structural evolution and impact the dielectric properties of the nanocomposite. The interfacial interactions between polymer and filler significantly affect the polymer chain orientation and subsequent crystallization [253]. Of the various crystal polymorphisms of PVDF, the polar β-phase that can be induced by the addition of heterogeneous nucleating agents has greater molecular order and results in higher interfacial polarization, and thus strong electroactive properties in PVDF nanocomposites [211]. The higher interfacial polarization of the β phases originates from the higher cooperative orientational movement of the existing dipoles in the interphase between amorphous chains of PVDF and induced β crystals. It is well-known that the interphase characteristics in either polymer-filler or amorphous-crystalline regions differ from the bulk characteristics [254]. According to Gregorio et al. [255], the amorphous-crystalline interphase in β-PVDF maintains the characteristics of the molecular order of the β crystalline region without the mobility restrictions of the crystals. Thus, the mobile polar interphase takes part in enhancing the dipole polarization in an electromagnetic field and improves the EMI SE.

To investigate this phenomenon in the present nanocomposites, DSC and XRD analysis were conducted to characterize the effect of MX and MX_nAN_m nanoflakes on evolution of crystallinity and polymorphism of the PVDF nanocomposites. As illustrated in Figure 4.13-a, the addition of filler to the PVDF raised the crystallization temperature, indicating the nanoflakes' nucleation efficiency. The nanocomposites' thermal properties and degree of crystallinity were calculated and are summarized in Table 4.2. Neat PVDF had 34.88% crystal content. At 4.4 vol% filler content, the degree of crystallinity decreased to 25.77%, 27.87% and 28.09% for PVDF-MX, PVDF-MX_2AN_1 and PVDF-MX_2AN_1

nanocomposites, respectively. Generally, the addition of filler to semi-crystalline polymer matrices increases the crystallization temperature (T_c) due to the increase in the rate of nucleus formation. Nucleation efficiency of the filler is proportionally related to the size of increment in T_c. The more effective the nucleation efficiency, the larger is the increase in T_c. As illustrated in Table 4.2, MX_1AN_1 nanoflakes showed the highest nucleation efficiency, as T_c increased from 136.7°C in pure PVDF to 143.7°C in PVDF-MX_1AN_1 nanocomposite. The crystal structure of the nanocomposites was also investigated by XRD and is illustrated in Figure 4.8. Neat PVDF showed diffraction peaks at 18.3°, 19.9°, 26.5° and 39.5°, which correspond to the α-phase. The addition of 4.4 vol% MXene, MX_2AN_1 and MX_1AN_1 flakes reduced the peaks at 18.3° and 19.9° and induced a new diffraction peak at 20.8°. This peak corresponds to the sum of the diffractions in (110) and (200) planes of the β-phase [256]. Figure 4.13-c shows that the intensity of the β-phase peak increased with increasing MXene flake content in the nanocomposite. To quantify the β nucleation efficiency of the fillers, the relative percentage of β polymorphism was calculated by curve fitting on the XRD reflection peaks of PVDF nanocomposites at a filler loading of 4.4 vol% and using an equation that was described in a previous study [257]. The Gaussian function was used for curve fitting and the results are shown in Figure 4.13-d and f and Table 4.2. The addition of MX and MX_2AN_1 nanoflakes to PVDF resulted in comparable β-phase content of 20.77% and 20.87%, respectively. In comparison, MX_1AN_1 induced the highest β-phase content of 25.24%. This may be attributed to i) the high surface area of the nanoflakes to interact with PVDF chains and ii) the more effective nucleating agent behavior of positively charged polyaniline chains compared to the negatively charged MXene nanoflakes [253]. These results confirmed that polyaniline surface functionalization could increase the β nucleating efficiency of MXene nanoflakes and enhance the interfacial and dipole polarization and shielding efficiency of the nanocomposites.

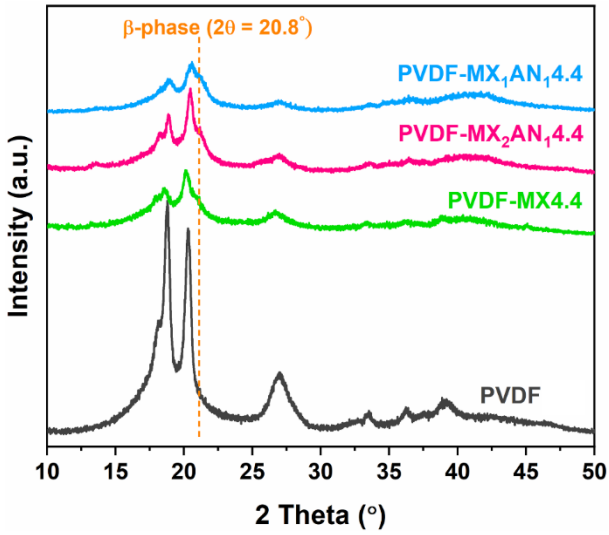

Figure 4.8 XRD graph of the pure PVDF and PVDF nanocomposites filled with 4.4 vol% of MXene, MX_2AN_1 and MX_1AN_1

Table 4.2 Calculated properties from DSC and XRD graphs of the PVDF and 4.4 vol% filled nanocomposites.

Nanocomposites	DSC					XRD
	T_C (°C)	T_{m1} (°C)	T_{m2} (°C)	X_c (%)*	ΔH_{melt} (J/g)	K_β (%)
PVDF	136.7	166.4	170.1	39.23	34.88	-
PVDF-MX 4.4	141.1	167.1	171.7	28.98	25.77	20.77
PVDF-MX_2AN_1 4.4	140.6	167	171.1	31.35	27.87	20.87
PVDF-MX_1AN_1 4.4	143.7	167.6	171.3	31.59	28.09	25.24

* The degree of crystallinity (X_c) from DSC calculated through $\boldsymbol{X_c} = (\frac{1}{1-\varphi_w^{filler}})(\frac{\Delta H_{melt}}{\Delta H_{crys}})$. A value of 104.6 J/g was considered as the heat of fusion for 100% crystalline PVDF.

4.3.6 Mechanical Properties of the Nanocomposites

The uniaxial tensile properties of the PVDF-MX, PVDF-MX_2AN_1 and PVDF-MX_1AN_1 nanocomposites at different filler loadings were measured using a universal testing machine. Typical

stress-strain curves of the neat PVDF and nanocomposites at 4.4 vol% and 6.9 vol% filler loading are illustrated in Figure 4.9-a. Young's modulus, tensile strength, elongation at break and tensile toughness of the nanocomposites were extracted from the stress-strain curves and collected in Table 4.3. As revealed in Figure 4.9-a, the nanocomposites experienced an increment in Young's modulus by increasing the reinforcing nanoflake content. Figure 4.9-a shows the evolution of Young's modulus for PVDF-MX nanocomposite as a function of the MXene content, and compares it with Young's modulus of pure PVDF. The addition of 2.2 vol% MXene to PVDF increased Young's modulus of the nanocomposite to a value of 0.734 GPa. The Young's modulus of the PVDF-MX nanocomposite reached 1.07 GPa at 6.9 vol%. The higher stiffness of the nanocomposites is due to the higher intrinsic mechanical properties of the MXene flakes and their interactions with the polymer chains. Along with good flake dispersion in the PVDF matrix, abundant surface groups of F and O in MXene could form hydrogen bonds with the hydrogen atoms in the PVDF backbone [233]. Hydrogen bonding interactions could participate in stress transfer from the polymer chains to the strong MXene flakes and enhance Young's modulus of the nanocomposites. It is also clear from Figure 4.9-a that the stiffness improvement of the nanocomposites occurred at the expense of a significant reduction in the elongation at break. This could be explained by the increase in the relaxation time of the polymer chains (time for polymer chain to respond to stress) due to the reduced molecular dynamics in the vicinity of the nanoflakes. Restricted dynamics could reduce the stretchability of the polymer chains and severely reduce the elongation at break.

Young's modulus and tensile strength of the PVDF-MX, PVDF-MX_2AN_1 and PVDF-MX_1AN_1 nanocomposites at 4.4 vol% and 6.9 vol% of the filler content were compared and are illustrated in Figure 4.9-c. PVDF-MX nanocomposite showed a stiffness value of 1.01 GPa at 4.4 vol%, while adding the same volume percentage of the modified MXene flakes enhanced Young's modulus to 1.11 GPa and 1.09 GPa for PVDF-MX_2AN_1 and PVDF-MX_1AN_1 nanocomposites, respectively. At 6.9 vol% filler content, Young's modulus of the PVDF-MX_2AN_1 and PVDF-MX_1AN_1 was further enhanced to 1.17 GPa and 1.12 GPa, respectively, compared to the 1.07 GPa of the PVDF-MX nanocomposite. The ultimate strength of the PVDF-MX_2AN_1 and PVDF-MX_1AN_1 nanocomposites at 4.4 vol% were comparable to that of the PVDF-MX nanocomposite. However, the ultimate strength of the PVDF-MX nanocomposite fell to 26.8 MPa at 6.9 vol%, while PVDF-MX_2AN_1 and PVDF-MX_1AN_1 nanocomposites showed 34.3 MPa and 36.2 MPa, which are nearly the same as the strength of the nanocomposites at 4.4 vol%. This might be related to the quality of the dispersion of the nanoflakes in

the PVDF matrix. Generally, the achievement of high-quality dispersion of the nano filler in a polymer matrix is a challenging issue, especially at higher loadings [206,258]. Although the processing conditions are an important parameter that could impact on the dispersion quality of the nanoflakes in nanocomposites, at the same ensured processing conditions, compatibility between the polymer and nano filler play a decisive role to reduce the risk of nano filler aggregation, and thus enhance the dispersion quality. Better nano filler dispersion could, not only reduce the stress concentration sites in the nanocomposite, but also improve the polymer-filler interactions and enhance the capability of the nanocomposite to withstand higher stress before failure. Therefore, the higher tensile strength of the PVDF-MX_2AN_1 and PVDF-MX_1AN_1 nanocomposites is very probably explained by the better nanoflake dispersion and high polymer-filler interactions causing better load transfer behaviour between the nanoflakes and the PVDF chains [246].

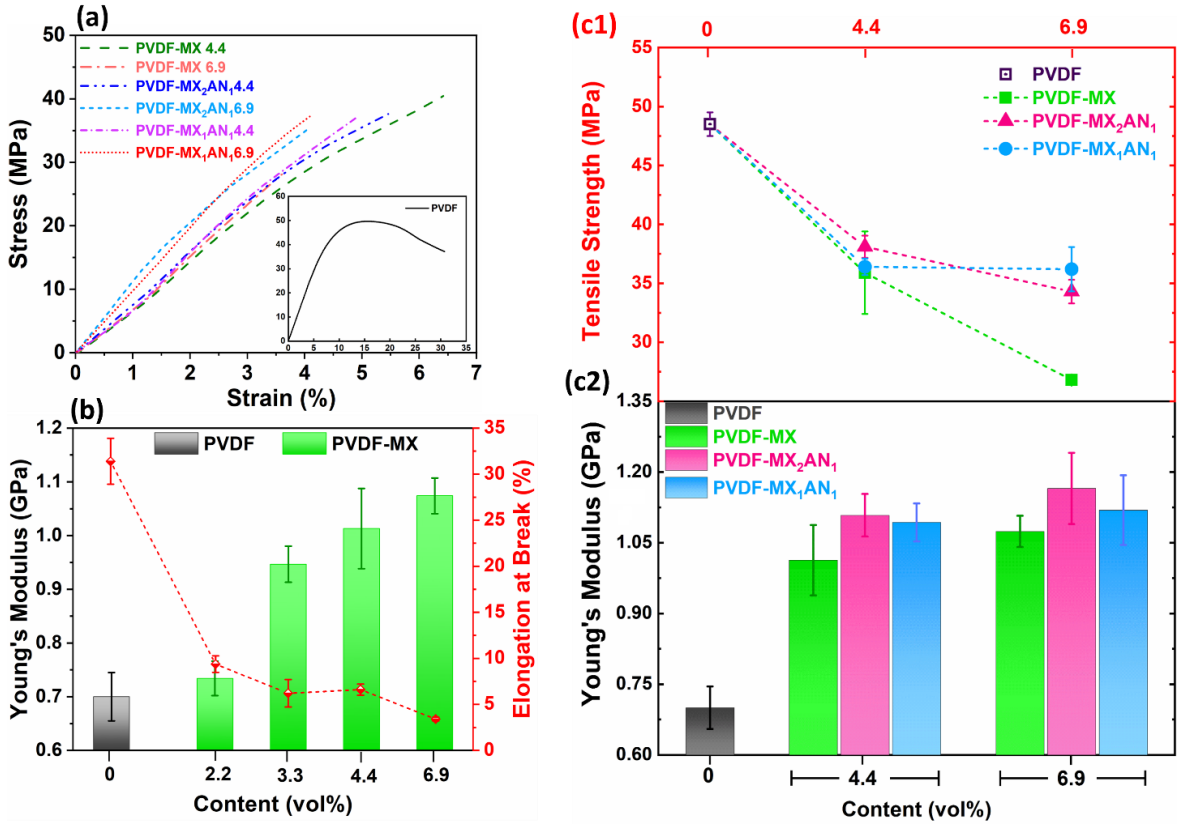

Figure 4.9 (a) Stress-strain curves of the pure PVDF (inset), PVDF-MX2AN1 and PVDF-MX1AN1 nanocomposites at 4.4 vol% and 6.9 vol%, (b) calculated Young's modulus and

elongation at break of the PVDF-MX nanocomposites, and (c1) calculated tensile strength and (c2) Young's modulus of the nanocomposites at 4.4 vol% and 6.9 vol%.

Table 4.3 Extracted mechanical properties of the nanocomposites from stress-strain curves

Nanocomposites	Mechanical Properties			
	Young's Modulus (GPa)	Tensile Strength (MPa)	Elongation at Break (%)	Tensile Toughness (MJ/m^3)
PVDF	0.70 ± 0.05	48.5 ± 2.1	31.1 ± 2.5	12.1 ± 2.08
PVDF-MX 2.2	0.73 ± 0.03	35.4 ± 3.6	9.4 ± 0.9	3.05 ± 0.92
PVDF-MX 3.3	0.95 ± 0.03	35.1 ± 5.3	6.2 ± 1.5	1.7 ± 0.39
PVDF-MX 4.4	1.01 ± 0.05	35.9 ± 3.5	6.6 ± 0.6	1.3 ± 0.015
PVDF-MX 6.9	1.07 ± 0.03	26.8 ± 0.4	3.4 ± 0.2	0.48 ± 0.18
PVDF-MX_2AN_1 4.4	1.11 ± 0.06	38.1 ± 0.9	5.5 ± 0.9	1.04 ± 0.18
PVDF-MX_2AN_1 6.9	1.17 ± 0.07	34.3 ± 1.0	4.4 ± 0.3	0.61 ± 0.07
PVDF-MX_1AN_1 4.4	1.09 ± 0.04	36.4 ± 0.7	5.2 ± 0.6	0.79 ± 0.22
PVDF-MX_1AN_1 6.9	1.12 ± 0.07	36.2 ± 1.9	4.1 ± 0.9	0.97 ± 0.27

4.4 Conclusions

Large and low defect MXene nanoflakes were synthesized via the MILD method. Surface functional groups of the nanoflakes were modified with polyaniline nanofibers through oxidant free polymerization of aniline from the MXene nanoflake surface. Successful MXene synthesis and surface modification were confirmed by SEM, XRD, FTIR and Raman spectroscopy. Surface modification of MXene nanoflakes resulted in excellent enhancement of EMI SE of the PVDF-based nanocomposites. 6.9 vol% loading of MX_2AN_1 and MX_1AN_1 nanoflakes in PVDF matrix, increased EMI SE to 35 dB and 38.84 dB, respectively, from 29.26 dB for the PVDF-MXene nanocomposite. The higher EMI SE of the modified nanocomposites at comparable electrical conductivity was attributed to three main reasons: i) exfoliation of the MXene nanoflakes by intercalation of polyaniline nanofibers in the inter-gallery spaces, ii) induction of abundant capacitor-like structures in the interfaces between PVDF

chains and nanofiller, especially after increased specific surface area with polyaniline modification, and iii) contribution of polyaniline conducting chains in the electron transfer mechanisms and responses to the EM field. The mechanical properties of the PVDF nanocomposites showed higher stiffness for polyaniline grafted MXene nanocomposites due to the high dispersion quality of nanoflakes and the better polymer-filler interactions, which resulted in facilitating load transfer between the nanoflakes and the PVDF chains.

4.5 Supporting information

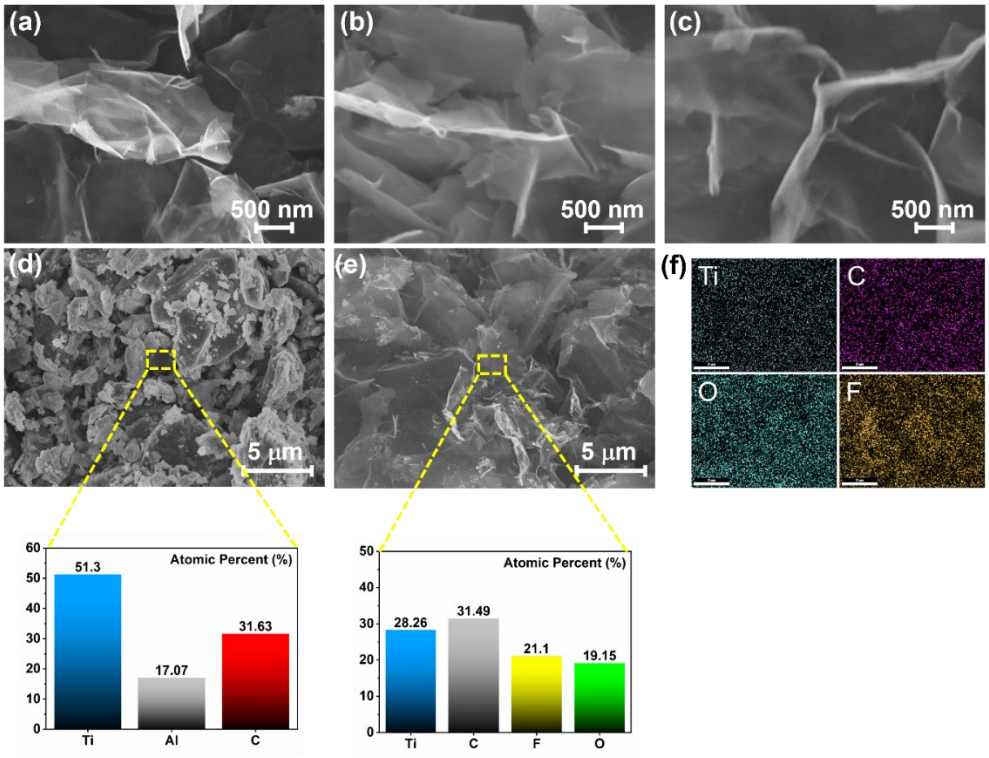

Figure 4.10 (a) High magnification SEM images of the MXene nanoflakes, (b) MX_2AN_1 nanoflakes, (c) MX_1AN_1 nanoflakes, (d) SEM and EDS analysis of the MAX phase, (e) SEM and EDS analysis of the MXene nanoflakes, and (f) EDS mapping of the MXene nanoflakes

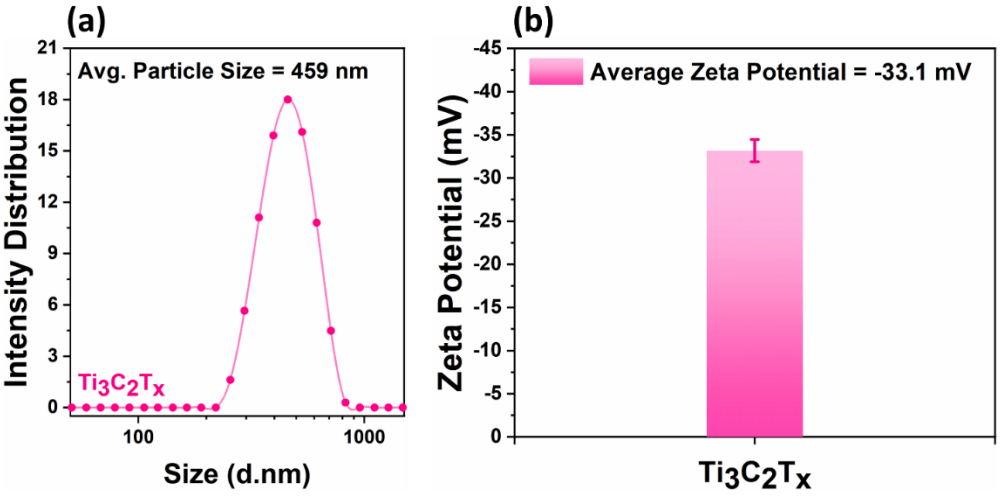

Figure 4.11 Particle size distribution (a) and average zeta potential of MXene nanoflakes

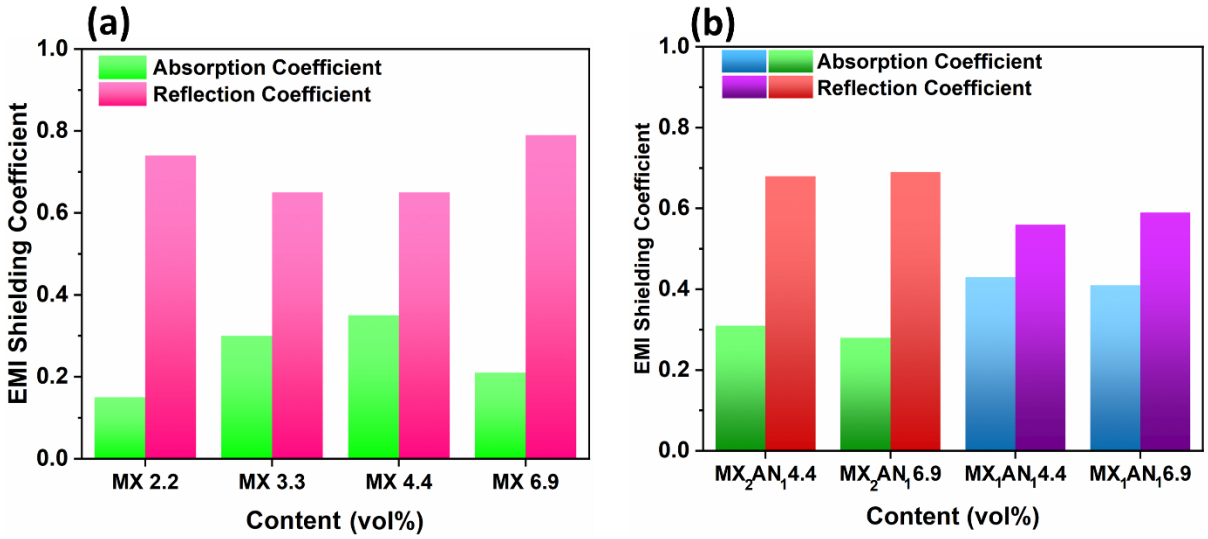

Figure 4.12 (a) Reflection and absorption coefficients of the PVDF-MX and (b) PVDF-MX_nAN_m nanocomposites.

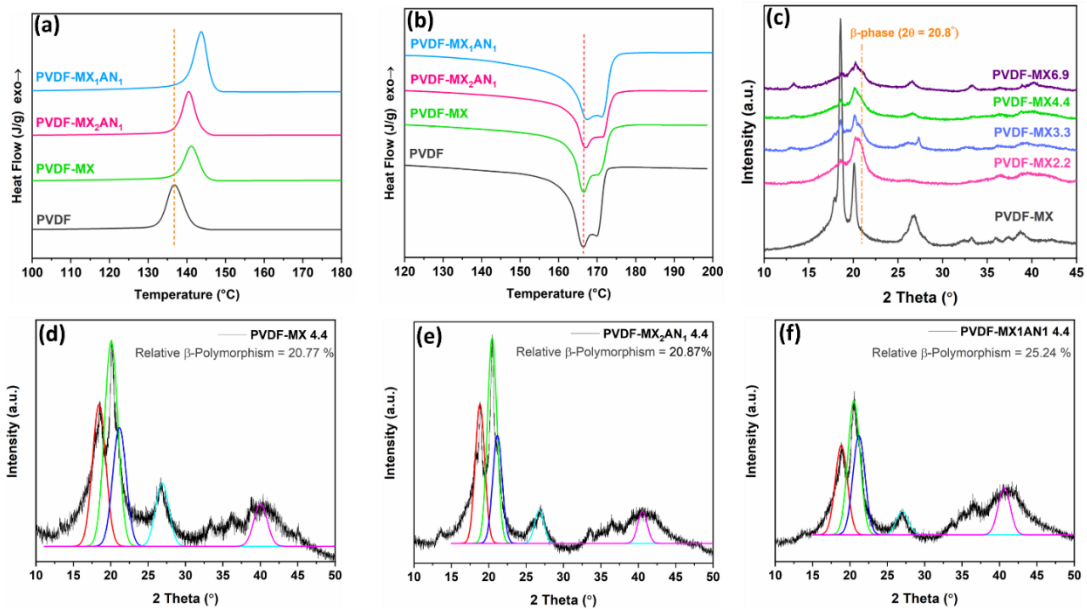

Figure 4.13 The crystallization (a) and melting (b) thermograms of PVDF and nanocomposites. XRD graphs of the PVDF-MX nanocomposites at different MX loadings (c), curve fitting and calculation of the relative percentage of β polymorphism in PVDF nanocomposites (e-f)

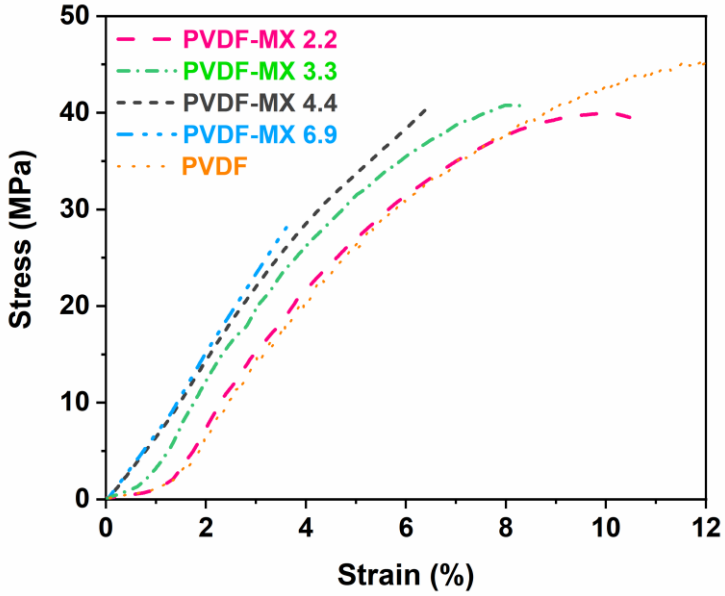

Figure 4.14 Stress-strain curve of the PVDF-MX nanocomposites at different MX loadings

Chapter 5

Excellent EMI Shielding Performance with Ultra High EM Wave Absorption by MXene Coated rGOnR/MXene Aerogel Based PDMS Nanocomposite

Saeed Habibpour, Yasaman Rahimi Darestani, Meysam Salari, Kiyoumars Zarshenas, Chul B. Park, Aiping Yu, "Excellent EMI Shielding Performance with Ultra High EM Wave Absorption by MXene Coated rGOnR/MXene Aerogel Based PDMS Nanocomposite"

5.1 Introduction

The swift growth of portable electronic and telecommunication devices, specifically with the advancement of 5G technology, has simplified human life by offering quicker data speeds and supporting emerging technologies such as smart cities, autonomous vehicles, virtual and augmented reality [32,108,227,247,259–261]. Nevertheless, similar to any wireless technology, there are potential concerns regarding the adverse effects of electromagnetic interference (EMI) on device functioning and human health [262,263]. Consequently, significant efforts have been continuously devoted to the development of advanced materials that are effective in shielding against EMI, while also being lightweight, durable, cost-effective, and easy to process [264]. Undoubtedly, sophisticated shielding materials are crucial for ensuring the safe and long-term use of electronic devices, as well as protecting the well-being of individuals exposed to EMI.

Various mechanisms, such as reflection, absorption, scattering, and multiple reflections between different interfacial layers, can attenuate the incident power of the EM waves and achieve efficient EMI shielding effectiveness (SE). Historically, metals and more recently, carbon-based nanomaterials as well as 2D transitional metal carbides or nitrides (MXene) have been the preferred choice for EMI shielding due to their high electrical conductivity, which directly contributes to high SE [4,265]. Fan et al. [266], demonstrated a very high EMI SE of 80 dB for a free-standing multilayer graphene film with a 54 μm thickness, while Iqbal et al. [267] reported an ultrahigh shielding effectiveness of 116 dB for a heat-treated Ti_3CNT_x MXene films at a lower thickness of 40 μm. while materials with ultrahigh electrical conductivity exhibit outstanding EMI SE, a greater impedance mismatch between the shielding material and the medium through which EM waves propagate often results in a significant

portion of incident waves being reflected rather than absorbed. EMI shielding materials that primarily rely on reflection as the dominant shielding mechanism are generally not preferred due to the potential for secondary pollution caused by reflected waves. Therefore, it is still a pressing matter to develop EMI shielding materials with ultra-high absorption-dominant shielding mechanism.

Lightweight, excellent chemical stability, easy to process, inexpensive, and tunable electrical properties of conductive polymer nanocomposites (CPnC) have brought them to the forefront of research as promising EMI shielding material. Zhao et al. [268] reported a highly conductive 3D $Ti_3C_2T_x$ MXene/rGO aerogel-based epoxy nanocomposite with an optimized EMI SE of 56.4 dB at 0.74 vol% loadings. Nevertheless, the portion of SE_R was 5.7 dB which means about 70% of the incident EM waves are reflected from the surface [269]. The absorption of EM waves in CPnCs can be improved by increasing interfacial polarizations that can be achieved through the creation of diverse hetero-structured surfaces using a combination of different nanomaterials [270–273]. Furthermore, in order to achieve EMI shielding materials with dominant absorption behavior, it is favorable to optimize the surface resistivity of CPnC while decreasing their dielectric permittivity, which enhances the impedance matching between the air and the shielding material [274]. High impedance matching allows incident EM waves to penetrate shielding material and dissipate by converting to heat through various mechanisms such as conduction loss, polarization relaxation and multiple scattering. Low impedance mismatch may be attainable by different strategies such as constructing a microcellular structure [275], constructing an anisotropic conductive network [276], optimizing the thickness, or adding impedance matching layers to the shielding structure to reduce reflections [277].

Zhao et al. [101], introduced microcellular foam structure (48% void fraction) in 10 wt.% loaded PVDF-GnP nanocomposite (5.2×10^{-3} S/cm) and obtained EMI SE of 27 dB. The nanocomposite demonstrated absorption-dominant shielding performance with SE_R of 2.6 dB, indicating a reflection efficiency of 46%, benefitting from the internal scattering and multiple reflections occurring within its unique cellular structure. Increasing the degree of microcellular structure can also decrease the effective dielectric permittivity, thereby allowing adjustment of surface impedance matching and resulting in higher absorption efficiency [111]. Duan et al. [278], adjusted surface impedance matching by constructing an anisotropic conductive network of microcellular nanocomposite and achieved high EMI SE. They employed a directional freeze drying and density-induced nanofiller segregation method and obtained Ag-coated expanded polymer bead/FeCo@rGO/waterborne polyurethane with gradient conductivity increase in EM wave penetrating direction. The surface's lower conductivity allowed for

proper impedance matching to absorb incident EM waves, while the higher bulk conductivity enabled sufficient EMI SE through reflection. Ma et al. [277], developed a layered film/foam structure with (PVDF/MWCNT 10 wt.%/GnP 10 wt.%) film layer and (PVDF-30 wt% SiCnw@MXene 7:1) foam layer with 65% void fraction (VF) and obtained EMI SE of 32.6 dB with SE_R of 3.1×10^{-4} dB. The foam layer absorbs EM waves by tuning the impedance mismatch between air and the nanocomposite, while the highly loaded conductive film layer shields EM waves by reflection mechanism. Although results demonstrated a very low reflection shielding mechanism, the total EMI SE is still have potential to improvement. Moreover, in the numerous attempts made to develop EMI materials that exhibit absorption-dominant properties, the thickness of the shielding material, which is a crucial variable affecting surface impedance matching and EM wave reflectivity, has been rarely investigated. Ma et al [279], evaluated the thickness dependence of the absorption/reflection (A/R) ratio in a monolayer microcellular shielding structure. They obtained absorption dominancy with an A/R ratio of 1.07 (65% VF) and 1.6 (85% VF) at thicknesses of 2.4 and 3.2 mm, respectively. However, despite these high A/R ratios, the total EMI shielding effectiveness (SE) obtained was around 22 dB and 15 dB, which falls short of meeting the commercial requirement of shielding material that can block 99.9% of incident EM waves [280].

Herein, we took an engineering design to develop a double layer shielding structure which provides excellent EMI SE along with a high A/R ratio. Shielding structure constructed by a very thin layer of higher electrical conductive MXene as a highly reflective shielding layer and lower electrical conductive reduced graphene oxide nanoribbon (rGOnR)/MXene (MX) aerogel based PDMS nanocomposite as an impedance matching layer. rGOnR/MX-PDMS nanocomposite was prepared via unidirectional freeze casting and subsequent PDMS impregnation method. It was found that low conductivity with a 3D interconnected network of nanocomposite can properly adjust surface impedance matching to absorb incident EM waves. Additionally, the nanocomposite synergistically enhanced the total EMI SE of the MXene layer through both conduction loss and multiple reflections between well distributed conductive nanomaterials in the nanocomposite. Furthermore, the effect of rGOnR and MXene hybridization on reducing the minimum required thickness for obtaining maximized A/R ratio was investigated and the influence of nanomaterials surface functional groups on enhancing the polarization relaxation was highlighted.

5.2 Experimental Section

5.2.1 Materials

Multiwalled carbon nanotubes (MWCNTs) with an average diameter of 20–30 nm and length of 10–30 μm were obtained from Cheap-Tubes Inc., (USA). Ti_3AlC_2 MAX phase (size ≤40 μm), lithium fluoride (LiF), hydrochloric acid (HCl; 12 M), hydrogen peroxide (30%), phosphoric acid, sulfuric acid and potassium permanganate were purchased from Sigma Aldrich, (USA) and used without further purification. Two-part polydimethylsiloxane (PDMS) (Sylgard 184) including base resin (part A) and curing agent (part B) was acquired from Dow corning Inc. and were mixed in a manufacturer recommended A:B mass ratio of 10:1.

5.2.2 Synthesis of graphene oxide nanoribbon (GOnR)

GOnR was synthesized through chemically oxidation and longitudinal opening of MWCNT, as reported in our previous work [165,202]. Briefly, MWCNT was dried in a 60 °C convection oven for 24 hours. Then, 2 g of MWCNT were dispersed in 360 ml of sulfuric acid and stirred for 1 hour in an ice bath. Afterwards, 40 ml of phosphoric acid was added to the solution and stirred for another 15 minutes. Next, 10 g of potassium permanganate was gradually added to the reactor over 30 minutes, and the mixture was stirred for 15 minutes until the solution turned dark green, indicating the dissolution of potassium permanganate. The ice bath was replaced with a silicon oil bath and the reactor temperature was raised to 65 °C over 1 hour. The mixture was stirred continuously for an additional 3 hours at 65 °C. Once the reaction was completed, the reactor cooled down to 0-4 °C and then poured into 400 ml of distilled de-ionized (DDI) ice containing 20 ml of hydrogen peroxide. The solution was allowed to precipitate for 24 hours. The precipitated slurry was washed twice with 10% HCl and then dialyzed for three days until the pH reached the range of ~5.5- 6.5.

5.2.3 Preparation of $Ti_3C_2T_x$ MXene (MX) nanoflakes

Aluminum layers of Ti_3AlC_2 MAX phase were selectively etched through the minimally intensive layer delamination (MILD) method to obtain $Ti_3C_2T_x$ MX nanoflakes [231]. Herein, an etchant mixture of 1.6 g of LiF in 20 ml of HCl (9 M) was prepared in a Teflon reactor at room temperature. Then, 1 g of Ti_3AlC_2 powder was gradually added to the reactor over 10 minutes to avoid excessive hydrogen bubbling due to the exothermic reaction of the etching process. The reactor was placed in a water bath at 37 °C and stirred for 24 hours. Afterward, the acidic slurry was repeatedly washed with DDI water

through centrifugation at 10000 RPM for 10 minutes until the pH reached a level of 5–6. The appearance of clay-like sediment at this step verified the expansion of the etched layers through the intercalation of water molecules between the inter gallery spaces of the MX nanoflakes. The dark green supernatant is also an indication of the starting of MX nanoflake delamination. Next, the mixture was sonicated for 1 hour in a bath sonicator under a nitrogen gas flow to facilitate the delamination process. The purpose of nitrogen gas flow in the solution is to extract potentially dissolved oxygen molecules and minimize oxidation of MX nanoflakes. Lastly, to obtain exfoliated $Ti_3C_2T_x$ MX powder, the suspension was centrifuged at 3500 RPM for 45 minutes and freeze dried at -65 °C and 25 μbar.

5.3 Preparation of unidirectionally aligned aerogel based PDMS nanocomposites

To prepare 3D unidirectionally aligned reduced GOnR (rGOnR) and hybridized rGOnR/MX aerogels, directional freezing of the nanomaterial's solution followed by freeze drying process was utilized, as illustrated in Figure 5.1. In a typical process, to prepare rGOnR15/MX15 aerogel, 60 mg GOnR was dispersed in 2 ml DDI water (30 mg/ml), stirred for 30 minutes, and then sonicated for 3 hours. Similarly, 60 mg of MX was also dispersed in 2 ml DDI water (30 mg/ml), stirred for 30 minutes and sonicated for 1 hour under Nitrogen gas flow. The shorter sonication time for the MXene solution compared to the GOnR solution was implemented to limit MXene oxidation and size reduction during the sonication process. Afterward, the two solutions were mixed to form a 4 ml GOnR15/MX15 hybrid solution with a total concentration of 30 mg/ml. The suspension was then poured into a homemade copper mould with the lower part of the mould immersed in a liquid nitrogen pool and the walls sealed with a Teflon sheet placed outside of the pool. Due to the high thermal conductivity of the copper, the immersed bottom part of the mould introduced a very large unidirectional temperature gradient, resulting in directional growth of ice crystals from the copper surface. The frozen GOnR15/MX15 solution was freeze dried for 72 hours, and the resulting aerogel were thermally annealed in a tube furnace at 450 °C for 3 hours, under Argon atmosphere, to restore the electrical conductivity of the graphene nanoribbons and obtain rGOnR15/MX15. It is important to note that MXene oxidation typically occurs at temperatures above 600°C due to the removal of surface terminations. As a result, annealing at 450°C not only does not adversely affect the stability of the MXene nanoflakes, but may also potentially enhance their electrical conductivity [108]. In a similar approach, rGOnR30, hybridized

rGOnR25/MX5 and rGOnR20/MX10 aerogels were also prepared and thermally annealed before nanocomposite preparation.

Aerogel based PDMS nanocomposites were prepared through the impregnation method on rGOnR/MX aerogels. First, PDMS base resin and curing agent in a mass ratio of 10:1 was prepared and mixed thoroughly for 10 minutes. Then the mixture was degassed at room temperature in a vacuum oven for 30 minutes. Next, the as-produced aerogels were placed at the surface of the mixture and allowed to immerse gradually in the PDMS mixture. After full immersion of the aerogels, the impregnation process was assisted by applying a vacuum for 2 hours. Afterward, the samples were placed in a convection oven at 80 °C for 4 hours to cure the polymer. Samples were post-cured at 60 °C for additional 24 hours before slicing into small slabs of 8×16 mm^2 and various thicknesses.

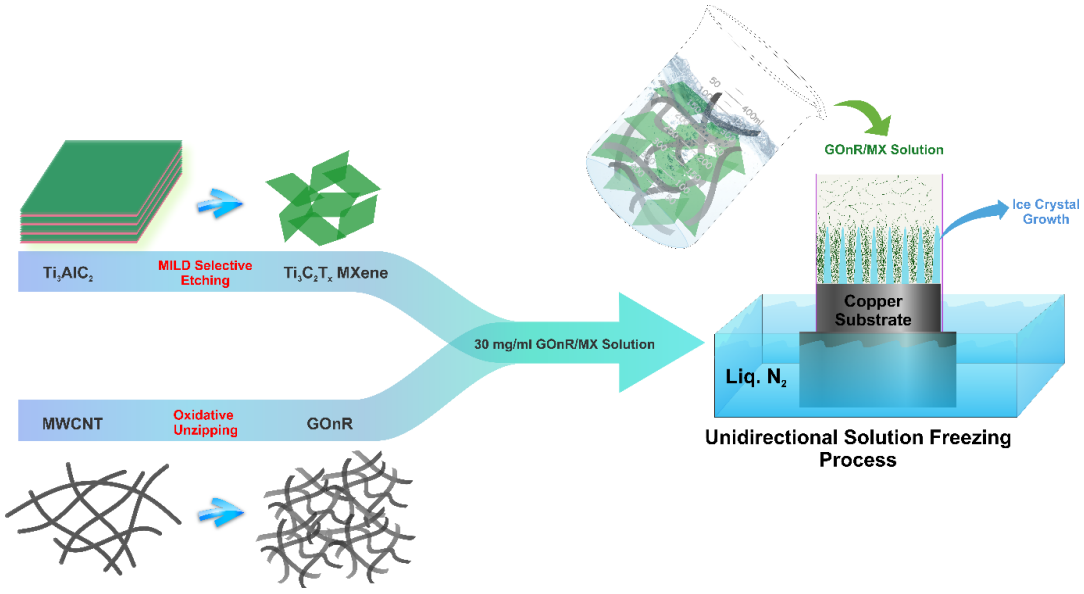

Figure 5.1 Schematic illustration of rGOnR/MX unidirectional foam preparation

5.3.1 Characterization

The morphology of the synthesized nanomaterials was observed with Zeiss UltraPlus field emission scanning electron microscope (FE-SEM). Additionally, the chemical elemental distribution of the nanoflakes was characterized via energy dispersive X-ray spectroscopy (EDS). The cross-sectional microstructure of the aerogel based PDMS nanocomposites was investigated using FE-SEM after cryofracture of the samples in liquid nitrogen, followed by a thin layer of gold sputtering. The successful longitudinal unzipping of the GOnR from its parent MWCNT was verified by detecting the

individual particles using transmission electron microscopy (TEM) (JEOL 2010F) with an accelerating voltage of 200 kV. The size and thickness of an isolated MXene nanoflake were also investigated through a Bruker Innova atomic force microscopy (AFM) in tapping mode. Crystallography of the nanoflakes was studied using a Rigaku Miniflex 600 wide-angle powder X-ray diffraction (XRD) with Cu-K_α radiation (λ=1.54184 Å). Raman spectra were acquired using a Bruker Senterra Raman spectroscopy with an excitation wavelength of 532 nm to analyze the composition, order, and disorder of the synthesized nanomaterials. The chemical functionalities of the nanomaterials were assessed by a Nicolet-670 Fourier transform infrared spectroscopy (FTIR) with a resolution of 4 cm^{-1} in the range of 600−4000 cm^{-1}. The elemental compositions and bonding information of the nanomaterials were measured by a Thermal Scientific K-Alpha XPS spectrometer. The thermal degradation properties of each nanomaterial were elucidated by heating them to 800°C with a constant heating rate of 10°C/min using a Q500 TA thermogravimetric analysis (TGA).

The linear sweep voltammetry (LSV) technique is used to measure DC electrical conductivity of the aerogel based PDMS nanocomposites via a through-plane controlled environment (CESH) sample holder coupled with a VSP-300 Biologic Potentiostat. Galvanostatic electrochemical impedance spectroscopy (GEIS) technique was also employed to measure the AC electrical conductivity and dielectric properties of the PDMS-based nanocomposites at a frequency range of 1 to 10^5 Hz. The EMI SE of the PDMS nanocomposites was analyzed by collecting S parameters (S_{11} and S_{21}) using the waveguide mode in the frequency range of 12.4−18.0 GHz (P-band) on a Keysight, PNA-L Series N5234B vector network analyzer. The following equations were used to calculate the reflectivity (R), transmittivity (T) and absorptivity (A) for the incident electromagnetic wave [202]:

$$\boldsymbol{R = |S_{11}|^2} \quad \textbf{5.1}$$

$$\boldsymbol{T = |S_{21}|^2} \quad \textbf{5.2}$$

$$\boldsymbol{A = 1 - R - T} \quad \textbf{5.3}$$

The total EMI shielding effectiveness (SE_T) of the nanocomposites was calculated by summing the reflection shielding effectiveness (SE_R) and absorption shielding effectiveness (SE_A), obtained from the calculated reflection and absorption coefficients, using the following equations:

Considering the calculated reflection and absorption coefficients, the total EMI shielding effectiveness (SE_T) of the nanocomposites obtained by the summation of the reflection shielding effectiveness (SE_R) and absorption shielding effectiveness (SE_A) according to the following equations [202]:

$$SE_T = SE_R + SE_A \quad (5.4)$$

$$SE_R = -10 \cdot log_{10}(1 - R) \quad (5.5)$$

$$SE_A = -10 \cdot log_{10}\left(1 - \frac{A}{1-R}\right) \quad (5.6)$$

5.4 Results and Discussion

5.4.1 Material characterization

Figure 5.2-a illustrates the large particles of the Ti_3AlC_2 MAX phase. High magnification FE-SEM images of the MAX phase in Figure 5.8 demonstrate the laminate structures of stacked titanium crystals. EDS analysis on MAX powder showed 17.6 atomic percent aluminum element. Considering the chemical composition of the MAX phase, the aluminum elements are interleaved between the titanium and carbon laminates. Figure 5.2-b and c are presenting exfoliated MXene nanoflakes after successful etching of the aluminum layers and the layers' delamination. EDS analysis of the MXene nanoflakes in Figure 5.8-d confirmed the successful removal of the aluminum layers. It also showed the appearance of oxygen and fluorine elements which are attributed to the fluoride and oxygen containing functional groups on the nanoflakes' surface. Although we have used a less intensive chemical etching condition method (MILD) to synthesize MXene nanoflakes, it is obvious from Figure 5.2-c that there was a lateral size reduction during the etching and sonication assisted delamination process. Figure 5.2-i shows the AFM topography image of a bilayer MXene nanoflake. The height profile in the inset of Figure 5.2-i represents the thickness of ~3 nm for the MXene bilayers along with micron size lateral dimensions which are in good agreement with the reported theoretical and experimental dimensions for a single layer MXene nanoflake [108,199]. Figure 5.2-e is presents the longitudinally unzipped GOnRs from their parent multiwalled carbon nanotubes illustrated in Figure 5.2-d. Despite the chemical oxidation of MWCNTs possibly shortening the length of the nanotubes [281], a higher magnification image from an isolated GOnR in Figure 5.2-f and Figure 5.8-c proved that the controlled reaction conditions along with the optimized chemical reagents' ratio can effectively reduce the nanotubes shortening. Lengthwise opening of the nanotubes resulted in an increased length to width aspect ratio of the

nanoribbons [282]. Comparing the TEM images of the MWCNT and GOnR in Figure 5.2-g and h also confirmed the unzipped nature of the GOnR strips. The presence of a clear line exactly in the middle of the MWCNT tubes confirms its hollow structure, whereas the lack of that in GOnR implies a layered 2D structure. EDS analysis of the GOnR showed about 31 atomic percent of oxygen element which is related to the oxidation of nanoribbons during the lengthwise opening process. After thermal annealing of the aerogels, the oxygen atomic percent reduced to about 8 percent, confirming the successful removal of the majority of the oxygen containing functional groups.

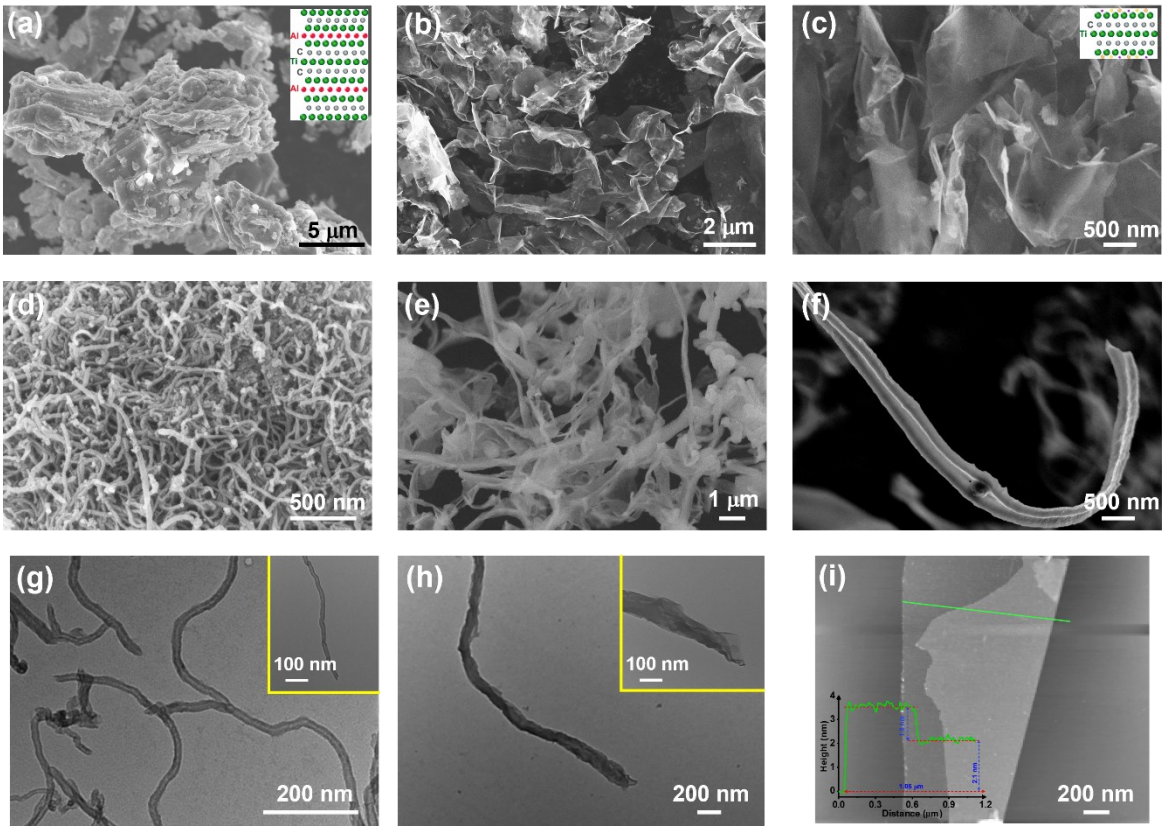

Figure 5.2 SEM images of (a) Ti_3AlC_2 MAX phase, (b) and (c) $Ti_3C_2T_x$ MXene, (d) MWCNT, (e) and (f) GOnR. TEM images of (g) MWCNT, (h) GOnR and (i) AFM topography of $Ti_3C_2T_x$ MXene. Inset in (i) shows the height profile of bilayer $Ti_3C_2T_x$ MXene nanoflakes.

The alteration of the crystalline structures of the nanomaterials was characterized with XRD in Figure 5.3-a and coupled with the Raman and FTIR spectroscopy in Figure 5.3-b and d to elucidate the integrity of the crystalline structures and functional groups. The selective etching of the aluminum layers from the MAX phase disappeared the characteristic peak at 2θ =39.04°, broadened the (002) peak at 2θ

=9.58°, and shifted it to a lower 2θ =7.98°. Using Bragg's equation, the interlayer d-spacing of the shifted (002) peak was calculated and showed that the spaces between the layers enlarged from 9.22 Å to 11.06 Å. The calculation of the average particle dimensions in the [000l] direction before and after layer delamination of the MAX phase showed a significant reduction from 25.95 to 4.11 nm which corresponds to the average number of layers of 28.3 and 3.7 in MAX phase and MXene, respectively [282]. These results also confirmed the height profile in the topographic image of MXene bilayer in Figure 5.2-i. The presence of chemical functional groups on MXene surface was confirmed by FTIR. A broad and strong peak at 3436 cm^{-1} and peak at 1386 cm^{-1} both reflected the OH groups while peaks at 1646, 1095 cm^{-1} and 558 cm^{-1} confirmed the C=O, C-F and Ti-O bonds, respectively. The appearance of these functional groups also rationalized the increase of the interlayer d-spacing in XRD results. The lack of Ti-Al vibrations at 180, 200 and 270 cm^{-1} and only the presence of Ti-C vibrations at 560 and 606 cm^{-1} in the Raman spectrum of MXene, also confirmed the successful elimination of aluminum layers from the Mxene nanoflakes [25].

Comparison of the XRD spectra of MWCNT with GOnR in Figure 5.3-a revealed that the peak corresponding to the graphitic crystalline structure at 2θ = 26.02° has shifted to a lower 2θ value of 9.95°. This shift indicated an oxidation-induced interlayer d-space expansion, attributed to the partial oxidation and lengthwise opening of the nanotubes through a chemical unzipping process. The oxidation process introduced oxygen containing functional groups such as carboxyl and hydroxyl groups to the edge of the opened nanoribbons. This is confirmed by the presence of a carbonyl stretching vibration bond peak at 1718 cm^{-1} in the FTIR spectrum of GOnR, as shown in Figure 5.3-b, providing evidence for the existence of oxygen functional groups along the edge of the graphene nanoribbons [165,283]. The restoration of graphitic structures in the nanoribbons' aerogel was achieved through annealing at high temperatures, which resulted in the removal of the oxygen-containing functional groups. This phenomenon was confirmed by analyzing the XRD spectrum of rGOnR in Figure 5.3-a, where the characteristic peak corresponding to graphene oxide disappeared, and the intensity of the graphitic peak at 2θ =25.9° increased. Additionally, the carbonyl functional group vibration bond also disappeared, providing further evidence for the reduction of the nanoribbons. The chemical fingerprints of the MWCNT, GOnR and rGOnR were also explored by Raman spectroscopy and exhibited in Figure 5.3-b. The characteristic peaks of carbonaceous materials appeared at 1335, 1580 and 2680 cm^{-1} which were associated with the D, G and 2D modes, respectively. The D peak represents the formation of structural defects on graphitic crystal structure, while G peak is related to

the first order scattering of E_{2g} due to the C–C bond stretching in graphitic carbon. As the oxidation reaction on MWCNT introduces defects and disorders on its sp^2 structure, the structural integrity of the graphitic crystal of carbonaceous material can be adequately quantified by the intensity ratio between D and G peaks. From Figure 5.3-c, MWCNT showed I_D/I_G ratio of 0.982, which indicates lower structural integrity compared to the reported disorder ratio of other graphitic materials such as GnP [284]. This can be attributed to the defects that occurred during the synthesis process [56]. The oxidative unzipping of the nanotubes increased I_D/I_G ratio to 1.01 and 2D peak disappeared. The formation of edge structures in GOnR by the lengthwise opening of the nanotubes is the potential reason for the increase in disorder ratio. Furthermore, the appearance of oxygen containing functional groups also could alter the structural integrity by inducing more sp^3 domains. Thermal reduction slightly increased the I_D/I_G ratio to 1.04 due to the creation of new sp^2 domains which are smaller than the sp^2 domains of GOnR in size yet larger in quantity [285].

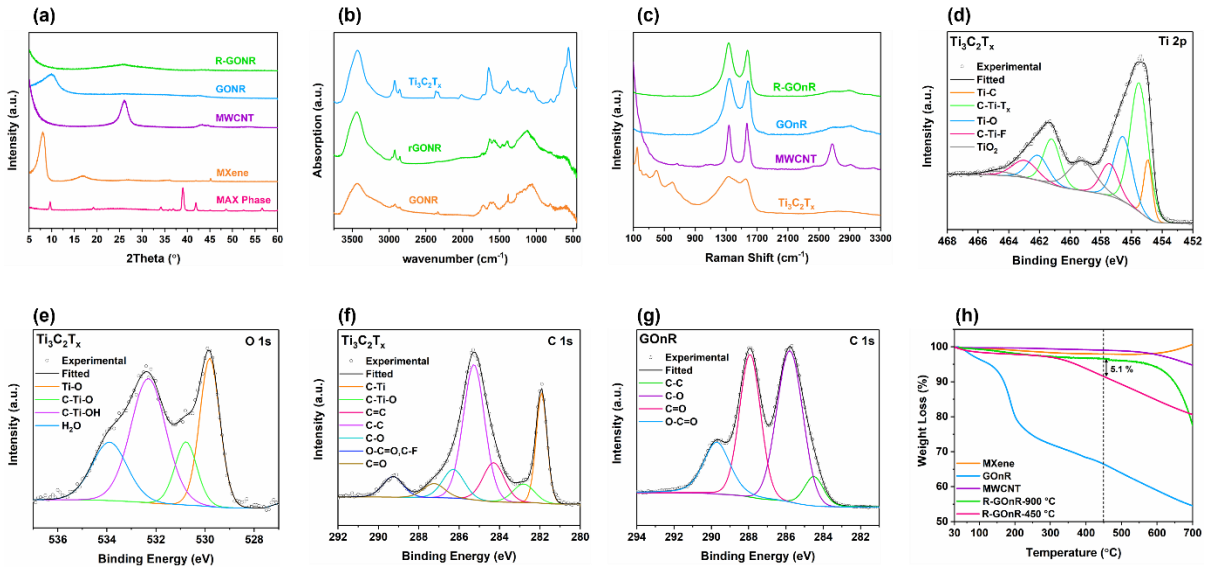

Figure 5.3 (a) XRD, (b) FTIR, (c) Raman and (d-h) XPS spectra of $Ti_3C_2T_x$ MXene, GOnR, rGOnR and their Ti_3AlC_2 MAX phase and MWCNT precursors.

The chemical state and atomic bonding of delaminated $Ti_3C_2T_x$ MXene nanoflakes, oxidized GOnR and its reduced counterpart were thoroughly explored by the X-ray photoelectron spectroscopy (XPS) and illustrated in Figure 5.3-d to g. The importance of XPS analysis is to investigate or even quantify the atomic composition of the nanomaterials [250]. The lack of Al 2s peak in the survey spectrum of $Ti_3C_2T_x$ MXene in Figure 5.9-a verified the successful removal of the aluminum layers from the MAX

precursor [286]. As seen from high resolution Ti 2p XPS spectra in Figure 5.3-d, the peak at binding energy value of 454.9 eV was belong to the Ti-C bond. The peaks at 455.6 and 461.2 eV were attributed respectively to the $2p_{3/2}$ and $2p_{1/2}$ of C-Ti-T_x bonds. The presence of these peaks is due to the formation of $Ti_3C_2O_x$ or $Ti_3C_2(OH)_x$ of Ti_3C_2OH-H_2O. These functional groups are responsible to endow very high hydrophilicity and strong negativity to the MXene nanoflakes [224,287]. The peaks at 456.6 and 462.1 eV were assigned to the Ti-O peaks. The weak intensity of these bonds indicated less amount of nanoflakes' oxidation. C-Ti-F bonds appeared at binding energy values of 457.5 and 463 eV and the peaks at 459.2 and 465 eV were assigned to TiO_2. Figure 5.3-e illustrates the O1s region of the XPS spectrum for MXene nanoflakes. Peaks at binding energy values of 529.8, 530.8, 532.3 and 533.9 eV were corresponded to the Ti-O, C-Ti-O_x, C-Ti-$(OH)_x$ and H_2O bonds, respectively [233]. The C1 s region of the XPS spectrum for MXene nanoflakes was also presented in Figure 5.3-f. In the C1s region, deconvoluted peaks at the binding energy values of 291.9, 282.8, 284.3, 285., 286.3, 287.2 and 289.3 eV were assigned to the Ti-C, C-Ti-O, C=C, C-C, C-O, O-C=O or C-F and C=O bonds, respectively [288]. The successful reduction of nanoribbons during thermal treatment was also studied through comparing the high resolution XPS spectra of C1s regions for GOnR and its reduced rGOnR counterpart. As illustrated in Figure 5.3-g, the peak for C-C bonds appeared at 284.5 eV. The three distinct peaks at 285.8, 287.9 and 289.7 eV were assigned to the C-O, C=O and O-C=O bonds which are indicating the generation of oxygen containing functional groups during chemical unzipping of MWCNTs [289]. However, comparing the TGA analysis of the two reduced GOnRs at 450 °C and 900 °C in Figure 5.3-h showed only 5.1 % different in the weight loss of the two reduced nanoribbons at 450 °C. This indicated that still a small amount of functional groups may exist in nanoribbons reduced at 450 °C. Despite the remaining functional groups may impede nanoribbons to show a high electrical conductivity by full restoration of the sp^2 domains of the graphitic crystal structure, they can play a role in dissipating EM waves by enhancing the polarization relaxations. It is noteworthy to mention that oxidation of MXene occurs after heating above 600 °C due to removal of surface terminations [108]. Hence, subjecting to annealing at 450 °C does not result in the oxidation of MXene, but it could potentially improve electrical conductivity by eliminating the absorbed intercalant water [290,291].

5.4.2 Microstructure of unidirectionally aligned PDMS nanocomposites

The unidirectional freezing and subsequent freeze drying technique for constructing a highly aligned 3D interconnected conductive network are typically controlled by the crystallization behaviour of the

solvent and the interactions between the solvent and all species in the solution. Crystallization is a two step process involving nucleation and growth. The freezing temperature plays a crucial role in determining the final pore sizes of the aerogels. Very low freezing temperature may increase the number of crystal nuclei while suppressing the crystal growth due to an inefficient amount of thermal energy. Sublimation of a large number of small ice crystals results in a smaller pore size in aerogels. Interactions between the species and their chemistry are other important parameters in the formation of a well structured and robust aerogel. For instance, highly oxidized graphene sheets may enhance the dispersion of the sheets in water while it could hinder the construction of a highly interconnected conductive network during the freezing process. It has been reported that partial reduction of graphene oxide leads to the formation of a better network due to reduced repelling forces [292]. The unzipping process of MWCNT partially oxidizes the nanoribbons and provides the privilege to GOnR to be well dispersed in water, along with the capabilities of constructing a robust 3D conductive network.

Figure 5.4 illustrates both the top and side view SEM images of rGOnR/MX aerogel based PDMS nanocomposites. As it is unambiguous from Figure 5.4, all the micro pores of the aerogels were fully filled after impregnation with PDMS and there are not any remaining pores in the nanocomposites that may act as stress concentration points and impact the mechanical properties of the final nanocomposites. Moreover, the lack of obvious interfacial cracks between the interconnected 3D aerogel networks and the PDMS matrix suggested proper interfacial adhesion. The cross-sectional SEM images from the top view of the nanocomposites in Figure 5.4 demonstrated a well distributed and interconnected networks of the rGOnR/MX hybrids, indicating a good mechanical strength of the aerogels, and the impregnation process did not compromise the 3D conductive network [293]. The lateral cross sectional SEM images of the nanocomposites clearly indicated that the highly aligned rGOnR/MX nanosheets were evenly dispersed with a particular orientation relative to the direction of the freezing [268]. These images demonstrated that the infiltrating PDMS in rGOnR/MX aerogel is an effective engineering technique for constructing polymer nanocomposites that retain the original conductive filler network without compromising it, leading to a high level of dispersion and electrical conductivity even at low filler loadings [289].

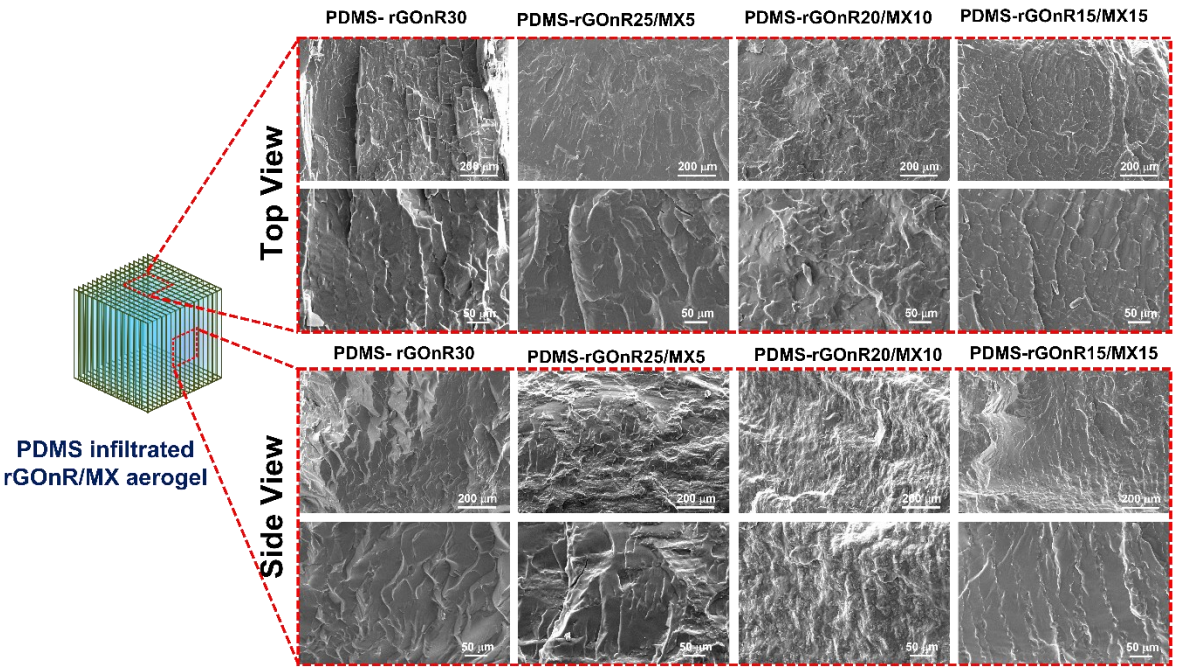

Figure 5.4 SEM images from the top and side view of the PDMS infiltrated rGOnR/MX aerogels

5.4.3 Electrical conductivity of nanocomposites

Broadband through-plane electrical conductivity of the rGOnR/MX aerogel based PDMS nanocomposites across the frequency range of 1 to 10^5 Hz are shown in Figure 5.5-a. The alternative current (AC) conductivity can be represented as a combination of a frequency-independent and a strongly frequency-dependent part. This conductivity can be expressed by $\sigma = \sigma_{DC} + \sigma_{AC}$, where σ_{DC} represents the frequency-independent part and σ_{AC} indicates the frequency-dependent part of the total electrical conductivity. An entirely frequency-dependent capacitive electrical conductivity is a typical characteristic of an insulative polymer nanocomposite. This behaviour is indicating that the conductive material loading in polymer nanocomposite is not enough to create a connected conductive network. When the content of the conductive material reaches the percolation threshold, the AC conductivity starts to show a frequency-independent behaviour at a critical frequency (f_c). The electrical charges applied by an external electrode will transport (as indicated by the frequency-independent behaviour) and build up (as indicated by the frequency-dependent behaviour) in the vicinity of the interfaces of various phases. This is due to the charge transportation capabilities of the conductive phase, the charge storage features of the ferroelectric phase and the various relaxation times for each of the phases [294].

As illustrated in Figure 5.5-a, through-plane electrical conductivity of rGOnR/MX aerogel based PDMS nanocomposites showed a frequency-independent behaviour in the whole frequency range. This is because of the presence of a 3D interconnected conductive nanomaterials network which has been constructed through unidirectional freezing and freeze drying process at a very low loadings. Such an interconnected conductive network would be able to transfer electrons without charge accumulations in the interfaces of different phases. Linear sweep voltammetry of the PDMS nanocomposites was also measured and exhibited in Figure 5.5-b. DC electrical conductivity of the nanocomposites calculated using $\sigma_{DC} = \frac{t}{R \times A}$, where t is the sample thickness, R is the resistivity and equals to the slope of V-I curve in Figure 5.5-b, and A is the sample's surface area. The electrical conductivity of nanocomposites showed an increasing trend with the addition of MXene nanoflakes in the structure of the aerogels, Figure 5.5-c,. The electrical conductivity of rGOnR30-PDMS nanocomposite showed 2.14×10^{-3} S/cm while hybridizing of rGOnR with 50 % of MXene nanoflakes enhanced the electrical conductivity to 1.90×10^{-2} S/cm. The higher electrical conductivity of the rGOnR15/MX15-PDMS nanocomposites was attributed to the synergistic effect of both graphene nanoribbons and MXene nanoflakes. Mxene improves electrical conductivity due to its higher intrinsic electrical conductivity and relatively larger particle size which leads to reduced contact resistance. On the other hand, graphene nanoribbons can bridge between the adjacent MXene nanoflakes, create a path to transfer charges between the MXene nanoflakes and subsequently reduce their intrinsically low intra-flake resistivity [289,295]. It was not surprising that the extracted DC electrical conductivity (σ_{DC}) values at the frequency of 1 Hz from the broadband electrical conductivity measurements were comparable to ones obtained from the linear sweep voltammetry, Table 5.1.

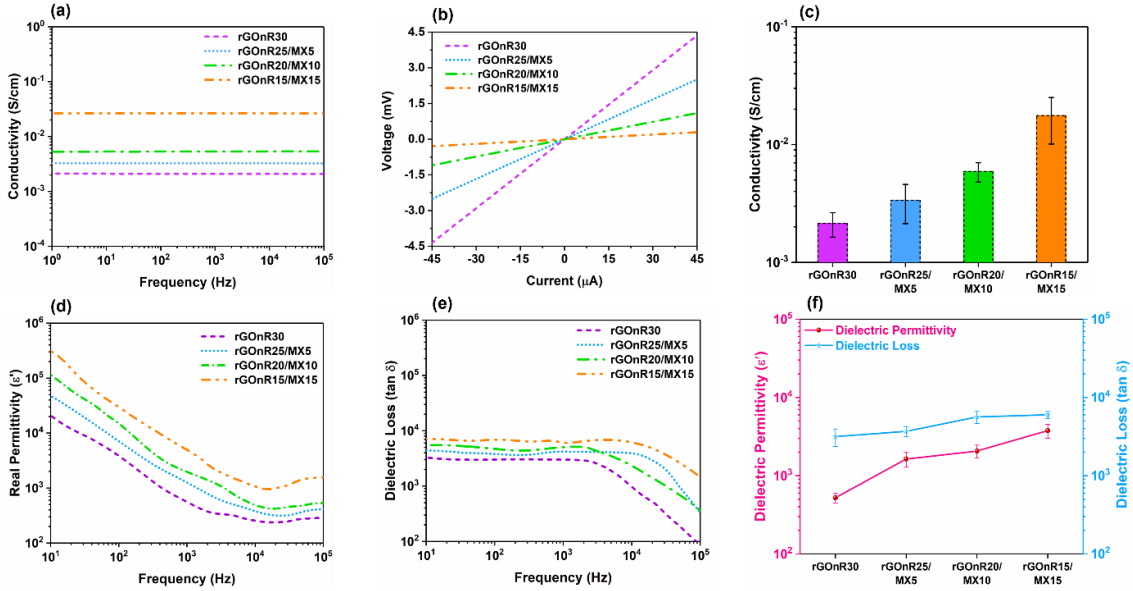

Figure 5.5 (a) Broad band electrical conductivity, (b) linear sweep voltammetry, (c) DC electrical conductivity, (d) real permittivity, (e) dielectric loss, and (f) comparison of dielectric properties at the frequency of 10^3 Hz for rGOnR/MX aerogel based PDMS nanocomposites

The frequency-dependent dielectric properties of the nanocomposites were also shown in Figure 5.5-d and e. The dielectric permittivity has a complex form, composed of a real part, ε', and an imaginary part, ε'' as shown below equation.

$$\boldsymbol{\varepsilon(\omega) = \varepsilon'(\omega) - i\,\varepsilon''(\omega)} \qquad \textbf{5.7}$$

where $\omega = 2\pi f$ is the angular frequency, ε'(ω) is the real part of permittivity and ε''(ω) is the imaginary part of the dielectric permittivity. The former pertains to the displacement of charge, which is controlled by the polarization within the material. A typical kind of polarization that takes place across frequencies of less than 1 MHz is interfacial polarization. This is based on the Maxwell–Wagner–Sillars (MWS) effect, which leads to the accumulation of charges at the polymer-filler interfaces due to their differences in relaxation times. The imaginary part of the dielectric permittivity (ε'') is used to calculate the dielectric loss ($tan\delta = \frac{\varepsilon''}{\varepsilon'}$), which is expressed as the ratio of ε'' to ε', and arises from ohmic loss, polarization loss and dipole movements. As illustrated in Figure 5.5-d, with increasing the content of MXene in the nanocomposites, the real permittivity increased and the critical frequency where the real permittivity starts to behave more frequency dependent shifted to higher values. When comparing the real permittivity at 1 KHz between the nanocomposites (Figure 5.5-f), it is clearly seen that increasing

the content of MXene in hybridized rGOnR/MX aerogels increased the real permittivity. For instance, the dielectric permittivity of the rGOnR30-PDMS nanocomposite was 522.78, while hybridizing rGOnR with 50% of MXene in the same nanocomposite soared the real permittivity to 3765.65. This could be attributed to the interfacial polarizations between polymer matrix and conductive nanomaterials (at frequency range of 10^{-6} to 1 Hz), nanomaterials' polarization which occur within the defects and disorders of rGOnR and MXene layers (at frequencies of >1 Hz), and dipole polarization of the dielectric PDMS matrix at higher frequencies [80]. In essence, the rGOnR/MX-PDMS nanocomposites can be considered as myriad nanoscale parallel plate capacitors, where the conductive rGOnR/MX nanoflakes are nanoelectrodes and the PDMS matrix is nanodielectric material [252]. The locally build up electric field in nanocapacitors is much higher than the applied external electric field and further intensified with increase in the nanoflakes' size and decrease in the thickness of confined PDMS matrix [296]. These local and strong electric fields causes charge polarization in PDMS matrix and contribute in increasing the real permittivity. As illustrated in Figure 5.5-d, the real part of the permittivity decreased with increasing frequency because of the reduced dipoles' mobility at higher frequencies. When the frequency of the applied electric field exceeds the relaxation frequency, the dipoles are not sufficiently mobile to displace [294]. Figure 5.5-e shows that an increase in MXene content in the hybrid nanocomposites leads to higher dielectric loss values with more frequency dependent behavior. This highly likely pertains to the enlarged ohmic loss and relaxation polarization loss [297]. The former arises from the higher conductivity of the MXene nanoflakes, which improves the charge carrying capability and dissipates electrical energy, especially at low frequencies. The latter is attributed to the abundant number of nanocapacitors and materials' functional groups, defects and disorders where the relaxation of induced molecular dipoles by locally built up EM fields occur [202,252]. At higher frequencies, the molecular dipoles are unable to rotate in the alternating electric field and absorb the energy by overcoming the momentum that suppresses the reorientation of dipoles [202]. The decrease of the ohmic loss with frequency can also been explained by the incapability of charge carriers to efficiently traverse through the conductive network in each half cycle of alternating electric field due to the shorter time frames [296]. Figure 5.5-f exhibits the variation of the dielectric loss as a function of increasing MXene content in the rGOnR/MX hybrid at a frequency of 1 KHz. The dielectric loss values increased as the content of MXene increased in the hybrid nanocomposites, consistent with the trend observed in electrical conductivity. This relationship is governed by the equation $tan\delta = \frac{\sigma}{2\pi f \varepsilon_0 \varepsilon'}$ which relates dielectric loss to electrical conductivity [298]. The dielectric

loss of the conductive polymer nanocomposites dramatically increases when the content of the fillers reached its percolation threshold. After percolation, the sufficient current leakage can lead to a transition from non ohmic to ohmic loss.

5.4.4 EMI shielding effectiveness of nanocomposites

Theoretically, electrical conductivity is the controlling factor of the EMI SE and impedance matching between the materials and the EM wave propagating media. There is a trade off between surface electrical conductivity of the shielding material and its impedance matching with the EM wave propagating media. An increase in the electrical conductivity could improve the EMI SE by conduction loss. However, very high electrical conductivity results in high EM wave reflection due to the impedance mismatch which is unfavored due to the potential secondary interferences [279]. For example, as illustrated in Figure 5.10, a thin sheet of MXene with 10 μm thickness showed an extremely high electrical conductivity of 5485.8 S/cm at room temperature. Such an excellent electrical conductivity resulted in a very high average total EMI SE of 39.82 dB with an almost equal contributions of SE_R and SE_A of 19.5 dB, Figure 5.6-a. This indicates that about 99.9% of the incident EM waves were shielded. However, the abundant free electrons directly interact with the incident EM waves and dissipate the radiation power by reflection [269]. As illustrated in Figure 5.6-b, the reflection coefficient of the MXene sheet is nearly one which means more than 98.9% of the incident EM waves were reflected from the surface of the MXene sheet before entering the sample. This high reflection shielding mechanism of the MXene sheet was attributed to the impedance mismatch between the highly conductive MXene sheet and air. Tuning the impedance mismatch between the media and the shielding material could be a promising approach to enhance the absorption shielding mechanism. Although, carbon based polymer nanocomposites can show absorption dominancy to some extent with their electric dipoles and turn the EM energy to heat [101,269], obtaining high SE values for these materials is hardly possible due to low electrical conductivity and EM wave dissipation capability [282]. Figure 5.6-c exhibits the thickness dependency of the average EMI SE of the rGOnR/MX aerogel based PDMS nanocomposites in the P-band frequency range. As it is expected from Simon's formula [108], EMI SE of the nanocomposites increased with an increase in the specimen thickness. Furthermore, there was a slight increase in the EMI shielding performance of the nanocomposites with increasing of MXene concentration in 3D constructed aerogels. For instance, rGOnR30-PDMS nanocomposite showed an average EMI SE of 2.95 dB at 1.5 mm thickness, while EMI SE of rGOnR15/MX15 hybrids increased

to 4 dB in the same nanocomposite thickness. This is in good agreement with the enhanced electrical conductivity of the aerogels by increasing of MXene concentration in the hybrid aerogels, as discussed in Figure 5.5-c. Figure 5.6-d to g illustrate the portion of reflection (R), transmission (T) and absorption (A) of the incident EM waves as a function of thickness. All rGOnR/MX aerogel based PDMS nanocomposites showed a significant dependency of power coefficients on the thickness of the hybrid nanocomposites. A-value increased with increasing of the nanocomposite thickness and then reached a plateau. The results presented in Figure 5.11 indicated that the nanocomposites exhibited a noteworthy level of T-value, ranging from 15% to 35%. Notably, the T-value decreased as the nanocomposites' thickness increased from 1.5 mm to 6.5 mm. This observation can be attributed to the parallel orientation of the conductive rGOnR/MX nanoflakes with respect to the propagating EM wave. Specifically, the rGOnR or MXene in the nanocomposite form channels or gaps between adjacent flakes, which are filled with non-conductive PDMS matrix. As a result, the EM wave can pass through these gaps with minimal attenuation or scattering, leading to a significant T-value in the nanocomposite. Figure 5.6-h showed that the R-value experienced an increasing trend until it reached a peak value, then decreased with thickness to a trough value and then slightly increased again to reach a plateau. The peak and trough R-values can be explained by the multi-reflection and phase cancellation of the EM waves within the shielding nanocomposite. When the EM waves encounter the surface of the shielding material, a portion of the wave is reflected due to the impedance mismatch between the material and the air. As the wave propagates within the material, it undergoes multiple reflections from various interfaces, leading to constructive and destructive interference patterns, depending on the thickness and composition of the material. These interference patterns ultimately result in the formation of peaks and troughs in the reflection coefficient [299]. The peak R-values increased by the hybridization of rGOnR with MXene nanoflakes. This increase in the R-values was attributed to the enhanced electrical conductivity and dielectric permittivity of the hybridized nanocomposites, which led to a significant impedance mismatch and then resulted in higher EM wave reflection. Figure 5.6-i exhibited the thickness dependence of the absorption/reflection (A/R) ratio for rGOnR/MX based PDMS nanocomposites. It is found that the lowest A/R ratio occurs at a thickness in which the R-value experienced a peak. By increase in thickness, the A/R ratio increased to an optimum value which corresponds to the trough R-value. Afterward, increasing the thickness slightly reduced the A/R ratio and thus reached a plateau [279]. Generally, if the A/R ratio is higher, the surface impedance matching is improved and more of the incident EM waves will be dissipated due to dielectric loss. If the A/R

ratio is greater than one, absorption-dominant EMI shielding behavior is obtained and most of the incident EM waves are absorbed instead of being reflected back into the environment. Therefore, it can be inferred that all the rGOnR/MX aerogel based PDMS nanocomposites demonstrated absorption dominant shielding mechanism across a range of thicknesses from 1.5 to 6.5 mm, yet lower total shielding performance, Figure 5.12.

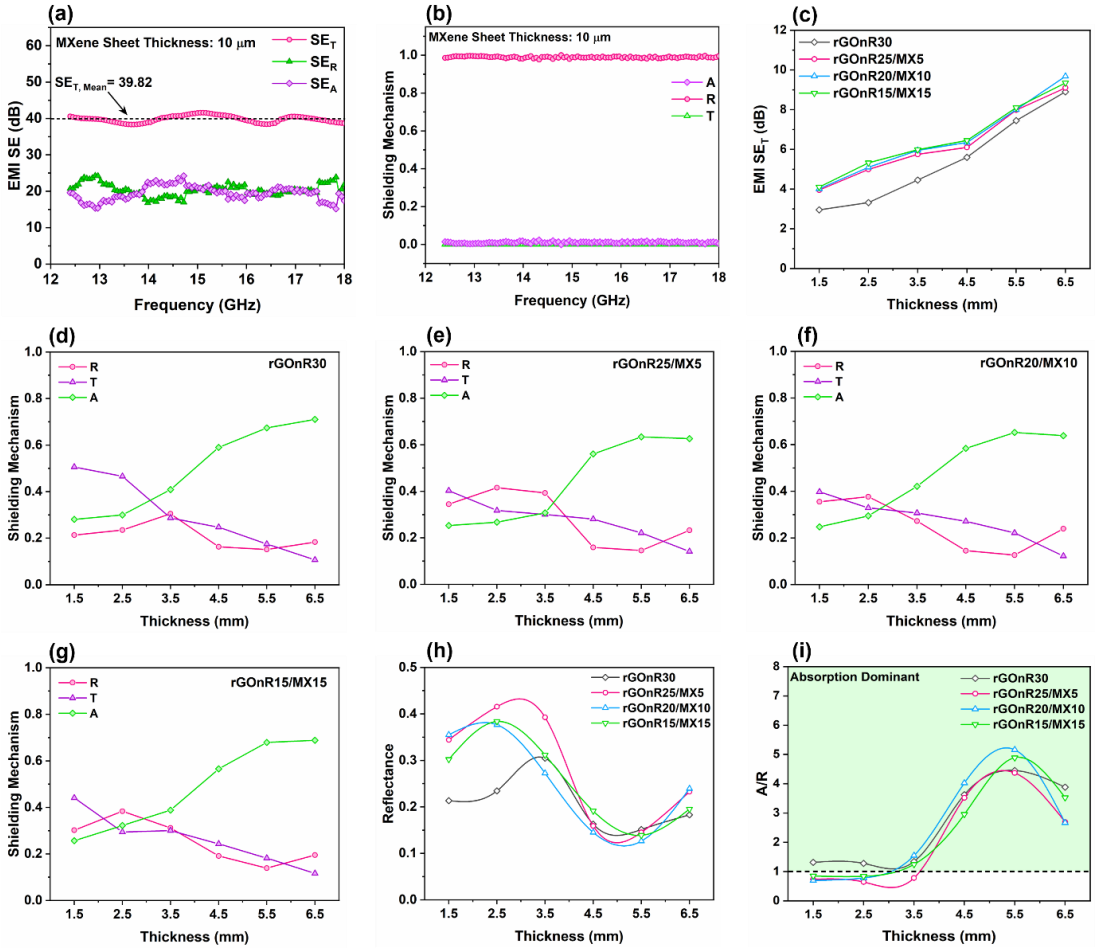

Figure 5.6 (a) EMI SE of a 10 μm thin MXene sheet in the P-band frequency range, (b) A-, T-, and R-values of MXene sheet, (c) average EMI SE of the rGOnR/MX aerogel based PDMS nanocomposites as a function of the specimen thickness, (d-g) A-, T-, and R-values of rGOnR/MX aerogel based PDMS nanocomposites, (h) average R-values of rGOnR/MX aerogel based PDMS nanocomposites as a function of thickness and (i) A/R ratio of rGOnR/MX aerogel based PDMS based nanocomposites

To explore the influence of rGOnR/MX-PDMS nanocomposites, which exhibited an absorption-dominant shielding mechanism, on enhancing total SE_T and transitioning the shielding mechanism from reflection-dominant to absorption-dominant in thin MXene layers, a 10 μm MXene sheet coated on rGOnR/MX-PDMS nanocomposite and evaluated for shielding performance. Figure 5.7-a illustrates the average total SE_T of the coated rGOnR/MX-PDMS nanocomposites as a function of their thickness. Similar to the uncoated rGOnR/MX-PDMS nanocomposites, the SE_T of the coated nanocomposites increased with thickness. Furthermore, hybridizing rGOnR aerogel with MXene nanoflakes further improved the total shielding performance of the coated nanocomposites possibly due to the higher electrical conductivity and dielectric permittivity devoted by the MXene nanoflakes. Interestingly, the EMI SE of the coated nanocomposites outperformed that of the MXene layer, with values ranging from 51.8 to 60.6 dB over the nanocomposites' thickness, indicating the synergistic effect of the nanocomposites in enhancing the EMI shielding of the thin MXene layer. For instance, the SE_T obtained for coated rGOnR15/MX15-PDMS nanocomposite at 1.5 mm thickness was 53.5 dB, while the individual SE_T of rGOnR15/MX15-PDMS nanocomposite and 10 μm MXene sheet were 4.1 and 39.82 dB, respectively. The average total, reflection and absorption SE of the coated nanocomposites as a function of sample thickness are presented in Figure 5.12. Absorption dominant shielding effectiveness is obtained when SE_R is less than 3.1 dB, which is associated with the absorption of more than 50% of the incident EM waves [269]. The rGOnR30-PDMS nanocomposite showed absorption dominance at a sample thickness of 3.5 mm (green area). On the other hand, the hybridization of this material with MXene resulted in a reduction of the critical thickness of absorption dominance to 2.5 mm for rGOnR25/MX5-PDMS and rGOnR20/MX10-PDMS, and 1.5 mm for rGOnR15/MX15-PDMS nanocomposites. Figure 5.7-b to e show the shielding mechanism of the coated nanocomposites based on A-, T- and R-values. The A-values throughout the sample thickness increased with increasing the concentration of MXene in hybridized nanocomposites. For instance, increasing the MXene concentration in aerogels from 0 to 16.7, 33.3 and 50% decreased R-value from 0.85 to 0.71, 0.55 and 0.48, respectively, at 1.5 mm of nanocomposite. It is worth noting that the hybridization of rGOnR with 50% Mxene resulted in an absorption-dominant coated nanocomposite across the entire thickness range of 1.5 to 6.5 mm, Figure 5.7-g. It is interesting that the coating of the nanocomposites with MXene layer diminished the portion of transmitted radiation power to nearly zero compared to the 15-35% of transmitted waves in uncoated nanocomposites shown in Figure 5.11. This is because of nearly zero (~0.01%) transmission radiation power of the MXene layer that reflects all the EM waves which passed

through the nanocomposite. Comparing the reflection and absorption values of the incident EM waves for coated rGOnR30-PDMS nanocomposite throughout the thickness in Figure 5.7-b revealed that the absorption coefficient is much lower than that of reflection at thickness below 3.5 mm, indicating the reflection dominant shielding mechanism. At 3.5 mm thickness, the absorption coefficient showed a peak A-value of 0.80 and then decreased to 0.67 and lastly slightly raised again across the sample thickness. A similar behaviour was observed for the coated hybridized rGOnR/MX-PDMS nanocomposites. However, the reflection to absorption dominant transition not only occurred at a lower thickness of 2.5 mm, also the peak A-value reached to 0.87, Figure 5.7-c to e. In addition to the multi-reflection and phase cancellation effect discussed earlier, the multi-reflected EM waves from the internal surfaces can interfere with the incident EM waves. This interference is due to the presence of a $\pi/2$ phase shift between the incident wave and the internal multi-reflected waves [300]. Through tuning the shielding material thickness, the above mentioned interference could either be weakened or intensified. The former results in the trough R-value and the latter leads to a peak A-value. The results clearly revealed that the hybridization led to lower trough R-values occurring at lower nanocomposite thickness than in the non-hybridized rGOnR-PDMS nanocomposite, Figure 5.7-f. This can be explained by the tuned surface impedance matching between the nanocomposite and air, which allows a significant portion of the incident EM waves to penetrate the material, resulting in a stronger effect of wave interference between surface reflection and rear-interface multiple reflections. Figure 5.7-g shows the A/R ratio of the coated nanocomposites at different thicknesses. The highest A/R ratio was obtained at the thickness corresponding to the trough R-value. The hybridized coated rGOnR15/MX15-PDMS nanocomposite demonstrated a significantly higher A/R ratio of approximately 7 at a lower thickness of 2.5 mm, while the non-hybridized rGOnR30-PDMS nanocomposite only reached an A/R ratio of 4 at a higher thickness of 3.5 mm. As the thickness of the nanocomposite increased, the A/R ratio decreased and reached its minimum value at thicknesses corresponding to the peak R-value. This observation further emphasizes the importance of tuning the thickness of the shielding material to achieve optimal surface impedance matching, high A/R ratio, and absorption-dominant shielding.

The schematic presented in Figure 5.7-h illustrates the mechanism behind EM wave dissipation for the MXene coated rGOnR/MX-PDMS nanocomposite developed in this study. The 3D interconnected conductive network with aligned nanomaterials parallel to the propagating direction of the EM wave optimizes the number of surface charge carriers and dielectric permittivity, which reduces the impedance mismatch. The reduced impedance mismatch allows the incident EM waves to penetrate the

nanocomposite instead of being reflected from the surface. The penetrating EM waves are then attenuated by various dissipation mechanisms, such as i) ohmic loss by travelling electrons in the 3D conductive network, ii) inter-flake electron hopping among the assembled rGOnR/MXene nanomaterials [108], and iii) interfacial and dipolar polarizations occurring at different interfaces that possess different relaxation times, such as interfaces between nanomaterials and PDMS, nano/micro capacitor-like structures, and nanomaterials' functional groups, defects, and disorders. Furthermore, a well-distributed 3D conductive network of nanomaterials can efficiently extend the EM wave propagating path and dissipate the radiation wave energy via internal reflections and multiple scattering. The remaining EM waves that reach the highly conductive MXene layer are being fully shielded and reflected due to the large impedance mismatch. The reflected waves are then propagated back into the 3D conductive network and at an optimized thickness being fully dissipated by the contribution of all the above-mentioned mechanisms and the wave interference effect originated from the $\pi/2$ phase shift between the incident EM wave and wave reflected from the surface.

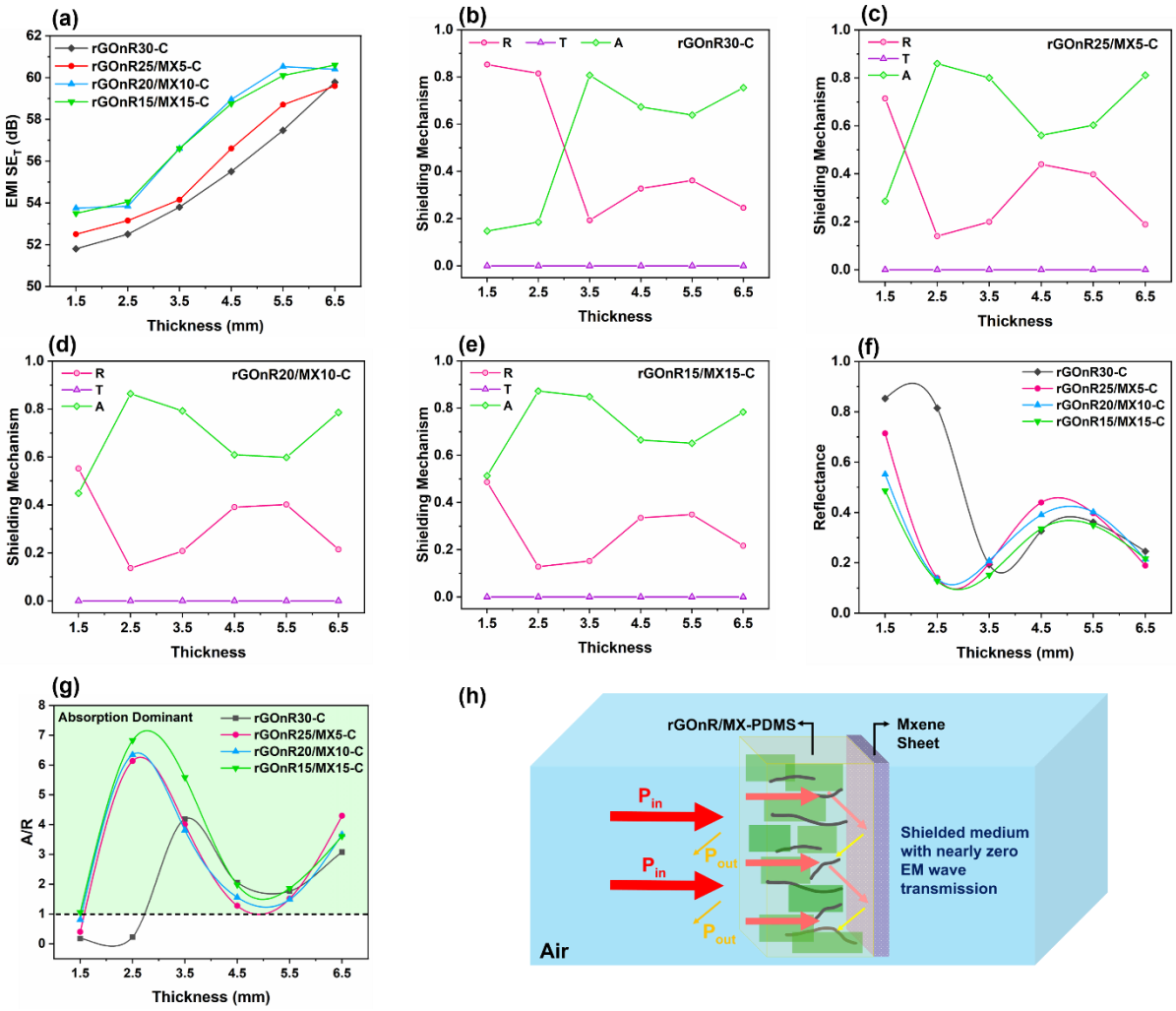

Figure 5.7 (a) average EMI SE of the rGOnR/MX aerogel based PDMS nanocomposites coated with 10 μm MXene sheet as a function of the specimen thickness, (b-e) A-, T-, and R-values of coated rGOnR/MX aerogel based PDMS nanocomposites, (f) average R-values of coated rGOnR/MX-PDMS nanocomposites as a function of thickness and (g) A/R ratio of coated rGOnR/MX-PDMS nanocomposites, and (h) schematic of impedance sections in series

5.5 Conclusions

Herein, semi-2D long strips of graphene nanoribbons and large and low defect 2D MXene nanoflakes were successfully synthesized via oxidative chemical unzipping of carbon nanotube and MILD method, respectively. Taking advantage of the freeze casting method, 3D percolated conductive networks of

rGOnR/MX aerogels were fabricated and then impregnated with PDMS to obtain a conductive rGOnR/MX-PDMS nanocomposite with very low loadings of 1.5 vol%. Hybridization of rGOnR with MXene enhanced electrical conductivity and dielectric properties of the nanocomposites due to the higher intrinsic metallic conductivity and abundant surface functional groups of the MXene nanoflakes. The PDMS nanocomposites were used as an absorbent layer to change the reflective dominant shielding mechanism of a highly conductive MXene sheet to absorption dominant shielding material. The PDMS nanocomposite not only enhanced the absorption coefficient of the shielded EM waves, also synergistically enhanced the total shielding performance of the coated nanocomposites. Hybridization of rGOnR with MXene decreased the minimum required thickness for absorption dominancy to 2.5 mm. These were attributed to i) a tuned impedance mismatch between the media and shielding material, ii) an efficient conduction loss by interfacial polarizations arising from the abundant surface functional groups of MXene and iii) multiple reflections occurred between the interfaces of the nanoflakes in the nanocomposite and MXene sheet-nanocomposite itself. This study demonstrated how rGOnR/MXene hybridization along with engineering design can dramatically enhance the EMI shielding performance of the conductive layer and change the shielding mechanism from a highly reflective to ultra high absorption mechanism.

5.6 Supporting information

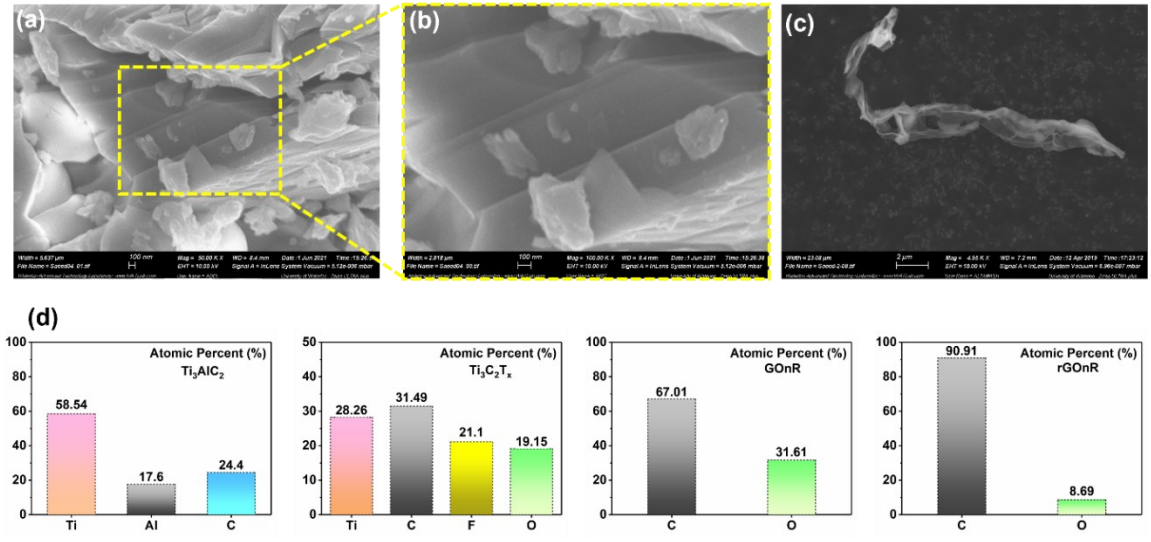

Figure 5.8 (a-b) High magnification FE-SEM images of Ti_3AlC_2 MAX phase, (c) isolated long and exfoliated GOnR, and (d) EDS analysis of the synthesized nano particles

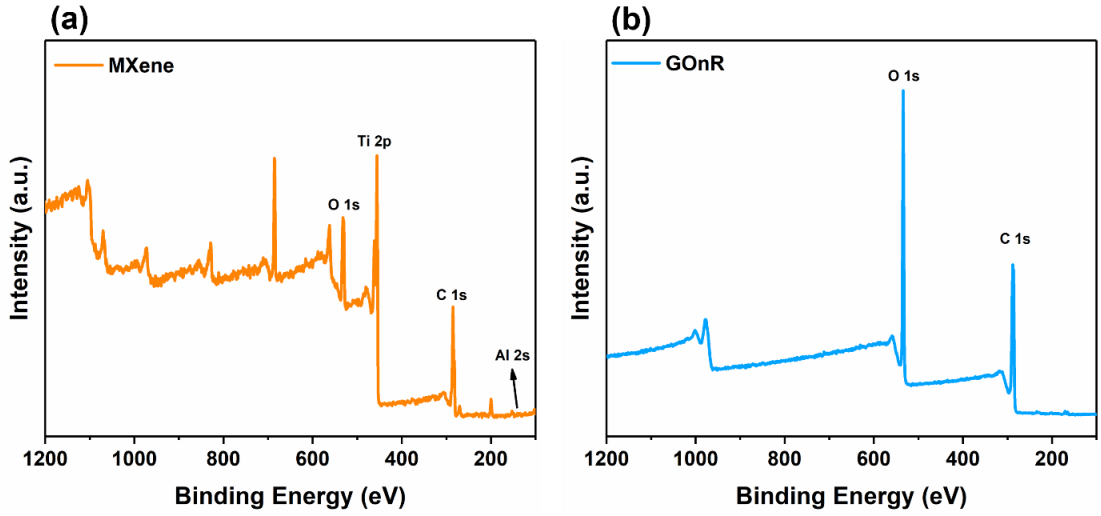

Figure 5.9 XPS survey of (a) MXene, (b) GOnR, and (c) rGOnR

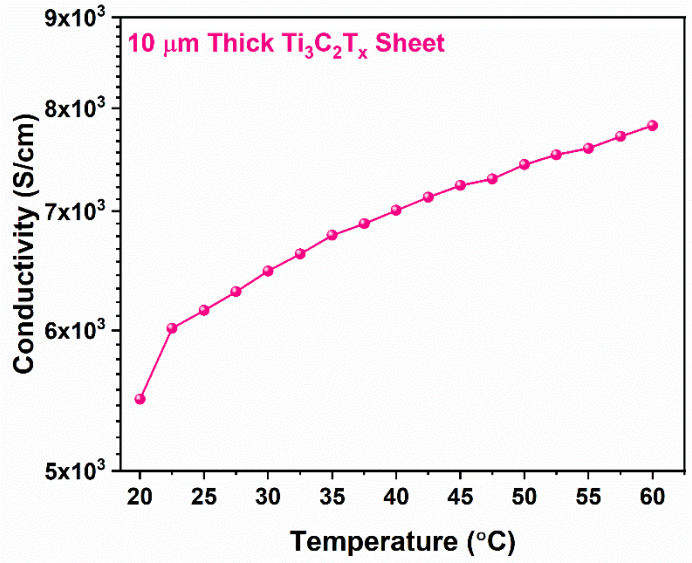

Figure 5.10 In-plane electrical conductivity of a 10 μm thick $Ti_3C_2T_x$ MXene sheet as a function of temperature

Table 5.1 Extracted DC conductivity at the frequency of 1 Hz from the broadband conductivity measurement and calculated DC conductivity using LSV technique.

Through Plane Conductivity (S/cm)		
Samples	**DC Conductivity**	**AC Conductivity at 1 Hz**
rGONR30-PDMS	2.14×10^{-3}	2.10×10^{-3}
rGONR25-MX5-PDMS	3.36×10^{-3}	3.27×10^{-3}
rGONR20-MX10-PDMS	5.91×10^{-3}	5.30×10^{-3}
rGONR15-MX15-PDMS	1.90×10^{-2}	2.04×10^{-2}

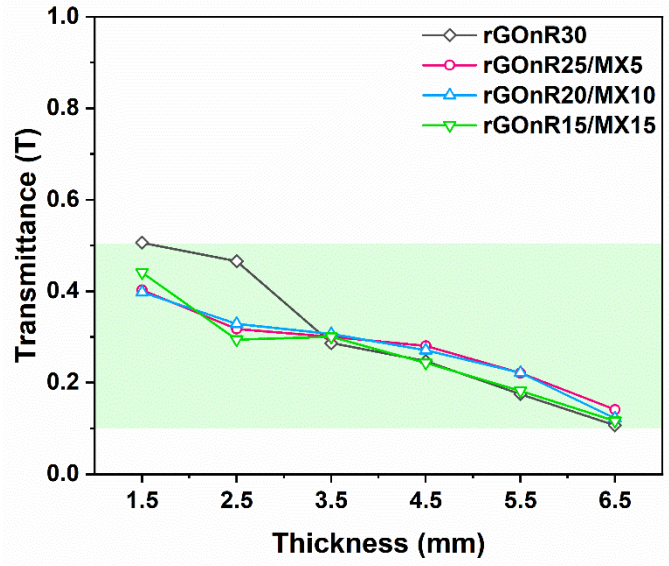

Figure 5.11 T-value of rGOnR/MX aerogel based PDMS nanocomposites

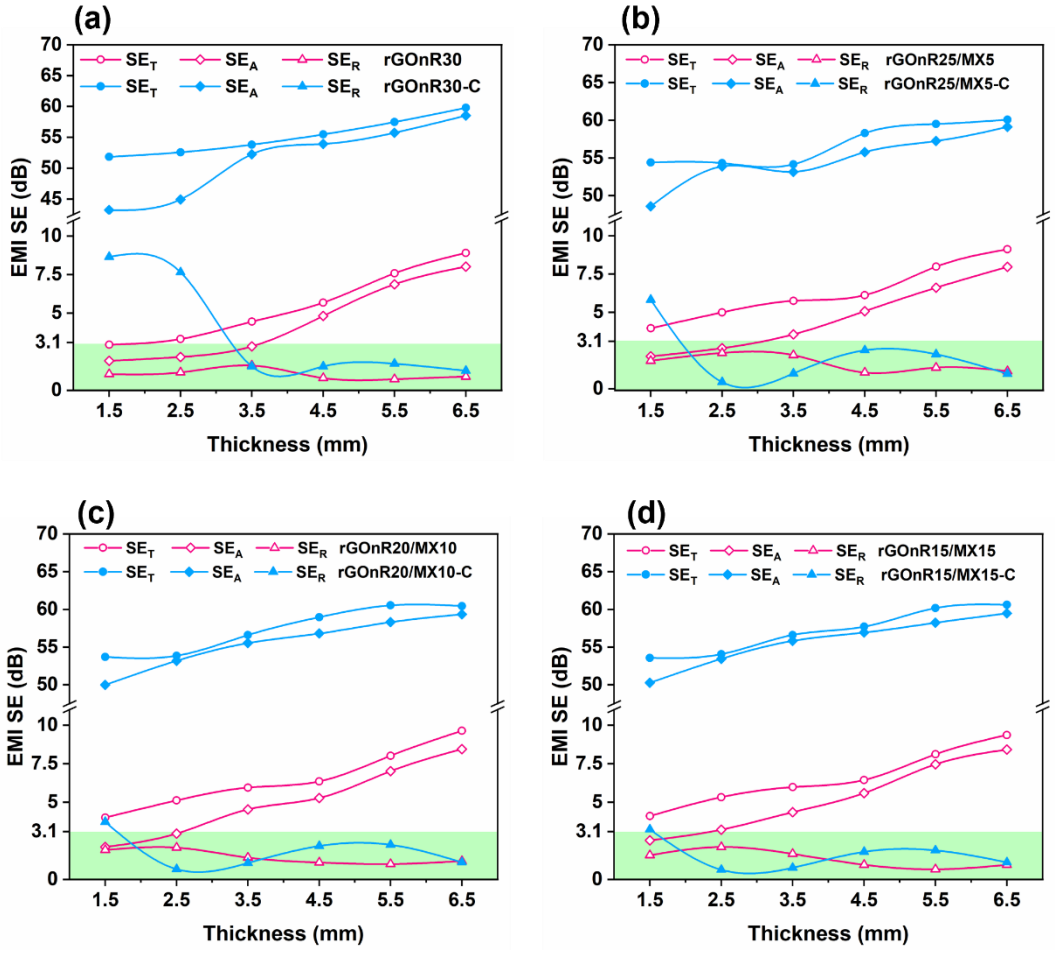

Figure 5.12 Average total EMI SE of the uncoated and coated nanocomposites versus sample thickness for (a) rGOnR30-PDMS, (b) rGOnR25/MX5-PDMS, (c) rGOnR20/MX10-PDMS, (d) rGOnR15/MX15-PDMS

Chapter 6
Conclusions and Recommendations

6.1 Conclusions

Thanks to their lightweight nature, high chemical resistance, and easy processability, polymers have demonstrated significant potential as a fundamental component of highly desirable advanced functional materials. Various types of polymer matrices are combined with a wide range of conductive nanomaterials for utilization in applications such as miniaturized electronic devices, EMI shielding, and energy storage involving dielectric materials. The objective of this Ph.D. research was to produce highly efficient EMI shielding materials by developing electrically conductive polymer nanocomposites. This work was divided into three parts:

- The synthesis of conductive graphene nanoribbons (GNRs) from their parent MWCNTs. The electrical properties and EMI SE of TPU based nanocomposites were investigated.
- The synthesis of $Ti_3C_2T_x$ MXene nanoflakes, followed by surface modification with conductive polyaniline nanofibers. The effect of surface modification on enhancing the EMI SE and EM wave absorption coefficient of PVDF based nanocomposites was examined.
- Hybridization of the synthesized nanomaterials from the first two parts of the thesis and investigation of the impact of nanomaterial hybridization, nanocomposite thickness, and engineering design on enhancing the EMI SE and absorption shielding coefficient of a PDMS based CPnC.

The detailed achievements of these three studies are presented below:

In part 1, GNRs were synthesized by chemically unzipping MWCNTs using the method developed by James Tour. The synthesis parameters were carefully optimized. TPU based CPnCs with varying nanomaterial loadings were prepared through the solution blending method. The impact of the geometrical alteration of MWCNTs on the electrical conductivity, dielectric properties, EMI shielding, and mechanical performance of the nanocomposites was investigated. The geometric alteration of graphene exhibited a significant effect on enhancing the electrical conductivity and dielectric properties of TPU-based CPnCs. This enhancement can be attributed to the formation of a more conductive network, resulting from an increased number density of nanofillers and a larger surface area of GNRs. Compared to the MWCNT nanocomposite, the GNR nanocomposite demonstrated superior electrical

conductivity and dielectric properties, leading to an EMI shielding effectiveness of 24.9 dB (shielding 99% of incident EM waves) as opposed to 9.3 dB. The enhanced shielding properties of the GNR nanocomposite can be attributed to the geometrical transformation of the nanofillers' contact interfaces from line-to-line to sheet-to-sheet, which facilitated the formation of a robust percolating network. Additionally, the geometrical conversion of MWCNTs to GNRs improved the mechanical performance of the nanocomposites, primarily due to stronger interactions between the polymer and the fillers. These stronger interactions in the GNR nanocomposite can be attributed to:

- The increased surface area of GNRs resulting from the unzipping and exfoliation of the nanotubes,
- The presence of numerous edge structures in GNRs after unzipping, which promote polymer-filler interactions,
- The ability of the polymer chains to lie flat on the planar surface of GNRs instead of wrapping around the smooth surfaces of MWCNTs.

In part 2, CPnCs were developed using MXene, a newly discovered 2D nanomaterial, to further enhance the EMI shielding effectiveness. Additionally, the study aimed to gain a deeper understanding of the impact of surface modification on the shielding mechanism of CPnCs. To achieve these goals, $Ti_3C_2T_x$ MXene nanoflakes were synthesized using the MILD method. The abundant surface functional groups of MXene were modified by grafting conductive polyaniline nanofibers through oxidative-free oxidation polymerization method. Remarkable EMI shielding performance (38.84 dB) was achieved after the surface modification of MXene. Furthermore, the investigation of the shielding mechanism of PVDF-based nanocomposites revealed that the modification of MXene increased the percentage contribution of the absorption shielding mechanism. Three reasons were proposed to explain the enhancement of EMI shielding in PVDF-based CPnCs:

- Exfoliation of MXene nanoflakes through the intercalation of polyaniline nanofibers between inter-gallery spaces.
- Formation of numerous capacitor-like structures at the interfaces between PVDF chains and nanomaterials, especially after an increase in specific surface area with polyaniline modification. These nano/microstructures contribute to EMI shielding through interfacial polarization loss.

- Contribution of polyaniline conducting chains in the electron transfer mechanisms and their response to the EM field.

The surface modification of MXene was found to improve the mechanical properties of CPnCs. This improvement attributed to the exfoliation of nanomaterials and their proper dispersion, which results in better load transfer between the matrix and reinforcing nanomaterials.

In order to enhance the efficiency of EMI shielding and ensure that the absorption-driven mechanism contributes to more than 50% of the shielding process, we have developed the third part of our thesis. In this part, we employed the freeze casting method to create a 3D interconnected conductive network by hybridizing rGOnR and MXene nanomaterials. The resulting aerogels were impregnated with PDMS to form CPnCs at low loadings. It is understood that the hybridization of nanomaterial is a promising approach for enhancing the intended properties of the CPnCs. To further optimize the design, the CPnCs were coated with a thin layer of MXene film (10 μm). The MXene layer, characterized by its high electrical conductivity (5485.8 S/cm), exhibited an EMI SE of 39.82 dB and a reflective shielding coefficient of 0.989. However, the coated CPnC design significantly increased the EMI shielding effectiveness to approximately 50 dB, with a greater contribution from absorption. Additionally, we observed that the hybridization of rGOnR with MXene reduced the minimum required thickness for achieving maximum absorption dominance in CPnCs. The following factors were proposed as reasons for the ultra-high absorption shielding effectiveness of the coated CPnCs:

- Tuned impedance mismatch between the media and the shielding material, allowing the penetration of incident EM waves into the CPnCs.
- Ohmic loss caused by traveling electrons in the 3D conductive network and inter-flake electron hopping among the assembled rGOnR/MXene nanomaterials.
- Interfacial and dipolar polarizations occurring at different interfaces, including those between nanomaterials and PDMS, as well as nano/micro capacitor-like structures and nanomaterials' functional groups, defects, and disorders.
- Re-absorption of reflected EM waves from the MXene coat through the 3D interconnected conductive network of the nanocomposite.

6.2 Recommendations

It is crucial that future work following this thesis will further develop CPnCs exhibiting engineered electrical conductivity with other properties of importance tailored for obtaining highly absorptive EMI shielding material. Below are the proposed future works for further research in this field:

6.2.1 Material research

- Investigate the influence of the different size and types (Vanadium based, etc.) of MXene nanoflakes on electrical percolation threshold and their efficacy on EMI SE.

6.2.2 Processing research

- Unidirectional freeze drying leads to the alignment of nanomaterials in the ice crystal growth direction. Our preliminary results showed that the electrical conductivity of the nanocomposites in the alignment direction is different than that in the normal direction. As EMI shielding is proportional to electrical conductivity, then it is worthy of research on the effect of nanomaterial alignment on the EMI shielding performance of the nanocomposite.
- Tuning the surface impedance matching between the shielding material and the air is crucial for the absorption dominant EMI shielding material. To enhance impedance matching, it is suggested to design CPnCs with anisotropic electrical conductivity. To achieve this target, an electric field can be used to induce a gradient nanomaterials segregation. Such segregation can induce lower conductivity at the nanocomposite's surface, while higher conductivity at the bulk. Surface lower conductivity tunes the surface impedance matching and absorbs EM waves. The higher bulk conductivity enhances EMI SE by conduction loss.
- Explore the effect of microcellular structure in enhancing EMI SE and absorption dominancy of shielding mechanism for the previous suggested research. Foam structure can enhance both impedance matching and multiple reflections in CPnC.
- To further tune the impedance matching and multiple reflections inside the nanocomposites, it is also suggested to sandwich 2 or 3 different layers of CPnCs where each layer is composed of different grades of the same polymer with different degrees of foamability. This way can induce heterogenous microcellular structure for tuning impedance matching and multiple reflections.

References

[1] H. Liu, Y. Shen, Y. Song, C.W. Nan, Y. Lin, X. Yang, Carbon nanotube array/polymer core/shell structured composites with high dielectric permittivity, low dielectric loss, and large energy density, Advanced Materials. 23 (2011) 5104–5108. https://doi.org/10.1002/adma.201102079.

[2] C. Yang, Y. Lin, C.W. Nan, Modified carbon nanotube composites with high dielectric constant, low dielectric loss and large energy density, Carbon N Y. 47 (2009) 1096–1101. https://doi.org/10.1016/j.carbon.2008.12.037.

[3] J. Huang, D.G. Baird, J.E. McGrath, Development of fuel cell bipolar plates from graphite filled wet-lay thermoplastic composite materials, J Power Sources. 150 (2005) 110–119. https://doi.org/10.1016/j.jpowsour.2005.02.074.

[4] S.A. Mirkhani, A. Shayesteh Zeraati, E. Aliabadian, M. Naguib, U. Sundararaj, High Dielectric Constant and Low Dielectric Loss via Poly(vinyl alcohol)/Ti3C2Tx MXene Nanocomposites, ACS Appl Mater Interfaces. 11 (2019) 18599–18608. https://doi.org/10.1021/acsami.9b00393.

[5] M. Hamidinejad, B. Zhao, A. Zandieh, N. Moghimian, T. Filleter, C.B. Park, Enhanced Electrical and Electromagnetic Interference Shielding Properties of Polymer − Graphene Nanoplatelet Composites Fabricated via Supercritical-Fluid Treatment and Physical Foaming, ACS Appl Mater Interfaces. 10 (2018) 30752–30761. https://doi.org/10.1021/acsami.8b10745.

[6] M. Hamidinejad, B. Zhao, R.K.M. Chu, N. Moghimian, H.E. Naguib, T. Filleter, C.B. Park, Ultralight Microcellular Polymer–Graphene Nanoplatelet Foams with Enhanced Dielectric Performance, ACS Appl Mater Interfaces. 10 (2018) 19987–19998. https://doi.org/10.1021/acsami.8b03777.

[7] B. Zhao, C. Zhao, R. Li, S.M. Hamidinejad, C.B. Park, Flexible, Ultrathin, and High-Efficiency Electromagnetic Shielding Properties of Poly (Vinylidene Fluoride)/ Carbon Composite Films, ACS Appl Mater Interfaces. 9 (2017) 20873−20884. https://doi.org/10.1021/acsami.7b04935.

[8] Y. Qiao, X. Yin, T. Zhu, H. Li, C. Tang, Dielectric polymers with novel chemistry, compositions and architectures, Prog Polym Sci. 80 (2018) 153–162. https://doi.org/10.1016/j.progpolymsci.2018.01.003.

[9] V.D. Punetha, S. Rana, H.J. Yoo, A. Chaurasia, J.T. McLeskey, M.S. Ramasamy, N.G. Sahoo, J.W. Cho, Functionalization of carbon nanomaterials for advanced polymer nanocomposites: A comparison study between CNT and graphene, Prog Polym Sci. 67 (2017) 1–47. https://doi.org/10.1016/j.progpolymsci.2016.12.010.

[10] MarketsandMarket, EMI Shielding market by material, method, industry - Global forecast to 2027, 2021. https://tinyurl.com/2vkvm2su.

[11] M. Moniruzzaman, K.I. Winey, Polymer nanocomposites containing carbon nanotubes, Macromolecules. 39 (2006) 5194–5205. https://doi.org/10.1021/ma060733p.

[12] L. Yang, F. Liu, H. Xia, X. Qian, K. Shen, J. Zhang, Improving the electrical conductivity of a carbon nanotube/polypropylene composite by vibration during injection-moulding, Carbon N Y. 49 (2011) 3274–3283. https://doi.org/10.1016/j.carbon.2011.03.054.

[13] C. Kingston, R. Zepp, A. Andrady, D. Boverhof, R. Fehir, D. Hawkins, J. Roberts, P. Sayre, B. Shelton, Y. Sultan, V. Vejins, W. Wohlleben, Release characteristics of selected carbon nanotube polymer composites, Carbon N Y. 68 (2014) 33–57. https://doi.org/10.1016/j.carbon.2013.11.042.

[14] A. Ameli, P.U. Jung, C.B. Park, Electrical properties and electromagnetic interference shielding effectiveness of polypropylene/carbon fiber composite foams, Carbon N Y. 60 (2013) 379–391. https://doi.org/10.1016/J.CARBON.2013.04.050.

[15] H. Khatoon, S. Ahmad, A review on conducting polymer reinforced polyurethane composites, Journal of Industrial and Engineering Chemistry. 53 (2017) 1–22. https://doi.org/10.1016/j.jiec.2017.03.036.

[16] M.L. Clingerman, Development and Modelling of Electrically Conductive Composite Materials, 2001.

[17] B. Berkowitz, R.P. Ewing, Percolation theory and network modeling applications in soil physics, Surv Geophys. 19 (1998) 23–72. https://doi.org/10.1023/A:1006590500229.

[18] Z. Spitalsky, D. Tasis, K. Papagelis, C. Galiotis, Carbon nanotube-polymer composites: Chemistry, processing, mechanical and electrical properties, Progress in Polymer Science (Oxford). 35 (2010) 357–401. https://doi.org/10.1016/j.progpolymsci.2009.09.003.

[19] iPolycond Consortium, Introduction to conductive polymer composites, Smithers Rapra, 2011.

[20] S. Iijima, Helical microtubules of graphitic carbon, Nature. 354 (1991) 56–58.

[21] A.K. GEIM, K.S. NOVOSELOV, The rise of graphene, Nat Mater. 6 (2007) 183–191. https://doi.org/https://doi.org/10.1038/nmat1849.

[22] T.K. Das, S. Prusty, Graphene-Based Polymer Composites and Their Applications, Polymer - Plastics Technology and Engineering. 52 (2013) 319–331. https://doi.org/10.1080/03602559.2012.751410.

[23] H. Pang, L. Xu, D.X. Yan, Z.M. Li, Conductive polymer composites with segregated structures, Prog Polym Sci. 39 (2014) 1908–1933. https://doi.org/10.1016/j.progpolymsci.2014.07.007.

[24] J.R. Potts, D.R. Dreyer, C.W. Bielawski, R.S. Ruoff, Graphene-based polymer nanocomposites, Polymer (Guildf). 52 (2011) 5–25. https://doi.org/10.1016/j.polymer.2010.11.042.

[25] M. Naguib, M. Kurtoglu, V. Presser, J. Lu, J. Niu, M. Heon, L. Hultman, Y. Gogotsi, M.W. Barsoum, Two-dimensional nanocrystals produced by exfoliation of Ti3AlC2, Advanced Materials. 23 (2011) 4248–4253. https://doi.org/10.1002/adma.201102306.

[26] C.J. Zhang, B. Anasori, A. Seral-Ascaso, S.H. Park, N. McEvoy, A. Shmeliov, G.S. Duesberg, J.N. Coleman, Y. Gogotsi, V. Nicolosi, Transparent, Flexible, and Conductive 2D Titanium Carbide (MXene) Films with High Volumetric Capacitance, Advanced Materials. 29 (2017) 1–9. https://doi.org/10.1002/adma.201702678.

[27] H. Wu, C. Zhu, X. Li, X. Hu, H. Xie, X. Lu, J.P. Qu, Layer-by-Layer Assembly of Multifunctional NR/MXene/CNTs Composite Films with Exceptional Electromagnetic Interference Shielding Performances and Excellent Mechanical Properties, Macromol Rapid Commun. 43 (2022) 1–11. https://doi.org/10.1002/marc.202200387.

[28] B. Shen, Y. Li, W. Zhai, W. Zheng, Compressible Graphene-Coated Polymer Foams with Ultralow Density for Adjustable Electromagnetic Interference (EMI) Shielding, ACS Appl Mater Interfaces. 8 (2016) 8050–8057. https://doi.org/10.1021/acsami.5b11715.

[29] Z. Xu, X. Ding, S. Li, F. Huang, B. Wang, S. Wang, X. Zhang, F. Liu, H. Zhang, Oxidation-Resistant MXene-Based Melamine Foam with Ultralow-Percolation Thresholds for Electromagnetic-Infrared Compatible Shielding, ACS Appl Mater Interfaces. 14 (2022) 40396–40407. https://doi.org/10.1021/acsami.2c05544.

[30] D.W. Schaefer, R.S. Justice, How Nano Are Nanocomposites?, Macromolecules. 40 (2007) 8501–8517. https://doi.org/10.1021/ma070356w.

[31] S.-Y. Fu, Z. Sun, P. Huang, Y.-Q. Li, N. Hu, Some basic aspects of polymer nanocomposites: A critical review, Nano Materials Science. (2019).

[32] M. Panahi-Sarmad, M. Noroozi, M. Abrisham, S. Eghbalinia, F. Teimoury, A.R. Bahramian, P. Dehghan, M. Sadri, V. Goodarzi, A comprehensive review on carbon-based polymer nanocomposite foams as electromagnetic interference shields and piezoresistive sensors, ACS Appl Electron Mater. 2 (2020) 2318–2350. https://doi.org/10.1021/acsaelm.0c00490.

[33] Vahab Solouki Bonab, POLYURETHANE (PU) NANOCOMPOSITES ; INTERPLAY OF COMPOSITION , MORPHOLOGY , AND PROPERTIES, Case Western Reserve University, 2018.

[34] I. Yilgör, E. Yilgör, G.L. Wilkes, Critical parameters in designing segmented polyurethanes and their effect on morphology and properties: A comprehensive review, Polymer (Guildf). 58 (2015) A1–A36. https://doi.org/10.1016/j.polymer.2014.12.014.

[35] K. Ke, V. Solouki Bonab, D. Yuan, I. Manas-Zloczower, Piezoresistive thermoplastic polyurethane nanocomposites with carbon nanostructures, Carbon N Y. 139 (2018) 52–58. https://doi.org/10.1016/j.carbon.2018.06.037.

[36] S. Das Ramôa, G.M. Barra, R.V. Oliveira, M.G. De Oliveira, M. Cossa, B.G. Soares, Electrical, rheological and electromagnetic interference shielding properties of thermoplastic polyurethane/carbon nanotube composites, Polym Int. 62 (2013) 1477–1484. https://doi.org/10.1002/pi.4446.

[37] Y.-S. Jun, B.G. Hyun, M. Hamidinejad, S. Habibpour, A. Yu, C.B. Park, Maintaining electrical conductivity of microcellular MWCNT/TPU composites after deformation, Compos B Eng. 223 (2021) 109113. https://doi.org/10.1016/j.compositesb.2021.109113.

[38] H. Ma, X. Zhang, L. Yang, L. Ma, C.B. Park, P. Gong, G. Li, Electromagnetic wave absorption in graphene nanoribbon nanocomposite foam by multiscale electron dissipation of atomic defects, interfacial polarization and impedance match, Carbon N Y. 205 (2023) 159–170. https://doi.org/10.1016/j.carbon.2023.01.028.

[39] V. Solouki Bonab, I. Manas-Zloczower, Revisiting thermoplastic polyurethane, from composition to morphology and properties, J Polym Sci B Polym Phys. 55 (2017) 1553–1564. https://doi.org/10.1002/polb.24413.

[40] P. Saxena, P. Shukla, A comprehensive review on fundamental properties and applications of poly(vinylidene fluoride) (PVDF), Adv Compos Hybrid Mater. 4 (2021) 8–26. https://doi.org/10.1007/s42114-021-00217-0.

[41] R. Dallaev, T. Pisarenko, D. Sobola, F. Orudzhev, S. Ramazanov, T. Trčka, Brief Review of PVDF Properties and Applications Potential, Polymers (Basel). 14 (2022) 1–29. https://doi.org/10.3390/polym14224793.

[42] R. Chatchaidech, Lubrication Forces In Polydimethylsiloxane (PDMS) Melts, Virginia Polytechnic Institute and State University, 2011.

[43] R. Ariati, F. Sales, A. Souza, R.A. Lima, J. Ribeiro, Polydimethylsiloxane composites characterization and its applications: A review, Polymers (Basel). 13 (2021) 1–21. https://doi.org/10.3390/polym13234258.

[44] Q. Zaman, K.M. Zia, M. Zuber, Y.N. Mabkhot, F. Almalki, T. Ben Hadda, A comprehensive review on synthesis, characterization, and applications of polydimethylsiloxane and copolymers, International Journal of Plastics Technology. 23 (2019) 261–282. https://doi.org/10.1007/s12588-019-09259-y.

[45] F. Qin, C. Brosseau, A review and analysis of microwave absorption in polymer composites filled with carbonaceous particles, J Appl Phys. 111 (2012). https://doi.org/10.1063/1.3688435.

[46] D.K. James, J.M. Tour, Graphene: Powder, Flakes, Ribbons, and Sheets, Acc Chem Res. 46 (2013) 2307–2318. https://doi.org/10.1021/ar300127r.

[47] H. Kim, A.A. Abdala, C.W. Macosko, Graphene/Polymer Nanocomposites, Macromolecules. 43 (2010) 6515–6530. https://doi.org/10.1021/ma100572e.

[48] M.Y. Han, B. Özyilmaz, Y. Zhang, P. Kim, Energy band-gap engineering of graphene nanoribbons, Phys Rev Lett. 98 (2007) 206805. https://doi.org/10.1103/PhysRevLett.98.206805.

[49] S.S. Datta, D.R. Strachan, S.M. Khamis, A.T.C. Johnson, Crystallographic Etching of Few-Layer Graphene, Nano Lett. 8 (2008) 1912–1915. https://doi.org/10.1021/nl080583r.

[50] L. Zhang, H. Dai, S. Lee, X. Wang, X. Li, Chemically Derived, Ultrasmooth Graphene Nanoribbon Semiconductors, Science (1979). 319 (2008) 1229–1232. http://www.sciencemag.org/content/319/5867/1229.full.html%5Cnhttp://www.sciencemag.org/content/319/5867/1229.full.pdf.

[51] L. Jiao, L. Zhang, X. Wang, G. Diankov, H. Dai, Narrow graphene nanoribbons from carbon nanotubes, Nature. 458 (2009) 877–880. https://doi.org/10.1038/nature07919.

[52] D. V. Kosynkin, A.L. Higginbotham, A. Sinitskii, J.R. Lomeda, A. Dimiev, B.K. Price, J.M. Tour, Longitudinal unzipping of carbon nanotubes to form graphene nanoribbons, Nature. 458 (2009) 872–876. https://doi.org/10.1038/nature07872.

[53] J. Campos-Delgado, J.M. Romo-Herrera, X. Jia, D.A. Cullen, H. Muramatsu, Y.A. Kim, T. Hayashi, Z. Ren, D.J. Smith, Y. Okuno, T. Ohba, H. Kanoh, K. Kaneko, M. Endo, H. Terrones, M.S. Dresselhaus, M. Terrones, Bulk Production of a New Form of sp 2 Carbon: Crystalline Graphene Nanoribbons, Nano Lett. 8 (2008) 2773–2778. https://doi.org/10.1021/nl801316d.

[54] A.L. Elías, A.R. Botello-Méndez, D. Meneses-Rodríguez, V. Jehová González, D. Ramírez-González, L. Ci, E. Muñoz-Sandoval, P.M. Ajayan, H. Terrones, M. Terrones, Longitudinal Cutting of Pure and Doped Carbon Nanotubes to Form Graphitic Nanoribbons Using Metal Clusters as Nanoscalpels, Nano Lett. 10 (2010) 366–372. https://doi.org/10.1021/nl901631z.

[55] A.G. Cano-Márquez, F.J. Rodríguez-Macías, J. Campos-Delgado, C.G. Espinosa-González, F. Tristán-López, D. Ramírez-González, D.A. Cullen, D.J. Smith, M. Terrones, Y.I. Vega-Cantú,

Ex-MWNTs: Graphene Sheets and Ribbons Produced by Lithium Intercalation and Exfoliation of Carbon Nanotubes, Nano Lett. 9 (2009) 1527–1533. https://doi.org/10.1021/nl803585s.

[56] M. a Rafiee, W. Lu, A. V Thomas, A. Zandiatashbar, J. Rafiee, J.M. Tour, N. a Koratkar, Graphene Nanoribbon Composites, ACS Nano. 4 (2010) 7415–7420. https://doi.org/10.1021/nn102529n.

[57] A. Joshi, A. Bajaj, R. Singh, P.S. Alegaonkar, K. Balasubramanian, S. Datar, Graphene nanoribbon-PVA composite as EMI shielding material in the X band, Nanotechnology. 24 (2013). https://doi.org/10.1088/0957-4484/25/23/239501.

[58] L. Li, A.-R.O. Raji, H. Fei, Y. Yang, E.L.G. Samuel, J.M. Tour, Nanocomposite of Polyaniline Nanorods Grown on Graphene Nanoribbons for Highly Capacitive Pseudocapacitors, ACS Appl Mater Interfaces. 5 (2013) 6622–6627. https://doi.org/10.1021/am4013165.

[59] D.J. Davis, A.-R.O. Raji, T.N. Lambert, J.A. Vigil, L. Li, K. Nan, J.M. Tour, Silver-Graphene Nanoribbon Composite Catalyst for the Oxygen Reduction Reaction in Alkaline Electrolyte, Electroanalysis. 26 (2014) 164–170. https://doi.org/https://doi.org/10.1002/elan.201300254.

[60] L. Li, G. Ruan, Z. Peng, Y. Yang, H. Fei, A.-R.O. Raji, E.L.G. Samuel, J.M. Tour, Enhanced Cycling Stability of Lithium Sulfur Batteries Using Sulfur–Polyaniline–Graphene Nanoribbon Composite Cathodes, ACS Appl Mater Interfaces. 6 (2014) 15033–15039. https://doi.org/10.1021/am5030116.

[61] K.S. Novoselov, A.K. Geim, S. V Morozov, D. Jiang, Y. Zhang, S. V Dubonos, I. V Grigorieva, A.A. Firsov, Electric Field Effect in Atomically Thin Carbon Films, Science (1979). 306 (2004) 666–669. https://doi.org/10.1126/science.1102896.

[62] K.R.G. Lim, M. Shekhirev, B.C. Wyatt, B. Anasori, Y. Gogotsi, Z.W. Seh, Fundamentals of MXene synthesis, Nature Synthesis. 1 (2022) 601–614. https://doi.org/10.1038/s44160-022-00104-6.

[63] B. Anasori, M.R. Lukatskaya, Y. Gogotsi, 2D metal carbides and nitrides (MXenes) for energy storage, Nat Rev Mater. 2 (2017). https://doi.org/10.1038/natrevmats.2016.98.

[64] M. Alhabeb, K. Maleski, B. Anasori, P. Lelyukh, L. Clark, S. Sin, Y. Gogotsi, Guidelines for Synthesis and Processing of Two-Dimensional Titanium Carbide (Ti 3 C 2 T x MXene), Chemistry of Materials. 29 (2017) 7633–7644. https://doi.org/10.1021/acs.chemmater.7b02847.

[65] R. Haggenmueller, H.H. Gommans, A.G. Rinzler, J.E. Fischer, K.I. Winey, Aligned single-wall carbon nanotubes in composites by melt processing methods, Chem Phys Lett. 330 (2000) 219–225. https://doi.org/10.1016/S0009-2614(00)01013-7.

[66] A.R. Bhattacharyya, T. V. Sreekumar, T. Liu, S. Kumar, L.M. Ericson, R.H. Hauge, R.E. Smalley, Crystallization and orientation studies in polypropylene/single wall carbon nanotube composite, Polymer (Guildf). 44 (2003) 2373–2377. https://doi.org/10.1016/S0032-3861(03)00073-9.

[67] Z. Fan, D. Wang, Y. Yuan, Y. Wang, Z. Cheng, Y. Liu, Z. Xie, A lightweight and conductive MXene/graphene hybrid foam for superior electromagnetic interference shielding, Chemical Engineering Journal. 381 (2020) 122696. https://doi.org/https://doi.org/10.1016/j.cej.2019.122696.

[68] K. Hu, H. Wang, X. Zhang, H. Huang, T. Qiu, Y. Wang, C. (John) Zhang, L. Pan, J. Yang, Ultralight Ti3C2Tx MXene foam with superior microwave absorption performance, Chemical Engineering Journal. 408 (2021) 127283. https://doi.org/https://doi.org/10.1016/j.cej.2020.127283.

[69] S. Ye, J. Feng, P. Wu, Highly elastic graphene oxide–epoxy composite aerogels via simple freeze-drying and subsequent routine curing, J Mater Chem A Mater. 1 (2013) 3495–3502. https://doi.org/10.1039/C2TA01142E.

[70] Y. Xu, K. Sheng, C. Li, G. Shi, Self-Assembled Graphene Hydrogel via a One-Step Hydrothermal Process, ACS Nano. 4 (2010) 4324–4330. https://doi.org/10.1021/nn101187z.

[71] L. Du, S.C. Jana, Highly conductive epoxy/graphite composites for bipolar plates in proton exchange membrane fuel cells, J Power Sources. 172 (2007) 734–741. https://doi.org/10.1016/j.jpowsour.2007.05.088.

[72] E.P. Mamunya, V. V. Davidenko, E. V. Lebedev, Effect of polymer-filler interface interactions on percolation conductivity of thermoplastics filled with carbon black, Compos Interfaces. 4 (1997) 169–176. https://doi.org/10.1163/156855497X00145.

[73] F. Lux, Models proposed to explain the electrical conductivity of mixtures made of conductive and insulating materials, J Mater Sci. 28 (1993) 285–301. https://doi.org/10.1007/BF00357799.

[74] S. Kirkpatrick, Percolation and Conduction, Rev Mod Phys. 45 (1973) 574–588. https://doi.org/10.1103/RevModPhys.45.574.

[75] S. Abbasi, P.J. Carreau, A. Derdouri, Flow induced orientation of multiwalled carbon nanotubes in polycarbonate nanocomposites: Rheology, conductivity and mechanical properties, Polymer (Guildf). 51 (2010) 922–935. https://doi.org/10.1016/j.polymer.2009.12.041.

[76] A. Bunde, W. Dieterich, Percolation in composites, J Electroceram. 5 (2000) 81–92. https://doi.org/10.1023/A:1009997800513.

[77] I. Balberg, Tunneling and Nonuniversal Conductivity in Composite Materials, Phys Rev Lett. 59 (1987) 1305–1308.

[78] C. Li, E.T. Thostenson, T.W. Chou, Dominant role of tunneling resistance in the electrical conductivity of carbon nanotube-based composites, Appl Phys Lett. 91 (2007). https://doi.org/10.1063/1.2819690.

[79] E.K. Sichel, J.I. Gittleman, P. Sheng, Transport properties of the composite material carbon-poly(vinyl chloride), Phys Rev B. 18 (1978) 5712–5716. https://doi.org/10.1103/PhysRevB.18.5712.

[80] Y. Chekanov, R. Ohnogi, S. Asai, M. Sumita, Electrical properties of epoxy resin filled with carbon fibers, J Mater Sci. 34 (1999) 5589–5592. https://doi.org/10.1023/A:1004737217503.

[81] G.R. Ruschau, S. Yoshikawa, R.E. Newnham, Resistivities of conductive composites, J Appl Phys. 72 (1992) 953–959. https://doi.org/10.1063/1.352350.

[82] R.M. Mutiso, K.I. Winey, Electrical properties of polymer nanocomposites containing rod-like nanofillers, Prog Polym Sci. 40 (2015) 63–84. https://doi.org/10.1016/j.progpolymsci.2014.06.002.

[83] S.H. Xie, Y.Y. Liu, J.Y. Li, Comparison of the effective conductivity between composites reinforced by graphene nanosheets and carbon nanotubes, Appl Phys Lett. 92 (2008) 243121. https://doi.org/10.1063/1.2949074.

[84] M. Safdari, M.S. Al-Haik, Synergistic electrical and thermal transport properties of hybrid polymeric nanocomposites based on carbon nanotubes and graphite nanoplatelets, Carbon N Y. 64 (2013) 111–121. https://doi.org/10.1016/J.CARBON.2013.07.042.

[85] A. Das, G.R. Kasaliwal, R. Jurk, R. Boldt, D. Fischer, K.W. Stöckelhuber, G. Heinrich, Rubber composites based on graphene nanoplatelets, expanded graphite, carbon nanotubes and their combination: A comparative study, Compos Sci Technol. 72 (2012) 1961–1967. https://doi.org/10.1016/j.compscitech.2012.09.005.

[86] Y. Gao, O.T. Picot, E. Bilotti, T. Peijs, Influence of filler size on the properties of poly(lactic acid) (PLA)/graphene nanoplatelet (GNP) nanocomposites, Eur Polym J. 86 (2017) 117–131. https://doi.org/10.1016/j.eurpolymj.2016.10.045.

[87] Y. Kazemi, A. Ramezani, L. Howe, T. Filleter, C.B. Park, Effects of polymer filler interactions on controlling the conductive network formation in polyamide 6/ multi-Walled carbon nanotube composites, Polymer (Guildf). 178 (2019) 121684. https://doi.org/10.1016/j.polymer.2019.121684.

[88] X. Zhang, Y. Shen, B. Xu, Q. Zhang, L. Gu, J. Jiang, J. Ma, Y. Lin, C.-W. Nan, Giant Energy Density and Improved Discharge Efficiency of Solution-Processed Polymer Nanocomposites for Dielectric Energy Storage, Advanced Materials. 28 (2016) 2055–2061. https://doi.org/https://doi.org/10.1002/adma.201503881.

[89] Y. Zhao, Q. Liao, G. Zhang, Z. Zhang, Q. Liang, X. Liao, Y. Zhang, High output piezoelectric nanocomposite generators composed of oriented BaTiO3 NPs at PVDF, Nano Energy. 11 (2015) 719–727. https://doi.org/10.1016/j.nanoen.2014.11.061.

[90] Z. Hu, B. Ma, S. Liu, M. Narayanan, U. Balachandran, Ceramic dielectric film capacitors fabricated on aluminum foils by chemical solution deposition, Mater Res Bull. 52 (2014) 189–193. https://doi.org/10.1016/j.materresbull.2013.11.030.

[91] Prateek, V.K. Thakur, R.K. Gupta, Recent Progress on Ferroelectric Polymer-Based Nanocomposites for High Energy Density Capacitors: Synthesis, Dielectric Properties, and Future Aspects, Chem Rev. 116 (2016) 4260–4317. https://doi.org/10.1021/acs.chemrev.5b00495.

[92] T.W. Dakin, Conduction and polarization mechanisms and trends in dielectric, IEEE Electrical Insulation Magazine. 22 (2006) 11–28. https://doi.org/10.1109/MEI.2006.1705854.

[93] L.A. Fredin, Z. Li, M.T. Lanagan, M.A. Ratner, T.J. Marks, Sustainable high capacitance at high frequencies: Metallic aluminum-polypropylene nanocomposites, ACS Nano. 7 (2013) 396–407. https://doi.org/10.1021/nn3044148.

[94] X. Huang, C. Zhi, Polymer nanocomposites: Electrical and thermal properties, Polymer Nanocomposites: Electrical and Thermal Properties. (2016) 1–351. https://doi.org/10.1007/978-3-319-28238-1.

[95] L.A. Fredin, Z. Li, M.T. Lanagan, M.A. Ratner, T.J. Marks, Sustainable High Capacitance at High Frequencies: Metallic Aluminum–Polypropylene Nanocomposites, ACS Nano. 7 (2013) 396–407. https://doi.org/10.1021/nn3044148.

[96] A. Ameli, S. Wang, Y. Kazemi, C.B. Park, P. Pötschke, A facile method to increase the charge storage capability of polymer nanocomposites, Nano Energy. 15 (2015) 54–65. https://doi.org/10.1016/j.nanoen.2015.04.004.

[97] M. Arjmand, M. Mahmoodi, S. Park, U. Sundararaj, An innovative method to reduce the energy loss of conductive filler/polymer composites for charge storage applications, Compos Sci Technol. 78 (2013) 24–29. https://doi.org/10.1016/j.compscitech.2013.01.019.

[98] A. Ameli, S. Wang, Y. Kazemi, C.B. Park, P. Pötschke, A facile method to increase the charge storage capability of polymer nanocomposites, Nano Energy. 15 (2015) 54–65. https://doi.org/https://doi.org/10.1016/j.nanoen.2015.04.004.

[99] J.W. Molyneux-Child, EMC Shielding Materials, Newnes, 1997. https://books.google.ca/books?id=NUUfAQAAIAAJ.

[100] N. Devi, S.S. Ray, Electromagnetic interference cognizance and potential of advanced polymer composites toward electromagnetic interference shielding: A review, Polym Eng Sci. 62 (2022) 591–621. https://doi.org/10.1002/pen.25876.

[101] B. Zhao, C. Zhao, M. Hamidinejad, C. Wang, R. Li, S. Wang, K. Yasamin, C.B. Park, Incorporating a microcellular structure into PVDF/graphene-nanoplatelet composites to tune their electrical conductivity and electromagnetic interference shielding properties, J Mater Chem C Mater. 6 (2018) 10292–10300. https://doi.org/10.1039/C8TC03714K.

[102] G.K. Sharma, N.R. James, Progress in Electrospun Polymer Composite Fibers for Microwave Absorption and Electromagnetic Interference Shielding, ACS Appl Electron Mater. 3 (2021) 4657–4680. https://doi.org/10.1021/acsaelm.1c00827.

[103] S. Sankaran, K. Deshmukh, M.B. Ahamed, S.K. Khadheer Pasha, Recent advances in electromagnetic interference shielding properties of metal and carbon filler reinforced flexible polymer composites: A review, Compos Part A Appl Sci Manuf. 114 (2018) 49–71. https://doi.org/10.1016/j.compositesa.2018.08.006.

[104] H.W. Ott, Noise reduction techniques in electronic systems, Second, Wiley, 1988.

[105] J. Kruželák, A. Kvasničáková, K. Hložeková, I. Hudec, Progress in polymers and polymer composites used as efficient materials for EMI shielding, Nanoscale Adv. 3 (2021) 123–172. https://doi.org/10.1039/d0na00760a.

[106] M.H. Al-Saleh, U. Sundararaj, Electromagnetic interference shielding mechanisms of CNT/polymer composites, Carbon N Y. 47 (2009) 1738–1746. https://doi.org/10.1016/j.carbon.2009.02.030.

[107] S. Naeem, V. Baheti, V. Tunakova, J. Militky, D. Karthik, B. Tomkova, Development of porous and electrically conductive activated carbon web for effective EMI shielding applications, Carbon N Y. 111 (2017) 439–447. https://doi.org/10.1016/j.carbon.2016.10.026.

[108] T. Yun, H. Kim, A. Iqbal, Y.S. Cho, G.S. Lee, M.K. Kim, S.J. Kim, D. Kim, Y. Gogotsi, S.O. Kim, C.M. Koo, Electromagnetic Shielding of Monolayer MXene Assemblies, Advanced Materials. 32 (2020) 1–9. https://doi.org/10.1002/adma.201906769.

[109] Y.K. Hong, C.Y. Lee, C.K. Jeong, D.E. Lee, K. Kim, J. Joo, Method and apparatus to measure electromagnetic interference shielding efficiency and its shielding characteristics in broadband

frequency ranges, Review of Scientific Instruments. 74 (2003) 1098–1102. https://doi.org/10.1063/1.1532540.

[110] J. Wang, C. Xiang, Q. Liu, Y. Pan, J. Guo, Ordered mesoporous carbon/fused silica composites, Adv Funct Mater. 18 (2008) 2995–3002. https://doi.org/10.1002/adfm.200701406.

[111] R. Li, L. Ding, Q. Gao, H. Zhang, D. Zeng, B. Zhao, B. Fan, R. Zhang, Tuning of anisotropic electrical conductivity and enhancement of EMI shielding of polymer composite foam via CO2-assisted delamination and orientation of MXene, Chemical Engineering Journal. 415 (2021) 128930. https://doi.org/10.1016/j.cej.2021.128930.

[112] R.B. Jagadeesh Chandra, B. Shivamurthy, S.D. Kulkarni, M.S. Kumar, Hybrid polymer composites for EMI shielding application- a review, Mater Res Express. 6 (2019). https://doi.org/10.1088/2053-1591/aaff00.

[113] Y. Zhang, J.R. Choi, S.-J. Park, Enhancing the heat and load transfer efficiency by optimizing the interface of hexagonal boron nitride/elastomer nanocomposites for thermal management applications, Polymer (Guildf). 143 (2018) 1–9. https://doi.org/https://doi.org/10.1016/j.polymer.2018.03.067.

[114] Z. Min, H. Yang, F. Chen, T. Kuang, Scale-up production of lightweight high-strength polystyrene/carbonaceous filler composite foams with high-performance electromagnetic interference shielding, Mater Lett. 230 (2018) 157–160. https://doi.org/10.1016/J.MATLET.2018.07.094.

[115] Y. Zheng, Y. Li, Z. Li, Y. Wang, K. Dai, G. Zheng, C. Liu, C. Shen, The effect of filler dimensionality on the electromechanical performance of polydimethylsiloxane based conductive nanocomposites for flexible strain sensors, Compos Sci Technol. 139 (2017) 64–73. https://doi.org/10.1016/j.compscitech.2016.12.014.

[116] J.F. Christ, N. Aliheidari, A. Ameli, P. Pötschke, 3D printed highly elastic strain sensors of multiwalled carbon nanotube/thermoplastic polyurethane nanocomposites, Mater Des. 131 (2017) 394–401. https://doi.org/10.1016/j.matdes.2017.06.011.

[117] Y. Li, B. Zhou, G. Zheng, X. Liu, T. Li, C. Yan, C. Cheng, K. Dai, C. Liu, C. Shen, Z. Guo, Continuously prepared highly conductive and stretchable SWNT/MWNT synergistically

composited electrospun thermoplastic polyurethane yarns for wearable sensing, J Mater Chem C Mater. 6 (2018) 2258–2269. https://doi.org/10.1039/c7tc04959e.

[118] Y. Zhou, Y. Zhou, H. Deng, Q. Fu, A novel route towards tunable piezoresistive behavior in conductive polymer composites: Addition of insulating filler with different size and surface characteristics, Compos Part A Appl Sci Manuf. 96 (2017) 99–109. https://doi.org/10.1016/j.compositesa.2017.02.002.

[119] H. Deng, M. Ji, D. Yan, S. Fu, L. Duan, M. Zhang, Q. Fu, Q.F. Hua Deng, Mizhi Ji, Dongxue Yan, Sirui Fu, Lingyan Duan, Mengwei Zhang, Towards tunable resistivity-strain behavior through construction of oriented and selectively distributed conductive networks in conductive polymer composites, J Mater Chem A Mater. 2 (2014) 10048–10058. https://doi.org/10.1039/c4ta01073f.

[120] R. Huang, M. Huang, X. Li, F. An, N. Koratkar, Z.-Z. Yu, Porous Graphene Films with Unprecedented Elastomeric Scaffold-Like Folding Behavior for Foldable Energy Storage Devices, Advanced Materials. 30 (2018) 1707025. https://doi.org/10.1002/adma.201707025.

[121] X. Wang, C. Yang, J. Jin, X. Li, Q. Cheng, G. Wang, High-performance stretchable supercapacitors based on intrinsically stretchable acrylate rubber/MWCNTs@conductive polymer composite electrodes, J Mater Chem A Mater. 6 (2018) 4432–4442. https://doi.org/10.1039/C7TA11173H.

[122] A. Ameli, M. Nofar, C.B. Park, P. Pötschke, G. Rizvi, Polypropylene/carbon nanotube nano/microcellular structures with high dielectric permittivity, low dielectric loss, and low percolation threshold, Carbon N Y. 71 (2014) 206–217. https://doi.org/10.1016/J.CARBON.2014.01.031.

[123] B. Zhao, C. Zhao, R. Li, S.M. Hamidinejad, C.B. Park, Flexible, Ultrathin, and High-Efficiency Electromagnetic Shielding Properties of Poly(Vinylidene Fluoride)/Carbon Composite Films, ACS Appl Mater Interfaces. 9 (2017) 20873–20884. https://doi.org/10.1021/acsami.7b04935.

[124] M. Hamidinejad, B. Zhao, A. Zandieh, N. Moghimian, T. Filleter, C.B. Park, Enhanced Electrical and Electromagnetic Interference Shielding Properties of Polymer-Graphene

Nanoplatelet Composites Fabricated via Supercritical-Fluid Treatment and Physical Foaming, ACS Appl Mater Interfaces. 10 (2018) 30752–30761. https://doi.org/10.1021/acsami.8b10745.

[125] A. Ameli, P.U. Jung, C.B. Park, Electrical properties and electromagnetic interference shielding effectiveness of polypropylene/carbon fiber composite foams, Carbon N Y. 60 (2013) 379–391. https://doi.org/10.1016/j.carbon.2013.04.050.

[126] G.G. Wang, L. Wang, L.H. Mark, V. Shaayegan, G.G. Wang, H. Li, G. Zhao, C.B. Park, Ultralow-Threshold and Lightweight Biodegradable Porous PLA/MWCNT with Segregated Conductive Networks for High-Performance Thermal Insulation and Electromagnetic Interference Shielding Applications, ACS Appl Mater Interfaces. 10 (2018) 1195–1203. https://doi.org/10.1021/acsami.7b14111.

[127] D. Lu, Z. Mo, B. Liang, L. Yang, Z. He, H. Zhu, Z. Tang, X. Gui, Flexible, lightweight carbon nanotube sponges and composites for high-performance electromagnetic interference shielding, Carbon N Y. 133 (2018) 457–463. https://doi.org/10.1016/j.carbon.2018.03.061.

[128] Z. Chen, C. Xu, C. Ma, W. Ren, H.M. Cheng, Lightweight and flexible graphene foam composites for high-performance electromagnetic interference shielding, Advanced Materials. 25 (2013) 1296–1300. https://doi.org/10.1002/adma.201204196.

[129] S.M. Hamidinejad, R.K.M. Chu, B. Zhao, C.B. Park, T. Filleter, Enhanced Thermal Conductivity of Graphene Nanoplatelet-Polymer Nanocomposites Fabricated via Supercritical Fluid-Assisted in Situ Exfoliation, ACS Appl Mater Interfaces. 10 (2018) 1225–1236. https://doi.org/10.1021/acsami.7b15170.

[130] Y. Kazemi, A. Ramezani, L. Howe, T. Filleter, C.B. Park, Effects of polymer filler interactions on controlling the conductive network formation in polyamide 6/ multi-Walled carbon nanotube composites, Polymer (Guildf). 178 (2019) 121684. https://doi.org/10.1016/j.polymer.2019.121684.

[131] Y. Yao, T. Lv, N. Li, Z. Chen, C. Zhang, T. Chen, Selected functionalization of continuous graphene fibers for integrated energy conversion and storage, Sci Bull (Beijing). (2019). https://doi.org/10.1016/J.SCIB.2019.11.013.

[132] A. Chaudhary, S. Kumari, R. Kumar, S. Teotia, B.P. Singh, A.P. Singh, S.K. Dhawan, S.R. Dhakate, Lightweight and Easily Foldable MCMB-MWCNTs Composite Paper with

Exceptional Electromagnetic Interference Shielding, ACS Appl Mater Interfaces. 8 (2016) 10600–10608. https://doi.org/10.1021/acsami.5b12334.

[133] S.M.N. Sultana, S.P. Pawar, U. Sundararaj, Effect of Processing Techniques on EMI SE of Immiscible PS/PMMA Blends Containing MWCNT: Enhanced Intertube and Interphase Scattering, Ind Eng Chem Res. 58 (2019) 11576–11584. https://doi.org/10.1021/acs.iecr.8b05957.

[134] S. Maiti, N.K. Shrivastava, S. Suin, B.B. Khatua, Polystyrene/MWCNT/Graphite Nanoplate Nanocomposites: Efficient Electromagnetic Interference Shielding Material through Graphite Nanoplate–MWCNT–Graphite Nanoplate Networking, ACS Appl Mater Interfaces. 5 (2013) 4712–4724. https://doi.org/10.1021/am400658h.

[135] S. Zhao, Y. Yan, A. Gao, S. Zhao, J. Cui, G. Zhang, Flexible Polydimethylsilane Nanocomposites Enhanced with a Three-Dimensional Graphene/Carbon Nanotube Bicontinuous Framework for High-Performance Electromagnetic Interference Shielding, ACS Appl Mater Interfaces. 10 (2018) 26723–26732. https://doi.org/10.1021/acsami.8b09275.

[136] A. Chaudhary, S. Kumari, R. Kumar, S. Teotia, B.P. Singh, A.P. Singh, S.K. Dhawan, S.R. Dhakate, Lightweight and Easily Foldable MCMB-MWCNTs Composite Paper with Exceptional Electromagnetic Interference Shielding, ACS Appl Mater Interfaces. 8 (2016) 10600–10608. https://doi.org/10.1021/acsami.5b12334.

[137] Y.S. Jun, S. Sy, W. Ahn, H. Zarrin, L. Rasen, R. Tjandra, B.M. Amoli, B. Zhao, G. Chiu, A. Yu, Highly conductive interconnected graphene foam based polymer composite, Carbon N Y. 95 (2015) 653–658. https://doi.org/10.1016/j.carbon.2015.08.079.

[138] J. Du, L. Zhao, Y. Zeng, L. Zhang, F. Li, P. Liu, C. Liu, Comparison of electrical properties between multi-walled carbon nanotube and graphene nanosheet/high density polyethylene composites with a segregated network structure, Carbon N Y. 49 (2011) 1094–1100. https://doi.org/10.1016/J.CARBON.2010.11.013.

[139] Y. Jun, J.G. Um, G. Jiang, G. Lui, A. Yu, Ultra-large sized graphene nano-platelets (GnPs) incorporated polypropylene (PP)/ GnPs composites engineered by melt compounding and its thermal , mechanical , and electrical properties, Composites Part B. 133 (2018) 218–225. https://doi.org/10.1016/j.compositesb.2017.09.028.

[140] J.G. Um, Y.S. Jun, A. Elkamel, A. Yu, Engineering investigation for the size effect of graphene oxide derived from graphene nanoplatelets in polyurethane composites, Canadian Journal of Chemical Engineering. (2020) 1–13. https://doi.org/10.1002/cjce.23696.

[141] J.G. Um, Y.S. Jun, H. Alhumade, H. Krithivasan, G. Lui, A. Yu, Investigation of the size effect of graphene nano-platelets (GnPs) on the anti-corrosion performance of polyurethane/GnP composites, RSC Adv. 8 (2018) 17091–17100. https://doi.org/10.1039/c8ra02087f.

[142] Y.S. Jun, J.G. Um, G. Jiang, A. Yu, A study on the effects of graphene nano-platelets (GnPs) sheet sizes from a few to hundred microns on the thermal, mechanical, and electrical properties of polypropylene (PP)/GnPs composites, Express Polym Lett. 12 (2018) 885–897. https://doi.org/10.3144/expresspolymlett.2018.76.

[143] Y. Wang, G.J. Weng, Electrical Conductivity of Carbon Nanotube- and Graphene-Based Nanocomposites BT - Micromechanics and Nanomechanics of Composite Solids, in: S.A. Meguid, G.J. Weng (Eds.), Micromechanics and Nanomechanics of Composite Solids, Springer International Publishing, Cham, 2018: pp. 123–156. https://doi.org/10.1007/978-3-319-52794-9_4.

[144] S. Niyogi, M.A. Hamon, H. Hu, B. Zhao, P. Bhowmik, R. Sen, M.E. Itkis, R.C. Haddon, Chemistry of Single-Walled Carbon Nanotubes, Acc Chem Res. 35 (2002) 1105–1113. https://doi.org/10.1021/ar010155r.

[145] A.K. Geim, K.S. Novoselov, The rise of graphene., Nat. Mater. 6 (2007) 183–191. https://doi.org/http://dx.doi.org/10.1038/nmat1849.

[146] K.S. Novoselov, a K. Geim, S. V Morozov, D. Jiang, M.I. Katsnelson, I. V Grigorieva, S. V Dubonos, a a Firsov, Two-dimensional gas of massless Dirac fermions in graphene., Nature. 438 (2005) 197–200. https://doi.org/10.1038/nature04233.

[147] A.K. Geim, Graphene: status and prospects., Science. 324 (2009) 1530–1534. https://doi.org/10.1126/science.1158877.

[148] S. Lepak-Kuc, K.Z. Milowska, S. Boncel, M. Szybowicz, A. Dychalska, I. Jozwik, K.K. Koziol, M. Jakubowska, A. Lekawa-Raus, Highly Conductive Doped Hybrid Carbon

Nanotube-Graphene Wires, ACS Appl Mater Interfaces. 11 (2019) 33207–33220. https://doi.org/10.1021/acsami.9b08198.

[149] S.H. Xie, Y.Y. Liu, J.Y. Li, Comparison of the effective conductivity between composites reinforced by graphene nanosheets and carbon nanotubes, Appl Phys Lett. 92 (2008). https://doi.org/10.1063/1.2949074.

[150] M. Safdari, M.S. Al-Haik, Synergistic electrical and thermal transport properties of hybrid polymeric nanocomposites based on carbon nanotubes and graphite nanoplatelets, Carbon N Y. 64 (2013) 111–121. https://doi.org/10.1016/J.CARBON.2013.07.042.

[151] X. Zhang, G. Liang, J. Chang, A. Gu, L. Yuan, W. Zhang, The origin of the electric and dielectric behavior of expanded graphite – carbon nanotube / cyanate ester composites with very high dielectric constant and low dielectric loss, Carbon N Y. 50 (2012) 4995–5007. https://doi.org/10.1016/j.carbon.2012.06.027.

[152] Y.S. Jun, M.G. Park, J.G. Um, S. Habibpour, S. Sy, C.B. Park, A. Yu, The conductivity of polydimethylsiloxane/graphene nano-ribbon foam composite with elongation, Carbon N Y. 162 (2020) 328–338. https://doi.org/10.1016/j.carbon.2020.02.024.

[153] D. V. Kosynkin, A.L. Higginbotham, A. Sinitskii, J.R. Lomeda, A. Dimiev, B.K. Price, J.M. Tour, Longitudinal unzipping of carbon nanotubes to form graphene nanoribbons, Nature. 458 (2009) 872–876. https://doi.org/10.1038/nature07872.

[154] F. Cataldo, G. Compagnini, G. Patané, O. Ursini, G. Angelini, P.R. Ribic, G. Margaritondo, A. Cricenti, G. Palleschi, F. Valentini, Graphene nanoribbons produced by the oxidative unzipping of single-wall carbon nanotubes, Carbon N Y. 48 (2010) 2596–2602. https://doi.org/10.1016/j.carbon.2010.03.063.

[155] L. Jiao, L. Zhang, X. Wang, G. Diankov, H. Dai, Narrow graphene nanoribbons from carbon nanotubes, Nature. 458 (2009) 877–880. https://doi.org/10.1038/nature07919.

[156] X. Li, X. Wang, L. Zhang, S. Lee, H. Dai, Chemically derived, ultrasmooth graphene nanoribbon semiconductors., Science (1979). 319 (2008) 1229–1232. https://doi.org/10.1126/science.1150878.

[157] J. Campos-Delgado, J.M. Romo-Herrera, X. Jia, D.A. Cullen, H. Muramatsu, Y.A. Kim, T. Hayashi, Z. Ren, D.J. Smith, Y. Okuno, T. Ohba, H. Kanoh, K. Kaneko, M. Endo, H.

Terrones, M.S. Dresselhaus, M. Terrones, Bulk Production of a New Form of sp 2 Carbon: Crystalline Graphene Nanoribbons, Nano Lett. 8 (2008) 2773–2778. https://doi.org/10.1021/nl801316d.

[158] M.Y. Han, B. Özyilmaz, Y. Zhang, P. Kim, Energy band-gap engineering of graphene nanoribbons, Phys Rev Lett. 98 (2007) 206805. https://doi.org/10.1103/PhysRevLett.98.206805.

[159] A.L. Higginbotham, D. V. Kosynkin, A. Sinitskii, Z. Sun, J.M. Tour, Lower-Defect Graphene Oxide Nanoribbons from Multiwalled Carbon Nanotubes, ACS Nano. 4 (2010) 2059–2069. https://doi.org/10.1021/nn100118m.

[160] M. Khajehpour, S. Sadeghi, A. Zehtab Yazdi, U. Sundararaj, Tuning the curing behavior of fluoroelastomer (FKM) by incorporation of nitrogen doped graphene nanoribbons (CNx-GNRs), Polymer (Guildf). 55 (2014) 6293–6302. https://doi.org/10.1016/j.polymer.2014.10.008.

[161] A. Sinitskii, A. Dimiev, D. V. Kosynkin, J.M. Tour, Graphene nanoribbon devices produced by oxidative unzipping of carbon nanotubes, ACS Nano. 4 (2010) 5405–5413. https://doi.org/10.1021/nn101019h.

[162] M. Yang, L. Weng, H. Zhu, F. Zhang, T. Fan, D. Zhang, Simultaneously improving the mechanical and electrical properties of poly(vinyl alcohol) composites by high-quality graphitic nanoribbons, Sci Rep. 7 (2017) 1–10. https://doi.org/10.1038/s41598-017-17365-3.

[163] M. Arjmand, S. Sadeghi, M. Khajehpour, U. Sundararaj, Carbon nanotube/graphene nanoribbon/polyvinylidene fluoride hybrid nanocomposites: Rheological and dielectric properties, Journal of Physical Chemistry C. 121 (2017) 169–181. https://doi.org/10.1021/acs.jpcc.6b10741.

[164] S. Sadeghi, M. Arjmand, I. Otero Navas, A. Zehtab Yazdi, U. Sundararaj, Effect of Nanofiller Geometry on Network Formation in Polymeric Nanocomposites: Comparison of Rheological and Electrical Properties of Multiwalled Carbon Nanotube and Graphene Nanoribbon, Macromolecules. 50 (2017) 3954–3967. https://doi.org/10.1021/acs.macromol.7b00702.

[165] S. Habibpour, J.G. Um, Y.-S. Jun, P. Bhargava, C.B. Park, A. Yu, Structural Impact of Graphene Nanoribbon on Mechanical Properties and Anti-corrosion Performance of

Polyurethane Nanocomposites, Chemical Engineering Journal. 405 (2021). https://doi.org/10.1016/j.cej.2020.126858.

[166] I. Zaman, T.T. Phan, H.C. Kuan, Q. Meng, L.T. Bao La, L. Luong, O. Youssf, J. Ma, Epoxy/graphene platelets nanocomposites with two levels of interface strength, Polymer (Guildf). 52 (2011) 1603–1611. https://doi.org/10.1016/j.polymer.2011.02.003.

[167] A.M. Dimiev, A. Khannanov, I. Vakhitov, A. Kiiamov, K. Shukhina, J.M. Tour, Revisiting the Mechanism of Oxidative Unzipping of Multiwall Carbon Nanotubes to Graphene Nanoribbons, ACS Nano. 12 (2018) 3985–3993. https://doi.org/10.1021/acsnano.8b01617.

[168] S. Pei, H.M. Cheng, The reduction of graphene oxide, Carbon N Y. 50 (2012) 3210–3228. https://doi.org/10.1016/j.carbon.2011.11.010.

[169] F. Tuinstra, J.L. Koenig, Raman Spectrum of Graphite, J Chem Phys. 53 (1970) 1126–1130. https://doi.org/10.1063/1.1674108.

[170] R. Nadiv, M. Shtein, M. Buzaglo, S. Peretz-Damari, A. Kovalchuk, T. Wang, J.M. Tour, O. Regev, Graphene nanoribbon-Polymer composites: The critical role of edge functionalization, Carbon N Y. 99 (2016) 444–450. https://doi.org/10.1016/j.carbon.2015.12.039.

[171] A.K. Barick, D.K. Tripathy, Preparation, characterization and properties of acid functionalized multi-walled carbon nanotube reinforced thermoplastic polyurethane nanocomposites, Mater Sci Eng B Solid State Mater Adv Technol. 176 (2011) 1435–1447. https://doi.org/10.1016/j.mseb.2011.08.001.

[172] M. Cao, C. Han, X. Wang, M. Zhang, Y. Zhang, J. Shu, H. Yang, X. Fang, J. Yuan, Graphene nanohybrids: Excellent electromagnetic properties for the absorbing and shielding of electromagnetic waves, J Mater Chem C Mater. 6 (2018) 4586–4602. https://doi.org/10.1039/c7tc05869a.

[173] M. Cao, C. Han, X. Wang, M. Zhang, Y. Zhang, J. Shu, H. Yang, X. Fang, J. Yuan, Graphene nanohybrids: Excellent electromagnetic properties for the absorbing and shielding of electromagnetic waves, J Mater Chem C Mater. 6 (2018) 4586–4602. https://doi.org/10.1039/c7tc05869a.

[174] S. Biswas, I. Arief, S.S. Panja, S. Bose, Absorption-dominated electromagnetic wave suppressor derived from ferrite-doped cross-linked graphene framework and conducting

carbon, ACS Appl Mater Interfaces. 9 (2017) 3030–3039. https://doi.org/10.1021/acsami.6b14853.

[175] B. Zhao, W. Zhao, G. Shao, B. Fan, R. Zhang, Corrosive synthesis and enhanced electromagnetic absorption properties of hollow porous Ni/SnO2 hybrids, Dalton Transactions. 44 (2015) 15984–15993. https://doi.org/10.1039/c5dt02715b.

[176] B. Wen, X.X. Wang, W.Q. Cao, H.L. Shi, M.M. Lu, G. Wang, H.B. Jin, W.Z. Wang, J. Yuan, M.S. Cao, Reduced graphene oxides: The thinnest and most lightweight materials with highly efficient microwave attenuation performances of the carbon world, Nanoscale. 6 (2014) 5754–5761. https://doi.org/10.1039/c3nr06717c.

[177] H. Bin Zhang, W.G. Zheng, Q. Yan, Z.G. Jiang, Z.Z. Yu, The effect of surface chemistry of graphene on rheological and electrical properties of polymethylmethacrylate composites, Carbon N Y. 50 (2012) 5117–5125. https://doi.org/10.1016/j.carbon.2012.06.052.

[178] S.T. Hsiao, C.C.M. Ma, H.W. Tien, W.H. Liao, Y.S. Wang, S.M. Li, Y.C. Huang, Using a non-covalent modification to prepare a high electromagnetic interference shielding performance graphene nanosheet/water-borne polyurethane composite, Carbon N Y. 60 (2013) 57–66. https://doi.org/10.1016/j.carbon.2013.03.056.

[179] N.Ch. Das, Y. Liu, K. Yang, W. Peng, S. Maiti, H. Wang, Single-Walled Carbon Nanotube/Poly(methyl methacrylate) Composites for Electromagnetic Interference Shielding, Polym Eng Sci. 49 (2009) 1627–1634. https://doi.org/https://doi.org/10.1002/pen.21384.

[180] J. Liang, Y. Wang, Y. Huang, Y. Ma, Z. Liu, J. Cai, C. Zhang, H. Gao, Y. Chen, Electromagnetic interference shielding of graphene/epoxy composites, Carbon N Y. 47 (2009) 922–925. https://doi.org/10.1016/j.carbon.2008.12.038.

[181] M. Arjmand, M. Mahmoodi, G.A. Gelves, S. Park, U. Sundararaj, Electrical and electromagnetic interference shielding properties of flow-induced oriented carbon nanotubes in polycarbonate, Carbon N Y. 49 (2011) 3430–3440. https://doi.org/10.1016/j.carbon.2011.04.039.

[182] Y. Li, B. Shen, D. Yi, L. Zhang, W. Zhai, X. Wei, W. Zheng, The influence of gradient and sandwich configurations on the electromagnetic interference shielding performance of

multilayered thermoplastic polyurethane/graphene composite foams, Compos Sci Technol. 138 (2017) 209–216. https://doi.org/10.1016/j.compscitech.2016.12.002.

[183] W. Yang, B. Shao, T. Liu, Y. Zhang, R. Huang, F. Chen, Q. Fu, Robust and Mechanically and Electrically Self-Healing Hydrogel for Efficient Electromagnetic Interference Shielding, ACS Appl Mater Interfaces. 10 (2018) 8245–8257. https://doi.org/10.1021/acsami.7b18700.

[184] M. Verma, S.S. Chauhan, S.K. Dhawan, V. Choudhary, Graphene nanoplatelets/carbon nanotubes/polyurethane composites as efficient shield against electromagnetic polluting radiations, Compos B Eng. 120 (2017) 118–127. https://doi.org/10.1016/j.compositesb.2017.03.068.

[185] M. Verma, S.S. Chauhan, S.K. Dhawan, V. Choudhary, Graphene nanoplatelets/carbon nanotubes/polyurethane composites as efficient shield against electromagnetic polluting radiations, Compos B Eng. 120 (2017) 118–127. https://doi.org/10.1016/j.compositesb.2017.03.068.

[186] Z. Liu, G. Bai, Y. Huang, Y. Ma, F. Du, F. Li, T. Guo, Y. Chen, Reflection and absorption contributions to the electromagnetic interference shielding of single-walled carbon nanotube/polyurethane composites, Carbon N Y. 45 (2007) 821–827. https://doi.org/10.1016/j.carbon.2006.11.020.

[187] A. Joshi, A. Bajaj, R. Singh, P.S. Alegaonkar, K. Balasubramanian, S. Datar, Graphene nanoribbon-PVA composite as EMI shielding material in the X band., Nanotechnology. 24 (2013) 455705. https://doi.org/10.1088/0957-4484/24/45/455705.

[188] A. Joshi, A. Bajaj, R. Singh, A. Anand, P.S. Alegaonkar, S. Datar, Processing of graphene nanoribbon based hybrid composite for electromagnetic shielding, Compos B Eng. 69 (2015) 472–477. https://doi.org/10.1016/j.compositesb.2014.09.014.

[189] M. Arjmand, S. Sadeghi, I.O. Navas, Y.Z. Keteklahijani, S. Dordanihaghighi, U. Sundararaj, Carbon nanotube versus graphene nanoribbon: Impact of nanofiller geometry on electromagnetic interference shielding of polyvinylidene fluoride nanocomposites, Polymers (Basel). 11 (2019). https://doi.org/10.3390/POLYM11061064.

[190] T. Kuang, L. Chang, F. Chen, Y. Sheng, D. Fu, X. Peng, Facile preparation of lightweight high-strength biodegradable polymer/multi-walled carbon nanotubes nanocomposite foams for

electromagnetic interference shielding, Carbon N Y. 105 (2016) 305–313. https://doi.org/10.1016/j.carbon.2016.04.052.

[191] M. a Rafiee, W. Lu, A. V Thomas, A. Zandiatashbar, J. Rafiee, J.M. Tour, N. a Koratkar, Graphene Nanoribbon Composites, ACS Nano. 4 (2010) 7415–7420. https://doi.org/10.1021/nn102529n.

[192] J.H. Choe, J. Jeon, M.E. Lee, J.J. Wie, H.J. Jin, Y.S. Yun, Nanoconfinement effects of chemically reduced graphene oxide nanoribbons on poly(vinyl chloride), Nanoscale. 10 (2018) 2025–2033. https://doi.org/10.1039/c7nr07098e.

[193] S. Kanagaraj, F.R. Varanda, T. V. Zhil'tsova, M.S.A. Oliveira, J.A.O. Simões, Mechanical properties of high density polyethylene/carbon nanotube composites, Compos Sci Technol. 67 (2007) 3071–3077. https://doi.org/10.1016/j.compscitech.2007.04.024.

[194] D. V. Kosynkin, W. Lu, A. Sinitskii, G. Pera, Z. Sun, J.M. Tour, Highly conductive graphene nanoribbons by longitudinal splitting of carbon nanotubes using potassium vapor, ACS Nano. 5 (2011) 968–974. https://doi.org/10.1021/nn102326c.

[195] M.A. Rafiee, J. Rafiee, Z. Wang, H. Song, Z.Z. Yu, N. Koratkar, Enhanced mechanical properties of nanocomposites at low graphene content, ACS Nano. 3 (2009) 3884–3890. https://doi.org/10.1021/nn9010472.

[196] M. Arjmand, S. Sadeghi, M. Khajehpour, U. Sundararaj, Carbon nanotube/graphene nanoribbon/polyvinylidene fluoride hybrid nanocomposites: Rheological and dielectric properties, Journal of Physical Chemistry C. 121 (2017) 169–181. https://doi.org/10.1021/acs.jpcc.6b10741.

[197] A. Iqbal, J. Kwon, M.K. Kim, C.M. Koo, MXenes for electromagnetic interference shielding: Experimental and theoretical perspectives, Mater Today Adv. 9 (2021) 100124. https://doi.org/10.1016/j.mtadv.2020.100124.

[198] G.Y. Li, J. Li, Z.J. Li, Y.P. Zhang, X. Zhang, Z.J. Wang, W.P. Han, B. Sun, Y.Z. Long, H. Di Zhang, Hierarchical PVDF-HFP/ZnO composite nanofiber–based highly sensitive piezoelectric sensor for wireless workout monitoring, Adv Compos Hybrid Mater. (2021). https://doi.org/10.1007/s42114-021-00331-z.

[199] L. Ma, M. Hamidinejad, C. Liang, B. Zhao, S. Habibpour, A. Yu, T. Filleter, C.B. Park, Enhanced electromagnetic wave absorption performance of polymer/SiC-nanowire/MXene (Ti3C2Tx) composites, Carbon N Y. 179 (2021) 408–416. https://doi.org/https://doi.org/10.1016/j.carbon.2021.04.063.

[200] M. Han, C.E. Shuck, R. Rakhmanov, D. Parchment, B. Anasori, C.M. Koo, G. Friedman, Y. Gogotsi, Beyond Ti3C2Tx: MXenes for Electromagnetic Interference Shielding, 2020. https://doi.org/10.1021/acsnano.0c01312.

[201] M.S. Cao, Y.Z. Cai, P. He, J.C. Shu, W.Q. Cao, J. Yuan, 2D MXenes: Electromagnetic property for microwave absorption and electromagnetic interference shielding, Chemical Engineering Journal. 359 (2019) 1265–1302. https://doi.org/10.1016/j.cej.2018.11.051.

[202] Y. seok Jun, S. Habibpour, M. Hamidinejad, M.G. Park, W. Ahn, A. Yu, C.B. Park, Enhanced electrical and mechanical properties of graphene nano-ribbon/thermoplastic polyurethane composites, Carbon N Y. 174 (2021) 305–316. https://doi.org/10.1016/j.carbon.2020.12.023.

[203] M. Carey, M.W. Barsoum, MXene polymer nanocomposites: a review, Mater Today Adv. 9 (2021) 100120. https://doi.org/10.1016/j.mtadv.2020.100120.

[204] M. Sang, S. Wang, S. Liu, M. Liu, L. Bai, W. Jiang, S. Xuan, X. Gong, A Hydrophobic, Self-Powered, Electromagnetic Shielding PVDF-Based Wearable Device for Human Body Monitoring and Protection, ACS Appl Mater Interfaces. 11 (2019) 47340–47349. https://doi.org/10.1021/acsami.9b16120.

[205] Z. Jia, C. Wang, A. Feng, P. Shi, C. Zhang, X. Liu, K. Wang, G. Wu, A low-dielectric decoration strategy to achieve absorption dominated electromagnetic shielding material, Compos B Eng. 183 (2020) 107690. https://doi.org/https://doi.org/10.1016/j.compositesb.2019.107690.

[206] L. Gao, C. Li, W. Huang, S. Mei, H. Lin, Q. Ou, Y. Zhang, J. Guo, F. Zhang, S. Xu, H. Zhang, MXene/Polymer Membranes: Synthesis, Properties, and Emerging Applications, Chemistry of Materials. 32 (2020) 1703–1747. https://doi.org/10.1021/acs.chemmater.9b04408.

[207] A. Ghaffarkhah, M. Kamkar, Z.A. Dijvejin, H. Riazi, S. Ghaderi, K. Golovin, M. Soroush, M. Arjmand, High-resolution extrusion printing of Ti3C2-based inks for wearable human motion

monitoring and electromagnetic interference shielding, Carbon N Y. 191 (2022) 277–289. https://doi.org/10.1016/j.carbon.2022.02.003.

[208] Y. Li, B. Zhou, Y. Shen, C. He, B. Wang, C. Liu, Y. Feng, C. Shen, Scalable manufacturing of flexible, durable Ti3C2Tx MXene/Polyvinylidene fluoride film for multifunctional electromagnetic interference shielding and electro/photo-thermal conversion applications, Compos B Eng. 217 (2021) 108902. https://doi.org/10.1016/j.compositesb.2021.108902.

[209] J. Chen, Y. Zhu, X. Chang, D. Pan, G. Song, Z. Guo, N. Naik, Recent Progress in Essential Functions of Soft Electronic Skin, Adv Funct Mater. 31 (2021) 1–34. https://doi.org/10.1002/adfm.202104686.

[210] H. Xu, X. Yin, X. Li, M. Li, S. Liang, L. Zhang, L. Cheng, Lightweight Ti 2 CT x MXene/Poly(vinyl alcohol) Composite Foams for Electromagnetic Wave Shielding with Absorption-Dominated Feature, ACS Appl Mater Interfaces. 11 (2019) 10198–10207. https://doi.org/10.1021/acsami.8b21671.

[211] K. Rajavel, S. Luo, Y. Wan, X. Yu, Y. Hu, P. Zhu, R. Sun, C. Wong, 2D Ti3C2Tx MXene/polyvinylidene fluoride (PVDF) nanocomposites for attenuation of electromagnetic radiation with excellent heat dissipation, Compos Part A Appl Sci Manuf. 129 (2020) 105693. https://doi.org/10.1016/j.compositesa.2019.105693.

[212] H. Cheng, Y. Pan, Q. Chen, R. Che, G. Zheng, C. Liu, C. Shen, X. Liu, Ultrathin flexible poly(vinylidene fluoride)/MXene/silver nanowire film with outstanding specific EMI shielding and high heat dissipation, Adv Compos Hybrid Mater. (2021). https://doi.org/10.1007/s42114-021-00224-1.

[213] G. Yin, Y. Wang, W. Wang, D. Yu, Multilayer structured PANI/MXene/CF fabric for electromagnetic interference shielding constructed by layer-by-layer strategy, Colloids Surf A Physicochem Eng Asp. 601 (2020) 125047. https://doi.org/10.1016/j.colsurfa.2020.125047.

[214] Y. Guo, D. Wang, T. Bai, H. Liu, Y. Zheng, C. Liu, C. Shen, Electrostatic self-assembled NiFe2O4/Ti3C2Tx MXene nanocomposites for efficient electromagnetic wave absorption at ultralow loading level, Adv Compos Hybrid Mater. 4 (2021) 602–613. https://doi.org/10.1007/s42114-021-00279-0.

[215] J. Wang, H. Kang, H. Ma, Y. Liu, Z. Xie, Y. Wang, Z. Fan, Super-fast fabrication of mxene film through a combination of ion induced gelation and vacuum-assisted filtration, Engineered Science. 15 (2021) 57–66. https://doi.org/10.30919/es8d446.

[216] M. Naguib, O. Mashtalir, J. Carle, V. Presser, J. Lu, L. Hultman, Y. Gogotsi, M.W. Barsoum, Two-dimensional transition metal carbides, ACS Nano. 6 (2012) 1322–1331. https://doi.org/10.1021/nn204153h.

[217] L. Wang, L. Chen, P. Song, C. Liang, Y. Lu, H. Qiu, Y. Zhang, J. Kong, J. Gu, Fabrication on the annealed Ti3C2Tx MXene/Epoxy nanocomposites for electromagnetic interference shielding application, Compos B Eng. 171 (2019) 111–118. https://doi.org/https://doi.org/10.1016/j.compositesb.2019.04.050.

[218] J.Q. Luo, S. Zhao, H. Bin Zhang, Z. Deng, L. Li, Z.Z. Yu, Flexible, stretchable and electrically conductive MXene/natural rubber nanocomposite films for efficient electromagnetic interference shielding, Compos Sci Technol. 182 (2019) 107754. https://doi.org/10.1016/j.compscitech.2019.107754.

[219] Y. Tong, M. He, Y. Zhou, X. Zhong, L. Fan, T. Huang, Q. Liao, Y. Wang, Hybridizing polypyrrole chains with laminated and two-dimensional Ti 3 C 2 T x toward high-performance electromagnetic wave absorption, Appl Surf Sci. 434 (2018) 283–293. https://doi.org/10.1016/j.apsusc.2017.10.140.

[220] S. Kumar, Arti, P. Kumar, N. Singh, V. Verma, Steady microwave absorption behavior of two-dimensional metal carbide MXene and Polyaniline composite in X-band, J Magn Magn Mater. 488 (2019) 165364. https://doi.org/10.1016/j.jmmm.2019.165364.

[221] M.K. Xu, J. Liu, H. Bin Zhang, Y. Zhang, X. Wu, Z. Deng, Z.Z. Yu, Electrically Conductive Ti3C2TxMXene/Polypropylene Nanocomposites with an Ultralow Percolation Threshold for Efficient Electromagnetic Interference Shielding, Ind Eng Chem Res. 60 (2021) 4342–4350. https://doi.org/10.1021/acs.iecr.1c00320.

[222] Y. Zhang, L. Wang, J. Zhang, P. Song, Z. Xiao, C. Liang, H. Qiu, J. Kong, J. Gu, Fabrication and investigation on the ultra-thin and flexible Ti3C2Tx/co-doped polyaniline electromagnetic interference shielding composite films, Compos Sci Technol. 183 (2019) 107833. https://doi.org/10.1016/j.compscitech.2019.107833.

[223] F. Shahzad, M. Alhabeb, C.B. Hatter, B. Anasori, S.M. Hong, C.M. Koo, Y. Gogotsi, Electromagnetic interference shielding with 2D transition metal carbides (MXenes), Science (1979). 353 (2016) 1137–1140. https://doi.org/10.1126/science.aag2421.

[224] R. Sun, H. Bin Zhang, J. Liu, X. Xie, R. Yang, Y. Li, S. Hong, Z.Z. Yu, Highly Conductive Transition Metal Carbide/Carbonitride(MXene)@polystyrene Nanocomposites Fabricated by Electrostatic Assembly for Highly Efficient Electromagnetic Interference Shielding, Adv Funct Mater. 27 (2017) 1–11. https://doi.org/10.1002/adfm.201702807.

[225] G.S. Lee, T. Yun, H. Kim, I.H. Kim, J. Choi, S.H. Lee, H.J. Lee, H.S. Hwang, J.G. Kim, D.W. Kim, H.M. Lee, C.M. Koo, S.O. Kim, Mussel Inspired Highly Aligned Ti3C2TxMXene Film with Synergistic Enhancement of Mechanical Strength and Ambient Stability, ACS Nano. 14 (2020) 11722–11732. https://doi.org/10.1021/acsnano.0c04411.

[226] Y. Wang, Q. Qi, G. Yin, W. Wang, D. Yu, Flexible, Ultralight, and Mechanically Robust Waterborne Polyurethane/Ti3C2T xMXene/Nickel Ferrite Hybrid Aerogels for High-Performance Electromagnetic Interference Shielding, ACS Appl Mater Interfaces. 13 (2021) 21831–21843. https://doi.org/10.1021/acsami.1c04962.

[227] Z. He, H. Xie, H. Wu, J. Chen, S. Ma, X. Duan, A. Chen, Z. Kong, Recent Advances in MXene/Polyaniline-Based Composites for Electrochemical Devices and Electromagnetic Interference Shielding Applications, ACS Omega. 6 (2021) 22468–22477. https://doi.org/10.1021/acsomega.1c02996.

[228] Q. Xue, H. Zhang, M. Zhu, Z. Pei, H. Li, Z. Wang, Y. Huang, Y. Huang, Q. Deng, J. Zhou, S. Du, Q. Huang, C. Zhi, Photoluminescent Ti3C2 MXene Quantum Dots for Multicolor Cellular Imaging, Advanced Materials. 29 (2017) 1604847. https://doi.org/10.1002/adma.201604847.

[229] R. Liu, M. Miao, Y. Li, J. Zhang, S. Cao, X. Feng, Ultrathin Biomimetic Polymeric Ti 3 C 2 T x MXene Composite Films for Electromagnetic Interference Shielding, ACS Appl Mater Interfaces. 10 (2018) 44787–44795. https://doi.org/10.1021/acsami.8b18347.

[230] Y. Li, Y. Qing, W. Li, M. Zong, F. Luo, Novel Magnéli Ti4O7/Ni/poly(vinylidene fluoride) hybrids for high-performance electromagnetic wave absorption, Adv Compos Hybrid Mater. 4 (2021) 1027–1038. https://doi.org/10.1007/s42114-021-00297-y.

[231] K. Zarshenas, H. Dou, S. Habibpour, A. Yu, Z. Chen, Thin Film Polyamide Nanocomposite Membrane Decorated by Polyphenol-Assisted Ti3C2TxMXene Nanosheets for Reverse Osmosis, ACS Appl Mater Interfaces. 14 (2022) 1838–1849. https://doi.org/10.1021/acsami.1c16229.

[232] M. Cai, H. Yan, Y. Li, W. Li, H. Li, X. Fan, M. Zhu, Ti3C2Tx/PANI composites with tunable conductivity towards anticorrosion application, Chemical Engineering Journal. 410 (2021) 128310. https://doi.org/10.1016/j.cej.2020.128310.

[233] S. Tu, Q. Jiang, X. Zhang, H.N. Alshareef, Large Dielectric Constant Enhancement in MXene Percolative Polymer Composites, ACS Nano. 12 (2018) 3369–3377. https://doi.org/10.1021/acsnano.7b08895.

[234] C.J. Zhang, S. Pinilla, N. McEvoy, C.P. Cullen, B. Anasori, E. Long, S.H. Park, A. Seral-Ascaso, A. Shmeliov, D. Krishnan, C. Morant, X. Liu, G.S. Duesberg, Y. Gogotsi, V. Nicolosi, Oxidation Stability of Colloidal Two-Dimensional Titanium Carbides (MXenes), Chemistry of Materials. 29 (2017) 4848–4856. https://doi.org/10.1021/acs.chemmater.7b00745.

[235] C.W. Wu, B. Unnikrishnan, I.W.P. Chen, S.G. Harroun, H.T. Chang, C.C. Huang, Excellent oxidation resistive MXene aqueous ink for micro-supercapacitor application, Energy Storage Mater. 25 (2020) 563–571. https://doi.org/10.1016/j.ensm.2019.09.026.

[236] A. Lipatov, M. Alhabeb, M.R. Lukatskaya, A. Boson, Y. Gogotsi, A. Sinitskii, Effect of Synthesis on Quality, Electronic Properties and Environmental Stability of Individual Monolayer Ti3C2 MXene Flakes, Adv Electron Mater. 2 (2016). https://doi.org/10.1002/aelm.201600255.

[237] M.H. Mohamadzadeh Moghadam, S. Sabury, M.M. Gudarzi, F. Sharif, Graphene oxide-induced polymerization and crystallization to produce highly conductive polyaniline/graphene oxide composite, J Polym Sci A Polym Chem. 52 (2014) 1545–1554. https://doi.org/10.1002/pola.27147.

[238] C. Chen, M. Boota, X. Xie, M. Zhao, B. Anasori, C.E. Ren, L. Miao, J. Jiang, Y. Gogotsi, Charge transfer induced polymerization of EDOT confined between 2D titanium carbide layers, J Mater Chem A Mater. 5 (2017) 5260–5265. https://doi.org/10.1039/c7ta00149e.

[239] M. Boota, B. Anasori, C. Voigt, M. Zhao, M.W. Barsoum, Y. Gogotsi, Pseudocapacitive Electrodes Produced by Oxidant-Free Polymerization of Pyrrole between the Layers of 2D Titanium Carbide (MXene), Advanced Materials. 28 (2016) 1517–1522. https://doi.org/10.1002/adma.201504705.

[240] Y. Liao, D.G. Yu, X. Wang, W. Chain, X.G. Li, E.M.V. Hoek, R.B. Kaner, Carbon nanotube-templated polyaniline nanofibers: Synthesis, flash welding and ultrafiltration membranes, Nanoscale. 5 (2013) 3856–3862. https://doi.org/10.1039/c3nr00441d.

[241] A. Vahidmohammadi, J. Moncada, H. Chen, E. Kayali, J. Orangi, C.A. Carrero, M. Beidaghi, Thick and freestanding MXene/PANI pseudocapacitive electrodes with ultrahigh specific capacitance, J Mater Chem A Mater. 6 (2018) 22123–22133. https://doi.org/10.1039/c8ta05807e.

[242] H. Xu, D. Zheng, F. Liu, W. Li, J. Lin, Synthesis of an MXene/polyaniline composite with excellent electrochemical properties, J Mater Chem A Mater. 8 (2020) 5853–5858. https://doi.org/10.1039/d0ta00572j.

[243] M. Shekhirev, C.E. Shuck, A. Sarycheva, Y. Gogotsi, Characterization of MXenes at every step, from their precursors to single flakes and assembled films, Prog Mater Sci. (2020) 100757. https://doi.org/10.1016/j.pmatsci.2020.100757.

[244] J.M. Jeong, B.G. Choi, S.C. Lee, K.G. Lee, S.J. Chang, Y.K. Han, Y.B. Lee, H.U. Lee, S. Kwon, G. Lee, C.S. Lee, Y.S. Huh, Hierarchical hollow spheres of Fe2O3@polyaniline for lithium ion battery anodes, Advanced Materials. 25 (2013) 6250–6255. https://doi.org/10.1002/adma.201302710.

[245] M. Shtein, R. Nadiv, N. Lachman, H. Daniel Wagner, O. Regev, Fracture behavior of nanotube-polymer composites: Insights on surface roughness and failure mechanism, Compos Sci Technol. 87 (2013) 157–163. https://doi.org/10.1016/j.compscitech.2013.07.016.

[246] Y.S. Jun, J.G. Um, G. Jiang, G. Lui, A. Yu, Ultra-large sized graphene nano-platelets (GnPs) incorporated polypropylene (PP)/GnPs composites engineered by melt compounding and its thermal, mechanical, and electrical properties, Compos B Eng. 133 (2018) 218–225. https://doi.org/10.1016/j.compositesb.2017.09.028.

[247] A. Iqbal, P. Sambyal, C.M. Koo, 2D MXenes for Electromagnetic Shielding : A Review, Adv Funct Mater. 2000883 (2020) 1–25. https://doi.org/10.1002/adfm.202000883.

[248] M.R. Lukatskaya, O. Mashtalir, C.E. Ren, Y. Dall'Agnese, P. Rozier, P.L. Taberna, M. Naguib, P. Simon, M.W. Barsoum, Y. Gogotsi, Cation intercalation and high volumetric capacitance of two-dimensional titanium carbide, Science (1979). 341 (2013) 1502–1505. https://doi.org/10.1126/science.1241488.

[249] M. Malaki, A. Maleki, R.S. Varma, MXenes and ultrasonication, J Mater Chem A Mater. 7 (2019) 10843–10857. https://doi.org/10.1039/c9ta01850f.

[250] C.E. Shuck, A. Sarycheva, M. Anayee, A. Levitt, Y. Zhu, S. Uzun, V. Balitskiy, V. Zahorodna, O. Gogotsi, Y. Gogotsi, Scalable Synthesis of Ti3C2Tx MXene, Adv Eng Mater. 22 (2020) 1–8. https://doi.org/10.1002/adem.201901241.

[251] W. Wu, C. Wang, C. Zhao, D. Wei, J. Zhu, Y. Xu, Facile strategy of hollow polyaniline nanotubes supported on Ti3C2-MXene nanosheets for High-performance symmetric supercapacitors, J Colloid Interface Sci. 580 (2020) 601–613. https://doi.org/10.1016/j.jcis.2020.07.052.

[252] M. Hamidinejad, B. Zhao, A. Zandieh, N. Moghimian, T. Filleter, C.B. Park, Enhanced Electrical and Electromagnetic Interference Shielding Properties of Polymer-Graphene Nanoplatelet Composites Fabricated via Supercritical-Fluid Treatment and Physical Foaming, ACS Appl Mater Interfaces. 10 (2018) 30752–30761. https://doi.org/10.1021/acsami.8b10745.

[253] Ying Wu, Shaw Ling Hsu, The Role of Surface Charge of Nucleation Agents on the Crystallization Behavior of Poly(vinylidene fluoride), Journal of Physiscal Chemistry B. 116 (2012) 7379–7388. https://doi.org/10.1021/jp3043494.

[254] S. Cheng, B. Carroll, W. Lu, F. Fan, J.M.Y. Carrillo, H. Martin, A.P. Holt, N.G. Kang, V. Bocharova, J.W. Mays, B.G. Sumpter, M. Dadmun, A.P. Sokolov, Interfacial Properties of Polymer Nanocomposites: Role of Chain Rigidity and Dynamic Heterogeneity Length Scale, Macromolecules. 50 (2017) 2397–2406. https://doi.org/10.1021/acs.macromol.6b02816.

[255] JR. R. GREGORIO, E. M. UENO, Effect of crystalline phase, orientation and temperature on the dielectric properties of poly (vinylidene fluoride) (PVDF), Material Science. 34 (1999) 4489–4500.

[256] N. Maity, A. Mandal, A.K. Nandi, Hierarchical nanostructured polyaniline functionalized graphene / poly (vinylidene fl uoride) composites for improved dielectric performances, Polymer (Guildf). 103 (2016) 83–97. https://doi.org/10.1016/j.polymer.2016.09.048.

[257] S. Habibpour, J. Zabihirad, N. Mohammadi, H. Mohammadi, Modeling of polystyrenic nanoparticles driven β-trans-crystalline efficiency in isotactic polypropylene, RSC Adv. 6 (2016) 72500–72509. https://doi.org/10.1039/c6ra12219a.

[258] J. Guo, Z. Chen, X. Xu, X. Li, H. Liu, S. Xi, W. Abdul, Q. Wu, P. Zhang, B. Bin Xu, J. Zhu, Z. Guo, Enhanced electromagnetic wave absorption of engineered epoxy nanocomposites with the assistance of polyaniline fillers, Adv Compos Hybrid Mater. (2022). https://doi.org/10.1007/s42114-022-00417-2.

[259] M. Han, D. Zhang, C.E. Shuck, B. McBride, T. Zhang, R. (John) Wang, K. Shevchuk, Y. Gogotsi, Electrochemically modulated interaction of MXenes with microwaves, Nat Nanotechnol. (2023). https://doi.org/10.1038/s41565-022-01308-9.

[260] D. Munalli, G. Dimitrakis, D. Chronopoulos, S. Greedy, A. Long, Electromagnetic shielding effectiveness of carbon fibre reinforced composites, Compos B Eng. 173 (2019) 106906. https://doi.org/10.1016/j.compositesb.2019.106906.

[261] M. Yang, Y. Yuan, Y. Li, X. Sun, S. Wang, L. Liang, Y. Ning, J. Li, W. Yin, Y. Li, Anisotropic Electromagnetic Absorption of Aligned Ti3C2T xMXene/Gelatin Nanocomposite Aerogels, ACS Appl Mater Interfaces. 12 (2020) 33128–33138. https://doi.org/10.1021/acsami.0c09726.

[262] G.M. Weng, J. Li, M. Alhabeb, C. Karpovich, H. Wang, J. Lipton, K. Maleski, J. Kong, E. Shaulsky, M. Elimelech, Y. Gogotsi, A.D. Taylor, Layer-by-Layer Assembly of Cross-Functional Semi-transparent MXene-Carbon Nanotubes Composite Films for Next-Generation Electromagnetic Interference Shielding, Adv Funct Mater. 28 (2018) 1–9. https://doi.org/10.1002/adfm.201803360.

[263] Z. Chen, C. Xu, C. Ma, W. Ren, H.M. Cheng, Lightweight and flexible graphene foam composites for high-performance electromagnetic interference shielding, Advanced Materials. 25 (2013) 1296–1300. https://doi.org/10.1002/adma.201204196.

[264] X. Wu, B. Han, H. Bin Zhang, X. Xie, T. Tu, Y. Zhang, Y. Dai, R. Yang, Z.Z. Yu, Compressible, durable and conductive polydimethylsiloxane-coated MXene foams for high-performance electromagnetic interference shielding, Chemical Engineering Journal. 381 (2020) 122622. https://doi.org/10.1016/j.cej.2019.122622.

[265] B.V.S.R.N. Santhosi, K. Ramji, N.B.R.M. Rao, Design and development of polymeric nanocomposite reinforced with graphene for effective EMI shielding in X-band, Physica B Condens Matter. 586 (2020) 412144. https://doi.org/10.1016/j.physb.2020.412144.

[266] C. Fan, B. Wu, R. Song, Y. Zhao, Y. Zhang, D. He, Electromagnetic shielding and multi-beam radiation with high conductivity multilayer graphene film, Carbon N Y. 155 (2019) 506–513. https://doi.org/https://doi.org/10.1016/j.carbon.2019.09.019.

[267] A. Iqbal, F. Shahzad, K. Hantanasirisakul, M.-K. Kim, J. Kwon, J. Hong, H. Kim, D. Kim, Y. Gogotsi, C.M. Koo, Anomalous absorption of electromagnetic waves by 2D transition metal carbonitride Ti3CNTx (MXene), Science (1979). 369 (2020) 446–450. https://doi.org/10.1126/science.aba7977.

[268] S. Zhao, H. Bin Zhang, J.Q. Luo, Q.W. Wang, B. Xu, S. Hong, Z.Z. Yu, Highly Electrically Conductive Three-Dimensional Ti3C2Tx MXene/Reduced Graphene Oxide Hybrid Aerogels with Excellent Electromagnetic Interference Shielding Performances, ACS Nano. 12 (2018) 11193–11202. https://doi.org/10.1021/acsnano.8b05739.

[269] U. Hwang, J. Kim, M. Seol, B. Lee, I.K. Park, J. Suhr, J. Do Nam, Quantitative Interpretation of Electromagnetic Interference Shielding Efficiency: Is It Really a Wave Absorber or a Reflector?, ACS Omega. 7 (2022) 4135–4139. https://doi.org/10.1021/acsomega.1c05657.

[270] H. Liu, Z. Huang, T. Chen, X. Su, Y. Liu, R. Fu, Construction of 3D MXene/Silver nanowires aerogels reinforced polymer composites for extraordinary electromagnetic interference shielding and thermal conductivity, Chemical Engineering Journal. 427 (2022) 131540. https://doi.org/10.1016/j.cej.2021.131540.

[271] H. Niu, X. Tu, S. Zhang, Y. Li, H. Wang, G. Shao, R. Zhang, H. Li, B. Zhao, B. Fan, Engineered core-shell SiO2@Ti3C2Tx composites: Towards ultra-thin electromagnetic wave absorption materials, Chemical Engineering Journal. 446 (2022) 137260. https://doi.org/10.1016/j.cej.2022.137260.

[272] F. Wu, Z. Tian, P. Hu, J. Tang, X. Xu, L. Pan, J. Liu, P. Zhang, Z. Sun, Lightweight and Flexible PAN@PPy/MXene Films with Outstanding Electromagnetic Interference Shielding and Joule Heating Performance, Nanoscale. (2022) 18133–18142. https://doi.org/10.1039/d2nr05318g.

[273] Z. Deng, P. Tang, X. Wu, H. Bin Zhang, Z.Z. Yu, Superelastic, Ultralight, and Conductive Ti3C2T xMXene/Acidified Carbon Nanotube Anisotropic Aerogels for Electromagnetic Interference Shielding, ACS Appl Mater Interfaces. 13 (2021) 20539–20547. https://doi.org/10.1021/acsami.1c02059.

[274] B. Zhao, J. Deng, C. Zhao, C. Wang, Y.G. Chen, M. Hamidinejad, R. Li, C.B. Park, Achieving wideband microwave absorption properties in PVDF nanocomposite foams with an ultra-low MWCNT content by introducing a microcellular structure, J Mater Chem C Mater. 8 (2020) 58–70. https://doi.org/10.1039/C9TC04575A.

[275] B. Zhao, R. Wang, Y. Li, Y. Ren, X. Li, X. Guo, R. Zhang, C.B. Park, Dependence of electromagnetic interference shielding ability of conductive polymer composite foams with hydrophobic properties on cellular structure, J Mater Chem C Mater. 8 (2020) 7401–7410. https://doi.org/10.1039/d0tc00987c.

[276] Z. Zeng, C. Wang, G. Siqueira, D. Han, A. Huch, S. Abdolhosseinzadeh, J. Heier, F. Nüesch, C. Zhang, G. Nyström, Nanocellulose-MXene Biomimetic Aerogels with Orientation-Tunable Electromagnetic Interference Shielding Performance, Advanced Science. 7 (2020) 1–9. https://doi.org/10.1002/advs.202000979.

[277] L. Ma, M. Hamidinejad, B. Zhao, C. Liang, C.B. Park, Layered Foam/Film Polymer Nanocomposites with Highly Efficient EMI Shielding Properties and Ultralow Reflection, Nanomicro Lett. 14 (2022) 1–18. https://doi.org/10.1007/s40820-021-00759-4.

[278] H. Duan, H. Zhu, J. Gao, D.X. Yan, K. Dai, Y. Yang, G. Zhao, Y. Liu, Z.M. Li, Asymmetric conductive polymer composite foam for absorption dominated ultra-efficient electromagnetic interference shielding with extremely low reflection characteristics, J Mater Chem A Mater. 8 (2020) 9146–9159. https://doi.org/10.1039/d0ta01393e.

[279] L. Ma, M. Hamidinejad, L. Wei, B. Zhao, C.B. Park, Absorption-dominant EMI shielding polymer composite foams: Microstructure and geometry optimization, Materials Today Physics. 30 (2023). https://doi.org/10.1016/j.mtphys.2022.100940.

[280] M. Hamidinejad, Thermal and Electrical Properties of Graphene-Based Polymer Nanocomposite Foams, University of Toronto, 2018.

[281] M. Kierkowicz, E. Pach, A. Santidrián, S. Sandoval, G. Gonçalves, E. Tobías-Rossell, M. Kalbáč, B. Ballesteros, G. Tobias, Comparative study of shortening and cutting strategies of single-walled and multi-walled carbon nanotubes assessed by scanning electron microscopy, Carbon N Y. 139 (2018) 922–932. https://doi.org/10.1016/j.carbon.2018.06.021.

[282] M. Salari, S. Habibpour, M. Hamidinejad, S. Mohseni Taromsari, H.E. Naguib, A. Yu, C.B. Park, Enhanced Electrical Properties of Microcellular Polymer Nanocomposites via Nanocarbon Geometrical Alteration: A Comparison of Graphene Nanoribbon and its Parent Multiwalled Carbon Nanotube, Mater Horiz. (2023). https://doi.org/10.1039/d2mh01303g.

[283] D.C. Marcano, D. V. Kosynkin, J.M. Berlin, A. Sinitskii, Z. Sun, A. Slesarev, L.B. Alemany, W. Lu, J.M. Tour, Improved synthesis of graphene oxide, ACS Nano. 4 (2010) 4806–4814. https://doi.org/10.1021/nn1006368.

[284] J.G. Um, Y.S. Jun, A. Elkamel, A. Yu, Engineering investigation for the size effect of graphene oxide derived from graphene nanoplatelets in polyurethane composites, Canadian Journal of Chemical Engineering. (2019) 1–13. https://doi.org/10.1002/cjce.23696.

[285] S. Stankovich, D.A. Dikin, R.D. Piner, K.A. Kohlhaas, A. Kleinhammes, Y. Jia, Y. Wu, S.B.T. Nguyen, R.S. Ruoff, Synthesis of graphene-based nanosheets via chemical reduction of exfoliated graphite oxide, Carbon N Y. 45 (2007) 1558–1565. https://doi.org/10.1016/j.carbon.2007.02.034.

[286] W. Ma, K. Yang, H. Wang, H. Li, Poly(vinylidene fluoride- co-hexafluoropropylene)-MXene Nanosheet Composites for Microcapacitors, ACS Appl Nano Mater. 3 (2020) 7992–8003. https://doi.org/10.1021/acsanm.0c01459.

[287] R. Kang, Z. Zhang, L. Guo, J. Cui, Y. Chen, X. Hou, B. Wang, C. Te Lin, N. Jiang, J. Yu, Enhanced Thermal Conductivity of Epoxy Composites Filled with 2D Transition Metal

Carbides (MXenes) with Ultralow Loading, Sci Rep. 9 (2019) 1–14. https://doi.org/10.1038/s41598-019-45664-4.

[288] J. Zhang, N. Kong, S. Uzun, A. Levitt, S. Seyedin, P.A. Lynch, S. Qin, M. Han, W. Yang, J. Liu, X. Wang, Y. Gogotsi, J.M. Razal, Scalable Manufacturing of Free-Standing, Strong Ti3C2Tx MXene Films with Outstanding Conductivity, Advanced Materials. 32 (2020). https://doi.org/10.1002/adma.202001093.

[289] Y.S.Y.-S. Jun, M.G.G. Park, J.G.G. Um, S. Habibpour, S. Sy, C.B.B. Park, A. Yu, The conductivity of polydimethylsiloxane/graphene nano-ribbon foam composite with elongation, Carbon N Y. 162 (2020) 328–338. https://doi.org/10.1016/j.carbon.2020.02.024.

[290] C. Qiao, H. Wu, X. Xu, Z. Guan, W. Ou-Yang, Electrical Conductivity Enhancement and Electronic Applications of 2D Ti3C2Tx MXene Materials, Adv Mater Interfaces. 8 (2021) 1–19. https://doi.org/10.1002/admi.202100903.

[291] X. Zhao, D.E. Holta, Z. Tan, J.H. Oh, I.J. Echols, M. Anas, H. Cao, J.L. Lutkenhaus, M. Radovic, M.J. Green, Annealed Ti3C2TzMXene Films for Oxidation-Resistant Functional Coatings, ACS Appl Nano Mater. 3 (2020) 10578–10585. https://doi.org/10.1021/acsanm.0c02473.

[292] L. Qiu, J.Z. Liu, S.L.Y. Chang, Y. Wu, D. Li, Biomimetic superelastic graphene-based cellular monoliths, Nat Commun. 3 (2012) 1241. https://doi.org/10.1038/ncomms2251.

[293] D. Wang, Y. Lin, D. Hu, P. Jiang, X. Huang, Multifunctional 3D-MXene/PDMS nanocomposites for electrical, thermal and triboelectric applications, Compos Part A Appl Sci Manuf. 130 (2020) 105754. https://doi.org/10.1016/j.compositesa.2019.105754.

[294] Y. Jin, N. Xia, R.A. Gerhardt, Enhanced dielectric properties of polymer matrix composites with BaTiO3 and MWCNT hybrid fillers using simple phase separation, Nano Energy. 30 (2016) 407–416. https://doi.org/10.1016/j.nanoen.2016.10.033.

[295] S. Habibpour, K. Zarshenas, M. Zhang, M. Hamidinejad, L. Ma, C.B. Park, A. Yu, Greatly Enhanced Electromagnetic Interference Shielding Effectiveness and Mechanical Properties of Polyaniline-Grafted Ti3C2Tx MXene–PVDF Composites, ACS Appl Mater Interfaces. 14 (2022) 21521–21534. https://doi.org/10.1021/acsami.2c03121.

[296] M. Salari, N.D. Sansone, Z. Razzaz, S.M. Taromsori, M. Leroux, C.B. Park, P.C. Lee, Insights into synergy-induced multifunctional property enhancement mechanisms in hybrid graphene nanoplatelet reinforced polymer composites, Chemical Engineering Journal. 463 (2023) 142406. https://doi.org/10.1016/j.cej.2023.142406.

[297] M. Hamidinejad, M. Salari, L. Ma, N. Moghimian, B. Zhao, H.K. Taylor, T. Filleter, C.B. Park, Electrically and thermally graded microcellular polymer/graphene nanoplatelet composite foams and their EMI shielding properties, Carbon N Y. 187 (2022) 153–164. https://doi.org/10.1016/j.carbon.2021.10.075.

[298] B. Wang, G. Liang, Y. Jiao, A. Gu, L. Liu, L. Yuan, W. Zhang, Two-layer materials of polyethylene and a carbon nanotube/cyanate ester composite with high dielectric constant and extremely low dielectric loss, Carbon N Y. 54 (2013) 224–233. https://doi.org/10.1016/j.carbon.2012.11.033.

[299] M. Peng, F. Qin, Clarification of basic concepts for electromagnetic interference shielding effectiveness, J Appl Phys. 130 (2021) 225108. https://doi.org/10.1063/5.0075019.

[300] G. Xiong, Z. Yu, J.-S. Wang, L. Zhang, Phonon quarters-wave loss, New J Phys. 21 (2019) 093046. https://doi.org/10.1088/1367-2630/ab4330.